August 2017

Nanowired Human Cardiac Spheroids for Cardiac Regenerative Medicine

Yu Tan
Clemson University, tan3@g.clemson.edu

NANOWIRED HUMAN CARDIAC SPHEROIDS FOR CARDIAC REGENERATIVE MEDICINE

A Dissertation
Presented to
the Graduate School of
Clemson University

In Partial Fulfillment
of the Requirements for the Degree
Doctor of Philosophy
Bioengineering

---

by
Yu Tan
August 2017

Accepted by:
Dr. Ying Mei, Committee Chair
Dr. Hai Yao
Dr. Martine LaBerge
Dr. Donald Menick

ABSTRACT

3D scaffold-free spherical micro-tissue (spheroids) holds great potential in tissue engineering as building blocks to fabricate the functional tissues or organs *in vitro*. To date, agarose based hydrogel molds have been extensively used to facilitate fusion process of tissue spheroids. As a molding material, agarose typically requires low temperature plates for gelation and/or heated dispenser units. Here, we developed an alginate-based, direct 3D mold-printing technology: 3D printing micro-droplets of alginate solution into biocompatible, bio-inert alginate hydrogel molds for the fabrication of scaffold-free tissue engineering constructs. Specifically, we developed a 3D printing technology to deposit micro-droplets of alginate solution on calcium containing substrates in a layer-by-layer fashion to prepare ring-shaped 3D agarose hydrogel molds. Tissue spheroids composed of 50% human endothelial cells and 50% human smooth muscle cells were robotically dispensed into the 3D printed alginate molds using a 3D printer, and were found to rapidly fuse into toroid-shaped tissue units. Histological and immunofluorescence analysis indicated that the cells secreted collagen type I playing a critical role in promoting cell-cell adhesion, tissue formation and maturation.

The current inability to derive mature cardiomyocytes (CMs) from human pluripotent stem cells (hiPSC) has been the limiting step for transitioning this powerful technology into clinical therapies. To address this, scaffold-based tissue engineering approaches have been utilized to mimic heart development in vitro and promote maturation of CMs derived from hiPSC. While scaffolds can provide 3D microenvironments, current scaffolds lack the matched physical/chemical/biological

properties of native extracellular environments. On the other hand, scaffold-free, 3D cardiac spheroids prepared by seeding CMs into agarose microwells were shown to improve cardiac functions. However, CMs within the spheroids could not assemble in a controlled manner and led to compromised, unsynchronized contractions. Here we show, for the first time, that incorporation of a trace amount (i.e., ~0.004% w/v) of electrically conductive silicon nanowires (e-SiNWs) in otherwise scaffold-free cardiac spheroids can form an electrically conductive network, leading to synchronized and significantly enhanced contraction (i.e., >55% increase in average contraction amplitude), resulting in significantly more advanced cellular structural and contractile maturation.

Our previous results showed addition of e-SiNWs effectively enhanced the functions of the cardiac spheroids and improved the cellular maturation of hiPSC-CMs. Here, we examined two important factors that can affect functions of the nanowired hiPSC cardiac spheroids: (1) cell number per spheroid (i.e., size of the spheroids), and (2) the electrical conductivity of the e-SiNWs. To examine the first factor, we prepared hiPSC cardiac spheroids with four different sizes by varying cell number per spheroid (~0.5k, ~1k, ~3k, ~7k cells/spheroid). Spheroids with ~3k cells/spheroid was found to maximize the beneficial effects of the 3D spheroid microenvironment. This result was explained with a semi-quantitative theory that considers two competing factors: 1) the improved 3D cell-cell adhesion, and 2) the reduced oxygen supply to the center of spheroids with the increase of cell number. Also, the critical role of electrical conductivity of silicon nanowires has been confirmed in improving tissue function of hiPSC cardiac spheroids. These results lay down a solid foundation to develop suitable

nanowired hiPSC cardiac spheroids as an innovative cell delivery system to treat cardiovascular diseases.

We reasoned that the presence of e-SiNWs in the injectable spheroids improves their ability to receive exogenous electromechanical pacing from the host myocardium to enhance their integration with host tissue post-transplantation. In this study, we examined the cardiac biocompatibility of the e-SiNWs and cell retention, engraftment and integration after injection of the nanowired hiPSC cardiac spheroids into adult rat hearts. Our results showed that the e-SiNWs caused minimal toxicity to rat adult hearts after intramyocardial injection. Further, the nanowired spheroids were shown to significantly improve cell retention and engraftment, when compared to dissociated hiPSC-CMs and unwired spheroids. The 7-days-old nanowired spheroid grafts showed alignment with the host myocardium and development of sarcomere structures. The 28-days-old nanowired spheroid grafts showed gap junctions, mechanical junctions and vascular integration with host myocardium. Together, our results clearly demonstrate the remarkable potential of the nanowired spheroids as cell delivery vehicles to treat cardiovascular diseases.

ACKNOWLEDGMENTS

There are many people I would like to thank for their generous support, instruction and help during the past six years' study in the joint bioengineering program between Clemson University and Medical University of South Carolina, located in the historical and beautiful Charleston, SC.

Firstly, I would like to thank my academic supervisor, Dr. Ying Mei, who has taught me what it means to be a real researcher. Your mentorship and guidance have challenged me to think deeply and carefully about scientific problems and how to convey their importance to any audience. You have encouraged me to follow my interests, as well as pursue opportunities outside of lab. In addition, thank you to the all members of Dr. Ying Mei's Lab, Dylan, Robert and Jia for your insightful discussion and technical assistance. I would also like to thank Mei Li, for her tremendous help in the animal study.

Secondly, I would like to thank my committee: Dr. Martine LaBerge, Dr. Hai Yao, and Dr. Donald Menick. Thank you for your insightful and challenging questions and for the guidance you have provided to make me think like an engineer. To the department chair, Dr. LaBerge, thank you to support me to stay in the Clemson Bioengineering Department to complete my degree. To Dr. Hai Yao, thank you for your guidance and technical support on my patch clamp project. To Dr. Donald Menick, thank you for allowing me to use your facility and resources to conduct the animal study in your lab.

Thirdly, I would like to thank my first year advisors, Dr. Xuejun Wen and Dr. Ning Zhang, who brought me into the bioengineering program in Clemson University

and provided me with this great opportunity to start my Ph.D journey in my life. I would like to thank my previous lab mate and best friend, Dr. Xiaowei Li, for countless hours of training and discussion. His extensive experience and careful thought into experimental design and project management have provided me with the knowledge and skills to develop into a technically skilled researcher.

Fourthly, I would like to thank many faculties in MUSC campus and their labs' members to give me generous help and allow me to access the numerous state-of-the-art life science research facilities and resources for my research and experiment. They are Dr. Hongjun Wang, Dr. Thomas Trusk, Dr. Michael Yost, Dr. Richard Visconti, Dr. Andy Wessels, Dr. Martin Morad and Dr. Marion Cooley. In addition, Dr. Richard Swaja and Thomas Gallien deserve special thanks/recognition for being our program's biggest advocates on the MUSC campus. Thank you to Maria Torres, graduate student coordinator, for being a friendly voice on the Clemson campus over the phone to help solve any problems that distance students may have. Thank you to my scientific collaborators, Dr. Zhibo Tian and his students in the University of Chicago, for providing materials for my research.

Lastly, the success of my education can be largely attributed to the ongoing support of my family. Thank you to my parents, Zhili Tan and Guiju Zhang, who have supported me every step of the way towards earning my Ph.D; my Brother, Yun Tan, who helps me to take care of our parents all of the time despite the fact that I have been so far from home for so long. Most importantly, I would like to thank my wife, Xiwen

Zhang, who has provided me endless support and encouragement during my past six years in Charleston.

TABLE OF CONTENTS

Page

LIST OF TABLES

Table Page

LIST OF FIGURES

CHAPTER ONE

BACKGROUND AND SIGNIFICANCE

1. Introduction:

1.1. Cardiovascular diseases (CVD) and myocardial infarction (MI)

CVD can be attributed to about 1 in every 4 deaths in the United States and are regarded as the leading cause of death in the world [1]. The American Heart Association reports that there were 780,000 patient deaths from CVD in the United States in 2011. The most common type of CVD is coronary artery disease (CAD), which accounts for 370,000 deaths and costs $109 billion each year in United States, imposing a huge economic burden on our society [2]. CAD is a chronic process that is characterized by gradually occurring atherosclerosis in the epicardial coronary arteries of the heart. As shown in the Fig. 1.1, the progressive accumulation of a waxy substance named plaques (the hallmark of atherosclerosis) leads to the hardening of the coronary artery and narrowing of the lumen, impairing blood flow crucial to bring enough oxygen and nutrients to supply the heart tissue and maintain the normal function of the heart. In addition, the thrombosis caused by ruptured plaques could block the coronary arteries in the heart, which is known as MI [3-5].

MI is the irreversible necrosis of heart muscle due to the blocked coronary arteries, and approximately 1.5 million cases of MI occurred annually in the United States. Briefly, the first incidence of MI is the blockage of the coronary arteries, as consequence the blood supply to the myocardium is insufficient which result in cardiomyocytes death permanently. The pathological development of MI includes inflammation occurrence, myocardium necrosis (cardiac cells death), fibrosis formation,

the extension of the infarction area, and the remodeling of the heart (thinning and dilation of the left ventricular (LV) wall, enhanced roundness of LV cavity). MI causes a significant amount (around 25%) of irreversible cardiac cells death within the LV myocardium. The impaired heart function and the pathological development of MI could lead to some serious complications like atrial fibrillation, ventricular tachycardia, regurgitation of blood through the mitral valve, and fatal heart failure [4].

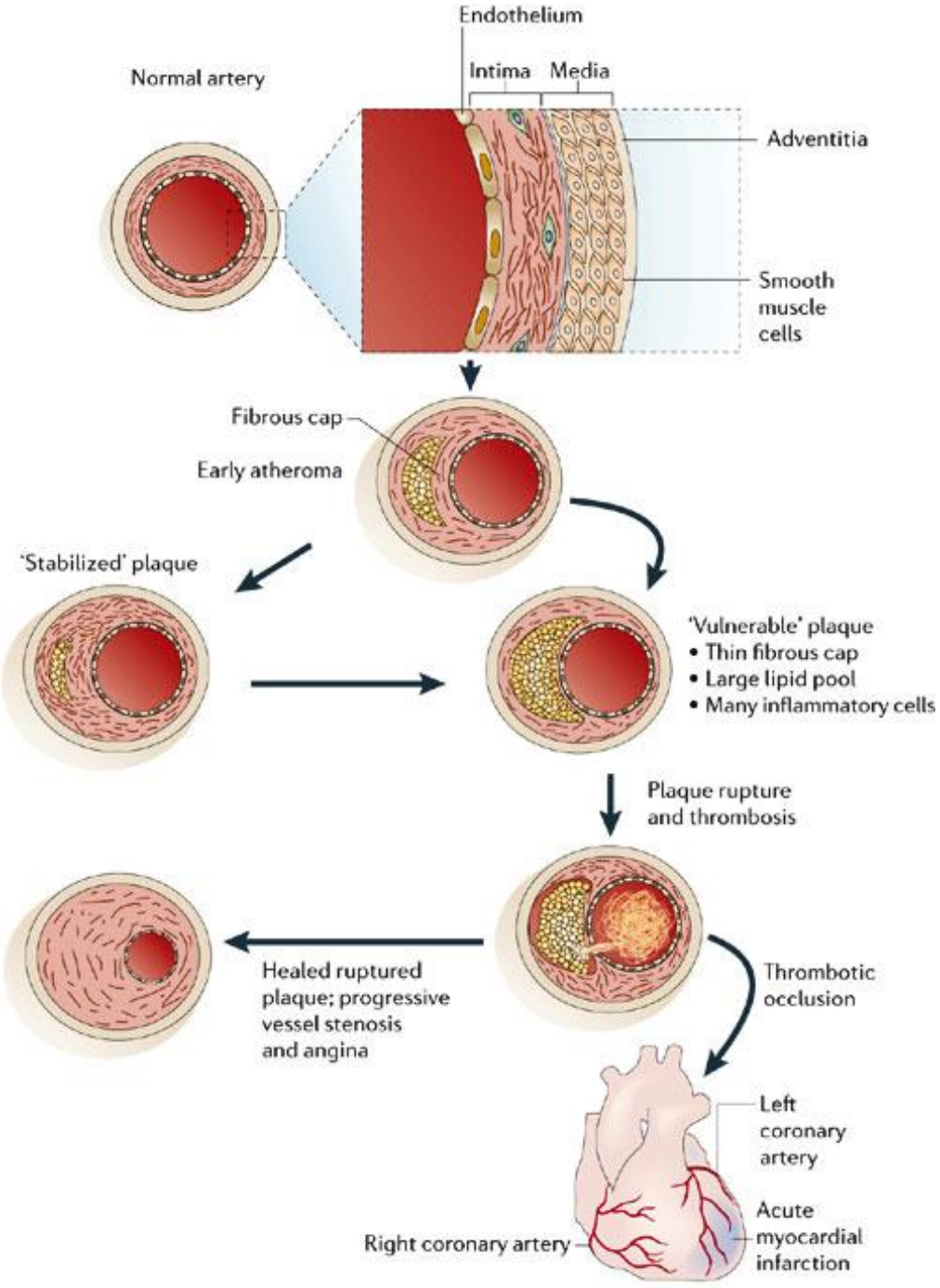

Figure 1.1 Schematics of myocardial infarction. As plaques encroach the coronary artery lumen, blood flow becomes limited on demand of the heart; alternatively, rupture or erosion of plaques can result in the formation of blood clot in the coronary artery. And the complete blockage of coronary artery would lead to a transmural MI. Reproduced from [5].

1.2 Current clinical treatments of MI

The regular treatments for MI is aiming of prompting revascularization with clinical interventions (coronary angioplasty, coronary artery bypass), or antiplatelet /anticoagulant therapy. While above mentioned strategies are helpful in promoting the revascularization of injured area to restore the blood supply post MI and prevent expansion of the infarction, they are limited in restoring impaired heart function resulted from the significant amount of myocardium death. Alternatively, the whole heart transplantation, the long-term solution for the treatment of MI, is regarded as the last resort providing effective treatment for heart failure patients but is greatly restricted by the severe shortage of donor hearts and tremendous cost burden [6]. On the other hand, the survival rates of whole heart transplantation is still not very satisfied and greatly influenced by the conditions of the recipient and donor. 83% of patients post whole heart transplantation could survive for over 1 year, while 5 years survival rate covers 72% patients and only 50% could survive over 9.4 years [7]. In addition, heart transplant recipients have to take immunosuppressive medicines routinely for the rest of their lives to avoid organ rejection, and the side effects brought by these drugs, can include tiredness, lack of strength, and nervousness [8, 9].

While above mentioned clinical interventions have shown to slow down the progression of heart failure, none of them can reverse this deleterious process and regenerate new myocardium to replace the necrotic regions of the LV [10]. Although the clinical treatment and understanding of the problem has improved over the last decade, the impact of MI on public health calls for further scientific exploration into new

technologies and tools to enable better treatment allowing for myocardium regeneration to restore the normal function of the heart.

1.3 Pathophysiology of MI

MI is mainly caused by the narrowing or blockage of the coronary arteries due to atherosclerotic processes and thrombotic incidence. Ischemic conditions caused by insufficient blood supply to the heart muscle lead to a significant amount of cardiomyocyte death, which could form necrotic area in the LV myocardium, causing heart function to deteriorate. Consequently, the defects of contractile function will initiate the LV remodeling (wall thinning and dilation of the heart, enhanced roundness of LV cavity) and fibrotic scar tissue will take over the infarction area over time. Although the following in situ fiborosis provides a temporary solution to maintain total LV wall integration, the progression of MI eventually leads to fatal heart failure [11].

2. Cell therapies for MI treatment

Current clinical approaches for the treatment of MI may improve symptoms and prolong life, but none of them can address the fundamental problem posed by MI: regeneration or remuscularization of the lost myocardium post MI. Cells therapies have emerged as a potential alternative strategy aiming heart tissue repair and regeneration. Since the first time of cell transplantation, the ultimate goal is not to control damage done to the heart, but to eliminate damage altogether with de novo myocardium replacement. The translational efforts of cell therapy with various cell types for MI treatment have proceeded rapidly since the beginning of the 21st century as shown in Fig. 1.2.

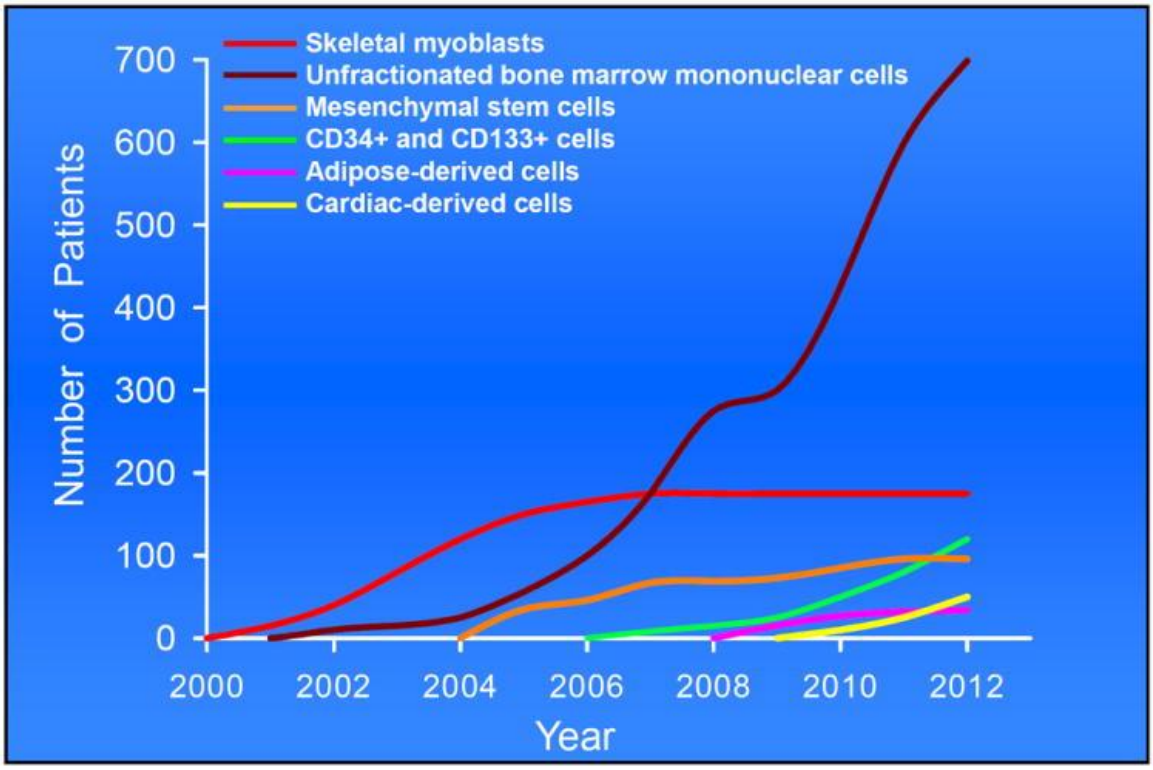

Figure 1.2. Trend of various types of cell therapies in patients with CVDs. Produced from [12].

During the past two decades, numerous studies and clinical trials have been conducted to demonstrate that various cell based therapies could improve cardiac function, reduce fibrosis, promote angiogenesis and attenuate adverse LV remodeling post MI. Despite this great advance achieved in this field, many fundamental issues remain in order to achieve a stable and consistent outcome after cell transplantation. There are five key aspects regarding cell therapy (shown in Fig. 1.3), which will be discussed in detail as below.

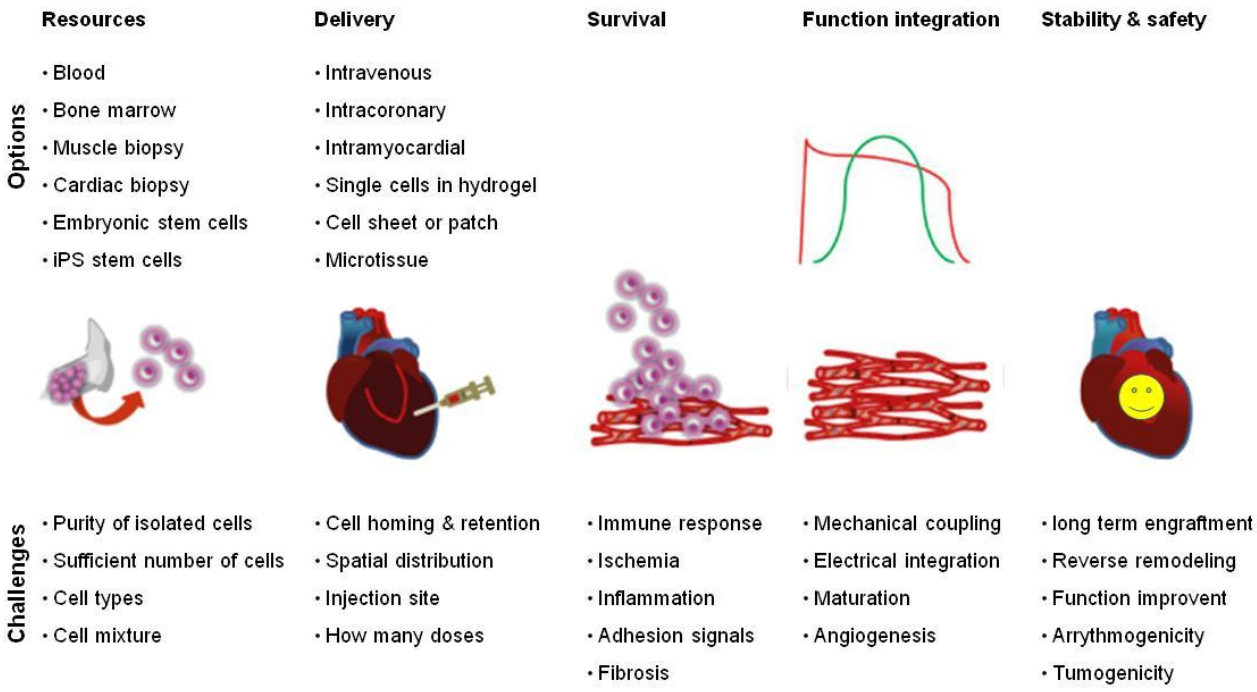

Figure 1.3. The summarized five key elements of cell therapies for cardiac regeneration. Produced from [13].

2.1 Resources for cell therapies

The types of cell to be used in cell therapy could be classified as xenogeneic, allogeneic, or autologous in origin. Nonhuman xenogeneic cells have restrictions in clinical outcomes due to considerable differences in antigens compared with human, which could lead to immune rejection after transplantation. Instead, human originated allogeneic cells are possible to have better outcomes post cell transplantation. However, these allogeneic cells may still have high possibility for severe immune response and graft rejection. In order to eliminate the risk of immune rejection post transplantation, the same individual derived autologous cells have become the best choice for cell therapy.

This autologous cells includes several types such as skeletal myoblasts, bone marrow derived cells, resident cardiac stem or progenitor cells, induced pluripotent stem cells and terminally differentiated cardiac cells.

It remains unknown which cell type is most effective for treatment of MI amongst the different types of stem/progenitor/terminally differentiated cells. Here we will review all the cell types of cell therapies for the treatment of MI, and we establish our standard to choose one cell type for our study as the cell should be 1) autologous: no immunoresponse after transplantation in vivo; 2) able to mass remuscularization: has solid evidence to regenerate large amount of myocardium in vivo; 3) capable of mass expansion in vitro: sufficient number of cells for transplantation to replace large area damaged myocardium.

2.1.1 Skeletal Myoblasts (SkMs)

The first cell type investigated for cardiac cell therapy is the skeletal myoblasts, which are defined as muscle progenitor cells that mediate regeneration of skeletal muscle [14-16]. Interestingly, some studies show that transplanted SkMs in rat MI model result in some beneficial effects like decreased LV diastolic dimension and MI size, improved heart function with increased fractional area change and reversed LV remodeling [17]. SkMs also have a lot of advantages for cell therapy including autologous derivation from muscle biopsies, large scale in vitro expansion and relative ischemia resistance. On the other hand, SkMs do have some negative aspect limited its efficacy for the treatment of MI, such as only differentiation into the wrong form of muscle like skeletal rather than

cardiac and lacking adhesion and gap junction proteins to form functional integration with host myocardium upon transplantation [18].

In addition, there is a clinical trial named MAGIC shows disappointing outcomes and an increased risk of arrhythmias in patients who received transplantation of autologous SkMs obtained via thigh muscle biopsy in patients [19]. Because of above mentioned discouraging results from clinical trials, studies of SkMs transplantation have decreased in recent decade.

2.1.2 Bone marrow derived cells (BMCs)

Many cell types have been studied as cell therapy resource for the MI treatment, but most clinical trials have applied autologous BMCs due to its proven clinical safety and familiarity in the hematopoietic disorders but it still has some problems such as heterogeneous results in terms of efficacy [20]. Bone marrow contains multiple types of cells, including mononuclear cells (MNCs), hematopoietic stem cells (HSCs), endothelial progenitor cells (EPCs), and mesenchymal stem cells (MSCs), which will be discussed in details later in this chapter. Transplanted BMCs in the damaged heart could enhance angiogenisis, reduce LV remodeling progress, and improve heart function in both animals model and humans clinical trials [21-25].

Bone marrow derived MNCs play an critical role in immune defense, inflammation suppression, and tissue healing process [26]. In addition, MNCs could promote angiogenesis post MI which has been proved by recent studies that MNCs include a population of potent EPCs actively contributed in postnatal vasculogenesis, although it is unsure if MNCs can become fully functional endothelial cells in vivo. Thus

transplantation of extracardiac MNCs harvested from bone marrow in patients could have potential to improve heart repair after MI occurs. However, no solid evidence has been shown to prove implanted MNCs have the capability to generate large amount of myocardium for heart repair, instead paracrine effects are the major mechanism underlying the beneficial effect from MNCs transplantation in both numerous animal studies and clinical trials in the past decades.

Bone marrow derived HSCs can differentiate into cells of myeloid and lymphoid lineages [27]. Interestingly, several reports suggest that HSCs has possibility to transdifferentiate into cardiomyocytes for cardiac repair [21, 28]. These promising results have prompted several clinical trials to investigate the potential application of HSCs in the treatment of MI. HSCs are a rare population of cells in bone marrow (1 in 10,000cells) and (1 in 100,000 cells) blood. The phenotype of human HSCs is still difficult to well defined due to the complexity of the specific markers. Generally, human HSCs are CD59+ CD34+ Lin- CD38- c-kit- cells, but several other cell types could express the Lin- CD34+, and CD38 is not a well-defined marker [29, 30]. On the other hand, some research indicates that HSCs readily adopt the hematopoietic phenotype post implantation into MI heart [31-33].

Bone marrow derived EPCs could migrate to peripheral blood post MI incidence and promote angiogenisis by differentiating into blood vessel lining cells (endothelial cells) [34, 35]. Their specific markers are CD34, CD133, and VEGFR-2 (vascular endothelial growth factor). Several researchers have shown that bone marrow-derived

EPC transplantation is capable of restoring vasculogenesis, reducing the myocardial infarcted area and improving cardiac function in MI models [36-39].

Bone marrow derived MSCs are the second most population of stem cells located in bone marrow as structural component cells without little ability to enter circulation. Their specific markers are a Lin-, CD34-, c-kit+, Sca-1+, CD45- and they can differentiate into multiple cell lines including chondrocytes, adipocytes, osteoblasts, skeletal muscle cells and cardiomyocytes [40, 41]. Although this cardiogenic potential remains controversial [42], the results of MSCs transplantation in animal models of MI are still encouraging to improve heart function and reduce fibrosis.

In summary, MNCs, HSCs, EPCs and MSCs are distinct stem/progenitor cell populations or mixture cells in bone marrow. These autologous cell types differ in size, surface markers, and the ability to proliferate and differentiate after transplantation in myocardium. Despite the lack of a significant amount of myocardium regeneration after transplantation, current research with BMCs based cell administration will be able to provide further evidence for a nonmyogenic and clinical safe pathway for the MI treatment.

2.1.3 Cardiac stem cells/ progenitor cells (CPCs)

During the past several decades, tremendous studies have proved that three fundamental principles for cardiac regeneration have now been established [43]. First, in the embryonic mammalian heart there is a small population of resident multi-potent CPCs, which are committed to differentiate into cardiac cells (cardiomyocytes, smooth muscle cells and endothelial cells) [44-50]; second, a limited number of new

cardiomyocytes after birth in mammals has been observed [51, 52]; and third, some vertebrates, such as amphibians [53, 54] and zebrafish [55-57] retain a very robust capacity for self cardiac regeneration throughout life, while only early stage of mammals, like neonatal mice, can fully regenerate damaged myocardium following experimental injury [58]. Actually, some studies have also shown that cardiomyocytes can continue to proliferate in adult mammals including humans, but with a very low rate (around 1% per year), and that the rate will decline over time [59, 60].

The obvious question would be: where does the regenerated myocardium come from? There are two major theories that have occurred over the past decade's research to implicate the cell sources of regenerated cardiomyocytes in adult mammals. First, the resident CPCs located in the heart possess the capacity to differentiate into cardiomyocytes, smooth muscle cells, and endothelial cells, which could lead to new myocardium; second, the mature cardiomyocytes could reenter the mitotic cell cycle to divide into more new cardiomyocytes for heart repair as shown in Fig 1.4.

In 2003, a special population of cells isolated from the adult rat myocardium that expressed the tyrosine kinase receptor c-kit (a marker of stemness) is commonly named CPCs, which may reside in the heart itself, or derive from a circulating bone marrow stem cell [61]. These cells have been proven to have capabilities as stem cells through self-renewing properties and multi-potent differentiation into cardiomyocytes, smooth muscle cells, and endothelial cells both in vitro and in vivo [46, 62]. Thus most researchers use the presence of the c-kit as a specific marker for identification of CPCs for cell harvesting and purification [63, 64]. Briefly, these CPCs can be isolated from

myocardium biopsy during heart surgery and then expanded in culture in vitro for application in autologous transplantation. However, a single specific marker as c-kit to harvest CPCs from myocardium has some limitations and the isolated c-kit+ CPCs are highly susceptible to contamination by non-CPCs, which may lead to compromised and inconsistent outcome after transplantation in vivo.

In the past decade, the ability of CPCs from both humans and rodents to improve heart function, promote cardiac regeneration and reduce fibrosis has been repeatedly demonstrated by several researchers in various animal models (mice, rat, dog and etc) of MI [62, 65-68]. In addition, there are two prominent clinical trials with CPSs transplantation in humans, which have reported early results post transplantation. The phase 1 results of the first clinical trial, SCIPIO, showed a 12.3% improvement in LV ejection fraction in patients post 1 year with intracoronary injection of autologous c-kit+ CPCs following MI [69]. And the second clinical trial (CADUCEUS) phase 1 trial recruited randomized patients with 2–4 weeks post MI receiving cardiosphere-derived autologous CPCs transplantation or regular treatment as control [70]. However, CPCs transplantation results in no critical benefits to improve heart function but only has reduced fibrosis and increased viable heart tissue and regional contractility evaluated MRI post half year [70].

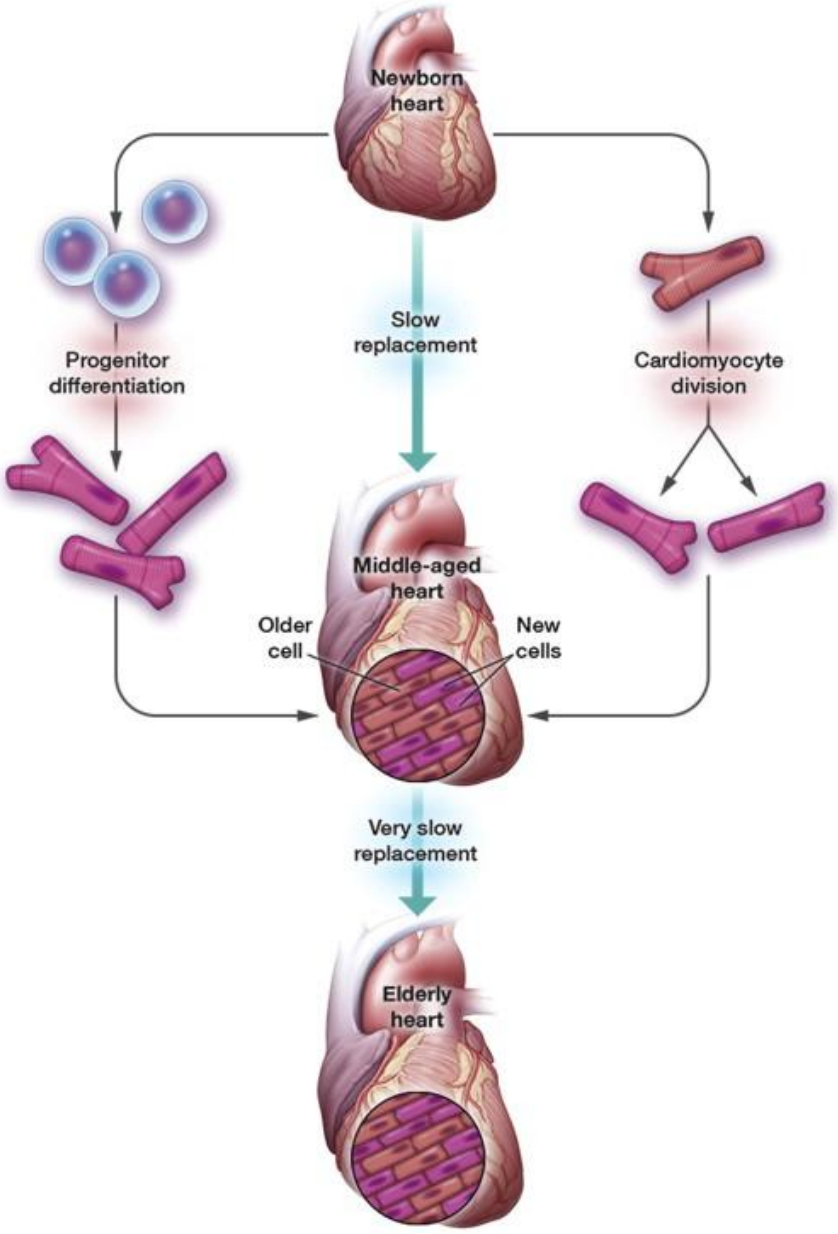

Figure 1.4 The mechanism of cardiac self –repair in mammals. Produced from [43].

There is another sub-type of CPCs [71, 72]in the adult mouse heart named Sca-1+ CPCs, which are capable to be differentiated into functional cardiomyocytes in vitro. In addition, in vivo data indicates that transplanted Sca-1+ CPCs into damaged myocardium in mouse MI model could attenuate LV remodeling due to their committed differentiation

into cardiac linage cells. However, the lack of homolog of Sca-1in human hinders this translational application in clinical trials [71, 72].

The side population cells (SPs) were considered as a sub-population of CPCs, which is first described in 1996 [73] as a way to enrich HSCs from the bone marrow of adult mice. First identified in mouse bone marrow as HSCs, SPs were subsequently isolated from both adult and embryonic mouse hearts with specific markers (CD31-, Sca-1+, c-kit-, CD34-, and CD45-). In vitro study shows that cardiac SPs have abilities to differentiate into cardiac cells and animal study indicates their potentials for cardac regeneration in cryoinjured heart. However, it is necessary to test their effectiveness in MI models before clinical trials [74-77].

The LIM-homeobox transcription factor islet-1 (Isl-1) is a distinct marker of undifferentiated CPCs [78]. The Isl-1+ CPCs are able to differentiate into myocardium, blood vessels and the conduction system in the heart. However, based on my knowledge there is no research shows that the Isl-1+ CPCs could induce myocardium regeneration in animal study. On the other hand, these Isl-1+ CPCs do not exist in the adult heart, which make them less possible in clinical application [79-81].

Initially cardiosphere-derived cells (CDCs) were found in 2004 [82]. The researchers are able to isolate CDCs from myocardium biopsy of both human and animal origins. The CDCs could grow into colonies in vitro and be able to differentiate into cardiac cells. These injected CDCs could improve cardiac function in mouse, rat, pig and dog MI models due to their cardiac regeneration in vivo [83-86].

Cardiac stem/progenitor cells cannot considerably repair injured myocardium, adverse LV remodeling and prevent deterioration in heart function post MI. In fact, the main mechanism underlying the efficacy of CPCs transplantation in vivo is paracrine effect, which could induce endogenous resident CSCs for in situ proliferation and differentiation of cardiac cells resulted in limited myocardium regeneration.

2.1.4 Embryonic Stem Cells

Human embryonic stem cells can proliferate without limit, and maintain the potential to differentiate into all the cells of the body. This remarkable potential makes them a useful cell resource for basic research on the function of the human body, drug screening and testing, and transplantation medicine. In 1998, James Thomson first successfully isolated embryonic stem cells (ESCs) from the inner cell mass of blastocysts stage (4–5 days post fertilization of egg) [87]. ESCs have been proven to be able to differentiate into all the derivatives of the three primary germ layers: ectoderm, mesoderm and endoderm. ESCs are considered as an unlimited supply of cardiac cells produced in vitro as the cell resource of cell therapy for heart repair and regeneration [88, 89].

Despite the proved capacity of ESCs for heart repair in vivo, they have restricted in clinical application for the treatment of MI patients due to both biological and ethical issues. Specifically, their allogeneic nature could induce graft rejection post transplantation and their pluripotency has potential of teratoma formation in vivo [90]. However, the recent development of autologous human induced pluripotent stem cells which have similar pluripotency comparable with ESCs is a more promising clinical cell

resource that could avoid these two major problems of ESCs (ethical and biological concerns).

2.1.5 Induced pluripotent stem cells (iPSCs)

In 2006, Yamanaka discovered that differentiated cells such as fibroblasts can be reprogramed into an undifferentiated state named ‘iPSCs’, which have similar characteristics with ESCs [91]. The beneficial effects in terms of cardiac contractility have been observed after transplantation of iPSCs into mice MI model [92]. In addition, a similar outcome involving enhanced regional perfusion and improved cardiac function, was reported in a porcine MI model [93]. However, the tumorgenetic stemness of iPSCs is not clinically safe in vivo and may lead to some negative effects such as in situ tumor incidence after iPSCs transplantation. And a study shows that heterogeneous teratoma formation in the heart was induced by transplantation of undifferentiated rat iPSCs in a rat model [94].

Thus terminally differentiated iPSCs cardiac cells (cardiomyocytes, endothelial cells and smooth muscle cells) have been widely used as cell resources for cell therapy to avoid the iPSCs tumorgenicity in vivo. The transplanted murine iPSCMs in adult mouse hearts can survive in long term in vivo and form electrical integration with host myocardium, which proves their potential application for the cardiac regeneration and heart repair [95]. The implanted bioengineered myocardium from mouse iPSCs in adult rat MI model could survive at the epicardial implantation site and result in attenuated LV remodeling [96]. The above mentioned research indicated iPSCs derived cardiomyocytes are a new promising cell resource for the treatment of MI.

hiPSC-CMs emerged as an unlimited supply of autologus cardiomyocytes produced in vitro as the cell resource of cell therapy for heart repair and regeneration. The transplanted hiPSC-CMs could engraft, survive and functional integrate with host myocardium to form electromechanical junctions within the healthy rat heart [97]. The inherent features of hiPSC-CMs strongly indicate that they are the ideal cell resource of cell therapy for MI treatment.

2.2 Delivery for cell therapies

2.2.1 Route for delivery

The most effective way to deliver targeted cells into myocardium for maximized outcomes post transplantation is still on the way to explore. The major applied delivery routes are intracoronary infusion and direct injection into the injured myocardium (intramyocardial). Practically in the clinical setting, the cell delivery by intracoronary infusion is the most favorable route for cell transplantation in MI patients. Compared with directly intramyocardial injection, intracoronary delivery provides several advantages: 1) it could induce much more uniformed cells distribution within injured myocardium, 2) it has minimal invasion to the infarcted myocardium during transplantation, and 3) it is relatively easier for physician to follow the similar existing procedure (bone marrow cells transplantation for leukemia) to conduct the operation. However, this intracoronary route has raised some negative effects compared with intramyocardial route: 1) the very low immediate retention of transplanted cells (eg, intracoronary: 2.6±0.3% vs intramyocardial: 11±3%), could be caused of the migration of major cell population into circulation, 2) the larger cells populations such as CDCs (≈21

μm in diameter), SkMs (≈20 μm in diameter), MSCs (10–20 μm in diameter) have high possibility to block the vascular structure to hinder the additional cells infusion into the injured myocardium once occlusion formation and 3) the blocked coronary arteries prevent the delivery of cells into myocardium in situ [98-101].

Intramyocardial injection through epicardial route offers direct visualization of infarcted myocardium but it is restricted by invasive opening chest procedure. On the other hand, endocardial injection route is a less invasive way to delivery cells by using an image-guided catheter to enter into the cavity of the heart, which has been widely used in the clinical settings. There are two advantages of endocardial injection route over intracoronary ones 1) the application of NOGA system can trace the distribution of the heart tissue with ischemia and fibrosis, which could enable precisely transplantation of cells into targeted area of injured myocardium such as border zone or center part of infarction; 2) in case of the totally blocked coronary artery it is feasible to delivery cells into infarcted area for targeted in situ cardiac regeneration. However, intramyocardial route also has some limitations and risks: 1) the distribution of transplanted cells within myocardium is not homogeneous and bulk transplanted cells could form big engraftment in situ without vascularization to maintain the long term survival in the heart. 2)direct delivery itself could invasively disrupt myocardium architecture and cause further damage to the myocardium in the injection location.

2.2.2 Engineered method for cell delivery

Single cell suspension in medium based injection is the first way to test cell therapy for the efficacy of the MI treatment, and this simple method achieved some

promising results in some studies [102, 103]. However, the consequence of very low cell retention and engraftment underestimates its great potential for better improvement of heart function post transplantation [104, 105].

In recent decade, new strategy has emerged by focusing on tissue engineering methods that could mimic native myocardium environment with the biological, physical and chemical cues to better maintain transplanted cell phenotype and survival. There are three engineered methods for cell delivery: 1) biomimetic scaffolds; 2) decellularized extracellular matrix (ECM); 3) scaffold-free engineered tissue. The scaffolding materials can provide a structural environment that supports cell adhesion, migration, differentiation, and organization with delivering soluble and insoluble biochemical cues, which leads to new tissue formation [106]. Engineered method for cell delivery has great potential to improve the cell engraftment and survival compared with single cell suspension in medium based injection. In a recent review, five natural materials (collagen, gelatin, Matrigel, alginate and fibrin) and seven synthetic materials (polyethylene glycol, polyhydroxyethylmethacrylate, polylactide-glycolic acid, and poly(N-isopropylacrylamide) and copolymers) have been discussed in application for cardiac regeneration but none of them seems the optimal scaffolding materials for cell transplantation for heart repair [107].

Natural biomaterials are biodegradable, biocompatible and less immunogenic than synthetic materials with better cell adhesion, migration, differentiation, and organization. Because they are naturally originated as the proteins or polysaccharides with similar structures to the native component of ECM [108-113]. The disadvantage of using natural

biomaterials as scaffolds for cell transplantation is their untailored poor mechanical property. In addition, the degradable byproducts from natural materials may be toxic or immunogenic in vivo.

While synthetic materials for the application in cardiac tissue engineering are easily tailored with predictable physical and chemical properties, but their potential adverse effects (induce inflammatory and immune response) might affect beneficial outcome post cell transplantation [113-116].

In summary, the optimal materials for cardiac tissue engineering should has no immunogenicity and should has mechanical stability, electrical conductivity for electrical signals propagation. Furthermore, it could allow sufficient oxygen and nutrient supply to cells, and have a appropriate degradation rate with native ECM replacement.

Recent study shows that decellularized ECM based injectable materials are very promising in the cardiac tissue engineering. In addition, some research indicates the composites of natural and synthetic materials could take advantage of both components to maxim the outcome for cell transplantation. However, the field in decellularization of ECM is developing to fulfill the need as scaffold materials cardiac tissue engineering [117, 118].

2.2.3 Cell patch

Engineered cardiac patches can be fabricated from stacking scaffold free cell sheets or by seeding the cells into the scaffolding material designed to mimic the native ECM. The tissue-engineered cardiac patch provides a better method to deliver cardiac cells to the injured myocardium to achieve better outcomes such as higher cell retention

and survival, larger and more controlled infarction area coverage, reduced LV remodeling post MI [119-122].

Though cardiac patch based cell transplantation leds to better engraftment, long-term survival, and progressive maturation of human cardiomyocytes, the human engraftment is totally isolated from host tissue by fibrosis and it does not contribute to functional improvements in MI model [123, 124].

2.2.4 Scaffold free cardiac tissue engineering

The cell density inside the material-engineered cardiac construct is very low compared with the very dense cell distribution in the natural myocardium. In addition, inflammatory reaction, immune response and fibrosis formation caused by the degradation of scaffolding materials led to the reconsideration of engineering tissue without the use of xenogeneic or allogenious scaffolding materials.

2.2.5 Cell sheet

As intact layers of cells, the scaffold-free two-dimensional (2D) myocardial sheets can be used to stack them in multiple layers to produce a 3D cardiac construct for cell transplantation.

The cell culture surface is coated with temperature-responsive hydrogel (poly N-isopropylacrylamide), which is hydrophobic at 37°C and allows for the cell attachment in the incubator; the surface becomes hydrophilic under 32°C and leads to the detachment of the cells as an intact layer to preserve the cell-to-cell junction proteins without digesting the ECM secreted by cells. .When the 2D cell sheets are stacked together, they can rapidly fuse into scaffold-free cardiac patch due to the presence of the intact ECM

secreted by cells. The research shows that spontaneously beating cardiac patch with rapid electrical coupling between the sheets from stacking multiple monolayers of neonatal rat cardiomyocytes indicate the rapid formation of functional gap junctions within patch [125, 126].

After transplantation of mono-layer of adipose tissue-derived MSCs in mouse MI model, angiogenesis, prevention of LV remodeling and improved cardiac function were observed post four weeks transplantation [127].

Another study shows that transplanted 3D sheets of neonatal rat cardiomyocytes in MI models in rats could attach to the host tissue with improved heart function, highly expressed gap junctions and enhanced angiogenesis in situ.[128]

However, application of scaffold-free cell sheets is still facing some problems. Firstly, the diffusion limitation of avascular tissue limit the thickness of sheets in vivo (only 80 μm), or three layers; even thicker engineered cardiac sheet resulted in cell death as necrosis [129]. Secondly, the transplantation of cell sheets in vivo is invasive procedure requiring opening the check and induce more damage to the mycadium post operation. Several strategies have been explored to increase the vascular structure within the cell sheets and thickness of engineered tissue like coculture with endothelial cells and treatment with VEGF and culture under bioreactor [130].

2.2.6 Spheroid

The survival rate of single cell transplantation for heart repair is very low partially due to harsh conditions within the damaged myocardium including hypoxia, fibrosis and inflammatory environment [131]. It is necessary to optimize delivery approach and form

of cell therapy, which includes intactness of the cell harvesting or specific cell pretreatment procedures prior to transplantation. Compared with cell sheet, spheroids can be tailored for suitable size for less invasive cell delivery as direct injection into myocardium post MI. Regarding cell delivery, spheroids avoid the harsh enzymatic treatment step in cell harvesting procedure of monolayer cultured single cells and reduce anoikis by multi-cellular interaction in the hypoxia environment post transplantation. In addition, spheroids could improve cell retention after transplantation due to their significantly bigger size compared with single cells.

The 3D spheroids mimic the natural microenvironment of tissue and enhance cell–cell interactions to better maintain the function and phenotype of cells compared with traditional 2D monolayer cell cultures. It has been reported that MSCs spheroids have better survive under ischemia compared with 2D cultured cells [132] And cells in 3D spheroid culture could up-regulate expression levels of hypoxia-inducible factor 1 and manganese superoxide dismutase, which could improve the resistance to cell apoptosis induced by oxidative stress [133]. Enhanced survival and engraftment post transplantation of 3D MSC spheroids transplantation was observed in the rat MI model [134].

Another study shows human CPCs spheroids transplantation significantly improve the engraftment capacity compare with single cell injection in both mouse healthy and injured hearts [135]. After 10 spheroids injection into the healthy myocardium of mice, human engraftment formed from transplanted CPC spheroids could be detected for 1 week post transplantation. While, no grafted cells could be observed

post three days following injection with the same amount of single cells delivery. In addition, the same level of engraftment capability has been observed with cells transplantation in spheroids in cardiotoxin-injured heart model [135].

The form of 3D scaffold-free spheroids for cell delivery represents unique opportunities in the improvement of the therapeutic potential post cell transplantation. Less invasive procedure, less harsh cell harvesting process, enhanced cell-cell interactions, and anti-anoikis features of cells in ischemic environment demonstrate this promising strategy of cell delivery for hiPSC-CMs transplantation aiming cardiac repair and regeneration in clinical settings.

2.3 Survival for cell therapies

hiPSCs and hESCs can be differentiated into functional cardiomyocytes and have the potential to repair large scale of injured heart tissue post MI. One of the key challenges towards clinical application of hiPSC-CMs is to enhance survival, retention and engraftment of the transplanted cells in hash infarction environment (ischemic, fibrosis and avascular). Immediately post transplantation, most cardiomyocytes are lost as a result of combined mechanical, cellular and host factors. In addition, a large portion of the remained cells in host tissue will undergo apoptosis or necrosis in short term due to incidence of inflammation and immunological response and the lacking adhesion signals, oxygen and nutrients supply in the ischemia environment. In order to improve cell retention and survival post transplantation, many strategies have been applied such as conditioning cells before transplantation, promoting angiogenesis in infraction regions, using pro-survival cocktails to delivery cells, blocking the apoptotic signaling pathways,

immunosuppressing the host myocardium and application of bioengineered methods [136].

Several studies have shown 10–30% of transplanted cells could remain post a few days, and only 1–5% of cells could survive post 10–12 weeks [137, 138]. Mechanical factors could extrude cell out of the host tissue by spontaneous contraction of the hearts [139]. Studies of radio-labeled cells [140] and microspheres [141] in a porcine MI model indicated that less than 10% cells remained immediately post transplantation. Here we summarize current strategies to improve cell retention and survival post transplantation listed in the Table 1.1-1.2.

Cell conditioning	Heat shock
	Hypoxic pre-conditioning
	Hypoxia inducible factor-1
	Diazoxide
	Isoflurane
	Erythropoietin
Anti-apoptotic pathways	Rho-associated kinase inhibition
	TGF-β_2 treatment
	SDF-1 signalling of PI3K/Akt
	p38 MAPK inhibition
Pro-survival cocktail	Akt and Bcl overexpression
	Pinacidil
	Cyclosporine
	ZVAD-fmk
	Insulin-like growth factor-1

Table 1.1 Cellular protection strategies described to improve transplanted cell survival. Reproduced from [136]

Inflammation inhibition	CD4/CD8/C3 inhibition
	Prednisone
	Cyclosporine
Angiogenic and homing factors	FGF
	VGEF
	SDF-1a/CXCR4
Co-transplant	Mesenchymal stem cells
	Fibroblasts
	Endothelial cell progenitors
Hydrogels and bioengineering solutions	Collagen
	Hyaluronic acid
	Matrigel
	Fibrin
	Chitosan
	Oligopolyethylene
	Alginate
	Magnetic targeting
	Engineered cell sheets
	Spheroid

Table 1.2 Optimizing host myocardium strategies described to improve transplanted cell survival. Reproduced from [136].

2.4 Function integration for cell therapies

The functional integration of graft with host myocardium is necessarily required to transmit contractile force and propagate the action potential for pumping out blood properly. Firstly, the mechanical integration between graft and host requires cell-cell and cell-ECM junction formation. Interestingly, the electrical integration is more complicated because of the complex gap junction coupling and ion channel expression required for action potential propagation [142]. Successful electromechanical integration could reverse the conduction block, synchronize the graft contraction with the host myocardium and prevent arrhythmogenicity of the heart [143].

The immature phenotypes of hESC-CMs or hiPSC-CMs pose a potential risk for arrhythmogenicity in vivo, which could hamper host conducting system and functional integration of transplanted cardiomyocytes with the host myocardium [43, 144]. In the past decade, physical stimuli (e.g. electrical and mechanical stimulation) has been applied to advance the immature cardiomyocytes towards more matured phenotypes with more organized sarcomere structures (width, length and alignment) and unregulated expression level of gap junction protein (Connexin-43) [145]. In order to mimic the electrically conductive properties of native myocardium, conductive nanomaterials (gold nanowires, carbon tubes) have been used as scaffolding materials to fabricate engineered cardiac tissue with stronger contractile and electrical properties for promoting cardiomyocyte maturation in vitro and in vivo [146, 147].

We recently utilized e-SiNWs to facilitate the self-assembly of hiPSC-CMs to form nanowired hiPSC cardiac spheroids and improve the functions of the microtissues,

which lead to significantly more advanced cellular structural and contractile maturation of hiPSC-CMs in nanowired spheroids system [148, 149]. Here, we reasoned that the presence of the e-SiNWs in the injectable cardiac spheroids improves their ability to receive exogenous electromechanical pacing from the host myocardium and enhance their functional integration with host tissues post-transplantation.

2.5 Stability and safety for cell therapies

The hiPSC-CMs or hESC-CMs can be directly differentiated into cardiomyoctes with high efficiency [150], which have emerged as an unlimited cell source for in vitro disease modeling for drug discovery and in vivo transplantation for heart repair post MI [151]. Although the electrophysiology of single hiPSC-CMs or hESC-CMs has been characterized in several studies [7–13], their risks of arrhythmogenicity in vivo has not yet been systematically and comprehensively investigated due to unmatched animal models with human [152]. Given the immature phenotypes of hiPSC-CMs and hESC-CMs at the single-cell level, both of them have risks of arrhythmias in vivo post transplantation. A recent study showed substantial arrhythmia development after injection of hESC-CMs into the myocardium of nonhuman primates [153]. In addition, hiPSC-CMs or hESC-CMs are heterogenous cell populations consisted of a mixture of ventricular, atrial and pacemaker cardiomyocytes [154]. In order to avoid the arrhythmia post transplantation, more mature homogenous cardiomyocyte types, like purified ventricular cardiomyocytes, should be used in vivo for cell transplantation.

The other safety issue associated with cell therapies is tumorgenicity in vivo post transplantation. Although the host myocardium released cardiotrophic factors guide

transplanted ESCs toward cardiac differentiation, the noncardiogenic signaling associated with pluripotency of ESCs for unguided differentiation can overcome the limited endogenous cardioinstructive signaling to form neoplastic transformation [155]. Thus transplantation of terminally differentiated cardiomyocytes may avoid this risk of tumorgenicity in vivo. A recent study shows that no teratomas or tumors were found in a rat MI model with engineered hESC-CMs patch transplantation at long term monitoring (110 or 220 days respectively) [123].

2.6 Other consideration regarding cell therapies

2.6.1 Timing for cell transplantation

There is a study aiming to determine the optimal time point for bone marrow derived MSCs transplantation post MI. The rats underwent MI procedure by LAD ligation, and received direct intramyocardial injection of MSCs at time points of 1h, 1 week and 2 weeks post MI, respectively. MSCs transplantation was shown to improve heart function and reduce infarct size in MI model rats with attenuated LV chamber dilation. Interestingly, the greatest benefit was observed in rats that received MSCs 1 week post MI with more abundant engrafted MSCs survival, in situ angiogenesis and functional cardiomyocytes than the other two groups. At the time point of one week post MI, scar formation had not occurred and the acute inflammation and immune response was reduced and stable, which could facilitate survival, engraftment and integration of transplanted MSCs with functional recovery [156]. Thus one week post MI is a good time point to perform the cell transplantation to achieve the better efficacy by avoiding the acute inflammation reaction, immune response and fibrosis formation.

2.6.2 Dose for cell therapies

The optimal cell dose of cell therapies aiming the treatment of MI still remains an open question. Obviously, a higher dose of cell transplantation could have better outcomes upon cell delivery to the injured myocardium. A study by direct intramyocardial injection of bone marrow derived MNCs or MSCs in rat MI models shows the maximum cell number after increasing injected cell number into the myocardium [157]. However, it is not always safe and feasible to deliver a large number of cells into the injured myocardium. One study that used the swine MI model while delivering CDCs isolated from human biopsies found that over 2.5×10^7 intracoronary-administrated cells infusion could increase the size of engraftment but meanwhile results in side effects such as partial myocardial damage, as evidenced by the elevating level of Troponin I (ischemia maker in blood serum) [158]. In addition, more transplanted cells can be found in other organs such the lungs, liver, kidneys and spleen with increased number of transplanted cells in short term, but few or no grafted cells were detected in long term (over six weeks). The long term low survival rate of transplanted cells in the heart may limit therapeutic efficacy of cell therapies, while the distribution of transplanted cells to other organs rather than heart must be manipulated to avoid adverse effects in all cell therapy applications [157]. Interestingly, there is a study using allogeneic mesenchymal precursor cell (MPCs) isolated from male crossbred sheep for transplantation in a female sheep transmural MI model. This study investigated the effects of different doses with injection of 25, 75, 225, or 450×10^6 MPCs respectively on the heart functional improvement post cell transplantation, and only the low dose cell

transplantation (25 and 75 x 10^6 MPCs) significantly attenuated infarct expansion and increased both LV end diastole and systole volumes [159]. The researchers concluded that the high cell doses lead to intense competition for limited oxygen and nutrient supply in the ischemia environment of injured heart, which could result in the limited cell survival and functional improvement. In addition, the large number of transplanted cells may initiate a more profound inflammation reaction and immune response that accelerates cell apoptosis and clearance [159]. The alternative strategy using multiple small doses for transplantation over an extended period (e.g. days to weeks) may represent a promising direction for optimizing the dose of cell therapies to achieve the better outcomes for the MI treatment.

Though cell therapies are promising approaches to heart regeneration post MI, the outcomes of the most current clinical trials show inconsistent, modest, borderline, or undetectable benefits (most of them applied only one dose of cells) [12, 160-162]. Roberto Bolli raised a good point, asserting that most pharmacological drugs are ineffective when only given one dose but can be highly effective when given repeatedly, so one time cell therapy may have no effect, or only be modestly effective, but multiple transplantations may turn out to be very effective due to the accumulated improvement. His studies in rodents have shown that repeated cell therapy is much more effective than single-dose therapy. When the rats with chronic ischemic cardiomyopathy (old MI) were given three doses of c-kit$^+$ CPCs 35 days respectively, each dose generated a similar increase in LV function, so the total cumulative improvement was approximately triple than that observed with one dose administered . In a following study in mice with chronic

ischemic cardiomyopathy, they found that three doses of cardiac mesenchymal cells (CMCs), given 14 days separately, generated a significantly greater outcomes as the bigger improvement in LV function and led to less myocardial fibrosis in the noninfarcted region compared with single dose [163, 164].

2.7 Cell therapy based future strategies for the treatment of MI

Recent researches on MI treatment are focused on reversing heart remodeling and reducing scar formation with stem/ progenitor/ terminally differentiated cells injection or replacing scar tissue with a functional engineered myocardium.

Among all the cell types for cell therapies for the MI treatment, hiPSCs have emerged as a more promising cell resource for heart repair due to their proven capacity to produce patient-specific functional cardiomyocytes (hiPSC-CMs) [165-169]. In addition, recent progress in cardiac differentiation of hiPSCs allows for the derivation of a large number of hiPSC-CMs (>10^9 cells/patient) needed for cardiac repair [124, 170-172]. To realize the therapeutic potential of hiPSC-CMs or hESC-CMs (cardiomyocytes derived from human embryonic stem cells), significant efforts have been made, transplanting hiPSC-CMs or hESC-CMs into animal MI models to improve cardiac function, with limited myocardium regeneration [97, 104, 124, 170, 173-178].

While most of research utilizes direct injection of the dissociated hiPSC-CMs or hESC-CMs into healthy/injured myocardium, the success of this cell delivery approach is limited by low cell retention and survival after cell transplantation. Dissociated hiPSC-CMs are rapidly redistributed to other organs (e.g., lung) after injection due to mechanical dispersion of beating hearts [140]. Additionally, lack of cell-to-cell adhesion

amongst single cells leads to cell death caused by anoikis and/or ischemia [179]. To improve the efficiency of cell delivery, significant efforts have been devoted to the development of tissue-engineered epicardial patches [175, 180-182]. In addition to the invasive surgical procedure to transplant the patches, recent research has shown there is limited electrical integration between the transplanted patches and host myocardium, largely attributed to the chronic fibrotic response that occurs after transplantation [180-182]. This highlights an urgent need to develop an innovative platform to improve the retention, engraftment and integration of the injected hiPSC-CMs with the adult myocardium after transplantation.

hiPSC cardiac spheroids have been proposed as an attractive cell delivery system for heart repair, given the recent literature showing spheroid/aggregate delivery improves cellular retention and post transplantation survival [183-189]. To this end, we recently utilized electrically conductive silicon nanowires (e-SiNWs) to facilitate the self-assembly of hiPSC-CMs to form nanowired hiPSC cardiac spheroids and improve the functions of the microtissues, resulting in significantly more advanced cellular structural and contractile maturation of hiPSC-CMs [148]. Here we reasoned that the presence of the e-SiNWs in the injectable spheroids improves their ability to receive exogenous electromechanical pacing from the host myocardium and enhances their integration with host tissues post-transplantation. This theory was inspired by our recent finding that the addition of e-SiNWs in hiPSC-CM spheroids are essential for exogenous electrical stimulation/pacing to promote hiPSC-CM development and maturation [190]. Furthermore, recent reports showed the presence of electrical nanomaterials (e.g., gold

nanowires) in cardiac tissue engineering constructs synergizes with exogenous electrical pacing to improve the function of the constructs [147, 191]. Compared to other electrical nanomaterials (e.g. gold nanowires, carbon nanotubes), e-SiNWs have distinct advantages, including their controllable electrical conductivity, tunable dimensions, and convenient surface tailorability [192, 193]. Additionally, both *in vitro* and *in vivo* biocompatibility studies have shown no significant cytotoxic effects for either undoped or n-type e-SiNWs [194-196]. Notably, the absence of a pre-aligned structure within the nanowired hiPSC cardiac spheroids has raised concerns over their suitability for transplantation. The ability of hiPSC-CMs from hiPSC cardiac spheroids to align and functionally engraft/integrate with the host tissue after transplantation remains an open question that needs to be investigated.

In our study, we plan to inject nanowired hiPSC cardiac spheroids into adult rat hearts and examine cell retention, engraftment and integration with host myocardium. In addition, we will examine the cardiac biocompatibility of e-SiNWs in the adult rat hearts to verify the safety of the application of nanowired cardiac spheroids in vivo.

3. Study objectives

3.1 Significance

The current inability to derive mature cardiomyocytes from hiPSCs has been the limiting step for transitioning this powerful technology into clinical therapies. To address this, scaffold-based tissue engineering approaches have been utilized to mimic heart development in vitro and promote maturation of cardiomyocytes derived from human pluripotent stem cells. While scaffolds can provide 3D microenvironments, current

scaffolds lack the matched physical/chemical/biological properties of native extracellular environments. On the other hand, scaffold-free, 3D cardiac spheroids (i.e., spherical-shaped microtissues) prepared by seeding cardiomyocytes into agarose microwells were shown to improve cardiac functions. However, cardiomyocytes within the spheroids could not assemble in a controlled manner and led to compromised, unsynchronized contractions.

To realize the enormous potential of hiPSC-CMs for heart repair and regeneration, significant efforts have been devoted during the last decade to the transplantation of hiPSC-CMs into damaged animal hearts to restore their. However, low cell retention and limited cell survival have been found regardless of cell delivery methods. For example, several researchers demonstrated that less than 10% cells stay in the hearts immediately after injection in the rat, porcine or monkey infarct models, and even lower cell retention was found for intracoronary and intravenous injection. For the cells retained in the hearts, most of them were found to undertake apoptotic and necrotic pathways. Murry and coworkers showed that as high as 90% retained cardiomyocytes died within the first few days after transplantation. This high cell death after injection has mainly been attributed to three major pathways: anoikis, due to the lack of matrix support after harvesting cells from culture substrates; ischemia, due to the lack of oxygen and nutrient supply within the avascular infarct regions; and inflammation as attributed to cytokines and free radicals. The low cell retention and engraftment after transplantation are major limiting factors to develop clinically applicable hiPSC-CM based therapies to treat cardiovascular diseases. Notably, both low retention and low survival of hiPSC-

CMs after transplantation can be attributed to the current utilization of dissociated single hiPSC-CM for cell transplantation. After injection, single cells can be rapidly redistributed to the other organs due to the mechanical dispersion of beating hearts and its small size going through circulation system. Further, the lack of cell-cell adhesion of single cell can lead to anoikis mediated cell death and/or low expression of pro-survival factors in a hypoxia environment and result in low cell survival after transplantation.

We propose that application of nanowired spheroids as cell delivery system could improve cell retention and survival after transplantation. The underlying hypotheses are: 1) spheroids can improve cell retention after transplantation due to their size, 2) the spheroid grafting can avoid the harsh enzymatic treatment step in cell harvesting procedure and reduce anoikis by multi-cellular interaction, 3) spheroids improve cell survival in a hypoxia environment due to their 3D microtissue configuration, and 4) the addition of electrically conductive e-SiNWs into spheroids effectively enhance electrical integration of transplanted cardiac spheroids with host myocardium and reduce the risk of arrhythmia.

3.2 Specific aims

To collectively address these challenges, we plan to use e-SiNWs to facilitate the self-assembly of hiPSC-CMs to form nanowired hiPSC cardiac spheroids aiming to accelerate structural and contractile maturation of hiPSC-CMs in vitro. Our central goal is to utilize nanowired human cardiac spheroids as a cell delivery system to improve cell retention, survival and integration after transplantation through intramyocardium delivery.

Aim #1: Accelerate structural and contractile maturation of hiPSC-CMs by using electrically conductive e-SiNWs in scaffold-free 3D spheroids system. We hypothesize that incorporation of e-SiNWs into hiPSC cardiac spheroids can create an electrically conductive microenvironment, leading to synchronized and enhanced contractions of hiPSC-CMs and resulting in hiPSC-CM maturation.

Aim #2: Optimize cell number per spheroid (i.e, spheroid size) to improve the functional maturation of hiPSC-CMs and examine the effects of electrical conductivity of e-SiNWs on the function of cardiac spheroids. We hypothesize that the optimal cell number per spheroid is determined by two competing factors: 1) the improved 3D cell-cell interaction with the increase of cell number, and 2) the reduced oxygen supply to the center of spheroids with the increase of cell number. In addition, we hypothesize that electrical conductivity of e-SiNWs plays a critical role in improving the function of cardiac spheroids, which leads to structural and contractile maturation of hiPSC-CMs.

Aim #3: Investigate the cardiac compatibility of e-SiNWs and validate the concept that cell delivery with nanowired spheroids can improve cell retention, survival and functional integration with host myocardium post transplantation in rat adult health hearts. We hypothesize that the e-SiNWs are biocompatible in vivo and would be degraded in the heart tissue over time with limited inflammatory and toxic effects. We also hypothesize that nanowired spheroids are not prone to leak out or migrate to other organ through blood circulation after transplantation, when compared with dissociated single cells due to their size. In addition, spheroids can avoid the harsh enzymatic treatment step in cell harvesting procedure of monolayer cultured single cells and reduce

anoikis by multi-cellular interaction in the hypoxia environment post transplantation. Most importantly, the presence of e-SiNWs within spheroids could improve their ability to receive exogenous electromechanical pacing from the host myocardium and enhances their integration with host tissues post-transplantation.

4. Organization of Dissertation

The following manuscript is arranged in chapters that highlight individual studies that relate to the overall aims of my project studying cardiac regenerative medicine.

Chapter 2 focuses on application of 3D printing technology to facilitate scaffold-free vascular tissue unit fabrication for engineered blood vessels construction. Briefly, we proposed and developed a 3D mold-printing technology to produce biocompatible, bio-inert alginate hydrogel molds, which can facilitate the fusion process of tissue spheroids to form scaffold-free tissue-engineered constructs with defined 3D structures. Specifically, we developed a 3D printing technology to print micro-droplets of alginate solution on calcium-containing substrates in a layer-by-layer manner to fabricate a variety of 3D structures. Further, we utilized this technology to fabricate ring-shaped 3D hydrogel molds for toroid-shaped tissue unit fabrication. Tissue spheroids composed of 50% endothelial cells and 50% smooth muscle cells were robotically placed into the 3D printed alginate molds, and they were found to rapidly fuse together into toroid-shaped tissue units. Histological and immunofluorescence analyses indicated the critical role of cell-secreted collagen I in tissue formation and maturation. These scaffold-free toroid-shaped tissue units could be used to stack together to fabricate a blood vessel-like tube for further clinical research and application.

In Chapter 3, we will present my core research on the application of trace amounts of electrically conductive silicon nanowires to induce maturation of cardiomyocytes derived from human induced pluripotent stem cells. Briefly, we incorporated a trace amount of e-SiNWs into rat-neonatal and hiPSC cardiac spheroids to create electrically conductive microenvironments and induce synchronized and enhanced contraction, which was shown to promote structural and contractile maturation. Although powerful, the addition of e-SiNWs into the human cardiac spheroids alone may not be able to derive fully matured hiPSC-derived cardiomyocytes. A longer term experiment (i.e., 3 weeks) was explored, and the improvements in hiPSC-WC spheroids in contraction amplitude and sarcomere structure seen at Day 7 were maintained through Day 21. However, the extended culture did not indicate further improvements in the maturation of hiPSC-derived cardiomyocytes. The sarcomere structure and nuclear shape in hiPSC-WC spheroids and hiPSC-NC spheroids at Day 21 resembled that of the Day 7 spheroids. Our future research will combine additional chemical/physical stimuli (e.g., growth factors, miRNA) with e-SiNW-reinforced human cardiac spheroids to produce fully matured hiPSC-cardiomyocytes.

In Chapter 4, we have experimentally identified the optimal cell number in the spheroids and developed a semi-quantitative theory to explain the finding. Briefly, the existence of the two competing factors (reduced oxygen supply vs. enhanced 3D cell adhesion with the increase of cell number per spheroid) indicates there could be an optimal cell number for spheroid fabrication, and our experimental data indicates that spheroids contain ~3k cells per spheroid maximizes the benefits of the 3D environment

of nanowired spheroids. In our previous report, we showed the addition of e-SiNWs in the human cardiac spheroids improved cellular maturation and tissue function. However, the role of electrical conductivity of the e-SiNWs has not been examined. In the second part of the chapter, we prepared three types of the spheroids: spheroids without the addition of nanowires (NC), spheroids with the addition of phosphorus doped silicon nanowires (WCD), and undoped silicon nanowires (WCN). We studied the functions of these three different types of spheroids and confirmed the critical role of electrical conductivity of e-SiNWs in improving tissue function for the hiPSC cardiac spheroids.

In Chapter 5, we examined the cardiac biocompatibility of the e-SiNWs and cell retention, engraftment and integration after injection of the nanowired hiPSC cardiac spheroids into adult rat hearts. Our results showed that the e-SiNWs caused minimal toxicity to rat adult hearts after intramyocardial injection. Further, the nanowired spheroids were shown to significantly improve cell retention and engraftment, when compared to dissociated hiPSC-CMs and unwired spheroids. The 7-days-old nanowired spheroid grafts showed alignment with the host myocardium and development of sarcomere structures. The 28-days-old nanowired spheroid grafts showed gap junctions, mechanical junctions and vascular integration with host myocardium. Together, our results clearly demonstrate the remarkable potential of the nanowired spheroids as cell delivery vehicles to treat cardiovascular diseases.

In Chapter 6, we will summarize overall conclusions drawn from the body of our research, discuss challenges and limitations involved in nanowired spheroids system regarding therapeutic efficacy and potential risks, establish research directions in the

future to apply our nanowired spheroids system in MI rat models aiming heart functional improvement, and suggest some potential applications of nanowired spheroids system in brain tissue regeneration.

CHAPTER TWO

3D PRINTING FACILITATED SCAFFOLD-FREE TISSUE UNIT FABRICATION

1. Abstract:

3D scaffold-free spherical microtissue (spheroids) holds great potential in tissue engineering as building blocks to fabricate the functional tissues or organs *in vitro*. To date, agarose based hydrogel molds have been extensively used to facilitate fusion process of tissue spheroids. As a molding material, agarose typically requires low temperature plates for gelation and/or heated dispenser units. Here, we proposed and developed an alginate-based, direct 3D mold-printing technology: 3D printing micro-droplets of alginate solution into biocompatible, bio-inert alginate hydrogel molds for the fabrication of scaffold-free tissue engineering constructs. Specifically, we developed a 3D printing technology to deposit micro-droplets of alginate solution on calcium containing substrates in a layer-by-layer fashion to prepare ring-shaped 3D hydrogel molds. Tissue spheroids composed of 50% endothelial cells and 50% smooth muscle cells were robotically placed into the 3D printed alginate molds using a 3D printer, and were found to rapidly fuse into toroid-shaped tissue units. Histological and immunofluorescence analysis indicated that the cells secreted collagen type I playing a critical role in promoting cell-cell adhesion, tissue formation and maturation.

2. Introduction:

Tissue engineering holds remarkable promise for providing architecturally and functionally competent replacements for tissues damaged by injury, disease and aging

[197-203]. During the last decades, both scaffold and scaffold-free tissue engineering strategies have been explored [184, 188, 204-207]. As the central portion of scaffold-based tissue engineering, biomaterials can provide molecular and mechanical signals to promote cell adhesion and proliferation, and enhance extracellular matrix (i.e., ECM) protein deposition and tissue formation [208, 209]. Although it retains a high potential for application, the scaffold-based approach faces numerous challenges. One of the key problems is that the ideal material to satisfy all the requirements for tissue engineering applications remains elusive. In addition, scaffold materials and their degradation products can introduce a variety of adverse effects [210]. As an alternative, bioprinting-based, scaffold-free tissue fabrication methods (i.e., organ printing) have been explored [210, 211]. For example, Cyrille Norotte and coworkers developed a 3D printing technology to fabricate scaffold-free, vascular tissue engineered constructs. This approach has several distinct advantages. In particular, it can allow for the creation of tissues with a high cell density. In addition, it can facilitate rapid tissue formation and accelerate tissue maturation [210, 212].

One core concept of organ printing is the use of tissue spheroids as building blocks to assemble functional tissues [210, 211]. Tissue spheroids are sphere-shaped micro-tissues formed by spontaneous self-assembly of cell suspensions in the absence of cell-adhesive substrates (e.g., inside agarose microwells). They hold great promise as a bioink for organ printing because they could potentially accelerate tissue formation and maturation [210, 211]. Notably, we have developed a robotic technology for rapid and scalable fabrication of a large number of tissue spheroids needed for organ printing [213].

To date, agarose molds have been extensively used to facilitate the assembly of tissue spheroids. The agarose molds can be fabricated by both direct (i.e., 3D printing) and indirect (i.e., casting) methods. In the case of indirect mold fabrication, the current technology typically involves microfabrication, including 3D printing, of the master mold (e.g., wax mold) for the subsequent agarose mold fabrication [214]. For direct mold fabrication, agarose has been printed into a mold to fabricate a small diameter vessel tissue engineering construct [212]. Here, we describe a proof-of-concept method to directly print a customized alginate mold for tissue fabrication. This has a distinct advantage in that printing alginate does not require low temperature plates for gelation nor heated dispenser units, as may be the case for printing agarose [212, 215, 216]. Similar to agarose, alginate is essentially a non-biodegradable, bio-inert, and biocompatible material. These are all highly desirable characteristics for printing a mold structure because it would maintain its shape fidelity to direct tissue morphology and not interact with the forming tissue. Also, it allows for the fabrication of customized molds for specific applications.

In this study, we proposed and developed a 3D mold-printing technology to produce biocompatible, bio-inert alginate hydrogel molds, which can facilitate the fusion process of tissue spheroids to form scaffold-free tissue-engineered constructs with defined 3D structures. Specifically, we have developed a 3D printing technology to print micro-droplets of alginate solution on calcium-containing substrates in a layer-by-layer manner to fabricate a variety of 3D structures. Further, we utilized this technology to

fabricate ring-shaped 3D hydrogel molds for toroid-shaped tissue unit fabrication. Tissue spheroids composed of 50% endothelial cells and 50% smooth muscle cells were robotically placed into the 3D printed alginate molds, and they were found to rapidly fuse together into toroid-shaped tissue units. Histological and immunofluorescence analyses indicated the critical role of cell-secreted collagen I in tissue formation and maturation. These scaffold-free toroid-shaped tissue units could be used to stack together to fabricate blood vessel-like tube for further clinical research and application.

3. Materials and methods:

3.1 Configuration of the Palmetto 3D bioprinter

The Palmetto 3D Printer (Fig. 2.1), is a fully automated 3D printer developed by the Medical University of South Carolina and Clemson University, and assembled by Izumi International (Greenville, SC). The core devices for 3D printing include a three-axis motion control stage (Janome R2300N, Mahwah, NJ), a linear liquid dispensing system (Fishman, Hopkinton, MA) and a digital microscope (Dino Lite, Torrance, CA) to record the printing process. The printing hardware is housed in a sterile chamber, and the control and monitoring systems are set outside of the chamber. This 3D printer is capable of accurately dispensing micro-droplets of 1 µl volume per second at a resolution of 10 □m in all three (X, Y, and Z) dimensions. The system utilizes tapered free-flow tips with a range of 250-840 µm inner diameters (Fishman, Hopkinton, MA) as printing nozzles. In this application, 250 µm inner diameter tips were used as a printing nozzle for alginate and Pasteur pipettes (diameter ~1000 µm) were used to deposit tissue spheroids.

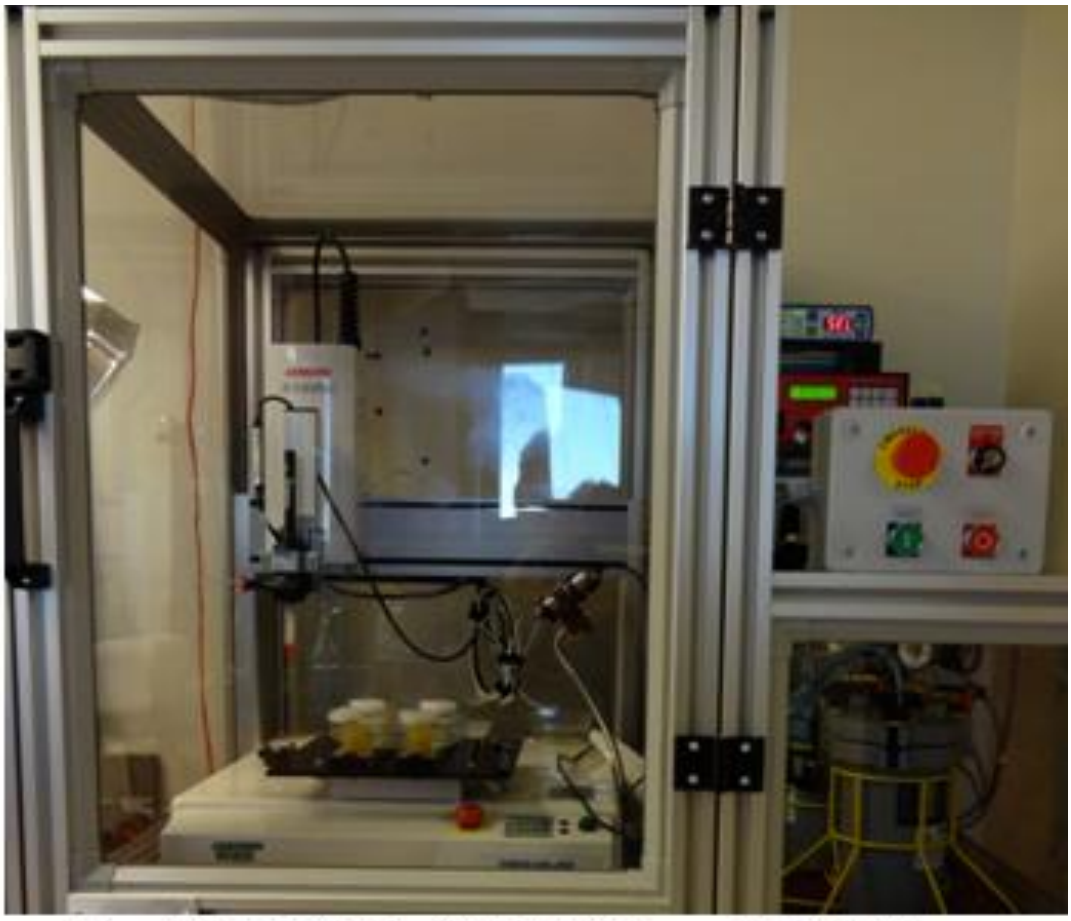

Figure 2.1. A picture of the Palmetto 3D Printer.

3.2 Alginate solution for 3D printing

3% sodium alginate solution (w/v) (FMC BioPolymer Co., Philadelphia, PA, USA) was selected as ink for 3D bioprinting because: 1) it can rapidly form hydrogels at the physiological condition by reacting with calcium ions and 2) it has suitable viscosity for robotic liquid dispensing, while maintaining the droplet shape after dispensing (i.e., a high contact angle). To rapidly crosslink micro-droplets of alginate solution into

hydrogel, 100 mM CaCl2 in 2% gelatin solution were utilized to prepare printing substrates according to the report of Brugger and coworkers [217].

3.3 Cell culture and spheroids fabrication

Human aortic smooth muscle cells (hSMCs) and human umbilical vein endothelial cells (HUVECs) (passage 3) were purchased from Lonza (Catalogue number: CC-2571 and C2517A respectively; Lonza, Basel, Switzerland). They were cultivated in media as suggested by the manufacturer (cell culture media: Lonza CC-3162 and CC-3182, respectively). At passage 5, the two cell types were mixed at a 1:1 ratio and then seeded into non-adhesive agarose hydrogels molds containing 35 concave recesses with hemispheric bottoms (400 μm diameter, 800 μm deep) to facilitate the formation of tissue cell spheroids.

The agarose hydrogel molds were prepared using commercial master micro-molds from Microtissues, Inc (Providence, RI) as negative replicates. 330 μl 1% sterile agarose solution was pipetted into the master micro-molds to form an agarose hydrogel mold, which was then carefully detached from the master mold and transferred into one well of a 24 well tissue culture plate.

The schematic presentation of cell spheroids fabrication is shown in the Fig. 2. 3M hSMCs (Passage 5) and 3M HUVECs (Passage 5) were suspended in 2ml media composed of 50% hSMC media and 50% HUVEC media. 75 μl of the cell suspension was pipetted into each agarose mold. After the cells had settled down into the recesses of the mold (10 min), additional media was added (1.0ml/well for a 24 well plate) and

exchanged as needed. In this way, 840 cell spheroids with diameter 300 µm can be routinely prepared using a 24 well plate containing 24 agarose hydrogel molds.

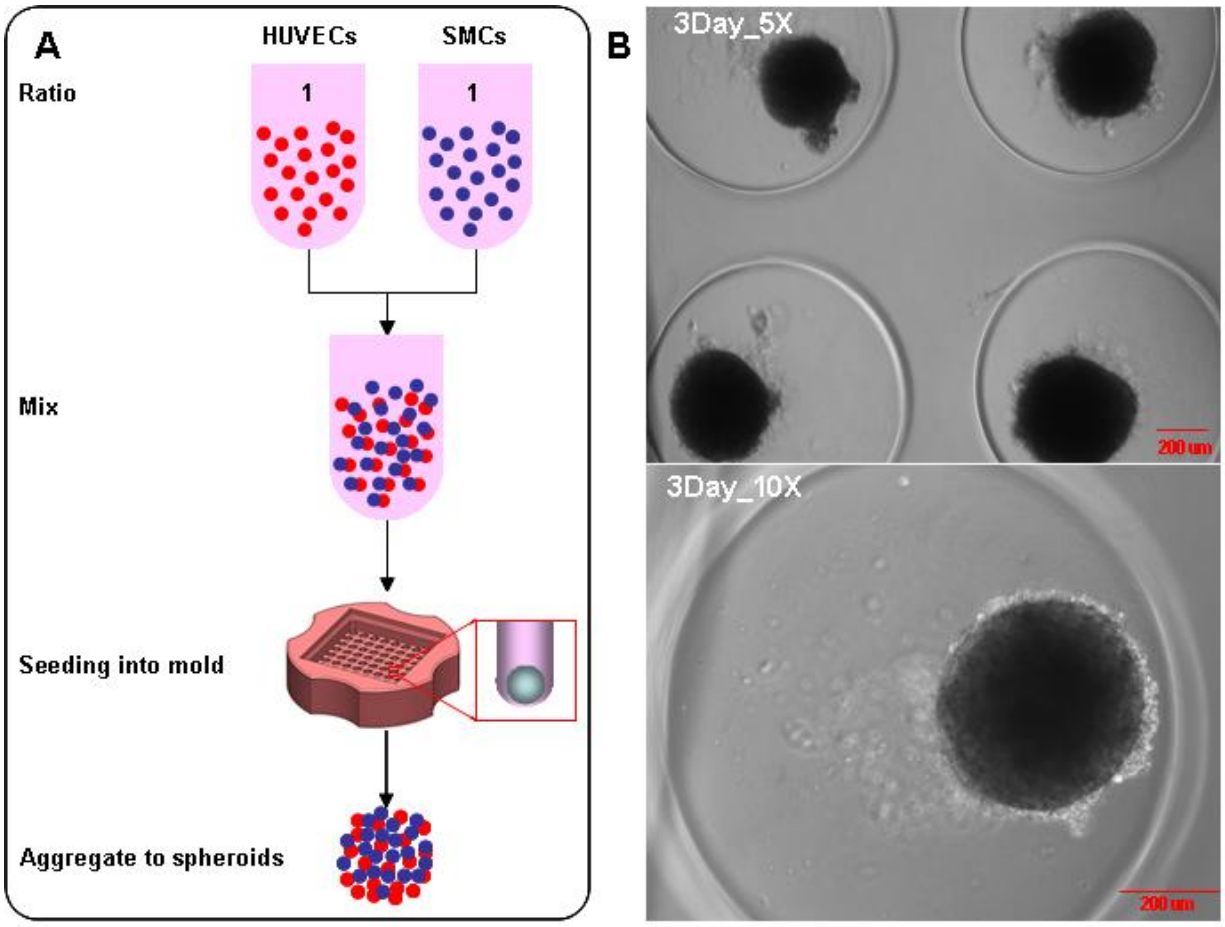

Figure 2.2: A: Schematic presentation of the protocol for spheroid fabrication by seeding the cells suspension into non-adhesive agarose model; B: bright field images of a 3-day-old tissue spheroids in low and high magnification. Scale bar is 200µm.

3.4 Histological and immunofluorescence analysis of tissue units

The printed tissue units were fixed for 30 minutes in 4% paraformaldehyde solution. After dehydration, tissues were processed for paraffin infiltration and embedding and sectioned. The paraffin sections were stained with hematoxylin–eosin and the images were captured using light microscope (Olympus BX40 equipped with a DP25

digital camera). For immunofluorescence staining, primary antibodies were rabbit anti-human collagen I (Cedarlane USA, Burlington, NC), mouse anti human α-smooth muscle actin (Sigma Aldrich, St. Louis, MO), and secondary antibodies were Alexa Fluor 546 and Alexa Fluor 647 (Invitrogen, Carlsbad, CA). First, a heat-induced epitope retrieval step was performed by 5 minutes pressure-cooking of the deparaffinized sections in 1.6 L PBS and 15ml antigen unmasking solution (H-3300, Vector Laboratories, Burlingame, CA). The sections were then permeabilized in a 0.1% Triton X-100 in PBS for 15 min at ambient temperature. After washing in PBS (3x), the tissues were incubated in Background Buster (Innovex Biosciences, Richmond, CA) for 30 minutes at ambient temperature. After washing in PBS (3 × 5 min), sections were incubated with primary antibodies diluted in 1.0% BSA in PBSA (PBS + 0.01% sodium azide) overnight in refrigerator. After washing in PBS (3 × 5 min), tissues were incubated with coordinate secondary antibodies diluted in 1.0% BSA in PBSA for 1h at ambient temperature. After copious washing in PBS, nuclei were counterstained with DAPI (Molecular Probes/Invitrogen, Eugene, OR) diluted in PBSA for 15 min at ambient temperature. Following the final wash procedure, individual slides were mounted under cover glass using Fluoro-Gel (Electron Microscopy Sciences, Hatfield, PA). A TCS SP5 AOBS laser scanning confocal microscope (Leica Microsystems, Inc., Exton, PA) was used to obtain fluorescent images.

4. Results and discussion

4.1 Optimization of printing parameters and printing algorithm

Alginate has been extensively used in the 3D bioprinting because it can robustly form cell compatible hydrogels in physiological conditions [218, 219]. Notably, native alginate is not adhesive for cells and is also not broken down enzymatically in mammals [220, 221]. These are all highly desirable characteristics as molding materials to facilitate tissue formation. As a bio-inert material, alginate does not compete with cell-cell adhesion and therefore promote fusion process of tissue spheroids. In addition, it has limited biodegradability and sufficient mechanical property for molding [222].

In this work, we have developed a technology to robotically deposit micro-droplets of alginate solution onto calcium-containing gelatin substrates to construct 3D hydrogels (Fig. 2.4) [218]. A substrate of 100 mM CaCl2 in 2% gelatin solution were prepare to serve as a reservoir for calcium ion. A lower concentration of calcium ions in the gelatin solution can lead to slow gelation process and undefined shape of microdroplets. It is important to note that some cell types may be sensitive to the free calcium ion that slowly diffuses from the physically crosslinked alginate mold [223, 224]. However, auxiliary tests confirmed high viability (>90%) post-printing using Ca2+-sensitive porcine chondrocytes with an atypical calcium concentration (100mM) (Fig. 2.3) [225, 226]. By using a layer-by-layer approach, we can fabricate hydrogels with a number of defined 3D structures. This has been attributed to the upward diffusion of calcium ion from the gelatin substrates (Fig. 2.4) [217].

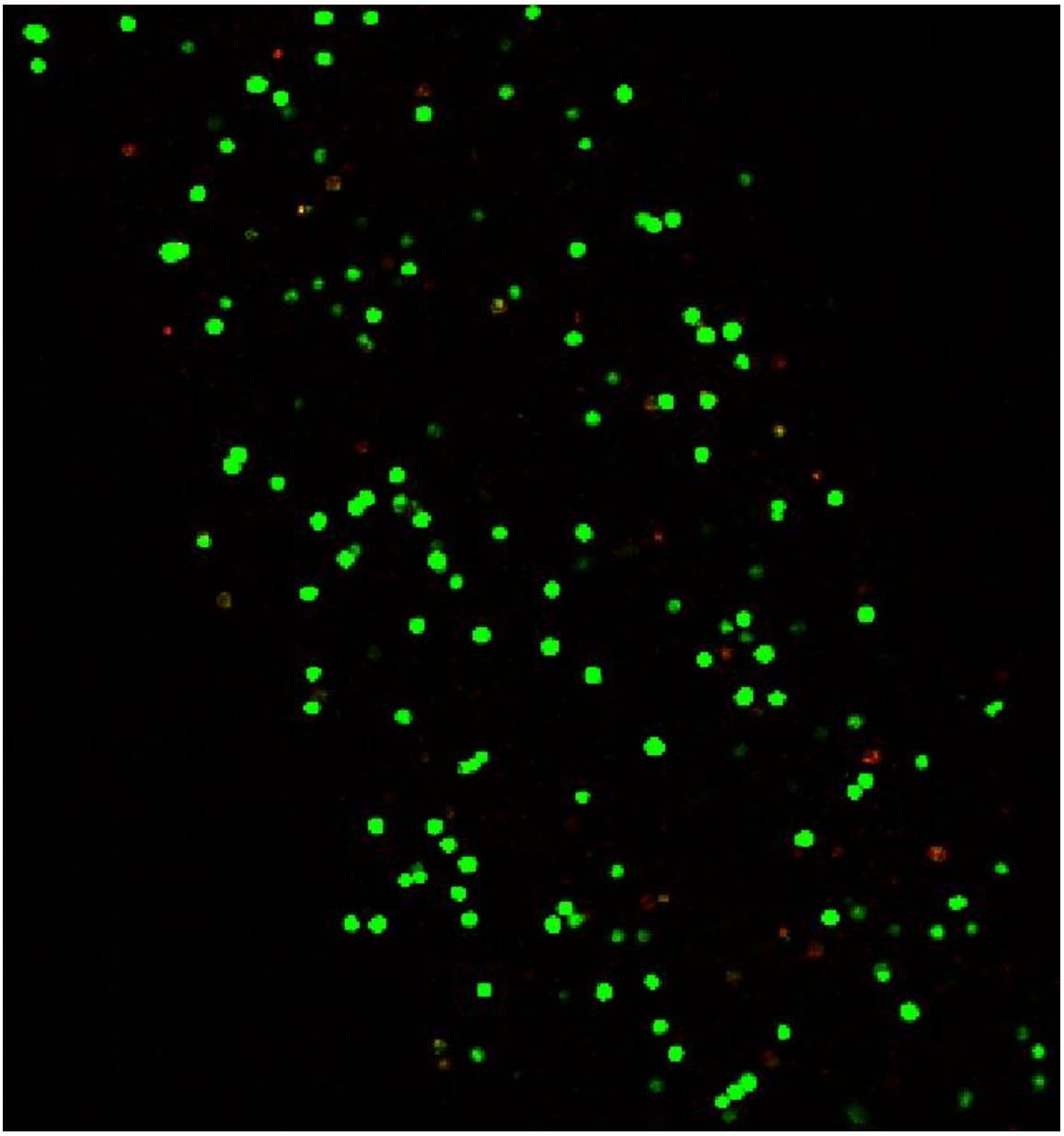

Figure 2.3: Live dead staining indicated high viability (>90%) post-printing using Ca^{2+}sensitive porcine chondrocytes suspended in an alginate solution printed on a high calcium concentration-containing gelatin substrate (100mM).

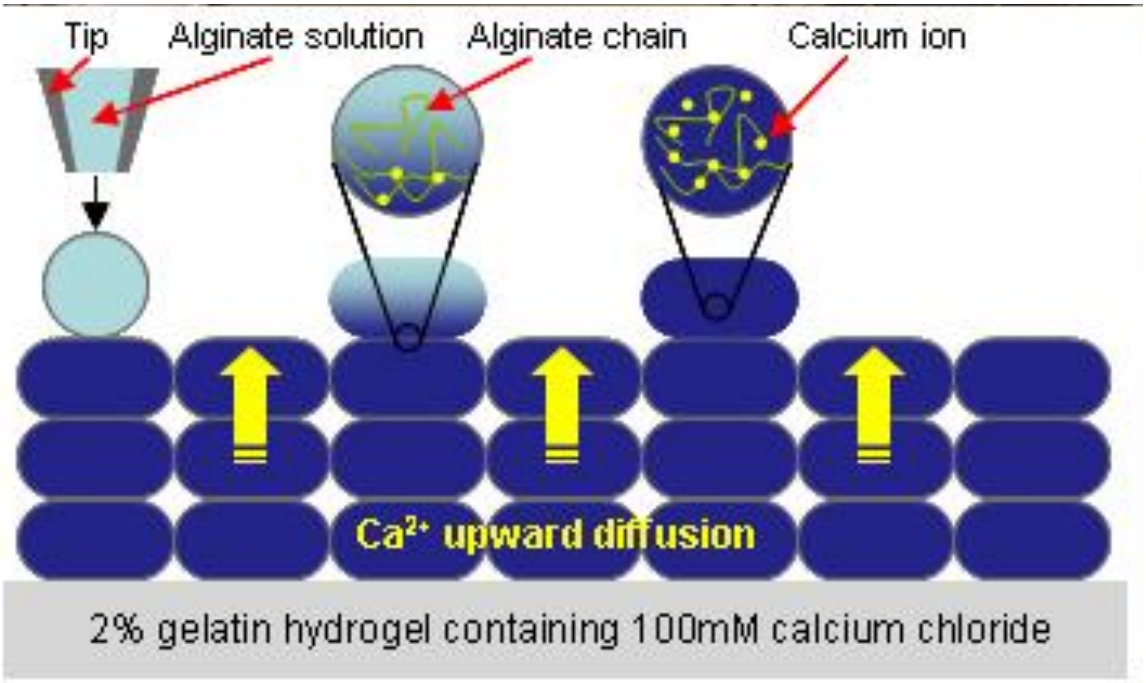

Figure 2.4: Schematic presentation of 3D alginate hydrogel printing on calcium-containing gelatin substrate. Adapted from the reference [217].

To ensure a high consistency among the alginate hydrogel micro-droplet formed on calcium-containing substrates, we have optimized both concentration of alginate solution and the volume of each droplet. A 3% sodium alginate solution (w/v) was found suitable for 3D printing because 1) it can rapidly form hydrogel micro-droplets on the calcium ion-containing gelatin substrates, and 2) it has proper viscosity for robotic liquid dispensing while maintaining the droplet shape after dispensing. The dispensing volume for 3% (w/v) alginate solution was set as 1 µl in this study because a smaller volume (0.5 µl) can give rise to larger variation among printed droplets (Fig. 2.5). To prevent the coalescence of newly printed droplets with their neighbors (Fig. 2.6a), we developed a printing algorithm to ensure that no printed droplet lands next to an un-gelled droplet and the final printed product maintained a defined structure as designed (Fig. 2.6b) [217].

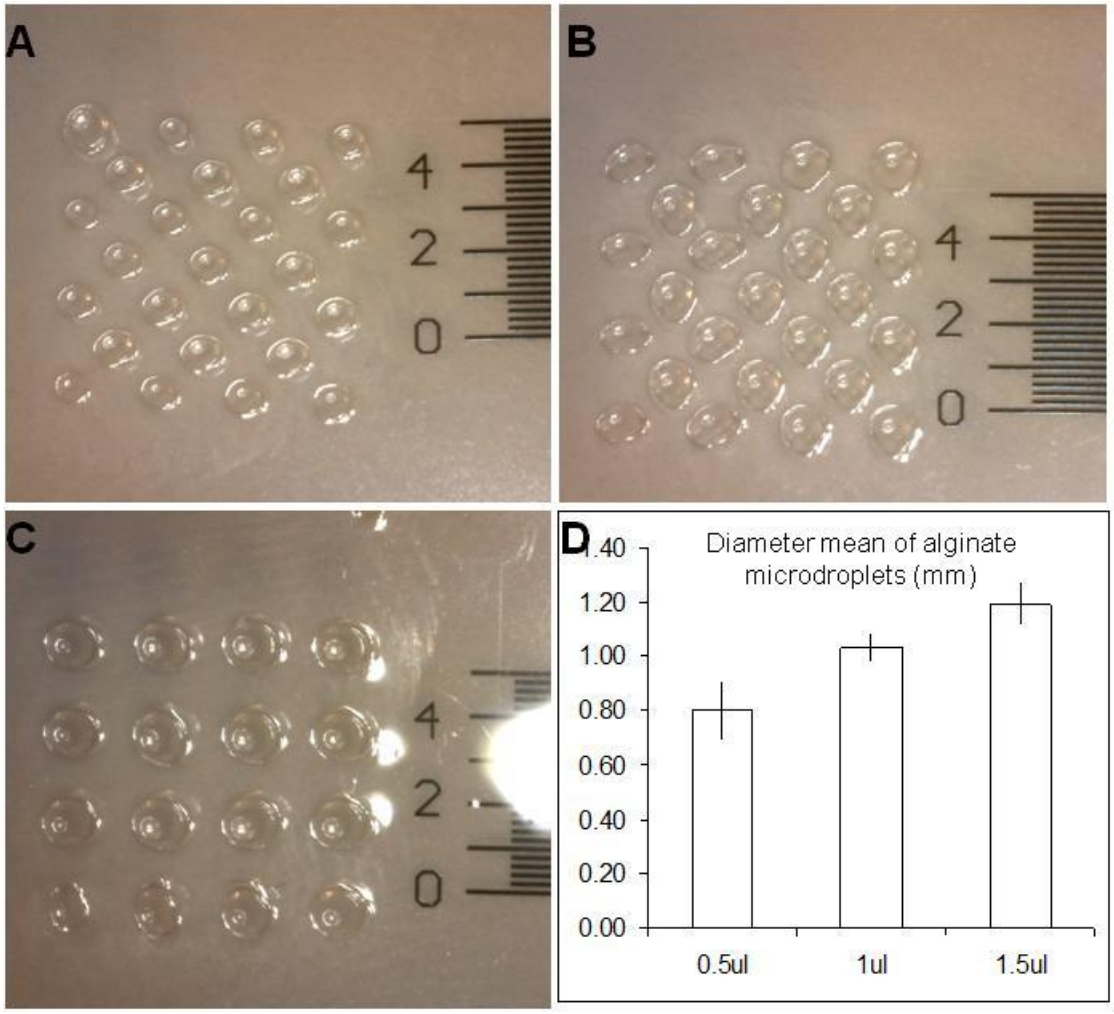

Figure 2.5: The different size of alginate microdroplets (A=0.5, B=1.0, and C=1.5µl) printed on calcium containing gelatin substrates. D: The averaged diameter of alginate microdroplets with different volume.

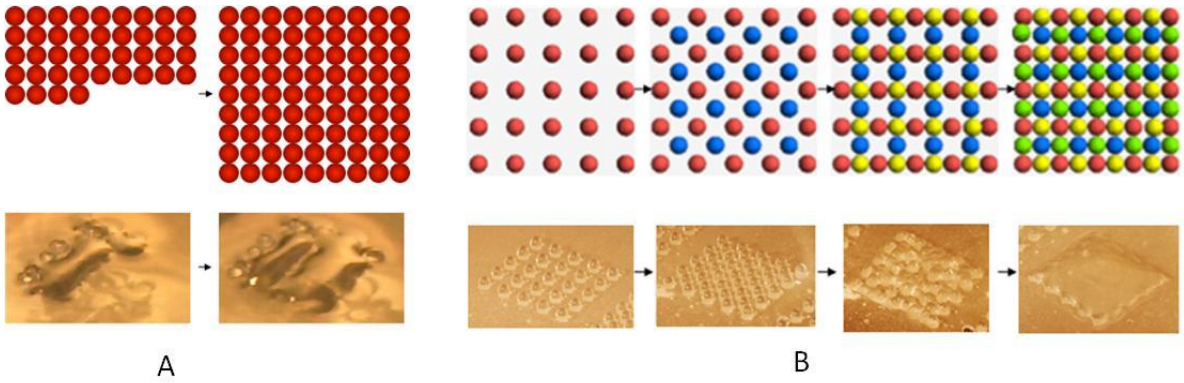

Figure 2.6: (a) Printing algorithm before optimization: printing microdroplets of alginate solution next to each other can lead to the coalescence of newly printed droplets. (b) Printing algorithm after optimization: printing microdroplets of alginate solution in 4 steps to to ensure that no printed droplet lands next to an un-gelled droplet and the final printed product can maintain a defined structure as designed.

To prove the feasibility of 3D hydrogel printing, we designed and printed hydrogels with different 3D geometries (cube, square frame, and pyramid). Both the printing scheme and the printed alginate hydrogel structures are shown in Fig. 2.7. This demonstrates the 3D hydrogel printing we developed here can allow for a proof-of-concept for the fabrication of alginate hydrogels with defined 3D structures. To quantify the printing accuracy, we measured the dimensions of a 3D printed cube structure and compared them to the design. As shown in Figure 2.7D, the cube structure was designed to have dimensions of 9.6 x 9.6 x 1.75 mm (X, Y, Z), which is a result of a printing design with dimensions of 9 mm x 9 mm (based on the center of dot) and a Z dimension defined by 5 layers. Typically, the first layer of alginate, which is printed onto the gelatin surface, has a height of ~0.7-0.8 mm, while the second and above layers of alginate, which is printed onto alginate surface, have heights of ~0.2-0.3 mm. The actual printed cube structure has dimensions of 9.6 x 9.8 x 1.8 mm, and it thus can be defined as an

accurate printed structure [227]. Using the cube structure as a model, overnight culture in PBS resulted in an average increase in dimension (X, Y) of 1.8%, thus maintaining the designed parameters. This demonstrates the 3D hydrogel printing we developed here can allow for a proof-of-concept for the fabrication of alginate hydrogels with defined 3D structures. Given the quickly advancing field in biofabrication, improved parameters and limitations to bioprinting must be further optimized to achieve the highest needed control.

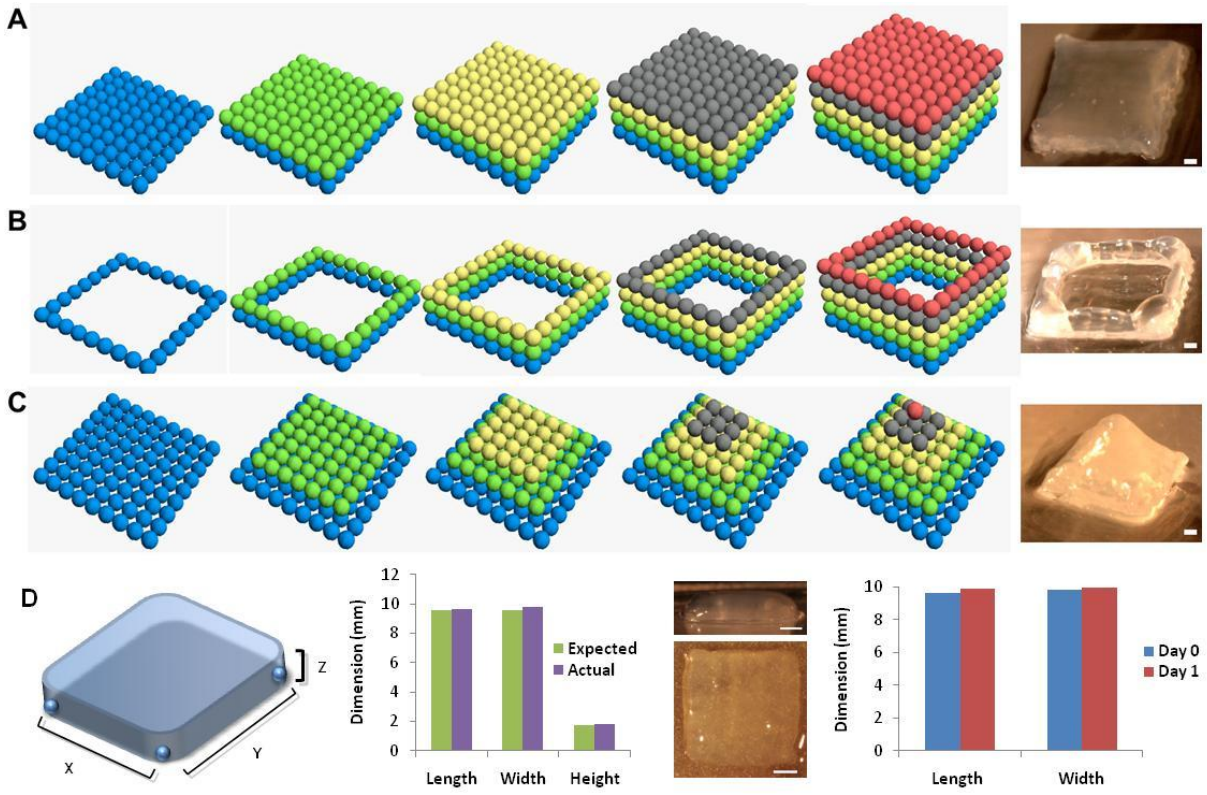

Figure 2.7: Microdroplets facilitated 3D printing alginate hydrogels with different geometries (cube (a), square frame (b) and pyramid (c)). : the left is the schematic presentation of 3D printing algorithm used to print 3D structures shown in the right. Each layer was printed using an multi-step algorithm similar to the one shown in Figure 3. The optimal expected dimensions of 9.6 x 9.6 x 1.75 mm were based on a design of 9 mm x 9 mm in the X and Y dimension (measured from the dot center) and a Z dimension defined by 5 layers (d). The scale bar for (a),(b), and (c) is 1 mm. The scale bar for (d) is 2 mm.

The blue, green, yellow, grey and red represent the 1st, 2nd, 3rd, 4th, and 5th layer of bioprinted alginate microdroplets, respectively.

4.2 3D Printing alginate molds and robotically seeded spheroids

To utilize the 3D printed alginate hydrogel molds to facilitate fusion processes of tissue spheroids, we have designed ring-shaped alginate molds to fabricate toroid-shaped tissue units, which can be utilized to produce tissue engineering constructs (Fig 2.8) [228]. To prepare the mold, 24 layers of alginate hydrogel was printed in a layer-by-layer fashion to generate ring-shaped molds with inner diameter 5 mm, outer diameter 7 mm and height 3 mm over a time span of approximately 30 min (~30 secs/layer with ~1 min gelation time between layers). Subsequently, 840 spheroids (average diameter ~300 μm) composed of 50% hSMCs and 50% HUVECs was robotically seeded into the mold to achieve a connected tissue [229, 230]. Tissue spheroids were selected as bioink for 3D bioprinting in this study because they have the potential to accelerate tissue formation and maturation [210, 211].

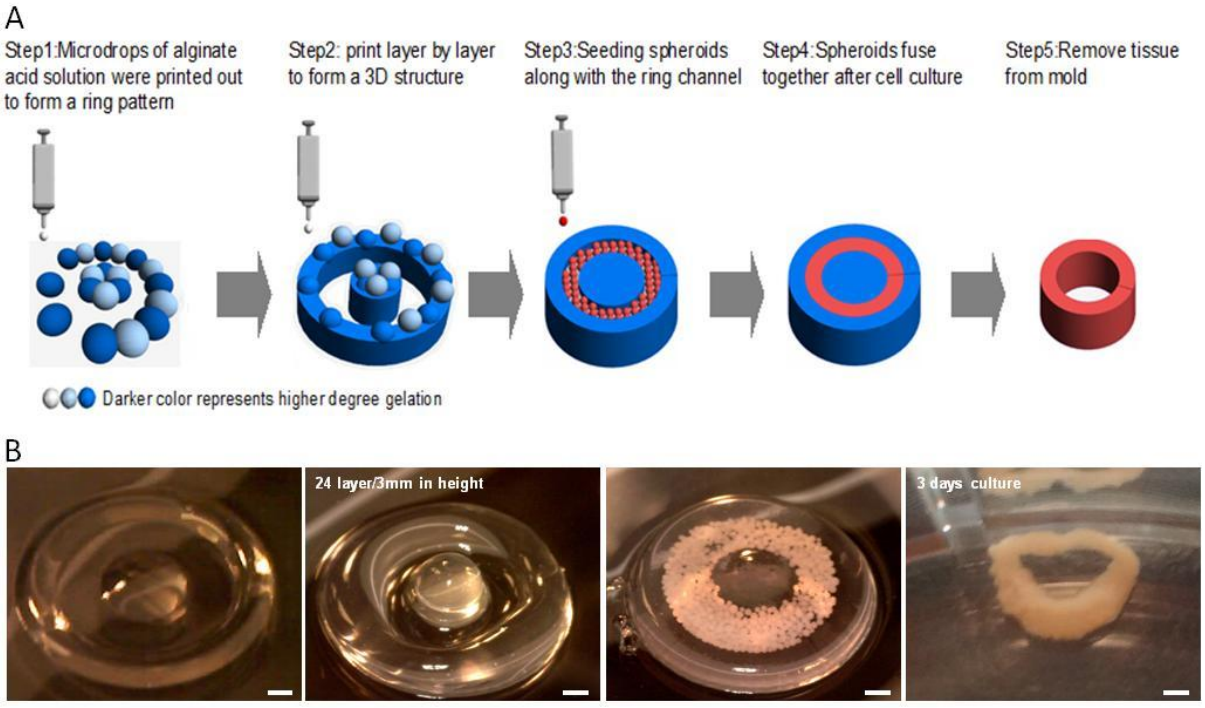

Figure 2.8: Schematic presentation (a) and actual product (b) of 3D alginate hydrogel printing for tissue unit fabrication using vascular spheroids (i.e., containing smooth muscle cells and endothelial cells). Scale bar is 1mm

To utilize the Palmetto 3D Printer to robotically seed the cell spheroids, a variety of dispensing nozzles have been examined. Interestingly, Pasteur pipettes have been found most suitable for robotic dispensing of cell spheroid due to the smooth transition from upper portion of the pipette to the tip of the pipette (i.e., dispensing nozzle) and the diameter of pipette tip (~1000 µm) (Fig. 2.9). Customized Pasteur pipettes with a smaller tip diameter (~750 µm) were found difficult to seed cell spheroids since spheroids often blocked the dispensing nozzle.

Figure 2.9: A picture showing the pasture pipette printing tip loaded with tissue spheroids for dispensing.

4.3 Fabrication of toroid-shaped tissue units

After seeding into ring-shaped molds, the construct was moved to an incubator for 15 min to melt the calcium-containing gelatin. The melted gelatin solution was immediately replaced with fresh cell culture media to minimize exposure to high calcium concentration environment. The cell spheroids quickly began fusing into toroid-shaped

tissue units after 3 days culture in a reliable manner, which is in agreement with previous research [210, 212]. Notably, the quality of the 3D printed mold can effectively affect the shape of the formed tissue units. These tissue units were cultivated for an additional 13 days to facilitate their maturation. To examine the fusion and maturation process, histological and immunofluorescence analysis were conducted. At day 4, the boundaries of many individual spheroids were clearly visible (Fig. 2.10a, b, j, and k) with many open spaces between spheroids (white arrow in Fig 2.10k). Notably, collagen I was often found between the boundaries of two adjacent spheroids (Fig. 2.10k and l). As a structural ECM protein with cell adhesion motifs (e.g., RGD peptide sequence), collagen I was thought to function as adhesive to facilitate the fusion process of the spheroids. At day 8, most spheroids were found to be closely associated to each other, while gaps between some spheroids were still found (white arrows in Fig. 2.10d and e). At day 16, the spheroids had fused into a complete tissue with abundant, newly synthesized collagen I (Fig. 2.10m). In addition, the collage I had filled all the gaps between spheroids (white arrows in Fig. 2.10o). This data indicates collagen I plays a critical role in promoting cell-cell adhesion, tissue formation and maturation. This is consistent with the previous report that cell-adhesive ECM proteins can crosslink adjacent cells together by binding to their cell surface receptor (e.g., integrin) and promote tissue cohesion [231]. In addition, the day 16-tissue units were stained for smooth muscle cells and endothelial cells (Fig 2.10p-r). The high expression of specific molecular markers for both cell types (i.e., smooth muscle actin and VWF) indicates high cell viability and normal cell behavior after 16-day cell culture.

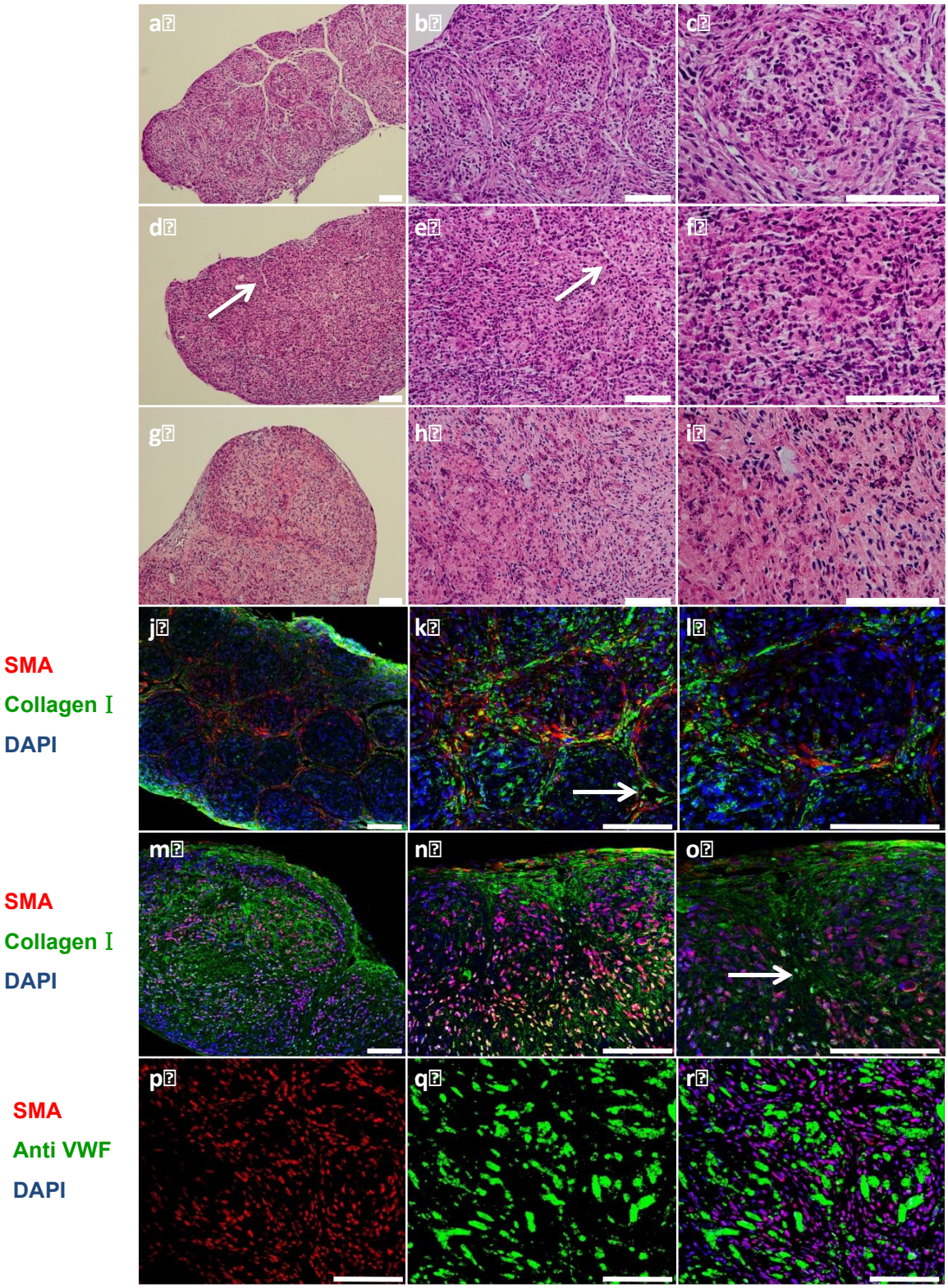
a
b
c
d
e
f
g
h
i
j
k
l
SMA
Collagen I
DAPI
m
n
o
SMA
Collagen I
DAPI
p
q
r
SMA
Anti VWF
DAPI

Figure 2.10: Histological and immunofluorescence analysis of the tissue units cultured for 4, 8 and 16 days. (a,b,c) H&E staining for tissue units cultured for 4 days at 10x, 20x and 40x magnification, respectively. (d,e,f) H&E staining for tissue units cultured for 8 days at 10x, 20x and 40x magnification, respectively. (g,h,i) H&E staining for tissue units cultured for 16 days at 10x, 20x and 40x magnification, respectively. (j,k,l) immunofluorescence analysis of tissue units cultured for 4 days at 20x, 40x and 63 x magnification. (m,n,o) immunofluorescence analysis of tissue units cultured for 16 days at 20x, 40x and 63 x magnification. (p,q,r) immunofluorescence analysis of tissue units cultured for 16 days at 40x magnification for smooth muscle actin, anti VWF and merge picture. Scale bar is 100μm

5. Conclusion

3D printing holds great promise for rapid, scalable fabrication of tissue engineering constructs. Here, we have developed a robust technology to robotically 3D print alginate hydrogel molds to facilitate fusion process of tissue-cell spheroids for the fabrication of scaffold-free tissue units. To this end, we have optimized both printing parameters and printing algorithm for constructions of alginate hydrogels with defined 3D architectures. In addition, we also utilized the Palmetto 3D Printer to robotically place tissues spheroids into the alginate molds to rapidly fuse into toroid-shaped tissue units. Our system has displayed the proof-of-concept for using alginate as a 3D printable, molding material to facilitate scaffold-free tissue unit fabrication. The approach developed in this manuscript could be used to fabricate various open-structured molds (e.g., honeycomb-shaped molds) for the construction of complex structures [214]. Further calibrations and improvements to the system are needed for the fabrication of non-open-structured molds to prepare tissues with more complex shapes, such as small diameter blood vessels, which require printing spheroids and alginate in a more controlled manner. Given the rapid development in printing technology, we expect that the technology

developed here can be used to fabricate tissues with complex structures for tissue engineering and drug testing applications.

CHAPTER THREE

SILICON NANOWIRE-INDUCED MATURATION OF CARDIOMYOCYTES DERIVED FROM HUMAN INDUCED PLURIPOTENT STEM CELLS

1. Abstract:

The current inability to derive mature cardiomyocytes from human pluripotent stem cells has been the limiting step for transitioning this powerful technology into clinical therapies. To address this, scaffold-based tissue engineering approaches have been utilized to mimic heart development in vitro and promote maturation of cardiomyocytes derived from human pluripotent stem cells. While scaffolds can provide 3D microenvironments, current scaffolds lack the matched physical/chemical/biological properties of native extracellular environments. On the other hand, scaffold-free, 3D cardiac spheroids (i.e., spherical-shaped microtissues) prepared by seeding cardiomyocytes into agarose microwells were shown to improve cardiac functions. However, cardiomyocytes within the spheroids could not assemble in a controlled manner and led to compromised, unsynchronized contractions. Here we show, for the first time, that incorporation of a trace amount (i.e., ~0.004% w/v) of electrically conductive silicon nanowires (e-SiNWs) in otherwise scaffold-free cardiac spheroids can form an electrically conductive network, leading to synchronized and significantly enhanced contraction (i.e., >55% increase in average contraction amplitude), resulting in significantly more advanced cellular structural and contractile maturation.

2. Introduction:

Cardiovascular disease is the leading cause of death worldwide [232]. Due to the limited regenerative capacity of adult hearts, human embryonic stem cell (hESC)- and

human induced pluripotent stem cell (hiPSC)-based therapy has been the focus of a significant amount of research [4, 233]. This is due to their proven capacity to produce de novo cardiomyocytes. However, the current cardiomyocytes derived from hESCs and hiPSCs retain an immature phenotype, including poorly organized sarcomere structures (i.e., functional units of the contractile machinery) [234-236]. Thus, these cells lack the ability to generate sufficient, anisotropic forces as adult cardiomyocytes. This has led to difficulties for electrical and mechanical integration with human adult myocardium [153, 174], which has limited the applications of hESC and hiPSC technology for cardiac repair.

During embryonic development, environmental factors (e.g., extracellular matrix, growth factors, mechanical and electrical stimulation) have major effects on the maturation of cardiomyocytes. To mimic the maturation process in vitro, hESC- and hiPSC-derived cardiomyocytes have been mixed with scaffolding materials (e.g., Matrigel and collagen type I gel) to prepare cardiac tissue-engineered constructs and then conditioned with electrical and/or mechanical stimulation [234, 237-239]. While these scaffolds can provide tissue-like 3D microenvironments, current scaffolding materials lack the matched physical/chemical/biological properties with the native extracellular environments during heart development. On the other hand, scaffold-free, 3D cardiac spheroids have emerged as promising model systems to mimic cardiac tissues [184, 187]. Unlike in the myocardium, cardiomyocytes in the spheroids do not organize in a controlled manner and led to compromised, unsynchronized contractions. To improve this, we reasoned the incorporation of e-SiNWs in cardiac spheroids can facilitate the

formation of an electrically conductive network, and provide synchronized and improved electrical/mechanical signals to advance structural and contractile maturation of the cardiomyocytes (Fig. 3.1 and Fig. 3.2).

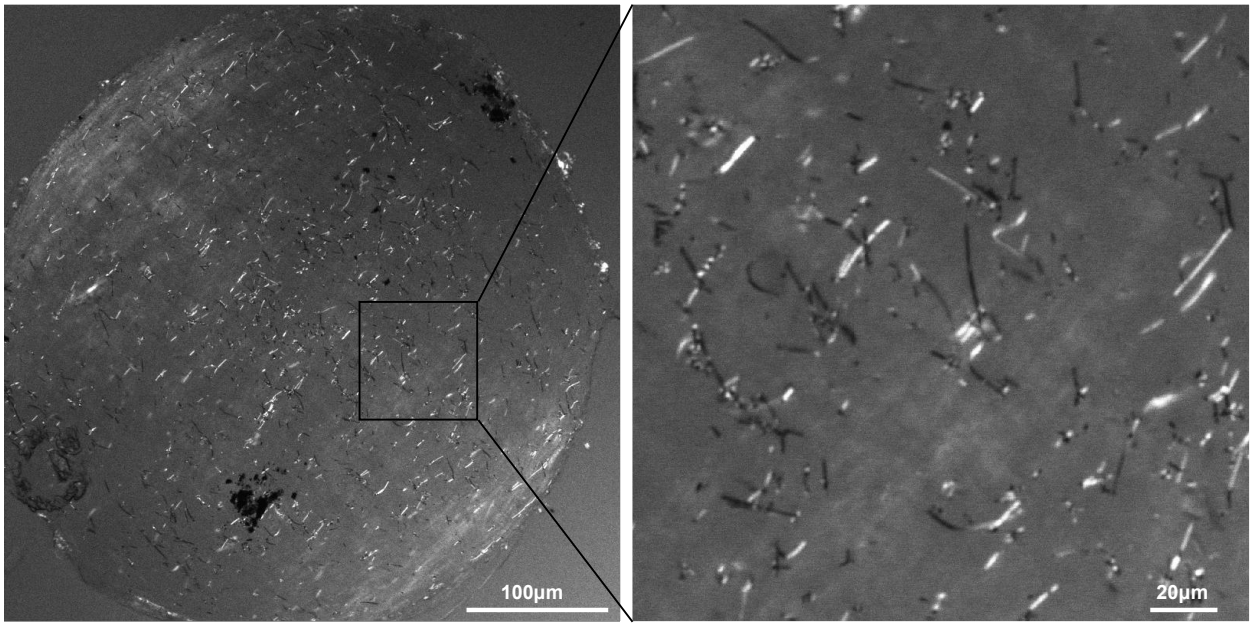

Figure 3.1. DIC image of the e-SiNW-reinforced human cardiac spheroids shows the uniform distribution of e-SiNWs within the spheroids at a 1:1 ratio (number of cells/number of e-SiNWs).

3. Materials and Methods:

3.1 Electrically conductive silicon nanowire fabrication and harvesting.

Single-crystalline SiNWs were synthesized using the nanocluster-catalyzed vapor-liquid-solid method described previously in a quartz tube connected to a gas manifold and vacuum pump and heated by a temperature controlled tube furnace.1 Monodisperse gold nanoparticles (100 nm, Ted Pella) were dispersed on SiO2/silicon substrates, which were placed within the central region of the quartz tube reactor. The SiNWs were synthesized at 470-485 oC using silane (SiH_4) as the silicon reactant source,

H2 as the carrier gas, and phosphine (PH_3, 1000 ppm in H_2) as the n-type dopants. In a typical synthesis of uniform n-type, 100 nm SiNWs, the flow rates of SiH4, PH3 and H2 were 1-2, 2-4 and 60 standard cubic centimetres per minute, respectively, and the total pressure 40 torr. The nanowires were collected from the oxidized silicon substrates by sonication in isopropanol for 1 min followed by centrifugation to obtain SiNWs with an average dimension of 100 nm diameter and 10 μm length. The electrical conductivity of the SiNWs were measured by using four-probe transport measurement.

3.2 Cell harvest and culture.

Rat-neonatal cardiac cells were isolated from 2-day-old Sprague-Dawley rats by using the neonatal isolation kit (Worthington Biochemical Corporation, Lakewood, NJ). Rat-neonatal cardiac cells and spheroids were cultured in Dulbecco's Modified Eagle Medium (DMEM, 4500 mg/L glucose) (Thermo Scientific, Pittsburgh, PA) containing 10% heat inactivated fetal bovine serum (HI FBS) (Life Technologies, Carlsbad, CA), 1% penicillin-streptomycin (Life Technologies, Carlsbad, CA), and 1% non-essential amino acids (Life Technologies, Carlsbad, CA). hiPSC-derived cardiomyocytes (iCell Cardiomyocytes, Cellular Dynamics International, Madison, WI, USA) were cultured according to the manufacturer's protocol. Briefly, hiPSC-derived cardiomyocytes were plated on 0.1% gelatin coated 6-well plates in iCell Cardiomyocyte Plating Medium (Cellular Dynamics International) at a density of about 3 × 105 to 4.0 × 105 cells/well and incubated at 37 °C in 5% CO2 for 4 days. Two days after plating, the plating medium was removed and replaced with 4 mL of iCell Cardiomyocytes Maintenance Medium (Cellular Dynamics International). After 4 days of monolayer pre-culture, cells were

detached using trypLE Express (Gibco Life Technologies, Grand Island, NY) and prepared for spheroid fabrication.

3.3 Spheroid fabrication and electrical stimulation.

The agarose hydrogel molds were prepared using commercial master micro-molds from Microtissues, Inc (Providence, RI) as negative replicates to create non-adhesive agarose hydrogels molds containing 35 concave recesses with hemispheric bottoms (800 µm diameter, 800 µm deep) to facilitate the formation of tissue cell spheroids. 330 µL 1% sterile agarose solution was pipetted into the master micro-molds and was then carefully detached after gelation from the master mold and transferred into one well of a 24-well tissue culture plate. The schematic presentation of cell spheroids fabrication is shown in the Fig. 2C. A suspension of rat-neonatal cardiac cells and e-SiNWs in media was prepared at a 1:1 ratio (number of cells/number of SiNWs) with a concentration of 5.0×10^6 cells/mL. Similarly, hiPSC-derived cardiomyocytes were mixed with e-SiNWs in the Maintenance media at a 1:1 ratio (number of cells/number of SiNWs) with a concentration of 3.0 x 106 cells/mL. Approximately 75 µl of the cell/e-SiNW suspension (rat-neonatal cardiac cells, 5.0 x 106 cells/mL; hiPSC-CMs, 3.0 x 106 cells/mL) was pipetted into each agarose mold. After the cells had settled down into the recesses of the mold (10 min), additional media was added (5 mL) and exchanged every 2 days for the length of the experiment. After 4 days of spheroid culture, an electrical stimulation treatment (C-Pace unit, Ion Optix, Milton, MA 02186) was started for designated groups for 7 days (15 V, 1 Hz, 2 ms). For the long term culture experiment of hiPSC cardiac

spheroids, the electrical stimulation treatment was performed for 21 days for the designated groups after the initial 4 days of spheroid culture.

3.4 Video and image analysis of beating spheroids.

Videos of 6 spheroids from each group were recorded starting after the initial 4 days of spheroid culture using Zen 2011 software (Zeiss, Göttingen, Germany) with capture rate of 14 frames per second. Then the videos were converted to a series of TIFF format pictures by Adobe Premiere (Adobe, San Jose, CA). Threshold edge-detecting in ImageJ software (National Institutes of Health) was used on high contrast spheroid pictures and graphed to realize contraction profiles, from which other quantifiers were calculated (i.e., fractional area change and beats per minute).

3.5 Histological and immunofluorescent analysis of spheroids and cells.

Freshly collected spheroids (~30-35) were placed onto a pre-labeled tissue base mold and the entire tissue block was covered with OCT. Immediately, the base mold containing spheroids was transferred into pre-cooled ethanol with dry ice to ensure that the spheroids were frozen completely. By using the cryotome, the frozen spheroids block were sectioned into 7 µm thickness layers onto glass slides for immunohistochemistry. The sections were fixed with pre-cooled acetone (-20 °C) for 10 min. The fixative was poured off and the acetone was allowed to evaporate from the sections for 20 min at room temperature. After washing (3 times at 5 min) in PBS with 0.1% Triton X-100 (PBST), 100 µl blocking buffer was added (10% goat serum in PBS) onto the sections of the slides and incubated in a humidified chamber at room temperature for 1 h. Sections were incubated with appropriately diluted primary antibody: alpha sarcomeric actinin (Abcam,

Cambridge, UK), troponin I (Santa Cruz, Dallas, TX), connexin-43 (Sigma Aldrich, St. Louis, MO) and beta myosin heavy chain (Millipore, Billerica, MA) overnight at 4 °C. After washing in PBST (3 times at 5 min), tissues were incubated with coordinate secondary antibodies diluted in PBST for 1h at ambient temperature. After washing in PBST (3 times at 5 min), nuclei were counterstained with DAPI (Molecular Probes/Invitrogen, Eugene, OR) diluted in PBST for 15 min at ambient temperature. Following the final wash procedure (PBST, 3 times at 5 min), glass cover slips were added to the slides using Fluoro-Gel (Electron Microscopy Sciences, Hatfield, PA). Finally, TCS SP5 AOBS laser scanning confocal microscope (Leica Microsystems, Inc., Exton, PA) was used to get fluorescent images. Fluorescent protein expression was calculated as the fluorescence area coverage divided by the number of nuclei.

3.6 TUNEL staining for the frozen section of spheroids.

In Situ Cell Death Detection Kit (Roche, Penzberg, Germany) was used to determine the viability of the cell in the frozen section of spheroids based on the protocol from website of Roche. Briefly, the frozen sections of spheroids were fixed with 4% paraformaldehyde in PBS for half hour at room temperature. Following washing in PBS for 30 minutes, samples were incubated in a permeabilization solution (0.1% Triton X-100 and 0.1% sodium citrate in PBS) for 2 minutes on ice. Then 50ul of the TUNEL reaction mixture were added to samples and incubated in 37 °C for 1 hour. After washing in PBST (3 times at 5 min), nuclei were counterstained with DAPI (Molecular Probes/Invitrogen, Eugene, OR) diluted in PBS for 15 min at ambient temperature. Following the final wash procedure (PBS, 3 times at 5 min), glass cover slips were added

to the slides using Fluoro-Gel (Electron Microscopy Sciences, Hatfield, PA). Finally, TCS SP5 AOBS laser scanning confocal microscope (Leica Microsystems, Inc., Exton, PA) was used to get fluorescent images.

3.7 Western blotting analysis.

Following 7 days of cell culture with or without electrical stimulation, 30-35 spheroids from each rat-neonatal group were harvested from agarose molds. After centrifugation and washing by PBS once, 30 µl lysis buffer with 1% protease and phosphatase inhibitor cocktails (Pierce Biotechnology, Rockford, IL) was added into the vials containing pellet of spheroids. Thereafter, the mixture was homogenized by the FastPrep24 instrument (MP Biomedicals, Santa Ana, CA) to break down spheroids into single cells. After 30 minutes to lyse cells on ice, then tubes were centrifuged for 10 min at 10 000g at 4 °C and the supernatant was collected as protein solution. After quantifying the protein concentration by using the bicinchoninic acid methods, the protein solution was mixed with 4x LDS sample loading buffer (Pierce Biotechnology) and boiled for 5 min. Protein samples of equal amount were separated in a 4%–12% Bis Tris NuPAGE gel (Life Technologies, Carlsbad, CA). Proteins were transferred to a PVDF membrane (Life Technologies) and blocked with 5% nonfat milk for one hour, followed by incubation with the following primary antibodies: alpha sarcomeric actinin (Abcam, Cambridge, UK), connexin-43 (Sigma Aldrich, St. Louis, MO), beta myosin heavy chain (Millipore, Billerica, MA), and GAPDH (Sigma Aldrich) overnight at 4°C. Blots were then probed with horseradish peroxidase-labeled secondary antibodies (Cell Signal, Danvers, MA) and visualized by an enhanced chemiluminescence detection kit

(Amersham Pharmacia Biotech (GE Healthcare), Pittsburgh, PA). The intensity of each signal was analyzed by using ImageJ software.

3.8 Spheroid spreading assay.

Spheroids were seeded onto 0.1% gelatin-coated glass cover slips and incubated at 37 °C, 5% CO2, 20% O2. Cell culture medium was changed every other day. After 12 days culture, the spheroids spread into a monolayer structure, which was suitable for immunofluorescent staining for high resolution, single cell, sarcomere structure analysis.

3.9 Single cell cardiomyocyte analysis.

The average sarcomere length was defined as spacing between α-SA striations and was measured using black and white renderings of confocal α-SA-stained cardiomyocyte images, according to previous methods.2 Using ImageJ, fluorescence profiles along lines passing perpendicular through 3 different striated regions of at least 9 cells, containing at least 6 consecutive sarcomere structures, were measured and divided by the number of sarcomeres (space between profile peaks). Z-line width, as previously explored,3 was measured directly on α-SA-stained cardiomyocyte images in 12 cells with 15 measurements per cell. Z-line alignment was defined to establish a sensitive method for sarcomere alignment to reflect the enhanced contraction and synchronization. Calculations were made using an ImageJ plug-in, OrientationJ, which creates an orientation distribution output.4 The area under the curve at ±20° the peak orientation degree divided by the total area under the curve was established as the fraction Z-line alignment.

3.10 Calcium transient imaging of cardiac spheroids.

Fluo-4 Direct Calcium Assay Kits (Life Technologies, Carlsbad, CA) was used to label calcium ion in the whole spheroids based on the protocol from Life Technologies. Briefly, spheroids were seeded onto 0.1% gelatin-coated glass cover slips and incubated at 37 °C, 5% CO2, 20% O2. Cell culture medium was changed every other day. After 4 days culture, the spheroids were rooted on the cover slips. Then cover slips with the spheroids were put into 12 wells plates with 2 ml calcium dye solution per well and incubated at 37 °C, 5% CO2, 20% O2 for 1h. TCS SP5 AOBS laser scanning confocal microscope (Leica Microsystems, Inc., Exton, PA) was used to collect the videos of the calcium transient of whole spheroids with a capture rate of 14 frames per second. Finally, we used the software of LAS AF from Leica to conduct the quantification of videos collected by confocal.

3.11 qRT-PCR analysis.

Total RNA was isolated according to the kit and protocol of an RNeasy Micro Kit (Qiagen, Vinlo, Netherlands) with the addition of the QIAShredder (Qiagen) during the homogenization step for spheroids. For each group, 20-35 spheroids were used for RNA isolation. At least 25 ng of total RNA for each group was subjected to cDNA synthesis using the Bio-Rad (Hercules, USA) iScript cDNA synthesis kit. qRT-PCR step was performed using “best coverage” validated Taqman primers (Life Technologies, Carlsbad, USA) in 10 μl reactions for the following genes: CACNA1C, CACNA1G, GAPDH, GJA1, MYL2, ACTB. Data was normalized as the change in cycle threshold (Ct) to GAPDH and ACTB (dCt) and analyzed using, mRNA expression = 2^(-(dCt)).

3.12 Transmission Electron Microscopy.

SiNWs were gently sonicated in isopropyl alcohol (IPA) and dispersed onto lacey carbon grids (Ted Pella Inc.). TEM imaging was conducted using a 300kv FEI Tecnai G2 F30 Super Twin Transmission Electron Microscope.

Spheroids were fixed with 2.5% glutaraldehyde, postfixed in PBS buffered 1% osmium tetroxide with 1.5% K+ ferricyanide, dehydrated in graded ethanol and Acetonitrile, and embedded in PolyBed 812 (Polysciences). 70-nm thick spheroid sections were prepared by using a Leica UltraCut R and a diamond knife, stained with Hanaichi Pb citrate and uranyl acetate, and imagined using a JOEL 200 CX transmission electron microscope.

3.13 Statistics Analysis

Differences between experimental groups were analyzed using a independent Student T-tests and one-way ANOVA followed by Tukey's post-hoc test. $P< 0.05$ was considered significantly difference for all statistical tests.

4. Results and Discussion:

This approach has the distinct advantage in that only a trace amount of e-SiNWs is utilized, minimizing the adverse effects of traditional scaffolds, such as unmatched physical/chemical/biological properties with the native extracellular environments during heart development. e-SiNWs were selected because of their controllable electrical conductivity, tunable dimensions, and convenient surface tailorability [240, 241]. Although SiNWs might not be well known as biocompatible materials, in vitro

biocompatibility studies have shown no significant cytotoxic effects for both undoped and n-type SiNWs [242]. Further, the recent research showed SiNWs are biodegradable, and their degradation products are found mainly in the form of $Si(OH)_4$ and are metabolically tolerant in vivo [195, 243-246]. This makes them advantageous over other non-biodegradable, electrically conductive nanomaterials (e.g., gold nanowires, carbon nanotubes and nanofibers), especially for potential in vivo applications.

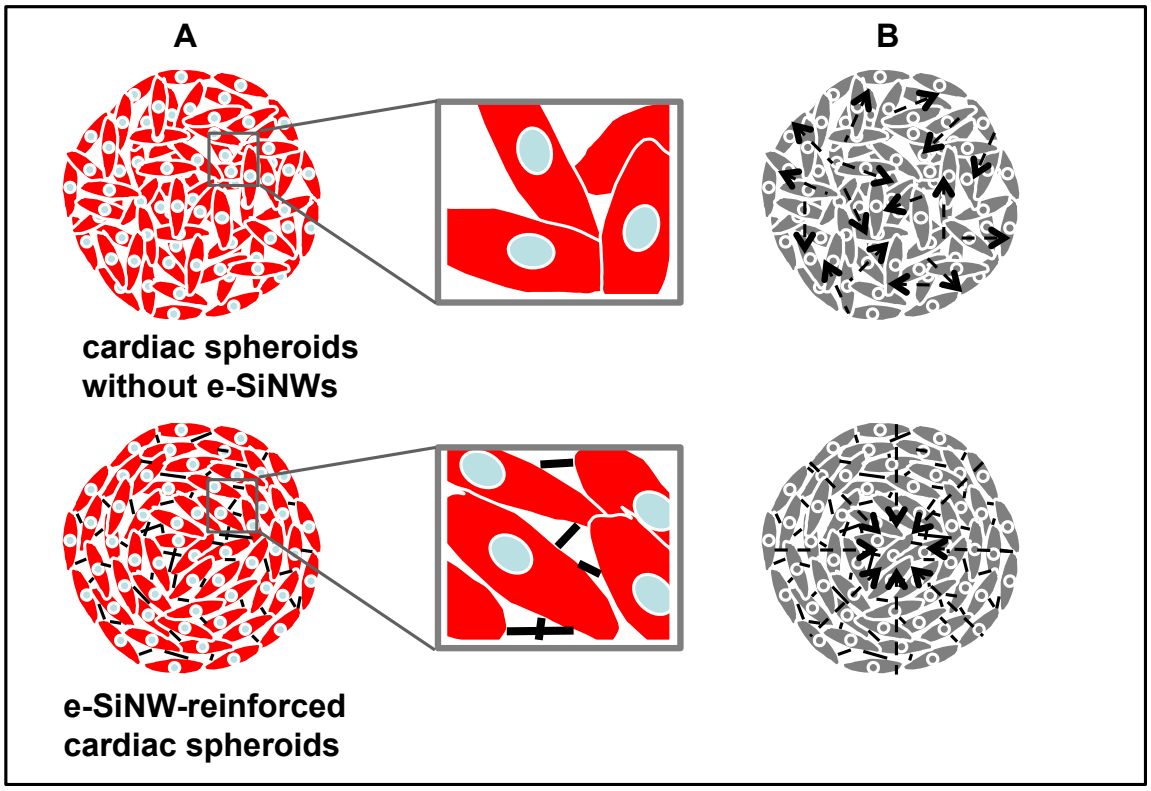

Figure 3.2. Schematic overview of e-SiNWs reinforced cardiac spheroids. (A) Structure of cardiac spheroids without (top) or with (bottom) e-SiNWs: cardiac cells (red), nuclei (blue) and e-SiNWs (black). e-SiNWs (bottom) can act as bridges to electrically connect cardiac cells and create electrically conductive microenvironments throughout the spheroids. (B) Cardiomyocytes in the cardiac spheroids without e-SiNWs (top) form electrically isolated small beating clusters with random contractions, while cardiomyocytes in the e-SiNWs-reinforced cardiac spheroids can produce synchronized and enhanced contractions (bottom). Arrows represent the directions of contractile forces.

In this study, n-type SiNWs (Diameter ≈ 100 nm; length ≈ 10 μm; Silane/Phosphane = 500) were prepared according to the previously established protocol [247] (Fig. 3.3A, B). The doping ratio and diameter of the e-SiNWs were chosen to obtain a high conductivity (150 - 500 μS/μm) compared to cell culture medium (~1.75 μS/μm) and myocardium (~0.1 μS/μm) to create highly electrically conductive microenvironments within spheroids[191, 248]. The length of the SiNWs was selected to inhibit cell internalization. As shown in the Fig. 3.3C-E, both rat neonatal cardiac cells and cardiomyocytes derived from human induced pluripotent stem cells have been used to prepare e-SiNWed-reinforced cardiac spheroids. The rat left-ventricle neonatal cardiac cells were utilized in the initial study due to their ready availability. They were mixed with e-SiNWs at a ratio of around 1:1 (number of cells/number of e-SiNWs) and seeded into agarose microwells to prepare e-SiNW-reinforced rat-neonatal cardiac spheroids (Fig. 3.3C, D and Fig. 1). The ratio between e-SiNWs and cardiac cells was selected to minimize the interference of e-SiNWs on the self-assembly process of cardiac cells due to their high density and high stiffness (Fig. 3.4). Notably, TEM images of e-SiNW-reinforced cardiac spheroid indicated the e-SiNWs located in the extracellular space in the spheroids, which supported our selection of dimensions of e-SiNWs (Fig. 3.3E).

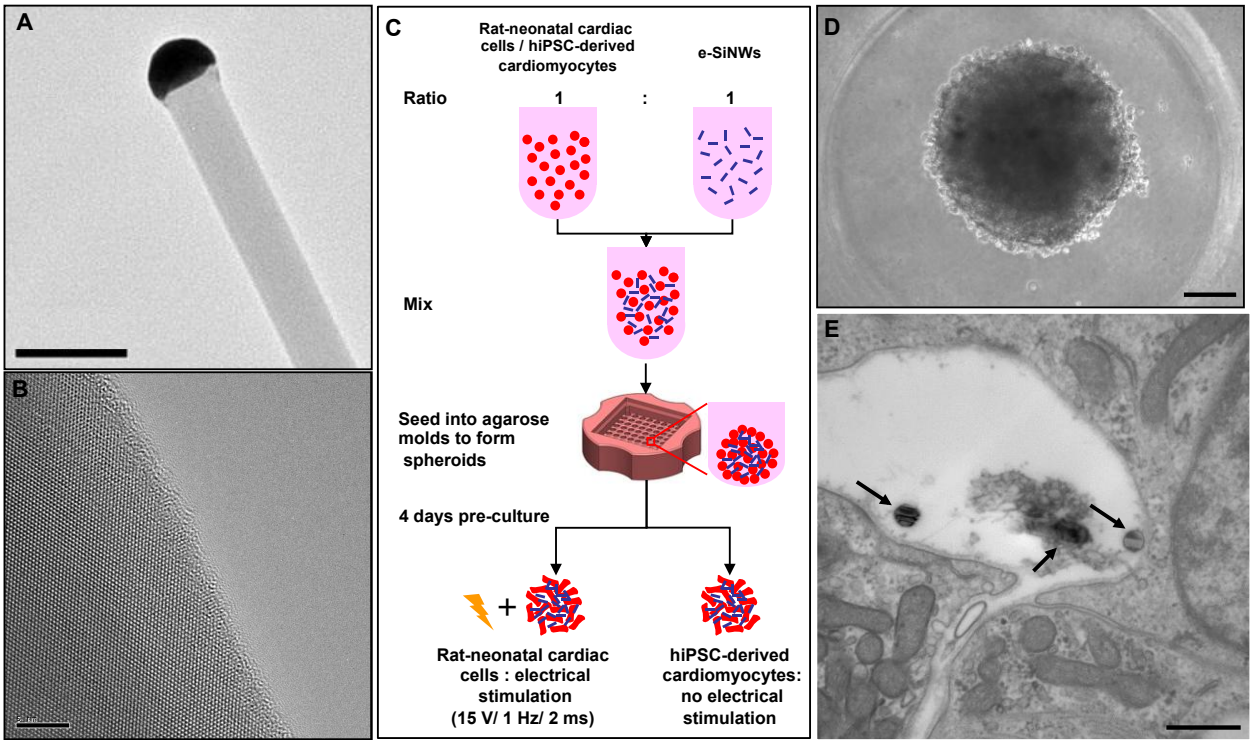

Figure 3.3. Electrically conductive silicon nanowires (e-SiNWs) introduced to cardiac spheroids. (A) Transmission electron microscopy (TEM) image of an e-SiNW (diameter ≈ 100 nm; length ≈ 10 µm) and (B) high-resolution TEM image of the e-SiNW. (C) Schematic representation of spheroid fabrication using rat-neonatal cardiac cells or human induced pluripotent stem cell (hiPSC)-derived cardiomyocytes at a ratio 1:1 (number of cells/number of e-SiNWs) with or without electrical stimulation. (D) Bright field image of hiPSC spheroid with e-SiNWs. (E) TEM image of hiPSC spheroid with e-SiNWs, black arrow indicates the e-SiNWs located in the extracellular area. Scale bars: (A) = 0.2 µm; (B) = 5 nm; (D) = 100 µm; (E) = 500nm.

Although few spontaneous contractions have been found in many rat-neonatal cardiac spheroids after 4 days in culture, both contraction frequency and amplitude can be significantly enhanced by electrical stimulation (Fig. 3.5A-D). To recapitulate the electrical pulses of native myocardium, the spheroids were stimulated at 15 V at 1 Hz, 2 ms[249]. To independently investigate the effects of e-SiNWs and electrical stimulation, four samples have been prepared and examined: rat-neonatal cardiac spheroids without e-

SiNWs and without electrical stimulation (i.e., r-NC spheroids), rat-neonatal cardiac spheroids with e-SiNWs but without electrical stimulation (i.e., r-WC spheroids), rat-neonatal cardiac spheroids without e-SiNWs but with electrical stimulation (i.e., r-NS spheroids), and rat-neonatal cardiac spheroids with e-SiNWs and with electrical stimulation (i.e., r-WS spheroids).

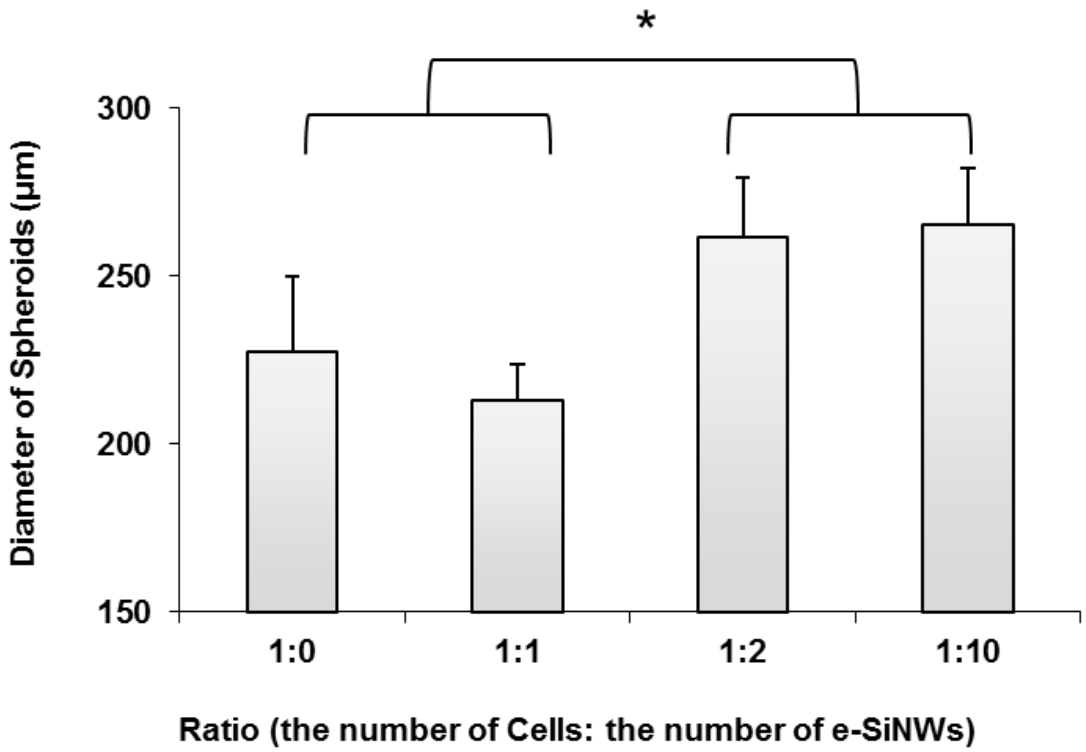

Figure 3.4. Changes in diameter of rat-neonatal cardiac spheroids using different ratios of cells to e-SiNWs on Day 0; n = 6 spheroids per condition. Asterisks (*) represent statistical significance with $p<0.05$; error bar represents standard deviation.

Video analysis revealed that the chronically stimulated spheroids (i.e., r-NS and r-WS spheroids) contract regularly and periodically, while the non-stimulated spheroids (i.e., r-NC and r-WC spheroids) did not contract consistently. As shown in Fig. 3.5A-D,

the average contraction amplitude gradually increased over time for the chronically stimulated spheroids (i.e., r-NS and r-WS) and was several-fold higher than the non-stimulated spheroids (i.e., r-NC and r-WC) with/without stimulation during measurement, which is consistent with the previous report [249]. When comparing r-NS spheroids with r-WS spheroids, significant improvement in the contraction amplitude and synchronization were found in the r-WS spheroids (Fig. 3.5 B, D), which indicate e-SiNWs can facilitate synchronized electrical signal propagation throughout the spheroids.

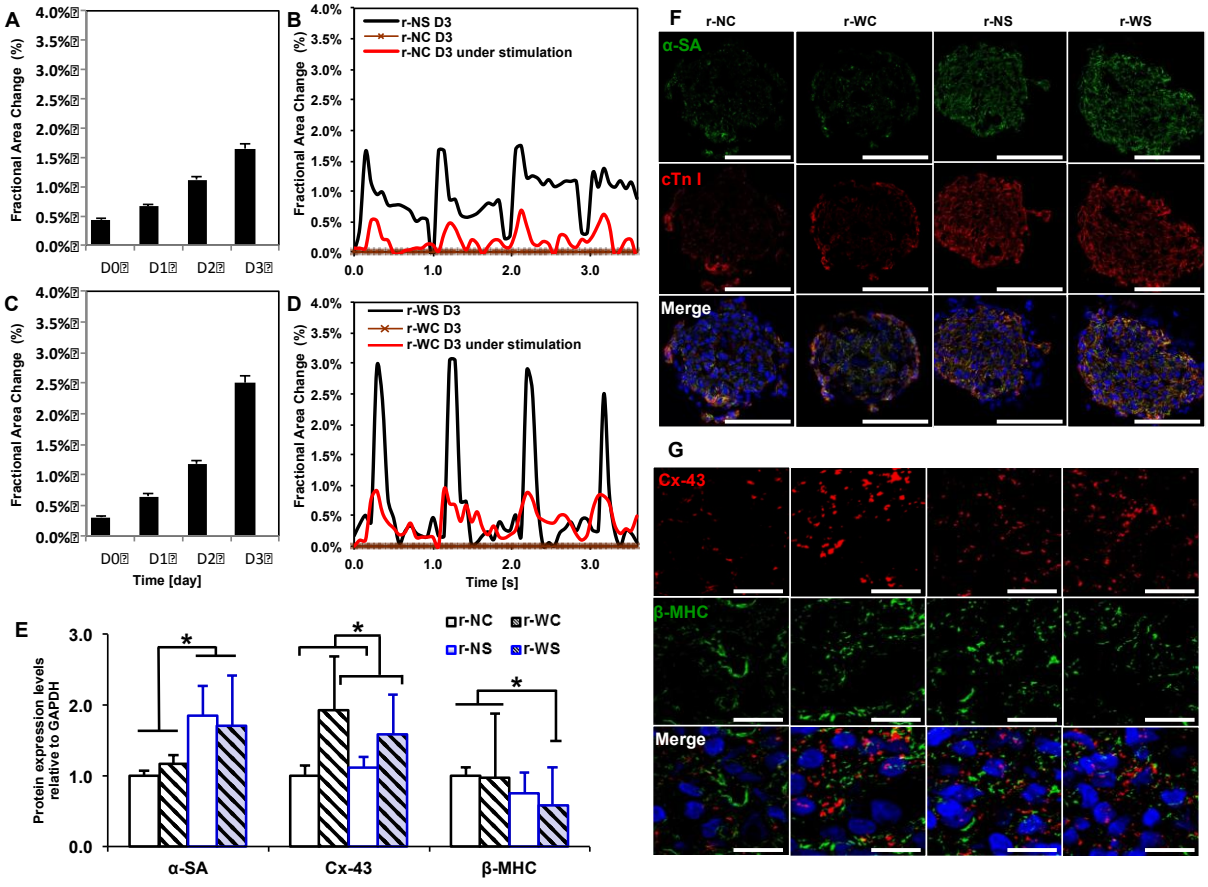

Figure 3.5. Functional and structural analysis of rat-neonatal cardiac spheroids. (A) Averaged fractional area change (i.e., contraction amplitude) over 3 days for r-NS spheroids and (B) a characteristic beating profile on day 3 for r-NC, r-NC under stimulation during measurement, and r-NS spheroids. (C) Averaged fractional area

change over 3 days for r-WS spheroids and (D) a characteristic beating profile on day 3 for r-WC, r-WC under stimulation during measurement, and r-WS spheroids. (E) Western blot analysis (averaged data of three separate experiments) of protein expression levels relative to GAPDH expression after 7 days with or without electrical stimulation normalized to the r-NC group. (F, G) Immunofluorescent staining of cardiac-specific contractile and conductive proteins for all groups after 7 days. r-NC= rat-neonatal cardiac spheroids, no e-SiNWs, no stimulation; r-NS= rat-neonatal cardiac spheroids, no e-SiNWs, with stimulation; r-WC= rat-neonatal cardiac spheroids, with e-SiNWs, no stimulation; r-WS= rat-neonatal cardiac spheroids, with e-SiNWs, with stimulation. n = 6 spheroids per condition (A-D). Asterisks (*) represent statistical significance with $p<0.05$; error bars represent standard deviation. Scale bars: (F) = 100 μm; (G) = 20 μm.

To understand the effects of e-SiNWs and chronic stimulation, the expressions of several key cardiac-specific proteins in all four different spheroids were examined using western blotting and immunofluorescence staining (Fig. 3.5E-G and Fig. 3.6A, B). Among them, connexin-43 (i.e., Cx-43) forms gap junction channels that regulate electrical signal propagation between cardiomyocytes[250, 251]. Cardiac α-sarcomeric actinin (α-SA) and cardiac troponin I (cTnI) are cardiac-specific contractile proteins, and β-myosin heavy chain (β-MHC) is neonatal isoform of myosin heavy chain in rat cardiomyocytes[249]. As shown in the Fig. 3.5E, F and Fig. 3.6A, B, chronic stimulation can significantly increase the expressions and assembly of contractile proteins (e.g., α-SA and cTnI), in agreement with the previous report [249]. On the other hand, the incorporation of e-SiNWs led to enhanced expression and clustering of Cx-43 (Fig. 3.5E, G), also consistent with the previous literature [146, 147, 252, 253]. The combination of SiNWs and chronic stimulation can result in the reduced expression of β-MHC, which indicates a transition from the neonatal isoform of myosin protein to the adult

isoform[249]. This could be attributed to the up-regulated Cx-43 expression (Fig. 3.6 E, G) and/or the increased contraction amplitude (Fig. 3.5 D).

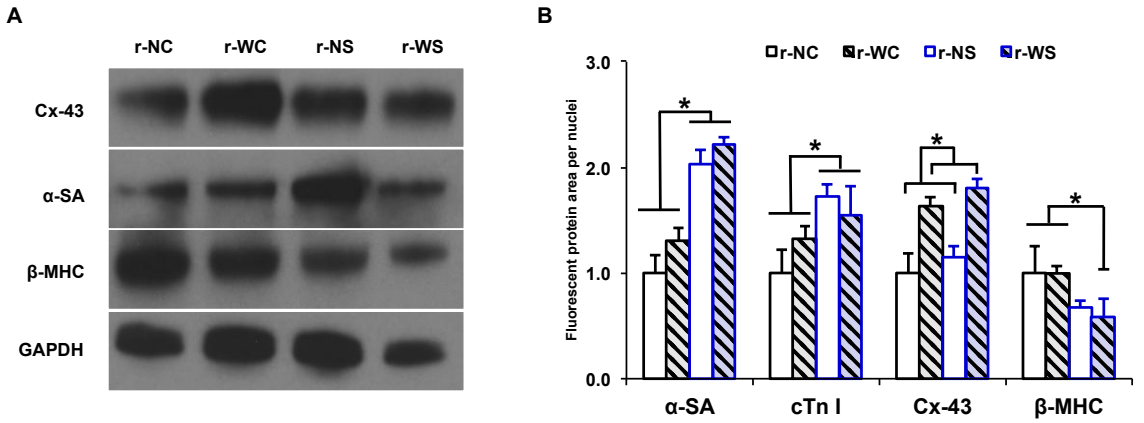

Figure 3.6. Protein expression analysis of rat-neonatal cardiac spheroids after 7 days of treatment. (A) Western blot of cardiac-specific proteins after 7 days for all 4 groups. (B) Protein expression levels based on fluorescent signal-covered area per nuclei normalized over r-NC expression; n = 3 picture regions; 50 µm x 80 µm picture regions, at least containing >24 nuclei. r-NC= rat-neonatal cardiac spheroids, no e-SiNWs, no stimulation; r-NS= rat-neonatal cardiac spheroids, no e-SiNWs, with stimulation; r-WC= rat-neonatal cardiac spheroids, with e-SiNWs, no stimulation; r-WS= rat-neonatal cardiac spheroids, with e-SiNWs, with stimulation. Asterisks (*) represent statistical significance with $p<0.05$; error bar represents standard deviation.

The results from rat-neonatal cardiac spheroids led to the development of hiPSC cardiac spheroids (i.e., cardiac spheroids prepared from hiPSC-derived cardiomyocytes, Fig. 3.3C). Unlike the rat-neonatal cardiac spheroids, strong spontaneous contractions with consistent contraction frequency were found for the non-stimulated hiPSC cardiac spheroids. Notably, a significant decrease in contraction amplitude was found for electrically stimulated hiPSC-derived cardiac spheroids (i.e., hiPSC-NS and hiPSC-WS spheroids) (Fig. 3.7A). TUNEL staining (marker of early apoptosis) of the spheroid sections revealed significant increase in cell death at the center of hiPSC-NS and hiPSC-WS spheroids, while not in the r-NS and r-WS spheroids (Fig. 3.8). Given the similar

sizes of the rat-neonatal and hiPSC cardiac spheroids, the increased cell death at the center of stimulated hiPSC-derived cardiomyocytes was attributed to the increased metabolic demands of the hiPSC-derived cardiomyocytes compared to rat-neonatal cardiac cells [254-256]. Accordingly, strong expression of the assembled cardiac contractile proteins (e.g., α-SA and c-TnI) can only be found on the periphery of the hiPSC-NS and hiPSC-WS spheroids (Fig. 3.9A, B).

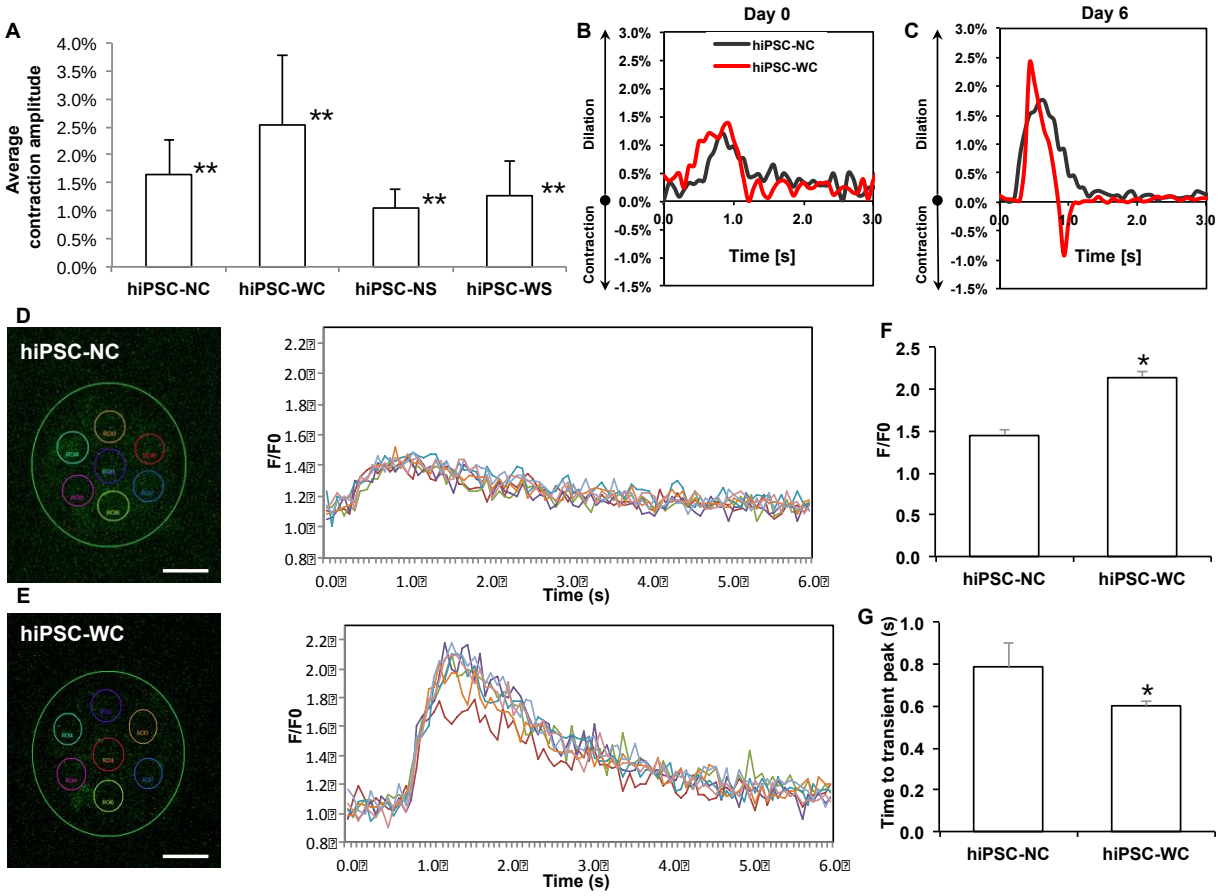

Figure 3.7. Functional analysis of hiPSC-derived cardiomyocyte spheroids. (A) Average contraction amplitude from Day 1 to Day 7 of each group. Double asterisk (**) represents statistical difference between all groups. (B, C) Representative fractional area change (i.e., contraction amplitude) of spontaneously beating spheroids with and without e-SiNWs at time points Day 0 and Day 6; n = 6 spheroids per condition. (D, E) Representative calcium transient imaging of 7 regions of interest (colored circles) per spheroid for each group. Fluorescence amplitude, F/F0, refers to measured fluorescence intensity normalized to background fluorescence intensity. (F) Comparison of the peak value of F/F0 for each group. (n=3) (G) Comparison of calcium release duration for each group. (n=3) hiPSC-NC= human induced pluripotent stem cell cardiac spheroids, no e-SiNWs, no stimulation; hiPSC-WC= human induced pluripotent stem cell cardiac spheroids, with e-SiNWs, no stimulation. Asterisks (*) represent statistical significance with $p<0.05$; error bar represents standard deviation. Scale bars = 100 µm.

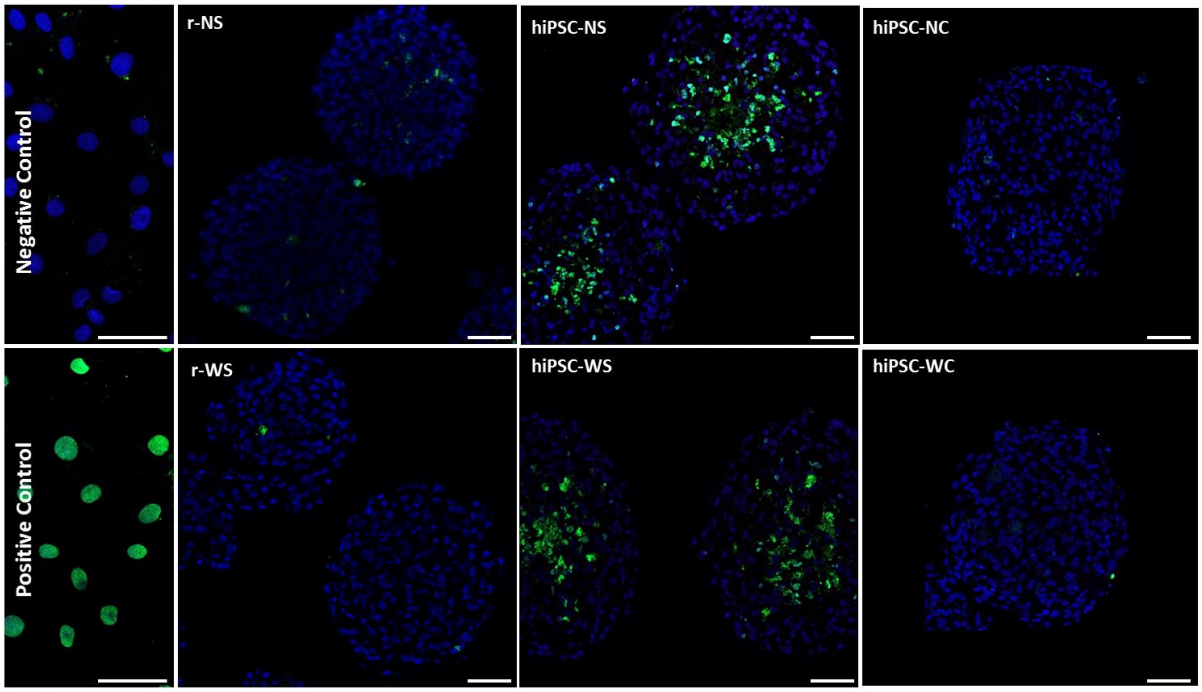

Figure 3.8. TUNEL staining for the frozen sections of spheroids. Blue color is DAPI staining for nuclei, which indicates the viable cells in spheroids. Green color is TUNEL staining for fragments of DNA, which indicates the apoptosis of cells in spheroids. Scale bars: 50μm.

On the other hand, the addition of e-SiNWs into hiPSC cardiac spheroids without electrical stimulation (i.e., hiPSC-WC spheroids) can lead to significant improvement in contraction amplitude and synchronization. As shown in the Fig. 3.7 A, the contraction amplitude of the hiPSC-WC spheroids averaged more than 55% higher than the hiPSC-NC spheroids from Day 1 to Day 7. The sharper peaks of fractional area change of the hiPSC-WC spheroids over the hiPSC-NC spheroids strongly indicated the enhanced contraction synchronization (Fig. 3.7B, C). This is further supported by calcium transient imaging of whole spheroids (Fig. 3.7D, E). The quantification of calcium imaging of spheroids revealed the hiPSC-WC spheroids have the increased overall amplitude (F/F0)

of calcium levels and the accelerated time to peak of the calcium transient (Fig. 3.7 F, G), which supported the enhanced synchrony during spontaneous contraction. The significant improvement in contraction amplitude and synchronization of hiPSC-WC spheroids is remarkable, considering only a trace amount of e-SiNWs (i.e., 0.004% w/v) was utilized to create e-SiNW-reinforced cardiac spheroids.

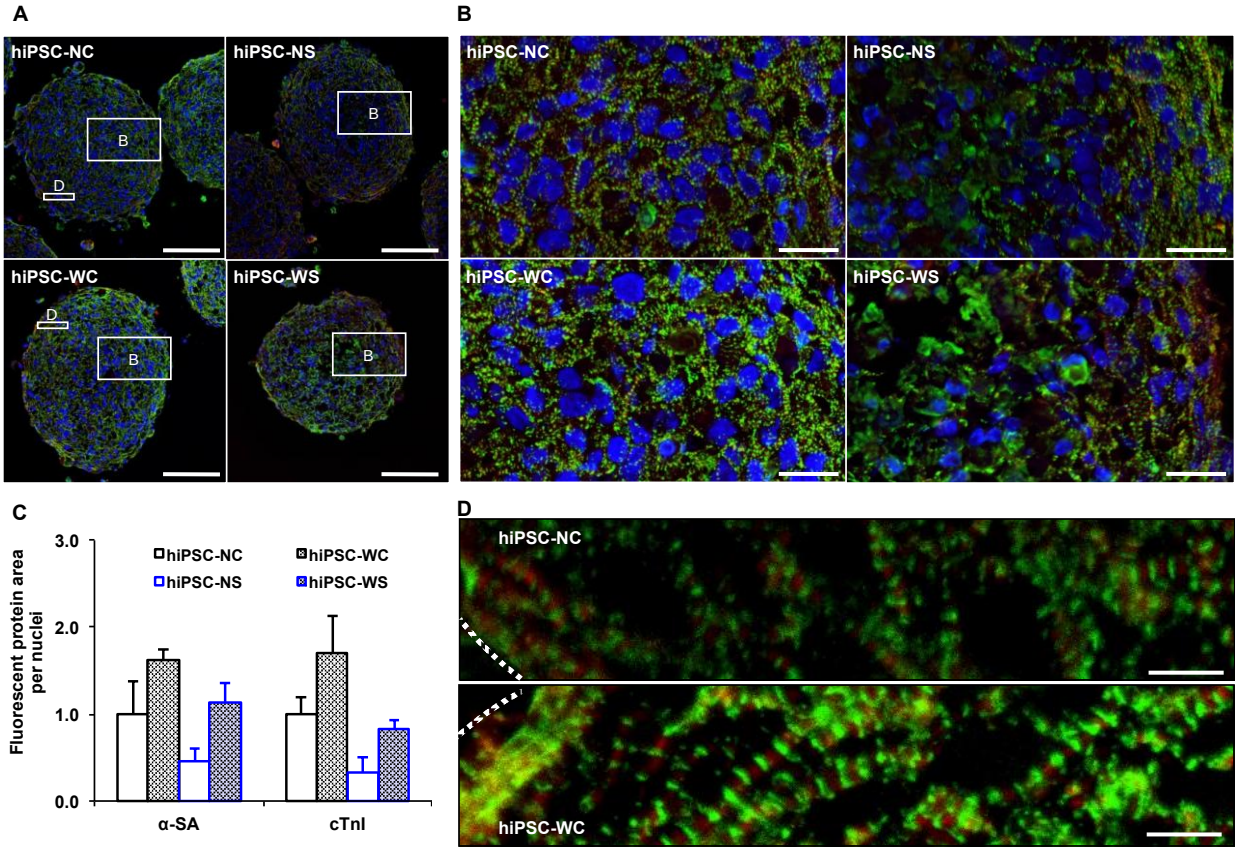

Figure 3.9. Cellular organization of hiPSC-derived cardiomyocyte spheroid cross-sections after 7 days of treatment. (A) Low and (B) high magnification confocal images (green, α-sarcomeric actinin (α-SA); red, troponin I; blue, DAPI nuclear stain) that display the difference in the sarcomere expression and organization within spheroids. (C) Protein expression analysis based on fluorescent signal-covered area per nuclei normalized over hiPSC-NC expression; n = 3 picture regions; 75 µm x 130 µm picture regions, at least containing >50 nuclei. (D) Characteristic images of hiPSC-NC and hiPSC-WC treatments to reveal differences in sarcomere alignment of each whole spheroid (dotted line = spheroid border). hiPSC-NC= human induced pluripotent stem cell cardiac spheroids, no e-SiNWs, no stimulation; hiPSC-NS= human induced

pluripotent stem cell cardiac spheroids, no e-SiNWs, with stimulation; hiPSC-WC= human induced pluripotent stem cell cardiac spheroids, with e-SiNWs, no stimulation; hiPSC-WS= human induced pluripotent stem cell cardiac spheroids, with e-SiNWs, with stimulation. Error bars represent standard deviation. Scale bars: (A) = 100 μm; (B) = 20 μm; (D) = 5 μm.

The enhanced contraction amplitude and synchronization of the hiPSC-WC spheroids resulted in improved functional maturation. As shown in the Fig. 3.10A-C and supplementary Fig. 3.10C, D, the immunofluorescence staining indicated the significant increase in expression level and assembly of both conductive and contractile proteins (e.g., Cx-43, α-SA, and cTnI) in the hiPSC-WC spheroids, which was further supported by the increased expression of conductive gene GJA1 (Cx-43) and contractile gene MYL2 (ventricle isoform of myosin light chain) (Fig. 3.11). In addition, the Fig. 3.7 D-G showed the improved peak calcium amplitude and the speed of calcium release, which suggest the improved calcium handling channels and indicates increased maturation. This is further supported by the increased ratio of gene expression of the calcium channel L-type/T-type subunits (CACNA1C/CACNA1G) (Fig. 3.11). The improved calcium handling properties can be attributed to the enhanced organization of the sarcomere structures in the hiPSC-WC spheroids[257].

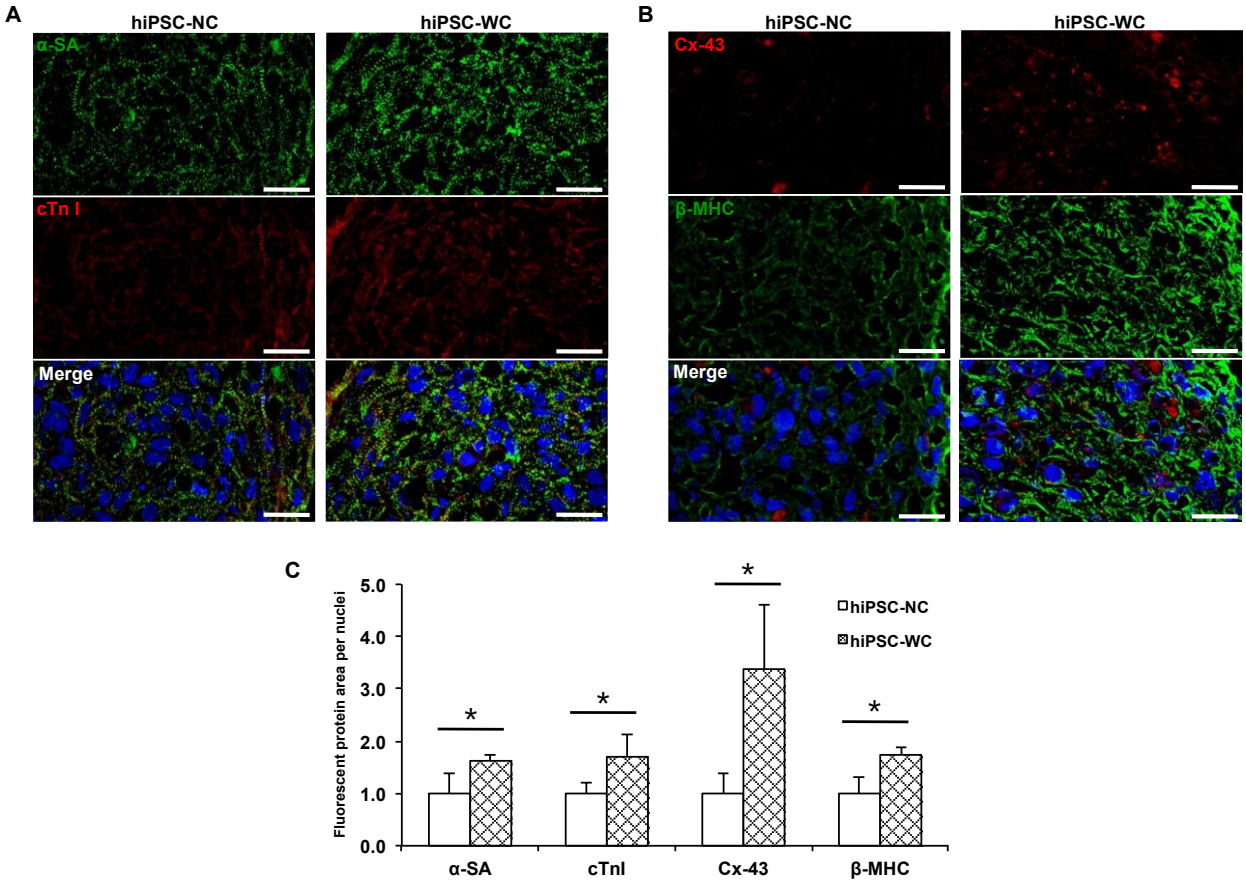

Figure 3.10. Structural analysis of hiPSC-derived cardiomyocyte spheroids. (A) Immunofluorescent staining of alpha sarcomeric actinin (α-SA) and troponin I (cTn I). (B) Immunofluorescent staining of connexin-43 (Cx-43) and beta myosin heavy chain (β-MHC). (C) Protein expression analysis based on fluorescent signal-covered area per nuclei normalized over hiPSC-NC expression (n = 3; 75 µm x 130 µm picture regions, at least containing >50 nuclei) based on (A, B). hiPSC-NC= human induced pluripotent stem cell cardiac spheroids, no e-SiNWs, no stimulation; hiPSC-WC= human induced pluripotent stem cell cardiac spheroids, with e-SiNWs, no stimulation. Asterisks (*) represent statistical significance with $p<0.05$; error bar represents standard deviation. Scale bars = 20 µm.

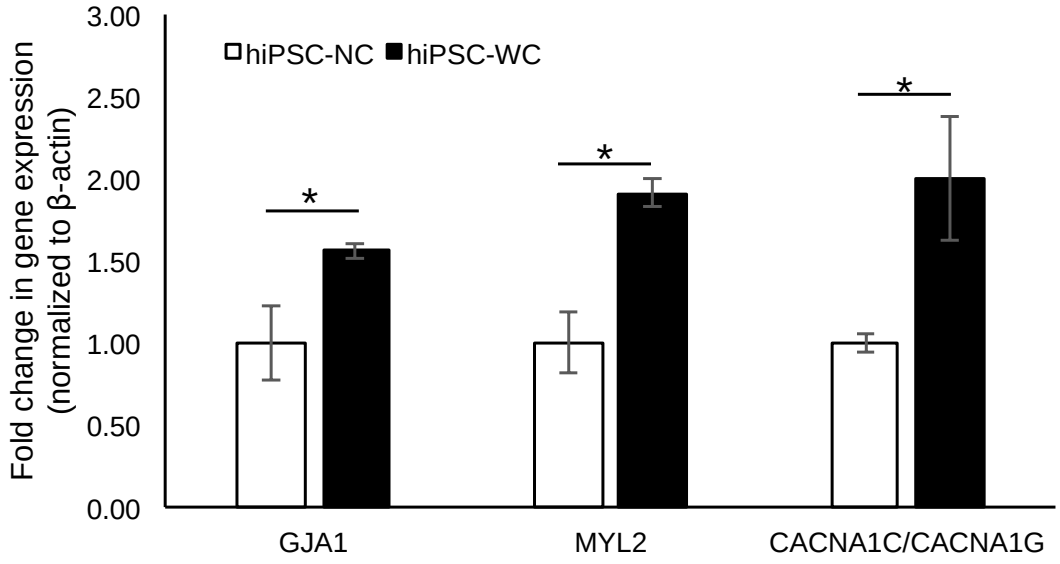

Figure 3.11. qPCR analysis of mRNA expression of conductive and contractile genes in hiPSC-NC and hiPSC-WC spheroids. GJA1 – connexin-43; MYL2 – myosin light chain ventricular isoform; CACANA1C – calcium L-type channel; CACNA1G – calcium T-type channel. Asterisks (*) represent statistical significance with $p<0.05$; error bar represents standard deviation, n = 3.

To confirm the effects of e-SiNW-reinforced 3D cell culture on the structural and contractile maturation of hiPSC-derived cardiomyocytes, monolayer cells were obtained from hiPSC cardiac spheroids by seeding them onto gelatin-coated substrates, which was thought to minimize dramatic stress usually associated with mechanical/enzymatic spheroid dissociation processes. Sarcomere length and Z-band width were measured as they were known as effective indicators of twitch force generated by cardiomyocytes[258, 259] (Fig. 3.12). As shown in Fig. 6A-C and G, cardiomyocytes harvested from both hiPSC-NC and hiPSC-WC spheroids showed significant improvement in Z-band width when compared to pre-spheroid hiPSC-derived cardiomyocytes. This indicates that 3D

culture can provide supportive microenvironments for the maturation of hiPSC-derived cardiomyocytes. Moreover, the hiPSC-WC cardiomyocytes showed significant improvement in both sarcomere length and Z-band width when compared to the hiPSC-NC cardiomyocytes (Fig. 3.12F, G). These improvements were attributed to the enhanced contraction of the hiPSC-WC spheroids. Notably, the alignment of Z-band in hiPSC-WC cardiomyocytes showed remarkable resemblance with adult rat cardiomyocytes (Fig. 3.12C-E, H). The increased sarcomere alignment in the hiPSC-WC spheroids was attributed to the e-SiNW-induced synchronized contractions (Fig. 3.7 B, C), which was hypothesized to provide an anisotropic mechanical environment to direct the assembly of contractile machinery of hiPSC-WC cardiomyocytes.

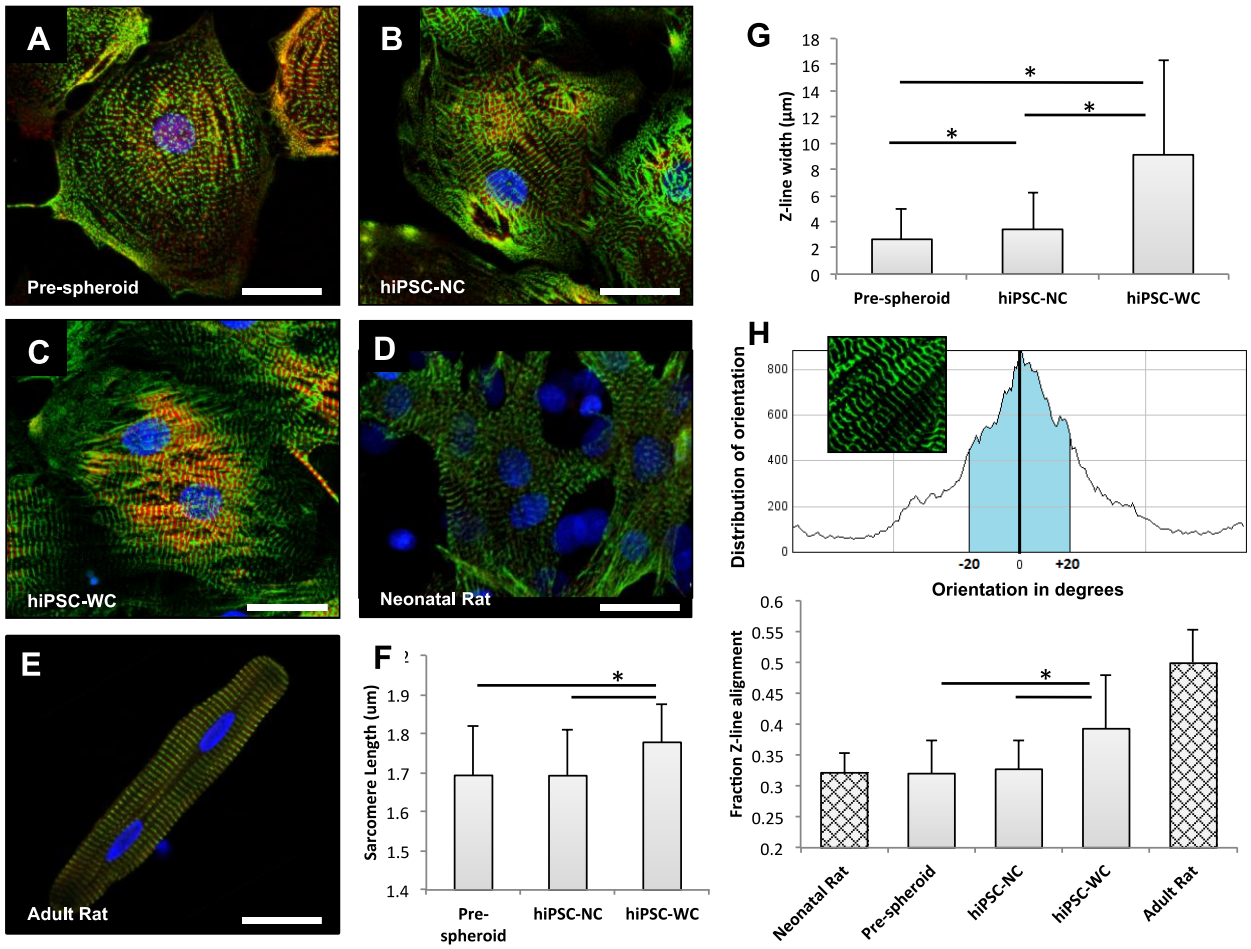

Figure 3.12. Single cell analysis of hiPSC-derived cardiomyocytes before and after spheroids, and rat-neonatal and adult cardiomyocytes. (A) Fluorescent confocal images (green, α-sarcomeric actinin (α-SA); red, troponin I; blue, DAPI nuclear stain) of single cells harvested before hiPSC spheroid fabrication, (B) after 7 days from hiPSC-NC spheroids, (C) and after 7 days from hiPSC-WC spheroids. (D) Rat-neonatal cardiomyocyte and (E) adult left ventricular cardiomyocyte for morphological comparison. (F) Sarcomere length measured as distance between α-SA-stained Z-line structures from cardiomyocytes with visible sarcomere structures; n = 9 cells per condition. (G) Z-line width measurements based on α-SA-stained Z-line structures in comparison to neonatal and adult rat cardiomyocyte references; n = 10 cells per condition. (H) Z-line alignment calculations were based on a fraction (±20° of the peak orientation degree) of aligned α-SA-stained structures; n = 12 cells (hiPSC), 4 cells (rat) per condition. hiPSC-NC= human induced pluripotent stem cell cardiac spheroids, no e-SiNWs, no stimulation; hiPSC-WC= human induced pluripotent stem cell cardiac spheroids, with e-SiNWs, no stimulation. Asterisks (*) represent statistical significance with $p<0.05$; error bars represent standard deviation. Scale bars = 25 µm.

5. Conclusion:

For the first time, we incorporated a trace amount of e-SiNWs into rat-neonatal and hiPSC cardiac spheroids to create electrically conducting microenvironments and induce synchronized and enhanced contraction, which was shown to promote structural and contractile maturation. Although powerful, the addition of e-SiNWs into the human cardiac spheroids alone may not be able to derive fully matured hiPSC-derived cardiomyocytes. A longer term experiment (i.e., 3 weeks) was explored, and the improvements in hiPSC-WC spheroids in contraction amplitude and sarcomere structure seen at Day 7 were maintained through Day 21 (Fig. 3.13). However, the extended culture did not indicate further improvements in the maturation of hiPSC-derived cardiomyocytes. The sarcomere structure and nuclear shape in hiPSC-WC spheroids and hiPSC-NC spheroids at Day 21 resembled that of the Day 7 spheroids (Fig. 3.9 and Fig. 3.13). Our future research will combine additional chemical/physical stimuli (e.g., growth factors, miRNA) with e-SiNW-reinforced human cardiac spheroids to produce fully matured hiPSC-cardiomyocytes.[145, 257]

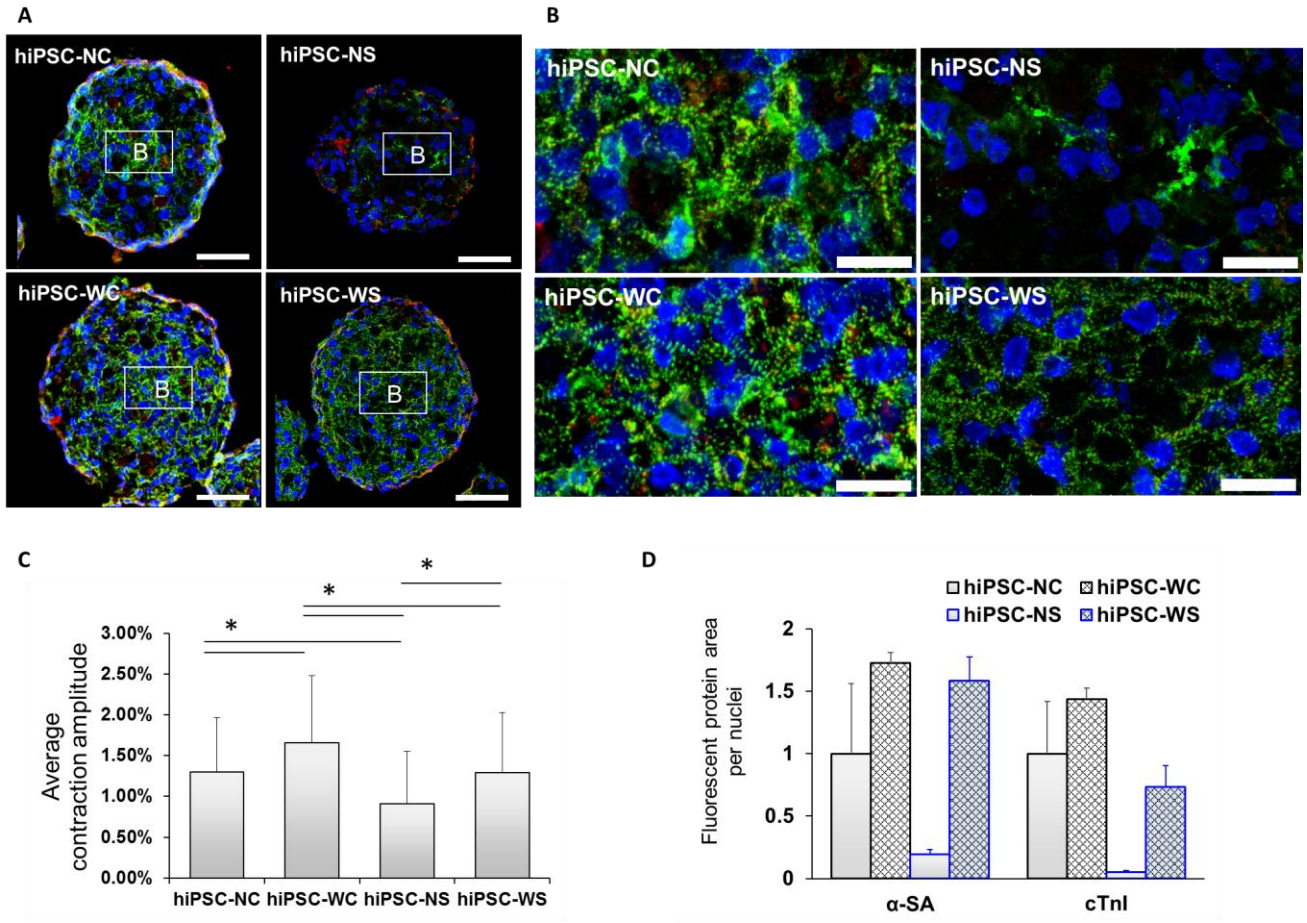

Figure 3.13. Analysis of hiPSC-derived cardiomyocyte spheroids after 3 weeks culture. (A) Low and (B) high magnification confocal images (green, α-sarcomeric actinin (α-SA); red, troponin I; blue, DAPI nuclear stain) that display the difference in the sarcomere expression and organization within spheroids after 21 days in culture. (C) Average contraction amplitude (i.e., fractional area change) of spontaneously beating spheroids with and without e-SiNWs and/or electrical stimulation after 21 days in culture; n=6 spheroids per condition. (D) Protein expression analysis based on fluorescent signal-covered area per nuclei normalized over hiPSC-NC expression; n = 3 picture regions; 40 µm x 40 µm picture regions. hiPSC-NC= human induced pluripotent stem cell cardiac spheroids, no e-SiNWs, no stimulation; hiPSC-NS= hiPSC cardiac spheroids, no e-SiNWs, with stimulation; hiPSC-WC= hiPSC cardiac spheroids, with e-SiNWs, no stimulation; hiPSC-WS= hiPSC cardiac spheroids, with e-SiNWs, with stimulation. Asterisk (*) represents statistical difference between groups with $p<0.05$; error bar represents standard deviation. Scale bars: (A) = 50 µm; (B) = 20 µm.

Recently, nanocomposite scaffolds composed of electrically conductive nanomaterials and hydrogels have been developed for cardiac tissue engineering

applications[146, 147, 191, 253]. The research reported here is the first demonstration of using nanoscale semiconductors to promote cardiac tissue formation and cardiomyocyte maturation without involving conventional scaffolding materials (e.g., polymers and hydrogels). Also, this research is the first example to directly utilize silicon-based nanomaterials for tissue engineering applications. Our results suggest that silicon-based nanomaterials can have major impacts in tissue engineering. Notably, e-SiNW induced synchronized contraction could have major implications in cell-based cardiac therapy, considering that arrhythmia caused by unsynchronized contraction is a major concern in cardiac surgery [170, 174]. Our future research will also include the transplantation of e-SiNW-reinforced hiPSC cardiac spheroids into infarcted hearts to examine their electrical integration with the host myocardium.

CHAPTER FOUR

CELL NUMBER PER SPHEROID AND ELECTRICAL CONDUCTIVITY OF NANOWIRES INFLUENCE THE FUNCTION OF SILICON NANOWIRED HUMAN CARDIAC SPHEROIDS

1. Abstract:

Human induced pluripotent stem cell-derived cardiomyocytes (hiPSC-CMs) provide an unlimited cell source to treat cardiovascular diseases, the leading cause of death worldwide. However, current hiPSC-CMs retain an immature phenotype that leads to difficulties for integration with adult myocardium after transplantation. To address this, we recently utilized electrically conductive silicon nanowires (e-SiNWs) to facilitate self-assembly of hiPSC-CMs to form nanowired hiPSC cardiac spheroids. Our previous results showed addition of e-SiNWs effectively enhanced the functions of the cardiac spheroids and improved the cellular maturation of hiPSC-CMs. Here, we examined two important factors that can affect functions of the nanowired hiPSC cardiac spheroids: (1) cell number per spheroid (i.e., size of the spheroids), and (2) the electrical conductivity of the e-SiNWs. To examine the first factor, we prepared hiPSC cardiac spheroids with four different sizes by varying cell number per spheroid (~0.5k, ~1k, ~3k, ~7k cells/spheroid). Spheroids with ~3k cells/spheroid was found to maximize the beneficial effects of the 3D spheroid microenvironment. This result was explained with a semi-quantitative theory that considers two competing factors: 1) the improved 3D cell-cell adhesion, and 2) the reduced oxygen supply to the center of spheroids with the increase of cell number. Also, the critical role of electrical conductivity of silicon nanowires has been confirmed in improving tissue function of hiPSC cardiac spheroids. These results lay down a solid

foundation to develop suitable nanowired hiPSC cardiac spheroids as an innovative cell delivery system to treat cardiovascular diseases.

2. Introduction:

Cardiovascular diseases are the leading cause of death and disability worldwide [232, 260]. Due to limited regeneration capacity of adult human hearts, human embryonic stem cells (hESCs) and human induced pluripotent stem cells (hiPSCs) have emerged as a powerful cell source for cardiac repair due to their proven capacity to produce functional human cardiomyocytes [124, 153, 165-169, 172, 261]. To this end, significant efforts have been devoted to transplanting hESC/hiPSC-derived cardiomyocytes (hESC/hiPSC-CMs) into damaged hearts to improve their functions in animal models [97, 104, 124, 153, 174-178, 262]. In particular, Murry and coworkers have demonstrated the injection of hESCs-CMs into the injured myocardium led to cardiac muscle regeneration in a non-human primate model [153]. Despite the progress, the current hESC/hiPSC-CMs retain an immature phenotype, including poorly organized sarcomere structures (i.e., functional units of the contractile machinery). This leads to difficulties for electrical and mechanical integration with human adult myocardium after transplantation and poses an arrhythmic risk [145, 153, 263, 264]. To address this challenge, we recently utilized electrically conductive silicon nanowires (e-SiNWs) to facilitate self-assembly of hiPSC-CMs to form nanowired human cardiac spheroids for heart repair [148]. We demonstrated that addition of e-SiNWs into the human cardiac spheroids creates an electrically conductive microenvironment and improves tissue function and cellular maturation of hiPSC cardiac spheroids. In addition, recent research has shown that

cellular spheroids/aggregates improve cell retention and survival after transplantation due to their 3D microtissue configuration [177, 183, 265]. In this manuscript, we aim to examine two major factors that can affect the functions of the nanowired human cardiac spheroids: (1) the number of cells per spheroid (i.e., size of the spheroids), and (2) the role of the electrical conductivity of the e-SiNWs in improving tissue functions of the spheroids.

The optimal cell number in the spheroids is affected by two competing factors: 1) the improved 3D cell-cell adhesion, and 2) the reduced oxygen supply to the center of spheroids with the increase of cell number. In the first part of the study, we experimentally identified the optimal cell number in the spheroids and developed a semi-quantitative theory to explain the finding. In our previous report, we showed the addition of e-SiNWs in the human cardiac spheroids improved cellular maturation and tissue function [148]. However, the role of electrical conductivity of the e-SiNWs has not been examined. In the second part of the manuscript, we prepared three types of the spheroids: spheroids without the addition of nanowires (NC), spheroids with the addition of phosphorus doped silicon nanowires (WCD), and undoped silicon nanowires (WCN). We studied the functions of these three different types of spheroids and confirmed the critical role of electrical conductivity of e-SiNWs in improving tissue functions of the hiPSC cardiac spheroids.

3. Materials and methods:

3.1 Cell culture

The hiPSC-CMs (Cellular Dynamics International, Madison, WI, USA) were cultured according to the manufacturer's protocol. Briefly, hiPSC-CMs were seeded on 0.1% gelatin coated 6-wells plate with plating medium (Cellular Dynamics International) at a density of about 3 × 105 to 4.0 × 105 cells per well and incubated at 37 °C / 5% CO2 for two days. Two days after plating, the plating medium was removed and replaced with 4 ml of maintenance medium (Cellular Dynamics International) for another 2 days. After 4 days of monolayer pre-culture, cells were detached using trypLE Express (Gibco Life Technologies, Grand Island, NY) and harvested for spheroid fabrication.

3.2 Spheroid fabrication

The agarose hydrogel molds were prepared using commercial master micro-molds from Microtissues, Inc (Providence, RI, USA) as negative replicates to create non-adhesive agarose hydrogels molds containing 35 concave recesses with hemispheric bottoms (800 μm diameter, 800 μm deep) to facilitate the formation of tissue cell spheroids. 330 μl 2% sterile agarose solution were pipetted into the master micro-molds and then carefully detached after gelation from the master mold and transferred into one well of an 8-well tissue culture plate. 75 μl of the cell suspension with different concentrations were pipetted into each agarose mold. After the cells had settled down into the recesses of the mold (10 min), additional media was added (5 ml) and exchanged every 2 days for the length of the experiment.

3.3 Video and image analysis of beating spheroids

Videos of 6 spheroids from each group were recorded using Zen 2011 software (Zeiss, Göttingen, Germany) with capture rate of 14 frames per second. Then the videos

were converted to a series of TIFF formatted pictures by Adobe Premiere (Adobe, San Jose, CA). Threshold edge-detecting in ImageJ software (National Institutes of Health) was used on high contrast spheroid pictures and graphed to realize contraction profiles, from which other quantifiers were calculated (e.g., fractional area change of single spheroids).

3.4 Histological and immunofluorescent analysis of spheroids

Freshly collected spheroids (~30-35) were placed onto a pre-labeled tissue base mold, and the entire tissue block was covered with OCT. Immediately, the base mold containing spheroids were transferred into pre-cooled ethanol with dry ice to ensure that the spheroids were frozen quickly and completely. Frozen spheroids were cryosectioned into 7 μm thick layers onto glass slides for immunohistochemistry. The sections were fixed with pre-cooled acetone (-20 °C) for 10 min. After washing (3 times at 5 min) in PBS with 0.1% Triton X-100 (PBST), 100 μl blocking buffer were added (10% goat serum in PBST) onto the sections of the slides and incubated in a humidified chamber at room temperature for 1 h. Sections were incubated with appropriately diluted primary antibody: alpha sarcomeric actinin (Abcam, Cambridge, UK), troponin I (Santa Cruz, Dallas, TX), connexin-43 (Sigma Aldrich, St. Louis,MO), and COX IV (Abcam) overnight at 4 °C. After washing in PBST (3 times at 5 min), tissues were incubated with coordinate secondary antibodies diluted in PBST for 1 h at ambient temperature. After washing in PBST (3 times at 5 min), nuclei were stained with DAPI (Molecular Probes/Invitrogen, Eugene, OR) diluted in PBST for 15 min at ambient temperature. Following the final wash procedure (PBST, 3 times at 5 min), cover slips were added to

the slides using Fluoro-Gel (Electron Microscopy Sciences, Hatfield, PA). Finally, TCS SP5 AOBS laser scanning confocal microscope (Leica Microsystems, Inc., Exton, PA) was for fluorescent imaging.

3.5 TUNEL staining for the frozen section of spheroids

In Situ Cell Death Detection Kit (Roche, Penzberg, Germany) was used to determine the viability of the cell in the frozen section of spheroids based on the Roche protocol. Briefly, the frozen sections of spheroids were fixed with 4% paraformaldehyde in PBS for half hour at room temperature. Following washing in PBS for 30 minutes, samples were incubated in a permeabilization solution (0.1% Triton X-100 and 0.1% sodium citrate in PBS) for 2 minutes on ice. Then 50 µl of the TUNEL reaction mixture were added to samples and incubated in 37 °C for 1 h. After washing in PBST (3 times at 5 min), nuclei were stained with DAPI (Molecular Probes/Invitrogen, Eugene, OR) diluted in PBS for 15 min at ambient temperature. Following the final wash procedure (PBS, 3 times at 5 min), glass cover slips were added to the slides using Fluoro-Gel (Electron Microscopy Sciences, Hatfield, PA). Finally, a TCS SP5 AOBS laser scanning confocal microscope (Leica Microsystems, Inc., Exton, PA) was used to obtain fluorescent images.

3.6 Calcium transient imaging of cardiac spheroids

Fluo-4 Direct Calcium Assay Kits (Life Technologies, Carlsbad, CA) was used to label calcium ion in the whole spheroids based on the protocol from Life Technologies. Briefly, spheroids were seeded onto 0.1% gelatin-coated glass cover slips and incubated at 37 °C, 5% CO2, 20% O2. Cell culture medium was changed every other day. After

four days culture, the spheroids were rooted on the cover slips. Then cover slips with the spheroids were put into 12-well plates with 2 ml calcium dye solution per well and incubated at 37 °C, 5% CO2, 20% O2 for 1 h. TCS SP5 AOBS laser scanning confocal microscope (Leica Microsystems, Inc., Exton, PA) was used to collect the videos of the calcium transient of whole spheroids at room temperature with a capture rate of 14 frames per second. Notably, temperature influences the calcium transient dynamics, indicated by changes in the beat rate of cardiac spheroids with temperature (Figure 4.1). Finally, we used the LAS AF software (Leica) to conduct quantification of videos collected by confocal imaging.

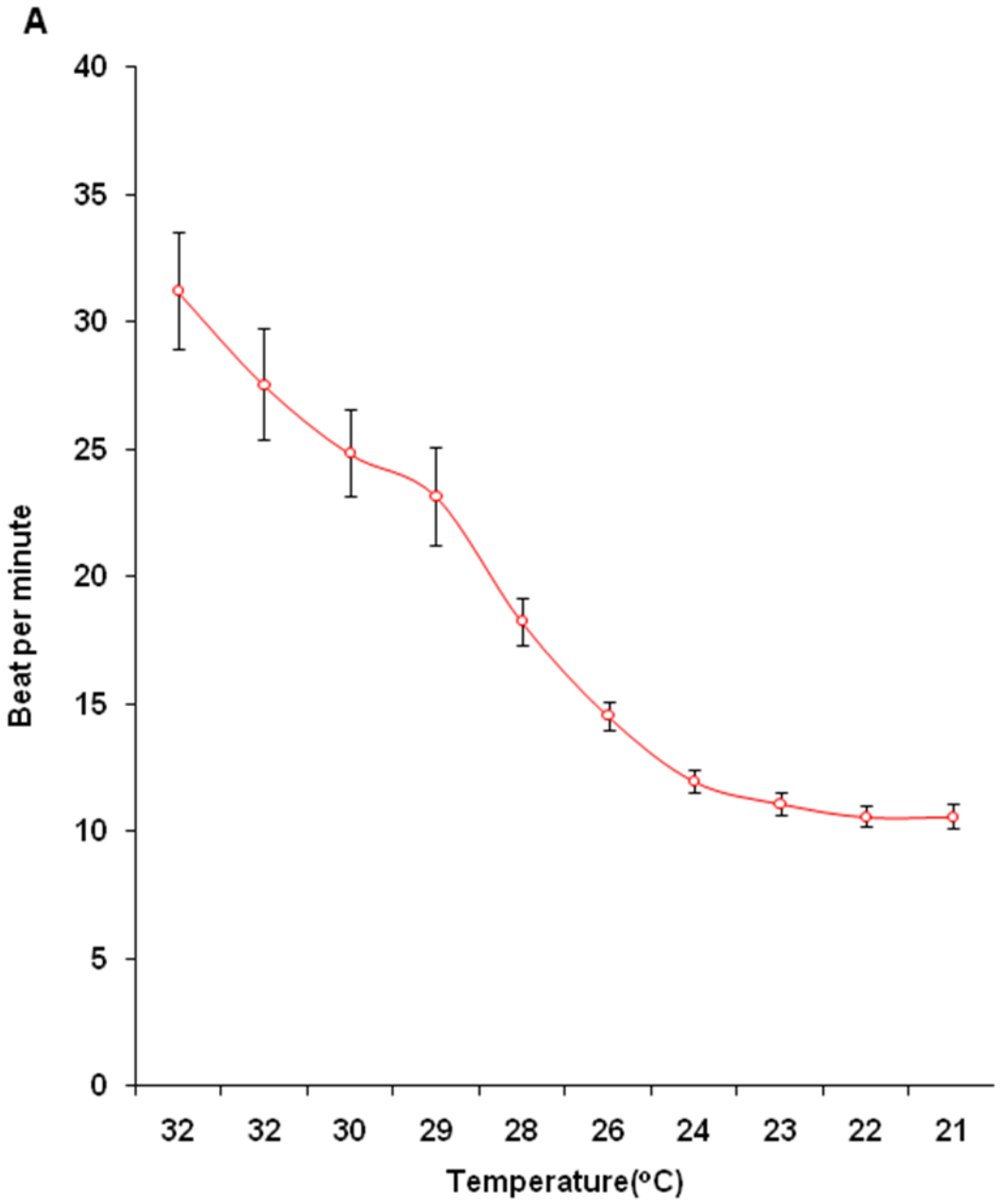

Figure 4.1. The beat rate of the spheroid's spontaneous contraction is dependent on the temperature. The relationship between beat rate (BPM – beats per minute) and medium temperature.

3.7 Transmission Electron Microscopy

Spheroids were fixed with 2.5% glutaraldehyde, postfixed in PBS buffered 1% osmium tetroxide with 1.5% K+ ferricyanide, dehydrated in graded ethanol and Acetonitrile, and embedded in PolyBed 812 (Polysciences). 70 nm thick spheroid sections were prepared using a Leica UltraCut R and a diamond knife, stained with Hanaichi Pb citrate and uranyl acetate, and imagined using a JOEL 200 CX transmission electron microscope.

3.8 Numerical modeling of oxygen transport in cardiac spheroids

The oxygen transport within spheroids under static culture conditions mainly depends on diffusion [266]. A finite element model of oxygen diffusion within cardiac spheroids was developed based on Fick's second law. In a spherical coordinate system, the oxygen concentration profile in cardiac spheroids is governed by:

$$\frac{D}{r^2}\frac{\partial}{\partial r}\left(r^2\frac{\partial C}{\partial r}\right) - R = 0$$

where C is oxygen concentration, r is radial distance from spheroid center, D is oxygen diffusivity, and R is oxygen consumption rate. The oxygen diffusivity through cells is significantly less than that through water. As used in previous studies [267, 268], $D=3.0\times10^{-6}$ cm^2/s for cardiomyocytes in suspension was adopted in the model. The concentration-dependent oxygen consumption rate (OCR) of cardiomyocytes can be modeled by the Michaelis-Menten equation:

$$R = \rho_c \frac{V_{max}\,[C]}{K_m + [C]}$$

where ρ_c is spheroid cell density, V_max is the maximum OCR, and K_m is the Michaelis-Menten constant. As the oxygen consumption rates of hiPSC-CMs or human cardiomyocytes are not readily availablein the previous literatures, the oxygen

consumption rate ($V_{max}=5.44\times10^{-8}$) nmol/cell/s and $K_m=3.79$ nmol/mL) of rat neonatal cardiomyocytes in a quiescent condition was used in the model [255]. The boundary condition is that on the spheroid surface, the oxygen concentration maintains constant at 20% O_2 (185 nmol/mL) [267]. The oxygen transport finite element model was numerically solved by the software COMSOL Multiphysics (COMSOL Inc, Burlington, MA). The oxygen concentration profiles were determined in spheroids with radius of ~70, ~100, ~150, and ~200 μm, corresponding to ~0.5k, ~1k, ~3k, and ~7k cells/spheroid.

3.9 Oxygen Consumption Rate Measurement

OCR of spheroids was measured according to the previous report [269]. Briefly, 30-60 spheroids of each group were placed in the OCR chamber equipped with fiber optic sensors (Instech Laboratories, Plymouth Meeting, PA), which could measure the declining oxygen partial pressure (pO2) over time. OCR measurements were conducted in high glucose DMEM medium without FBS at 37°C. The liquid volume in chamber was known as 175 μl, so the OCR (mol O2 per unit time) of spheroids could be calculated from the linear slope of the measured pO2. Each measurement usually took 90 minutes. Since the cell number of spheroids is known, the OCR value was normalized with cell number for each measurement with unit (pmol/hour/cell).

3.10 Statistics Analysis

Differences between experimental groups were analyzed using an independent Student T-test, one-way or two-way ANOVA followed by Tukey's post-hoc test. $P<0.05$ was considered significantly different for all statistical tests.

4. Results and Discussion

The scaffold-free 3D spheroids provide a conductive microenvironment to promote cell-cell interactions and electrical coupling, leading to enhanced maturation of hiPSC-CMs [270]. The number of cells in a spheroid plays a key role in its function. When a spheroid contains too many cells, the supply of nutrient and oxygen to the cells in the spheroid center will be limited or insufficient to maintain cellular viability and/or normal function. When a spheroid contains a too small number of cells, the benefit of the improved 3D cell-cell adhesion over 2D culture will diminish. In this study, we fabricated hiPSC-CM spheroids with four different cell numbers per spheroid (i.e., ~0.5k, ~1k, ~3k, ~7k cells/spheroid) with and without the addition of 1:1 e-SiNWs (number of cells : number of e-SiNWs) using our previously established method [148]. Spheroids without and with e-SiNWs were designated as "NC" and "WCD", respectively. As in the previous study, n-type SiNWs (Diameter ≈ 100 nm; length ≈ 10 μm; Silane/Phosphane = 500) were used to prepare WCD spheroids (Figure 4.2 A-C). The length of the SiNWs was selected to inhibit cell internalization, and the doping ratio and diameter of the e-SiNWs were chosen to obtain a high conductivity (150 - 500 μS/μm) to create highly electrically conductive microenvironments within spheroids [191, 248]. The addition of the e-SiNWs into the cardiac spheroids did not significantly influence the sizes of the spheroids at all four cell number/spheroid (Figure 4.3 A-B). This indicates the addition of e-SiNWs should not significantly affect the nutrient and oxygen supply to the cells in the spheroid center.

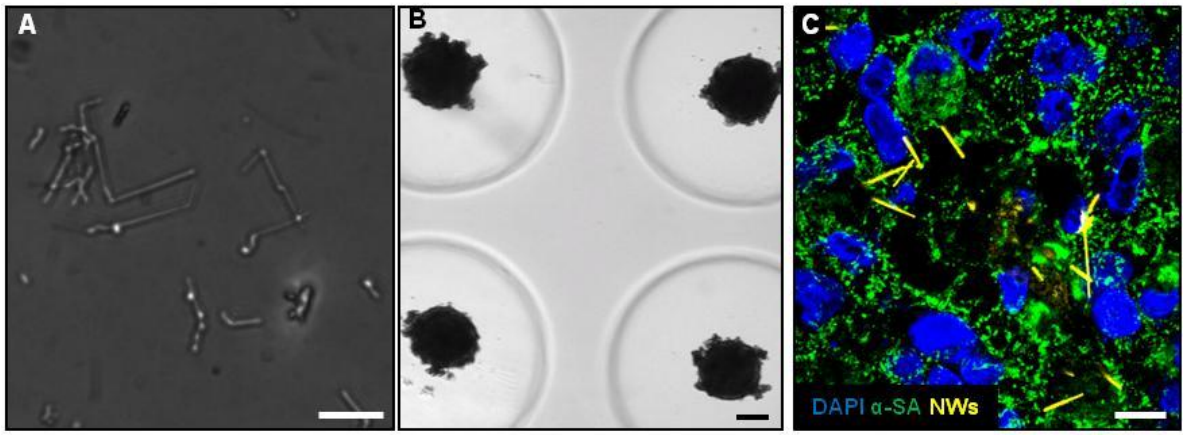

Figure 4.2. Fabrication of silicon nanowired human cardiac spheroids. (A) Bright field image of silicon nanowires (diameter ≈ 100 nm; length ≈ 10 μm). (B) Bright field images of silicon nanowired human cardiac spheroids in agarose molds. (C) Confocal image of frozen section of silicon nanowired human cardiac spheroids at Day 0 (Blue – DAPI; Green – α-SA: alpha sarcomeric actinin; Yellow-silicon nanowires). Scale bars: (A) = 10 μm; (B) = 100 μm; (C) = 10 μm.

Previous studies have shown that spheroids with a radius over 250 μm became apoptotic or necrotic over the time [271]. In addition, Radisic and coworkers have shown the diffusion of oxygen in the cardiac tissue engineering constructs is limited to 150~200 μm [256]. Thus, the ~7k cells per spheroid (~200 μm radius) was chosen to be the upper limit in this study. On the other hand, our data showed the lowest contraction amplitude (i.e., fractional area change) in spheroids with ~0.5k cells/spheroid (Figure 4.3 C), which is in agreement with previous research that indicates the beneficial impact of the 3D cell-cell adhesion is limited for smaller spheroids [272]. In addition, it is difficult to process and section these smaller spheroids. Therefore, this study mainly focused on the three larger sizes of spheroids (i.e., 1k, 3k and 7k cells/spheroid). As seen in Figure 4.4 A-B, TUNEL staining of the spheroid sections revealed a high level viability of hiPSC-CMs (>90%) for all three sizes after 7 days culture [205]. These results support our selection of

the range of cell numbers in the spheroids. In addition, the high cell viability of the WCD spheroids supports the high biocompatibility of e-SiNWs, which is consistent with the previous reports [195, 273, 274].

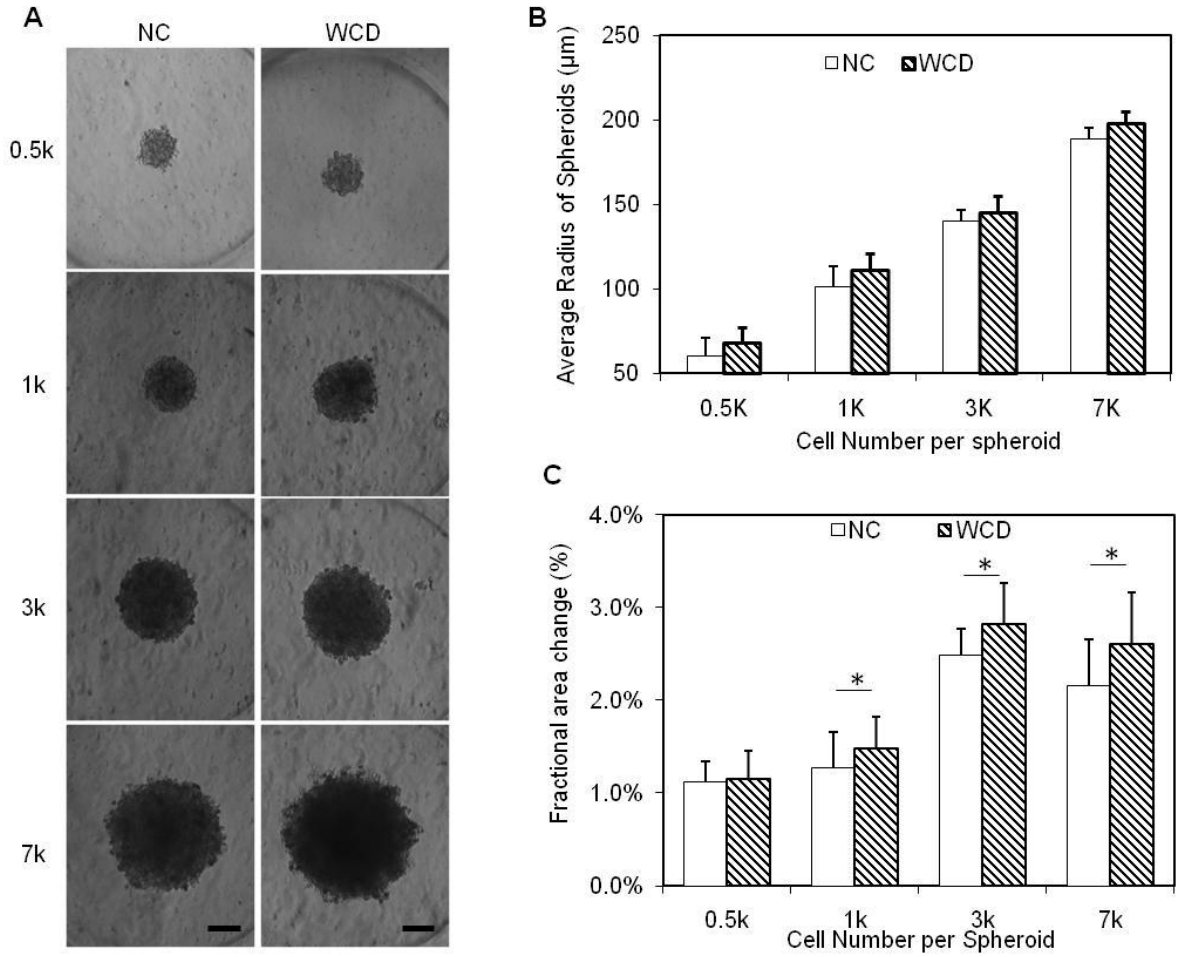

Figure 4.3. Human cardiac spheroids with controlled size and functional analysis. (A) Bright field images of spheroids with different cell number (0.5k, 1k, 3k, 7k) per spheroid. (B) Averaged radius of spheroid based on statistics (n=14). (C) Average fractional area change from Day 1 to Day 7 of each group (n=7). NC – without e-SiNWs; WCD – with e-SiNWs. Scale bars: (A) = 100 μm. Asterisks (*) represent statistical significance with $p<0.05$; error bars represent standard deviation.

As in our previous report, contraction amplitude (i.e., fractional area change) of the spontaneous, rhythmic beating of hiPSC-CM spheroids was used to examine the

functions of the spheroids [148]. Figure 4.3 C shows that the presence of e-SiNWs in WCD spheroids significantly increased the average contraction amplitude of 1k, 3k and 7k spheroids when compared with that of NC spheroids. This shows that the beneficial effects of adding e-SiNWs into human cardiac spheroids is not limited to a specific spheroid size, and this further supports our hypothesis that the addition of e-SiNWs into hiPSC cardiac spheroids creates an electrically conductive microenvironment and improves cardiac tissue function. In addition, the Figure 2C shows the WCD-3k spheroids, the WCD spheroids with ~3k cells/spheroid, have the highest fractional area change among all the groups.

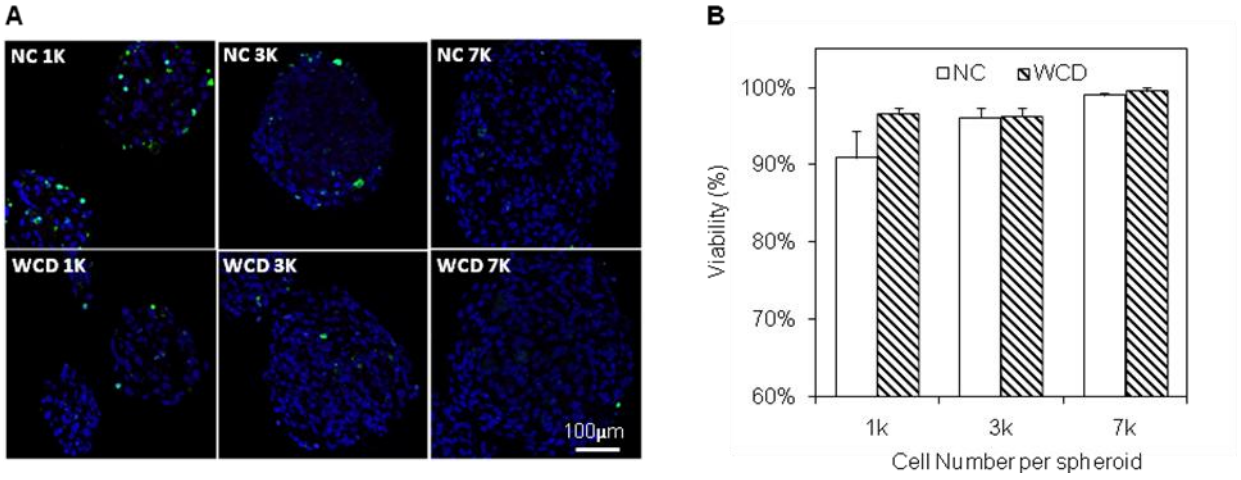

Figure 4.4. Viability analysis of spheroids using TUNEL staining. (A) TUNEL staining of the frozen sections of NC and WCD spheroids at day 7. Blue – DAPI; Green-TUNEL (apoptosis marker). (B) Quantification of viability from TUNEL staining (viability: blue colored area is divided by total colored area). NC – without e-SiNWs; WCD – with e-SiNWs. Error bars represent standard deviation. Scale bars: (A) = 100 µm.

The results from contraction amplitude analysis are further supported by the immunohistochemistry (IHC) analysis of cardiac contractile (α-SA : α-sarcomeric actinin)

and conductive (Cx-43: Connexin-43) proteins of the spheroids sections (Figure 4.5). α-SA was selected as it is a key component of the cardiac sarcomere structure, and connexin-43 (i.e., Cx-43) was selected as it forms gap junction channels that regulate electrical signal propagation between cardiomyocytes [250, 251]. Notably, the specificity of the Cx-43 antibody was confirmed by the staining of hiPSC-CMs in 2D culture, where cell-cell borders were more clearly visible than in 3D spheroid cross-sections (Figure 4.6). Consistent with functional analysis, structural analysis showed more organized structure and higher expression of contractile proteins (α-SA) (Figure 4.5 A-B) and cell-cell gap junction protein (Cx-43) (Figure 4.5 C-D) in the WCD spheroids, when compared with the NC spheroids. Notably, hallmarks of structural maturation (i.e., Cx-43 and α-SA structures) did not show a strong correlation with nanowires location (Figure 4.8). In addition, WCD-3k spheroids showed a highly organized sarcomere structure and highest expression level of α-SA and Cx-43 (Figure 4.5 A-D). To additionally support the functionality of Cx-43, the co-staining of spheroid cross sections with Cx-43 and N-cadherin (N-cad), a membrane junction protein, as shown in the Figure S4, in which the co-localization of N-cad and Cx43 indicates the formation of functional cellular junctions [275]. These results indicate the WCD-3k spheroids can maximize synergistic effects of the appropriate cell number per spheroid and the presence of e-SiNWs. It is also important to note that all the spheroids after 7 days culture (Figure 4.5 A) showed significantly improved sarcomere structure, when compared with that of the newly form spheroids (Figure 4.2 C). This result shows spheroids provide a supportive 3D microenvironment for the development of hiPSC-CMs.

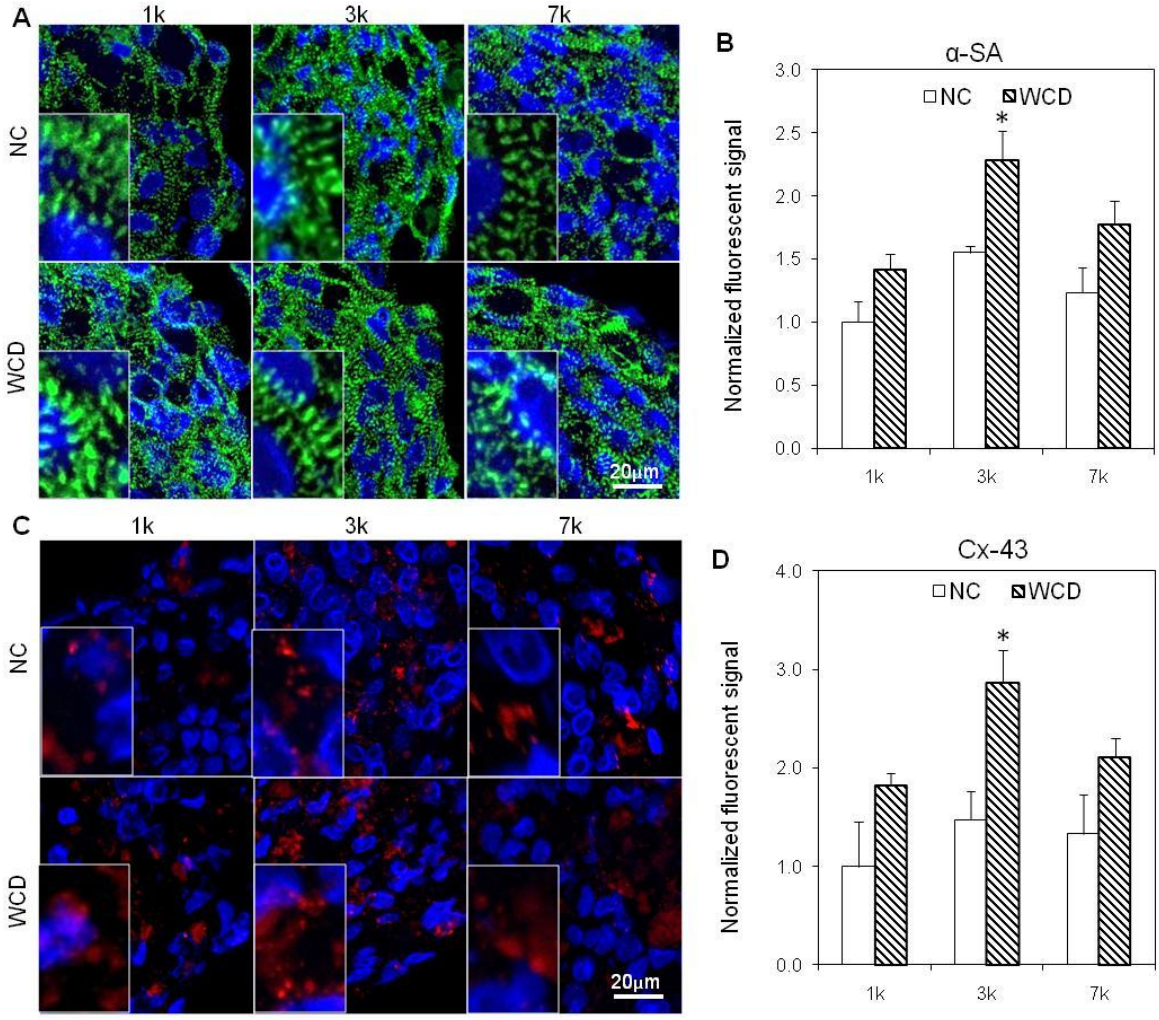

Figure 4.5. Histological analysis of spheroids. (A-B) Immunofluorescent staining and quantification of cardiac-specific contractile proteins (α-SA) for all groups after 7 days cell culture. Blue – DAPI; Green – α-SA; NC – without e-SiNWs; WCD – with e-SiNWs. (C-D) Immunofluorescent staining and quantification of conductive proteins (Cx-43) for all groups after 7 days cell culture. Blue – DAPI; Red – Cx-43. NC – without e-SiNWs; WCD – with e-SiNWs. Fluorescent signal area per nuclei on cross section are normalized to the NC-1k condition (n=3; 75 μm × 130 μm picture regions, at least containing >50 nuclei). Error bars represent standard deviation. Scale bars: (A)= 20 μm; (C)= 20 μm. Asterisks (*) represent statistical significance between WCD3k and other groups with $p<0.05$

Changing the number of cells per spheroids (i.e., size of spheroid) can alter the oxygen supply throughout the spheroid, which can have direct effects on the metabolic activity of the hiPSC-CMs within the spheroids. As an indicator for metabolic activity, a

COX IV stain was used to show differences in mitochondrial expression between different spheroid size groups (Figure 4.4 and Figure 4.7). IHC analysis showed the presence of significantly more COX IV-positive structure in WCD-3k spheroids compared to WCD-7k and WCD-1k spheroids (Figure 4.7 A,B). To support the IHC analysis, oxygen consumption rate (OCR) measurements have been conducted for the WCD spheroids with different sizes. Consistent with the IHC analysis, the hiPSC-CMs in WCD-3k spheroids have highest OCR, demonstrating a high level of metabolic activity (Figure 4.7 C and Figure 4.10). Notably, the measured OCRs are 0.34, 0.51 and 0.21 pmol/h/cell for the hiPSC-CMs in the WCD-1k, WCD-3k and WCD-7k spheroids respectively, which is similar to the reported OCR for hiPSC-CMs in 2D monolayer culture (0.71pmol/h/cell) [276]. While the size of 7k spheroids (i.e., radius: ~200 μm) approaches the diffusion limit of oxygen [256], the lower COX IV-stained structure and lower contraction amplitude of the WCD-1k spheroids suggests a functional limitation due to an insufficient amount of cells per spheroid.

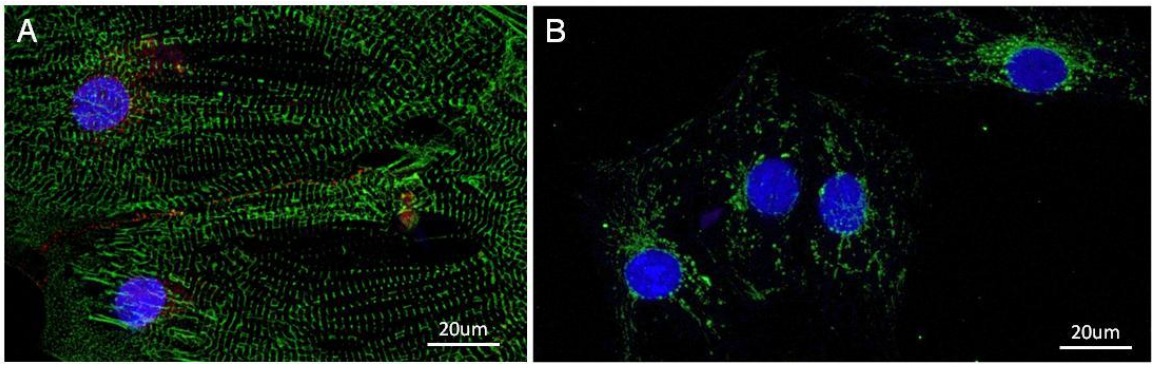

Figure 4.6 Specificity of immunofluorescent staining of Cx-43 and COX IV. (A) Cx-43 (red) shows specific labeling at the cell junction of α-SA (green) stained 2D monolayer hiPSC-CMs. (B) Mitochondria staining of COX IV (green) for 2D monolayer hiPSC-CMs on gelatin-coated cover slips. Blue – DAPI.

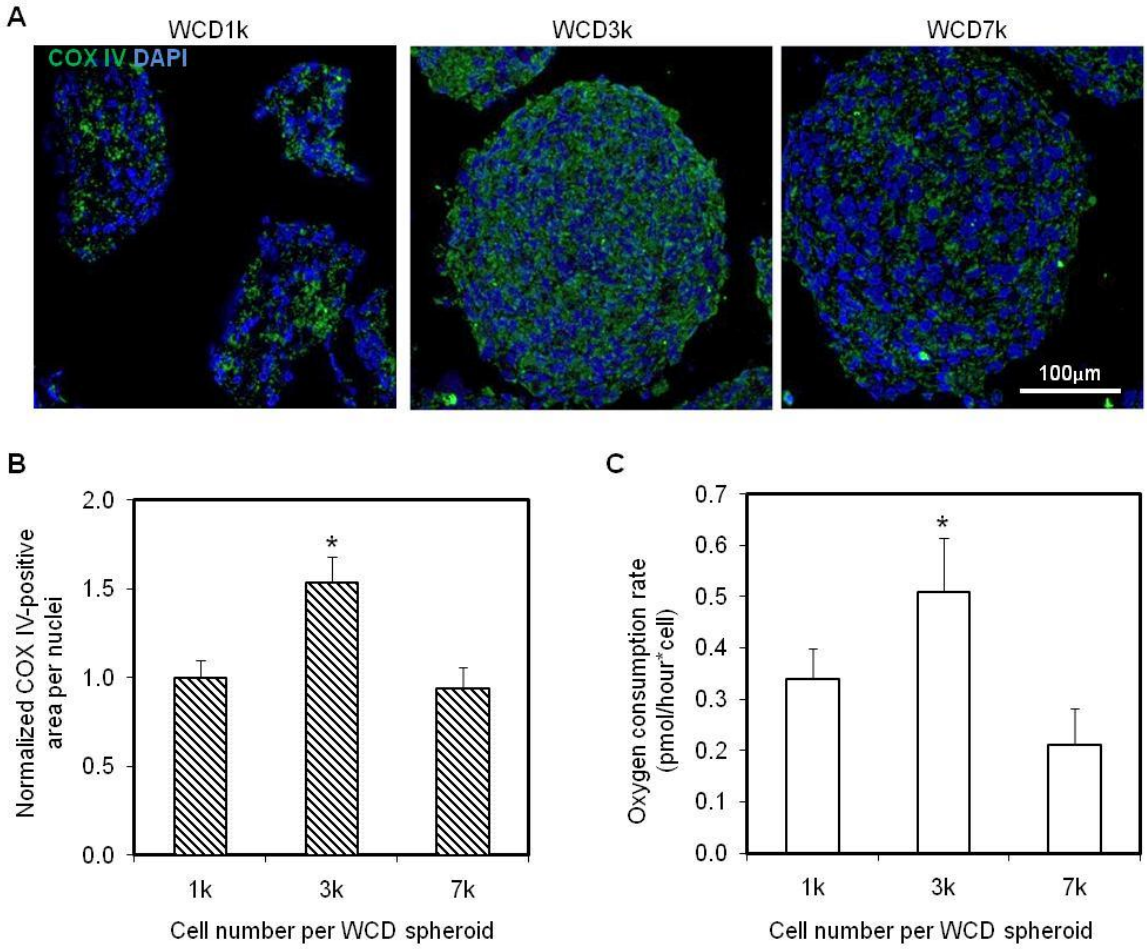

Figure 4.7 Metabolic analysis of nanowired spheroids with different cell numbers per spheroid. (A) Confocal images of cross-sections of WCD spheroids with different cell numbers per spheroid (Blue – DAPI; Green – COX IV). (B) COX IV positive area per nuclei of WCD spheroid sections are normalized to the WCD-1k (n=3; 75 μm × 130 μm picture regions, at least containing >50 nuclei). 7k (i.e., 7000), 3k, and 1k indicate number of cells per spheroid. WCD – with e-SiNWs. (C) Quantification of oxygen consumption rate of WCD spheroids with different cell numbers per spheroid. Asterisks (*) represent statistical significance with $p<0.05$; error bars represent standard deviation. Scale bars: (A)=100μm

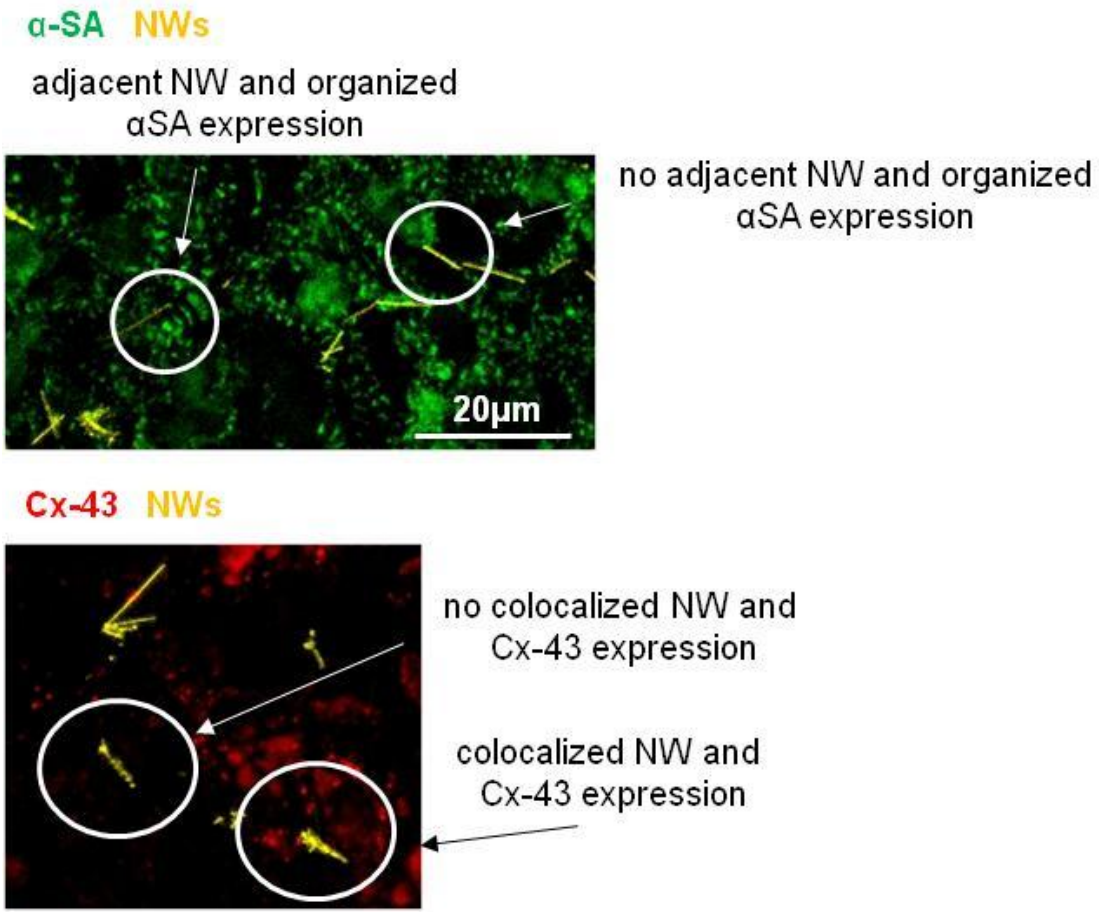

Figure 4.8 Immunofluorescent staining of α-SA/Cx-43 of the WCD-3k spheroid sections. Confocal imaging shows locations of α-SA (green) and Cx-43 (red) and e-SiNWs (yellow) in the WCD-3k spheroid sections. The α-SA and Cx-43 structures are not localized to regions close to e-SiNWs.

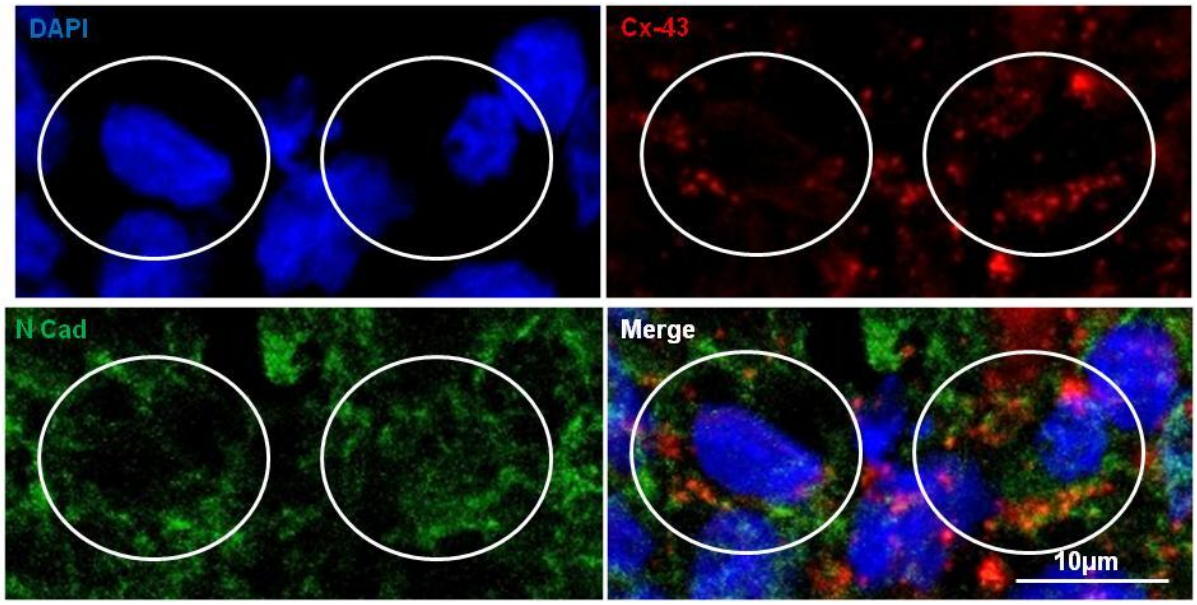

Figure 4.9. Immunofluorescent staining of N-Cad/Cx-43 of the WCD-3k spheroid sections. The white circles show the co-localization of Cx-43 (red) and N-Cad (green) surrounded in nuclei in the WC-D3k spheroids. Blue – DAPI.

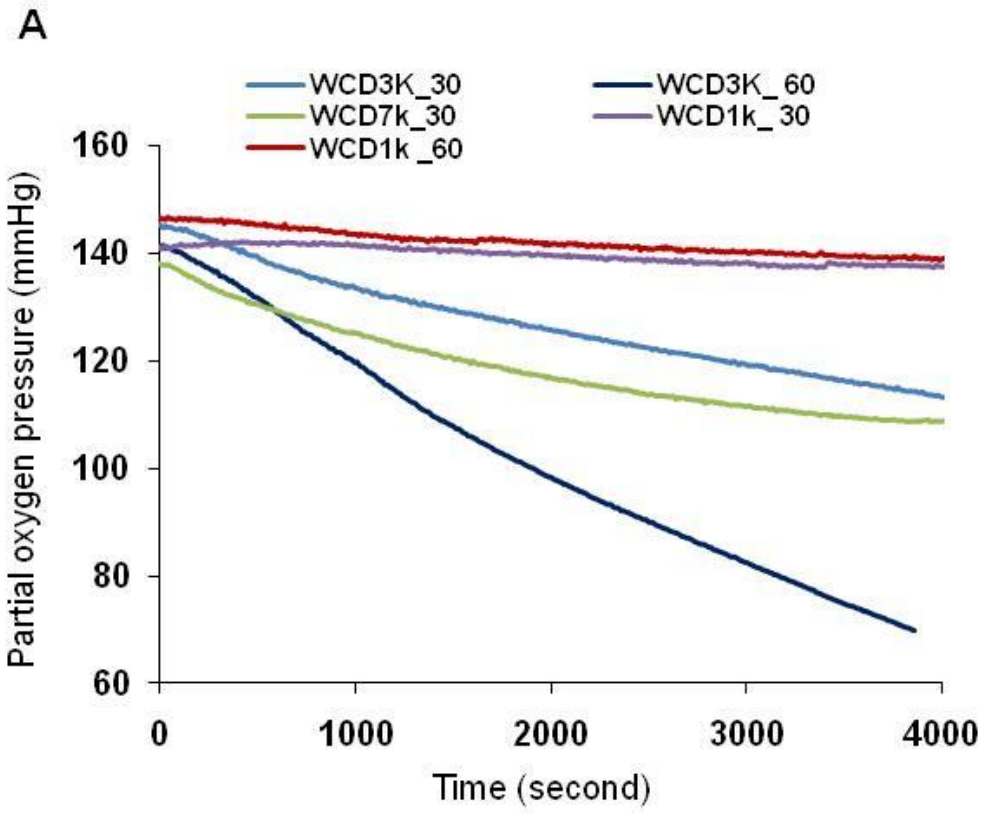

Figure 4.10 Metabolic analysis of the WCD spheroids with different cell numbers per spheroid. Oxygen consumption rate for WCD-1k, -3k and -7k spheroids were measured using Instech Oxygen Consumption Chamber. WCD1k_30: 30 x WCD-1k spheroids, WCD1k_60: 60 x WCD-1k spheroids, WCD3k_30: 30 x WCD3k spheroids, WCD3k_60: 60 x WCD-3k spheroids, WCD7k_30: 30 x WCD7k spheroids.

The size of the spheroid (i.e., cell number per spheroid) influences both oxygen diffusion and 3D cell-cell interactions. As oxygen consumption rates of hiPSC-CMs at different oxygen concentrations are not readily available, we used the existing data of the oxygen consumption rate of rat neonatal cardiomyocytes to model oxygen concentration within spheroids with radii of ~50, ~100, ~150 and ~200 μm [255]. A finite element model of oxygen diffusion within the cardiac spheroids was developed based on Fick's second law. As shown in the Figure 4.11A, the amount of available oxygen is rapidly

reduced from the edge of the spheroids to the center of the spheroids, and larger spheroids have lower oxygen supply for the cells in the center of the spheroids. On the other hand, the volume to surface area ratio increases with cell number, equaling 33.8, 47.5, and 66.0 for 1k, 3k, and 7k spheroids, respectively (Figure 4.11 B) [277]. This indicates an enhanced 3D cell-cell adhesion with the increase of cell number per spheroid. The existence of the two competing factors (reduced oxygen supply vs. enhanced 3D cell adhesion with the increase of cell number per spheroid) indicates there could be an optimal cell number for spheroid fabrication, and our experimental data indicates that spheroids contain ~3k cells maximizes the benefits of the 3D environment of nanowired spheroids (Figure 4.11 C).

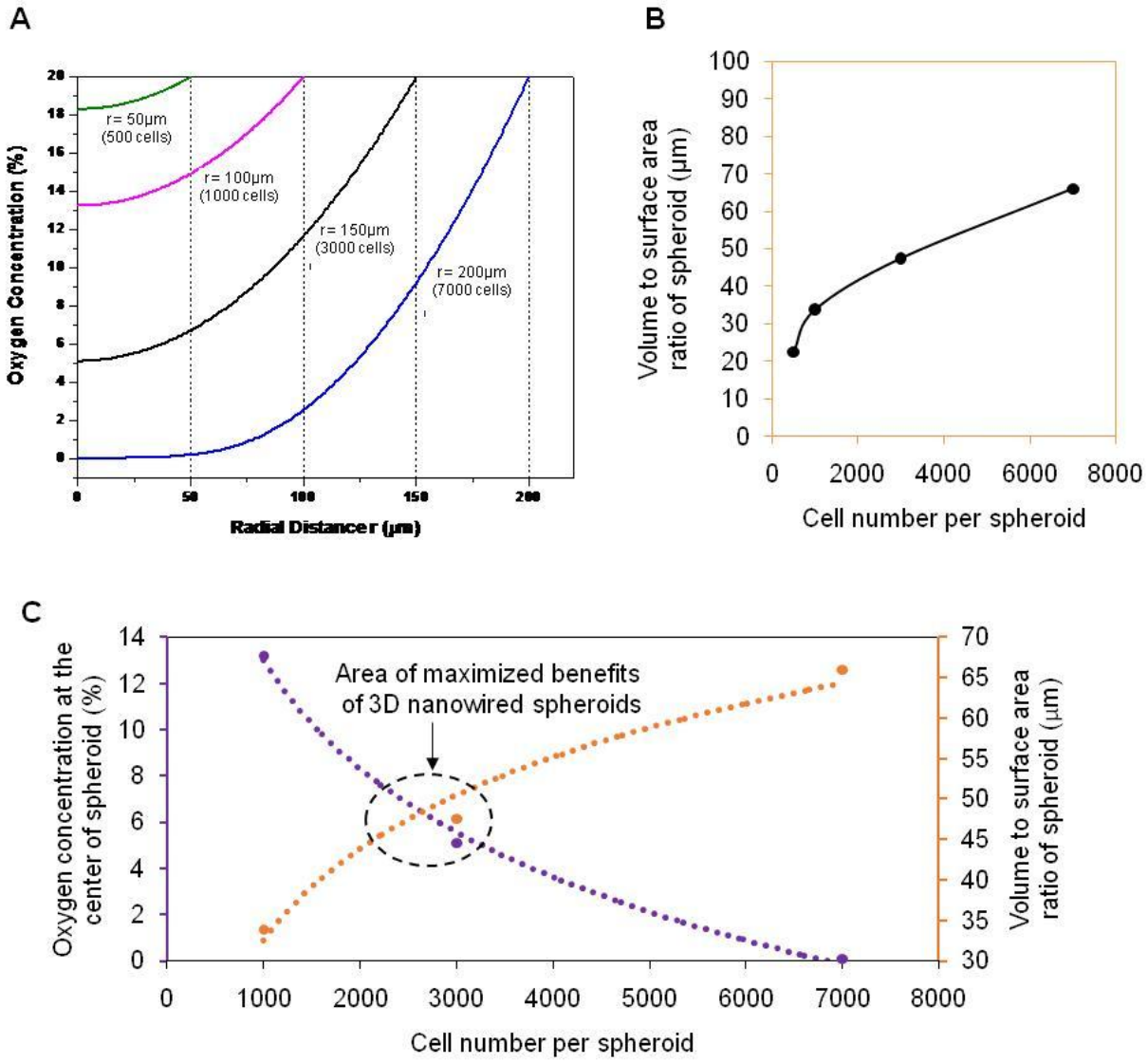

Figure 4.11 Functionally optimized range of cell number per spheroid. (A) A mathematical model of oxygen percentage using rat neonatal cardiomyocyte data for oxygen consumption (ref. 29), showing the range of oxygen concentration throughout theoretical spheroids of different sizes. (B) The volume to surface area ratio of different sized spheroids represents the amount of 3D cell-cell interaction, as a larger volume to surface ratio indicates more cells inside the spheroid with higher chance of multi-dimensional cell-cell interaction. (C) Data points from oxygen percentage and spheroid volume to surface area ratio at the 1k, 3k, and 7k cells per spheroid can be combined to summarize our findings on the size with maximized benefits centered around 3k cells per spheroid.

Using the newly established spheroid size (i.e., 3k cells per spheroid), we explored the role of the e-SiNWs in improving function and structural organization of hiPSC-CMs in spheroids, we fabricated three groups of human cardiac spheroids: spheroids without the addition of nanowires (NC), spheroids with the addition of doped silicon nanowire (WCD), and undoped silicon nanowires (WCN). Compared to the conductivity of the doped silicon nanowires (150 - 500 μS/μm), the undoped silicon nanowires have a conductivity of 0.001-0.1 μS/μm that is lower than culture medium (~1.75 μS/μm) and myocardium (~0.1 μS/μm) [191, 248]. This allowed for the examination of both the necessity of the electrical conductivity of nanowires and the effects of the mere presence of a silicon nanowire structure within the spheroid. Contraction amplitude analysis showed that the average fractional area change of WCD-3k group was significantly higher than that of NC-3k, while the average fractional area change of WCN-3k spheroids is significantly lower than that of NC-3k (Figure 4.12 A). These results confirmed the beneficial effects of electrically conductive silicon nanowires on function of spheroids. This was further supported by calcium transient imaging of whole spheroids (Figure 4.12 B-D). The WCD-3k spheroids showed a significantly increased overall amplitude of calcium transient levels during contraction and an accelerated time to peak of the calcium transient when compared with NC-3k, while WCN-3k showed a lower peak amplitude of calcium transient level than that of NC-3k.

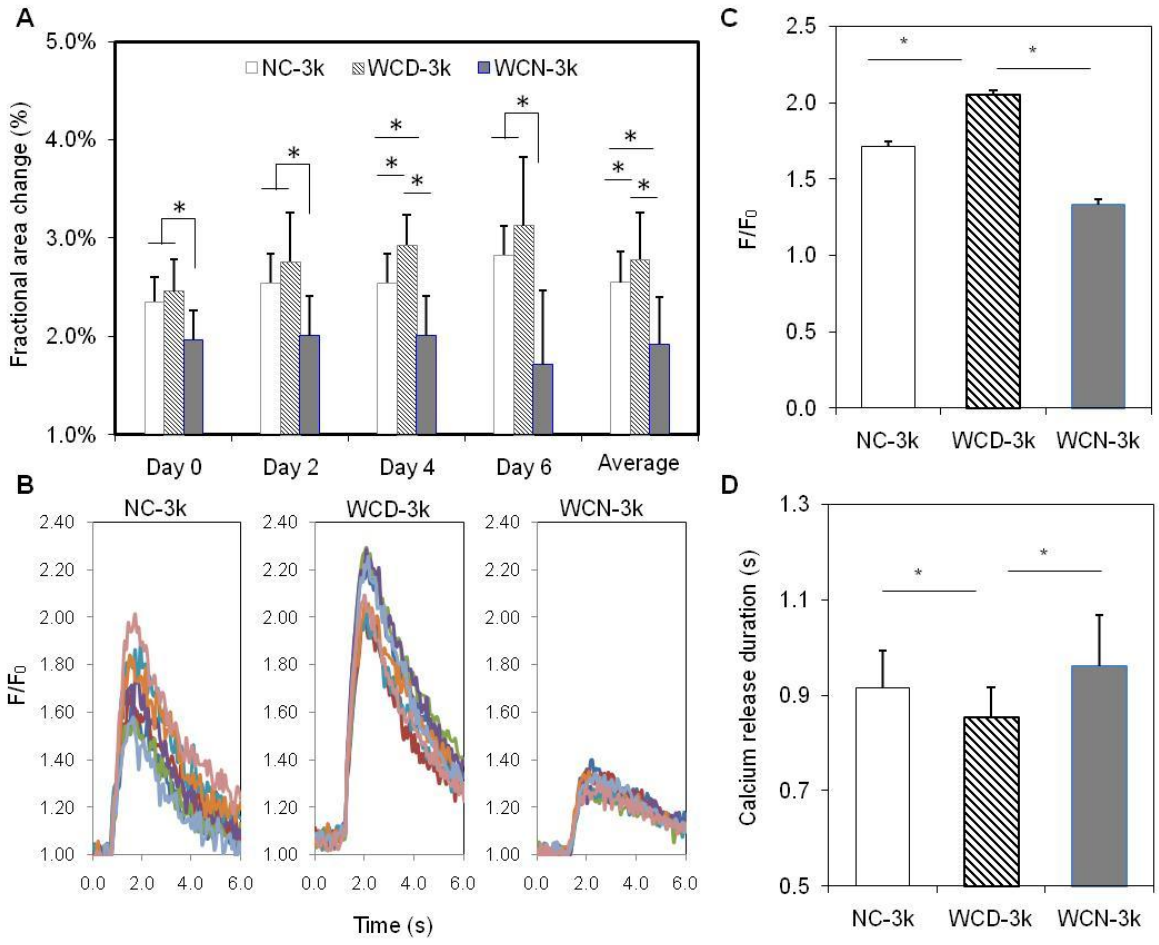

Figure 4.12. The effects of electrically conductivity of silicon nanowires on the function of 3k spheroids. (A) Average fractional area change of NC-3k, WCD-3k and WCN-3k spheroids at Day 0, 2, 4, 6 and their averages (n=7). (B) Calcium transient of 7 regions of interest per spheroid for each group. Fluorescence amplitude, F/F0, refers to measured fluorescence intensity normalized to background fluorescence intensity. (C) Comparison of the peak value of F/F0 for each group (n=3). (D) Comparison of calcium release duration for each group (n=3). NC – without e-SiNWs; WCD – with doped SiNWs; WCN – with undoped SiNWs. Asterisks (*) represent statistical significance with $p<0.05$; error bar represents standard deviation.

Consistent with the functional analysis, structural analysis showed that the WCD-3k spheroids had higher organization of αSA-stained sarcomere structures as well as an

increase in Cx-43-positive stained area (Figure 4.13 and Figure 4.14). Also, the ultrastructural analysis conducted by using electron microscopic imaging revealed a significantly higher presence of I bands per Z disc, H zones per sarcomere and more desmosomes per area in WCD-3k spheroids (Figure 4.15). Notably, the WCD-3k spheroids showed a visible organization of mitochondria around sarcomere structures similar to that of adult cardiomyocyte phenotype, as shown in Figure 8A-middle [165]. This supported our previous report that the presence of electrically conductive silicon nanowires in the hiPSC cardiac spheroids promotes cellular maturation of hiPSC-CMs. Collectively, these data showed the critical role of the electrical conductivity of the silicon nanowires in improving the tissue functions of hiPSC cardiac spheroids.

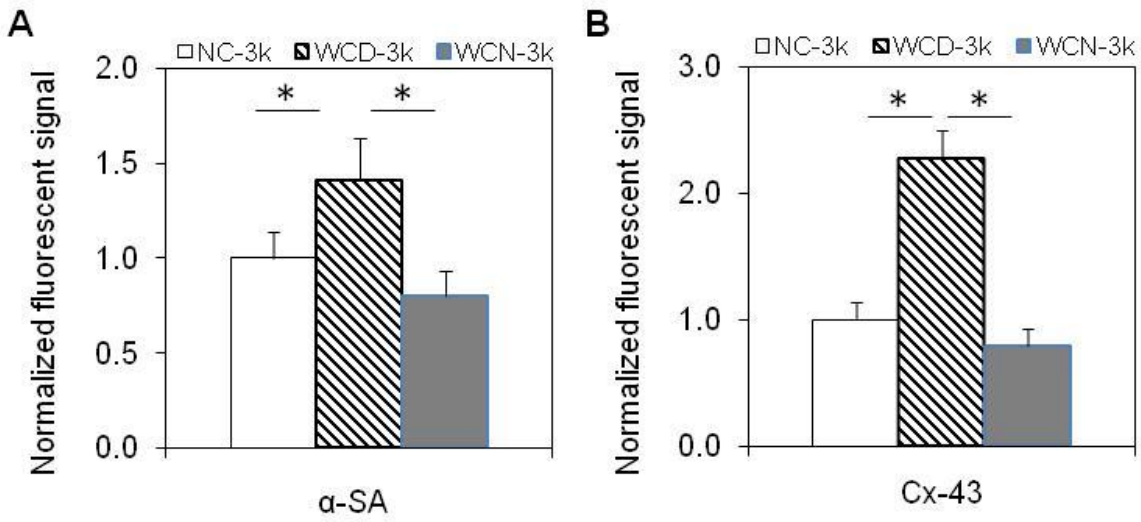

Figure 4.13 Immunofluorescent analysis of NC, WCD, and WCN-3k spheroids. (A-B) Quantified expression of α-SA and Cx-43 of NC-3k, WCD-3k and WCN-3k spheroids, respectively. Fluorescent signal area per nuclei on cross section are normalized to the NC-3k condition (n=3; 75 μm × 130 μm picture regions, at least containing >50 nuclei). NC – without e-SiNWs; WCD – with doped SiNWs; WCN – with undoped SiNWs. Asterisks (*) represent statistical significance with $p<0.05$; error bar represents standard deviation.

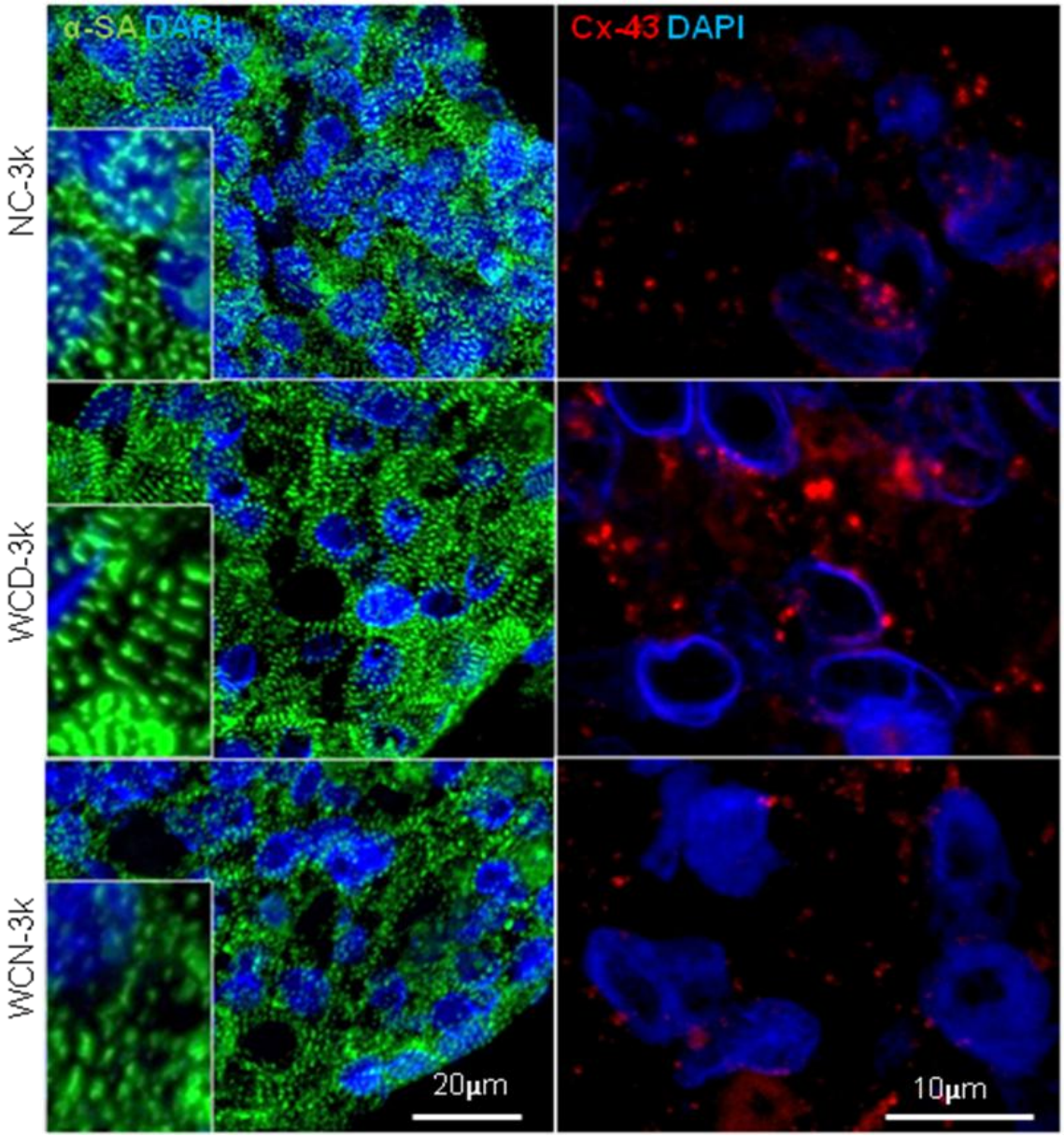

Figure 4.14 Immunofluorescent staining of NC, WCD, and WCN-3k spheroids. Contractile protein (α-SA) and conductive protein (Cx-43) staining were performed after 7 days cell culture in spheroids without e-SiNWs (NC), with doped e-SiNWs (WCD), and undoped SiNWs (WCN).

5. Conclusion

The silicon nanowired hiPSC cardiac spheroids hold remarkable promise as an effective cell delivery system to treat heart failure [185, 278, 279]. Using our previously established silicon nanowired hiPSC-CM spheroid system, we identified a cell number-defined size of spheroids that advances the function and organization of hiPSC-CMs. The functional analysis of contraction amplitude, IHC analysis of contractile and conductive proteins, and metabolic investigation demonstrated that 3k spheroids maximize the beneficial effects of the 3D spheroid microenvironment. Additionally, the electrical conductivity of silicon nanowires was confirmed to play a critical role in accelerating structural and functional development of hiPSC-CMs in spheroids.

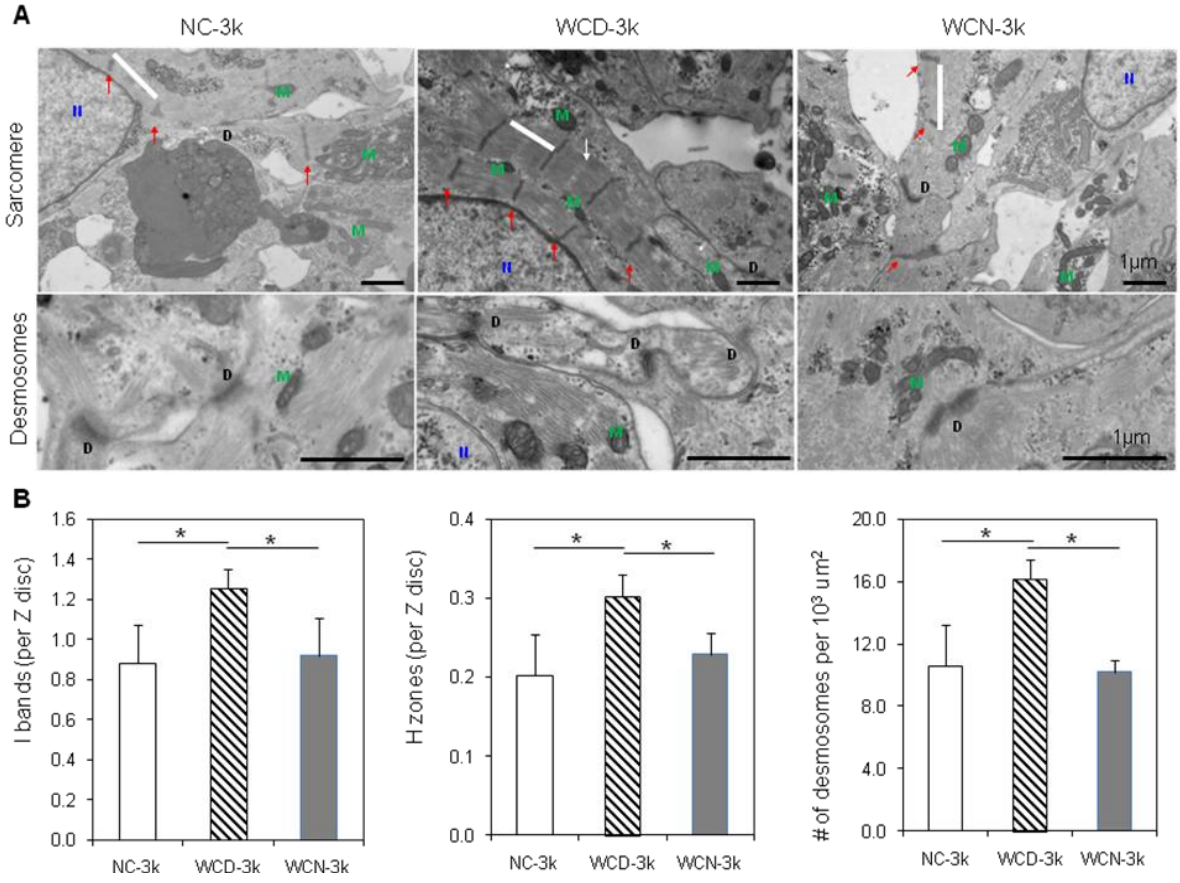

Figure 4.15 Ultrastructural analysis of NC, WCD, and WCN-3k spheroids. (A) Representative TEM images of NC-3k, WCD-3k and WCN-3k spheroids showing sarcomere structure (sarcomere, white bar; Z disks, Red arrows; H zones, white arrows; M, mitochondria; N, nucleus) and presence of desmosomes (D, desmosomes). Scale bar, 1 μm. (B) Morphometric analysis (average ± s.d.; n =3-8 per group) showing ratio of I bands to Z disk, ratio of H zones to sarcomeres and number of desmosomes per 10^3 um^2. NC – without e-SiNWs; WCD – with doped e-SiNWs; WCN – with undoped SiNWs. Asterisks (*) represent statistical significance with $p<0.05$.

While hiPSC-CMs hold remarkable promise to treat injured hearts, the current hiPSC-CMs retain an immature phenotype, which makes them difficult to integrate with adult myocardium and pose an arrhythmic risk. Further, the current utilization of dissociated single cells for cell transplantation leads to low cell retention and survival

[136]. To collectively address this challenge, we utilized e-SiNWs to facilitate self-assembly of hiPSC-CMs to form nanowired hiPSC cardiac spheroids. We demonstrated the e-SiNWs improved the spheroid functions and cellular maturity of hiPSC-CMs. In addition, recent research has shown improved cell retention and survival when using 3D cellular spheroids/aggregates. In this study, we identified an optimal cell number-defined spheroid size (~3k/spheroid) and confirmed the critical role of electrical conductivity of e-SiNWs. As the hiPSC-CMs in the WCD-3k spheroids lack characteristics of adult cardiomyocytes (e.g., sarcomere M lines, T tubules) [145], our future research will focus on using additional physical/chemical stimuli (e.g., electrical stimulation and/or microRNA) to further improve the tissue functions and cellular maturity of the nanowired hiPSC cardiac spheroids. In addition, we will explore the addition of vascular cells (e.g., endothelial cells) to the nanowired spheroids to prepare pre-vascularized spheroids for the improved integration with host vasculature after transplantation. Results from these studies will allow for the development of suitable nanowired spheroids to repair damaged hearts and advance the field of cell-based cardiac regenerative medicine.

CHAPTER FIVE

NANOWIRED HIPSC CARDIAC SPHEROIDS IMPROVE CELL RETENTION, ENGRAFTMENT AND INTEGRATION AFTER TRANSPLANTATION INTO ADULT RAT HEARTS

1. Abstract

Human induced pluripotent stem cell-derived cardiomyocytes (hiPSC-CMs) hold remarkable potential as a powerful cell source to repair injured hearts. After significant efforts of injecting hiPSC-CMs into animal hearts, it has become clear that current cell delivery strategies are limited by low cell retention and low engraftment/integration. To address this, we recently pioneered the use of electrically conductive silicon nanowires (e-SiNWs) to facilitate the self-assembly of hiPSC-CMs to form nanowired spheroids as injectable microtissues to deliver hiPSC-CMs. Our previous data showed that the incorporation of e-SiNWs into the spheroids improved cell/tissue level function and maturation. Here, we reasoned that the presence of e-SiNWs in the injectable spheroids improves their ability to receive exogenous electromechanical pacing from the host myocardium to enhance their integration with host tissue post-transplantation. In this study, we examined the cardiac biocompatibility of the e-SiNWs and cell retention, engraftment and integration after injection of the nanowired hiPSC cardiac spheroids into adult rat hearts. Our results showed that the e-SiNWs caused minimal toxicity to rat adult hearts after intramyocardial injection. Further, the nanowired spheroids were shown to significantly improve cell retention and engraftment, when compared to dissociated hiPSC-CMs and unwired spheroids. The 7-days-old nanowired spheroid grafts showed

alignment with the host myocardium and development of sarcomere structures. The 28-days-old nanowired spheroid grafts showed gap junctions, mechanical junctions and vascular integration with host myocardium. Together, our results clearly demonstrate the remarkable potential of the nanowired spheroids as cell delivery vehicles to treat cardiovascular diseases.

2. Introduction

Cardiovascular disease is the leading cause of death and disability worldwide [260]. Ischemic heart disease (IHD) and myocardial infarction (MI) are major contributors to cardiovascular morbidity and mortality and are associated with death of cardiomyocytes and permanent loss of heart function [232]. Due to the limited regeneration capacity of adult hearts, human induced pluripotent stem cell (hiPSC) has emerged as a powerful cell source for cardiac repair due to its proven capacity to produce patient-specific functional cardiomyocytes (hiPSC-CMs) [165-169]. In addition, recent progress in cardiac differentiation of hiPSCs allows for the derivation of the large number of hiPSC-CMs ($>10^9$ cells/patient) needed for cardiac repair [124, 170-172]. To realize the therapeutic potential of hiPSC-CMs or hESCs-CMs (cardiomyocytes derived from human embryonic stem cells), significant efforts have been devoted to transplanting hiPSC-CMs or hESCs-CMs into damaged animal hearts to improve their functions [97, 104, 124, 170, 173-178]. While significant efforts have been used to directly inject dissociated hESC-CMs into healthy/injured hearts, this approach is limited by low cell retention and survival after cell transplantation. Dissociated hiPSC-CMs are rapidly redistributed to other organs (e.g., lung) after injection due to mechanical dispersion of

beating hearts [140]. In addition, lack of cell-cell adhesion of single cells leads to cell death caused by anoikis and/or ischemia [179]. To improve the efficiency of cell delivery, significant efforts have been devoted to the development of tissue-engineered epicardial patches [175, 180-182]. In addition to the invasive surgical procedure to transplant the patches, recent research has shown the limited electrical integration between the transplanted patches and host myocardium, largely attributed to the chronic fibrotic response that occurs after transplantation [180-182]. This highlights an urgent need to develop an innovative platform to improve the retention, engraftment and integration of the injected hiPSC-CMs with adult myocardium.

hiPSC cardiac spheroids have been proposed as an attractive cell delivery system for heart repair, given the recent literature showing spheroid/aggregate delivery improved cellular retention and survival after transplantation [183-189]. To this end, we recently utilized electrically conductive silicon nanowires (e-SiNWs) to facilitate the self-assembly of hiPSC-CMs to form nanowired hiPSC cardiac spheroids and improve the functions of the microtissues [148, 280]. Here, we reasoned that the presence of the e-SiNWs in the injectable spheroids improves their ability to receive exogenous electromechanical pacing from the host myocardium and enhance their integration with host tissues post-transplantation. This was inspired by our recent finding that the addition of e-SiNWs in hiPSC-CM spheroids are essential for exogenous electrical stimulation/pacing to promote hiPSC-CM development and maturation [190]. Further, the recent reports showed the presence of electrical nanomaterials (e.g., gold nanowires) in the cardiac tissue engineering constructs synergizes with exogenous electrical pacing

to improve the functions of the constructs [147, 191]. Compared to other electrical nanomaterials (e.g. gold nanowires, carbon nanotubes), e-SiNWs have distinct advantages, including their controllable electrical conductivity, tunable dimensions, and convenient surface tailorability [192, 193]. Further, both *in vitro* and *in vivo* biocompatibility studies have shown no significant cytotoxic effects for either undoped or n-type SiNWs [194-196]. Notably, the absence of a pre-aligned structure within the nanowired hiPSC cardiac spheroids has raised concerns over their suitability for transplantation. The ability of hiPSC-CMs from hiPSC cardiac spheroids to align and functionally engraft/integrate with the host tissue after transplantation is an open question that needs to be investigated.

In this study, we injected nanowired hiPSC cardiac spheroids into adult rat hearts and examined cell retention, engraftment and integration. In addition, we examined the cardiac biocompatibility of e-SiNWs in the adult rat hearts. For the first time, we demonstrated that the nanowired spheroids significantly improve hiPSC-CM retention and engraftment after intramyocardial injection, when compared to the dissociated single hiPSC-CMs and unwired hiPSC cardiac spheroids. 7 days post-injection, the transplanted nanowired spheroids showed alignment with the local myocardium and improved the development of cellular contractile structures. By 28 days post-injection, the nanowired spheroid grafts formed electrical/mechanical/vascular junctions with the host myocardium, supporting functional integration with host myocardium.

3. Materials and methods

3.1 Cell culture

The hiPSC-CMs (Cellular Dynamics International, Madison, USA) were cultured according to the manufacturer's protocol. Briefly, hiPSC-CMs were plated on 0.1% gelatin coated 6-well plates in plating medium and incubated at 37 °C in 5% CO2 for 4 days. Two days after plating, plating medium was removed and replaced with 4 mL of maintenance medium. After 4 days of monolayer pre-culture, cells were detached using trypLE (Life Technologies, Grand Island, NY) and prepared for spheroid fabrication.

3.2 Fabrication of nanowired hiPSC cardiac spheroids

The details of the fabrication process can be found in our recent publication (32). Briefly, the n-type SiNWs (Diameter ≈ 100 nm; length ≈ 10 μm; Si/P = 500) were prepared according to the previously established protocol (32). The length and diameter of the e-SiNWs were selected to inhibit cell internalization. The doping ratio was chosen to obtain a high conductivity (150 - 500 μS/μm) compared to cell culture medium (~1.75 μS/μm) and myocardium (~0.1 μS/μm) to create highly electrically conductive microenvironments within the spheroids.

3.3 Video and image analysis of beating spheroids

Videos of 6 spheroids from each group were recorded using Zen 2011 software (Zeiss, Göttingen, Germany) with capture rate of 14 frames per second. Then the videos were converted to a series of TIFF format pictures by Adobe Premiere (Adobe, San Jose, CA). Threshold edge-detecting in ImageJ software (National Institutes of Health) was used on high contrast spheroid pictures and graphed to realize contraction profiles, from which the fractional area change was calculated.

3.4 Injection of e-SiNWs and nanowired cardiac spheroids into rat hearts

To evaluate the cardiac biocompatibility of e-SiNWs, young male Sprague–Dawley rats (8-10 weeks old) were prepared for surgery, anesthetized, given analgesia, intubated, and a left thoracotomy was performed to expose the heart. The pericardium was opened and 5 million silicon nanowires in 50 μl PBS were injected to the 3 different sites in left ventricular region using syringes with a 31-gauge needle. For nanowired hiPSC cardiac spheroid injection, athymic young male rats (8-10 weeks old) were prepared for surgery, anesthetized, given analgesia, intubated, and left thoracotomy were performed to expose the heart. The pericardium was opened and a total of ~30 nanowired hiPSC cardiac spheroids per rat (i.e., 30,000 hiPSC-CMs per rat) or 30,000 single hiPSC-CMs in Matrigel were injected to three different sites (50 μl at each site) in the left ventricular region using 29-gauge needles. After injection, the thoracotomy incision was sutured and the animal was allowed to recover for 1 day, 7 days and 28 days before heart harvest for histological analysis. The influences of the injected e-SiNWs and cellular therapies on the rat cardiac function were examined on day -1, 1, 7 and 28 post-injection by using electrocardiogram and echocardiogram as described below. All the surgical procedures and pre-/post-operative care were performed following NIH guidelines for the care and use of laboratory animal (NIH publication No. 86-23, revised 1996), and they were under the supervision of the Institutional Animal Care and Use Committee (IACUC) of the Medical University of South Carolina (MUSC).

3.5 Cardiac function measurement

To examine rat echocardiography, the Vevo2100 imaging system (VisualSonics,

Toronto, Canada) was used with 22–55 MHz linear transducer probe (MS400 or MS250) for 2-D B-mode and M-mode analysis. During the measurement, heart rate was maintained at 300–400 bpm via isoflurane anesthesia. Left ventricular (LV) volume was calculated from Simpson's method of disks, the ejection fraction (EF) was determined from the equation: EF= (LV end diastolic volume – LV end systolic volume)/ (LV end diastolic volume) and the fractional shortening was calculated by the equation: FS = (LV end diastolic dimension - LV end systolic dimension)/ LV end diastolic dimension. Offline image analyses were performed using the dedicated VisualSonics Vevo2100 1.2.0 software. Electrocardiogram (ECG) and rectal temperature (RT) were recorded by MouseMonitor S (Indus Instruments, Webster, TX). Briefly, the rats were anesthetized using 3% isoflurane and placed on the heated pad (37°C). The ECG (leads I, II, and III) and RT were obtained from four needle electrodes subcutaneously inserted into the four paws and one temperature probe placed in rectal location while the rat was in supine position.

3.6 Histological analysis for in vitro cultured nanowired cardiac spheroids

The freshly collected spheroids (~30-35) were flash frozen in Tissue-Tek OCT compound (Sakura, Torrance, CA) and cryo-sectioned into 7μm thickness layers onto glass slides for immunohistochemistry. The frozen sections were fixed with pre-cooled acetone (-20 °C) for 10 min. The fixative was poured off and the acetone was allowed to evaporate from the sections for 20 min at room temperature. After washing (3 times at 5 min) in PBS with 0.1% Triton X-100 (PBST), 100 μl blocking buffer (10% goat serum (Sigma) in PBST) was added onto the sections of the slides and incubated in a humidified

chamber at room temperature for 1 h. The sections were incubated with appropriately diluted primary antibody overnight at 4 °C. After washing in PBST (3 times at 5 min), tissues were incubated with coordinate secondary antibodies diluted in PBST for 1h at ambient temperature. After washing in PBST (3 times at 5 min), nuclei were counterstained with DAPI (Molecular Probes/Invitrogen, Eugene, OR) diluted in PBST for 15 min at ambient temperature. Following the final wash procedure (PBST, 3 times at 5 min), glass cover slips were added to the slides using Fluoro-Gel (Electron Microscopy Sciences, Hatfield, PA). Finally, TCS SP5 AOBS laser scanning confocal microscope (Leica Microsystems, Inc., Exton, PA) was used to get fluorescent images. The detailed information of the antibodies used in this study was listed in the Table 5.1.

Antigen	Antibody	type	Company	Catalog number	Dilution
Vimentin	Rabbit	polyclonal	Abcam	ab92547	1:200
CD68	Mouse	monoclonal	AbD Serotec	MCA341GA	1:200
pan Troponin I	Rabbit	polyclonal	santa cruz	SC-15368	1:200
connexin 43	Rabbit	polyclonal	sigma	C6129	1:200
alpha sacomeric actin	Rabbit	polyclonal	abcam	ab9465	1:200
alpha sacomeric actin	Mouse	monoclonal	Gene Tech	GTX29465	1:200
N cadherin	Mouse	monoclonal	BD	610921	1:200
Laminin	Mouse	monoclonal	Sigma	L9393	1:200
Collagen I	Rabbit	polyclonal	abcam	ab34710	1:200
Human Nuclear	Mouse	monoclonal	abcam	ab191181	1:200
Isolectin B4 Alexa488 Conjugate			life Tech	I21411	1:50
DAPI			life Tech	R37606	1:10
Live/dead staining kit			life Tech	L3224	EthD-1 (1:500) / calcein (1:2000)
TUNEL staining kit			Roche	11684795910	enzyme solution: label solution=1:9

Table 5.1: The details (vendor source, catalogue number and dilution ratio) of the antibodies used in this study.

3.7 Histological analysis for the harvested cardiac tissues

The fresh rat hearts were fixed overnight in 4% paraformaldehyde solution and embedded in a paraffin block. Using an automated microtome (LeicaRM2255, Leica, Exton, PA), paraffin embedded hearts were sectioned into 8 μm thickness ribbon with

~1000 sections per heart in total. Three sections were picked up with every 25 sections gap for mounting on the glass slide and 40 slides (~120 total sections per heart) were processed and stained for each rat heart in order to avoid missing the human spheroids in rat myocardium for staining. Paraffin-embedded hearts were sectioned (8 μm) dewaxed and processed with antigen retrieval solution (Vector Laboratories, Burlingame, CA) in pressure cooker for 10 min before staining. Sections were incubated with appropriately diluted primary antibody overnight at 4 °C. After washing in PBST (3 times at 5 min), tissues were incubated with coordinate secondary antibodies diluted in PBST for 1h at ambient temperature. After washing in PBST (3 times at 5 min), nuclei were counterstained with DAPI (Molecular Probes/Invitrogen, Eugene, OR) diluted in PBST for 15 min at ambient temperature. Following the final wash procedure (PBST, 3 times at 5 min), glass cover slips were added to the slides using Fluoro-Gel (Electron Microscopy Sciences, Hatfield, PA). Finally, TCS SP5 AOBS laser scanning confocal microscope (Leica Microsystems, Inc., Exton, PA) was used to get fluorescent images. The average grafts per heart for spheroid transplantation was calculated as the number of slides per heart (out of ~30-40 total slides per heart) with visible grafts (N=5 rats, total of ~150 observed slides per treatment). The detailed information of the antibodies used in this study was listed in the Table 5.1.

3.8 TUNEL staining

In Situ Cell Death Detection Kit (Roche, Penzberg, Germany) was used to determine the viability of the cells in the paraffin section of rat hearts and frozen sections of spheroids. Briefly, the paraffin sections of spheroids were dewaxed and processed with

antigen retrieval solution (Vector Laboratories, Burlingame, CA) in pressure cooker for 10 min , then washed in PBS for 30 minutes. For frozen section spheroids, sections were fixed in 4% paraformaldehyde solution for 10 min, then washed in PBS for 30 min. After PBS washes, sections were incubated in permeabilisation solution (0.1% Triton X-100 and 0.1% sodium citrate in PBS) for 2 minutes on ice. Then 50 µl TUNEL reaction mixture samples was added and incubated in 37 °C for 1 hour. After washing in PBST (3 times at 5 min), nuclei was counterstained with DAPI (Molecular Probes/Invitrogen, Eugene, OR) for 15 min at ambient temperature. Following the final wash procedure (PBS, 3 times at 5 min), glass cover slips were added to the slides using Fluoro-Gel (Electron Microscopy Sciences, Hatfield, PA).

3.9 Transmission Electron Microscopy

e-SiNWs were gently sonicated in isopropyl alcohol (IPA) and dispersed onto lacey carbon grids (Ted Pella Inc.). TEM imaging was conducted using a 300kv FEI Tecnai G2 F30 Super Twin Transmission Electron Microscope (Fig. 5.1).

4. Results

4.1 Cardiac compatibility of e-SiNWs

Our previous in vitro research showed the minimal cytotoxicity of e-SiNWs (n-type SiNWs: Diameter $\approx$ 100 nm; length $\approx$ 10 µm; Silane/Phosphane = 500, Figure 5.1) when co-cultured with hiPSC-CMs [148, 190]. To use e-SiNW nanowired hiPSC cardiac spheroids for heart repair, in vivo cardiac biocompatibility of e-SiNWs must be established. In addition to cellular compatibility, functional compatibility in the heart

must be considered due to the possible electrical interference of the conductive e-SiNWs with the innate cardiac electrical signal conduction system. To examine these concerns, 5 million e-SiNWs were injected into the healthy adult rat myocardium. The cardiac function of the rats injected with e-SiNWs and PBS (control) was examined using electrocardiogram (ECG) and echocardiography on day -1, 1, 7 and 28 post-injection (Fig. 5.2A-D). As shown in the Figure 2A, ECG results revealed no detectable arrhythmia of the rat hearts after e-SiNW injection. This indicates the injected e-SiNWs do not significantly affect the electrical conduction system of adult rat myocardium. In addition, left ventricle ejection fraction (EF) (~70%) and fractional shortening (FS) (~35%) of the rat hearts did not show significant differences between before and after e-SiNW injection (Figure 5.2B-D). In addition, the left ventricle EF and FS of the e-SiNW injected rats were found to be very similar to that of the PBS injected control rats. These data strongly indicated the e-SiNWs do not alter the cardiac function after a high dose injection into adult rat myocardium.

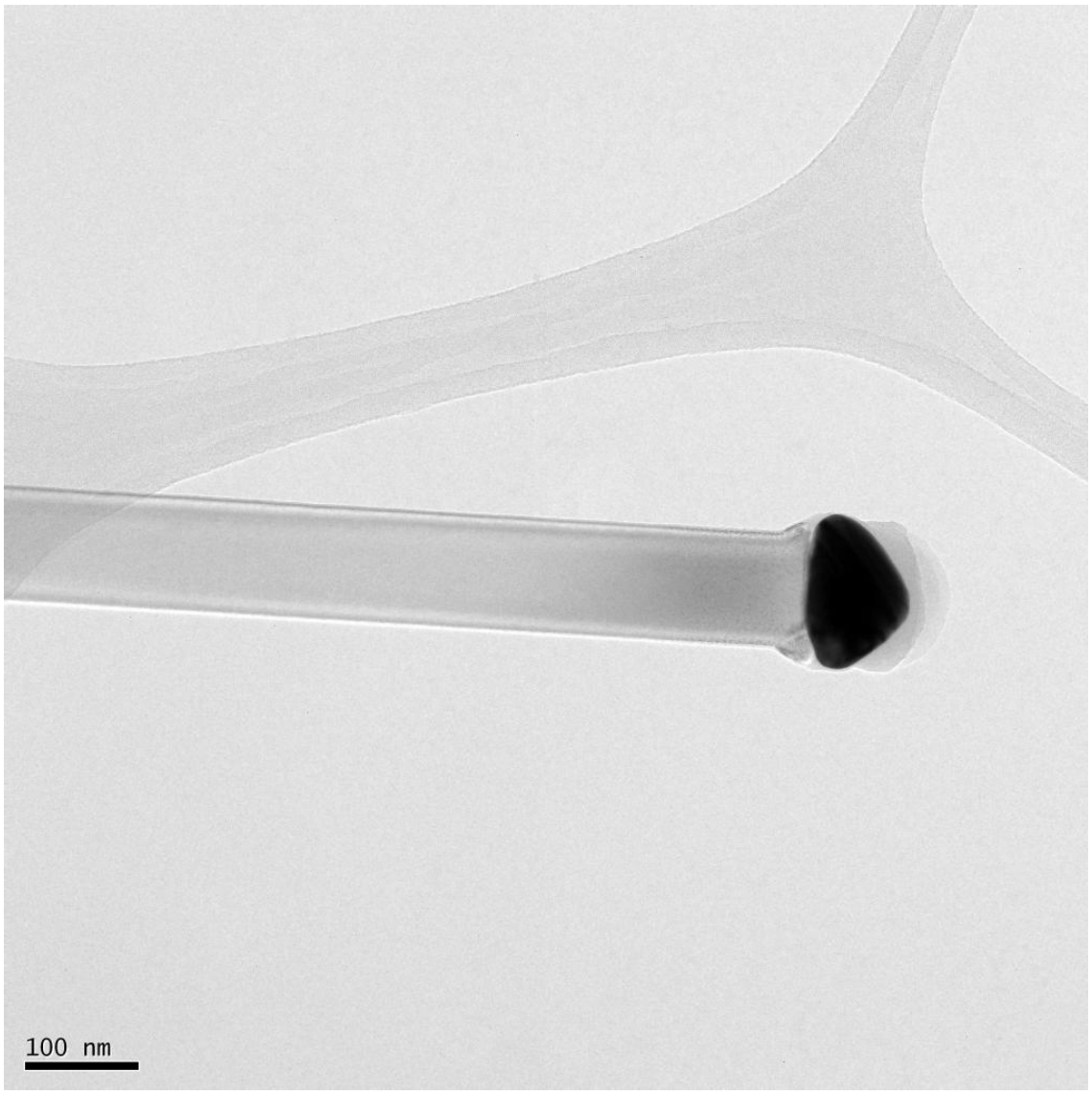

Figure 5.1: Transmission electron micrograph of an e-SiNW. TEM image of a typical n-type e-SiNW used in this study on a carbon grid.

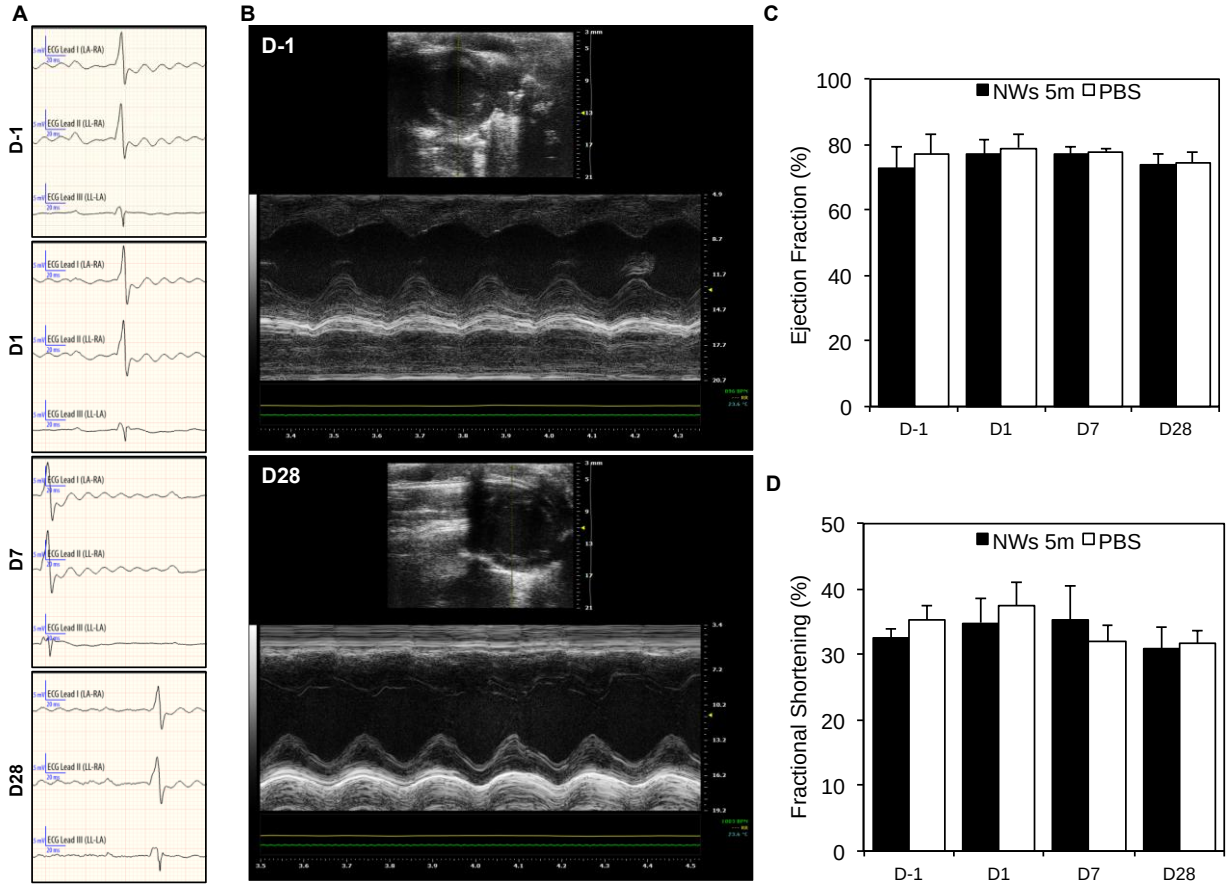

Figure 5.2: Cardiac functional compatibility analysis after e-SiNWs injection into adult rat myocardium. (A) Representative ECG profiles of rats with 5 million e-SiNWs injection in the left ventricular myocardium at time points of before injection (D-1) and after injection (D1, D7 and D28). (B) Representative echocardiogram images in short axis of rat hearts with 5 million e-SiNWs injection in the left ventricular myocardium at time points of D-1 and D28. (C) Ejection fraction and (D) fractional shortening were used for quantitative analysis of cardiac function after e-SiNWs and PBS injection. Error bars represent standard deviation (N=4).

In addition to evaluating the cardiac function, the blood samples of the rats injected with e-SiNWs and the control rats were collected on day -1, 1, 7, 14 and 28 post-injection. As shown in Figure 5.3 and Table 5.2, the total white blood cell counts from the e-SiNW injected rats are in the normal physiological range without statistically

differences between the rats with the e-SiNW injections and the control rats. This showed that the intramyocardial injection of e-SiNWs did not significantly affect the hematological characteristics of the rats. Supported by a normal growth curve, heart beat rate and body temperature (Figure 5.4-5.5), our data indicated the intramyocardial injection of e-SiNWs resulted in a minimal global inflammatory response.

Total White Blood Cells (k/ul)_ Normal range: 2.9~20.9					
Group	Pre-surgery	Post surgery			
	Day -1	Day 1	Day 7	Day 14	Day 28
5m e-SiNWs (n=5)	15.80	16.82	16.06	15.76	14.60
	23.48	13.38	19.88	17.84	11.74
	7.76	12.98	18.66	12.18	11.36
	8.86	11.76	18.52	19.76	19.74
	16.10	11.90	19.74	13.96	13.32
PBS (n=3)	13.04	12.14	17.22	20.32	19.66
	16.46	17.24	12.32	22.78	19.20
	17.86	19.86	12.86	18.46	17.58

Table 5.2: Total white blood cells counts for nanowires biocompatibility test. Hematology profiles of rats blood samples with 5 million e-SiNWs or PBS (control) intramyocardial injection at time points of before injection (D-1) and after injection (D1, D7 and D28) indicate minimal inflammation response post surgery. n=5 rats for e-SiNWs injection group and n=3 rat for PBS injection group.

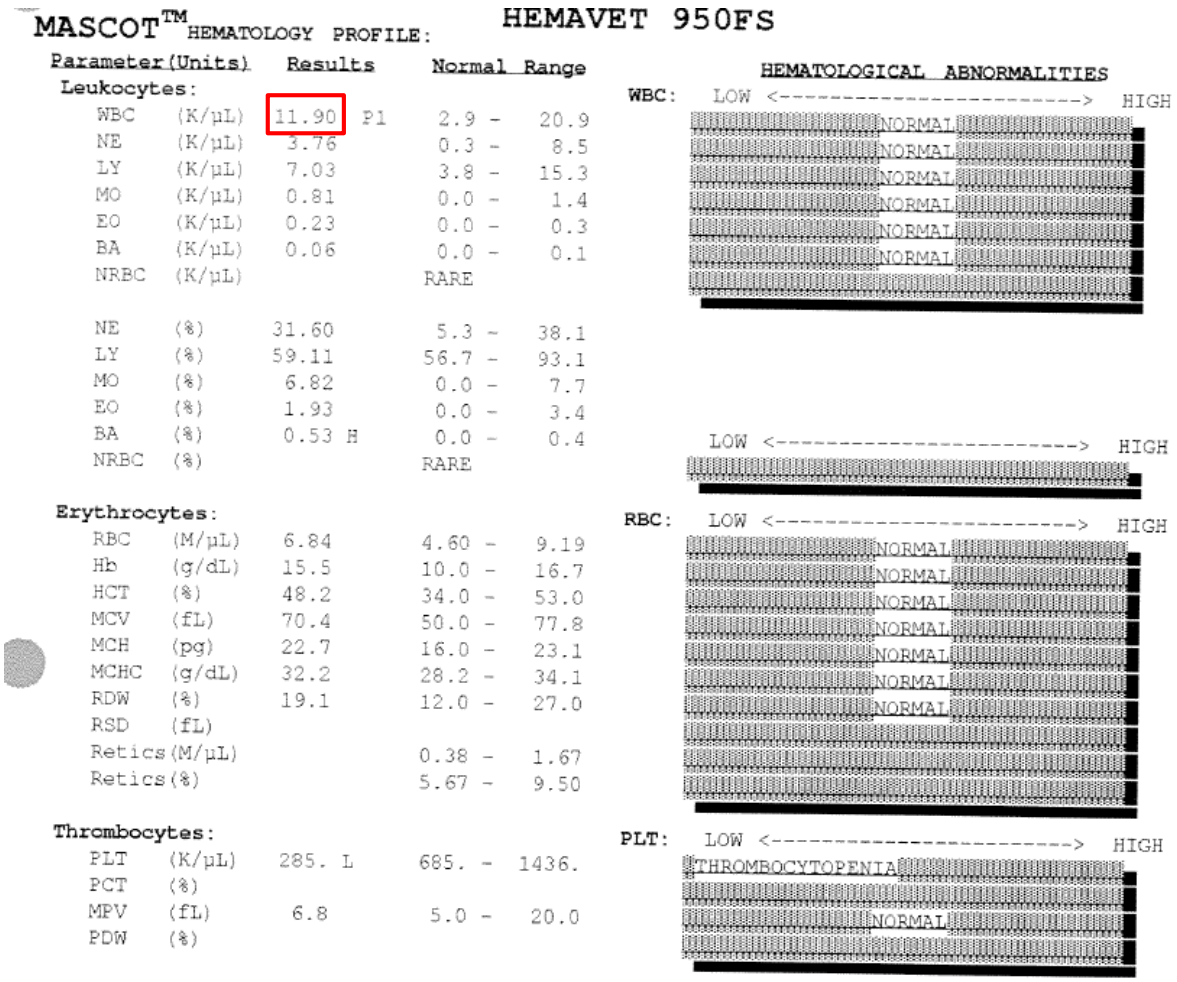

MASCOT™ HEMATOLOGY PROFILE: HEMAVET 950FS

Parameter	(Units)	Results		Normal Range
Leukocytes:				
WBC	(K/µL)	11.90	P1	2.9 - 20.9
NE	(K/µL)	3.76		0.3 - 8.5
LY	(K/µL)	7.03		3.8 - 15.3
MO	(K/µL)	0.81		0.0 - 1.4
EO	(K/µL)	0.23		0.0 - 0.3
BA	(K/µL)	0.06		0.0 - 0.1
NRBC	(K/µL)			RARE
NE	(%)	31.60		5.3 - 38.1
LY	(%)	59.11		56.7 - 93.1
MO	(%)	6.82		0.0 - 7.7
EO	(%)	1.93		0.0 - 3.4
BA	(%)	0.53	H	0.0 - 0.4
NRBC	(%)			RARE
Erythrocytes:				
RBC	(M/µL)	6.84		4.60 - 9.19
Hb	(g/dL)	15.5		10.0 - 16.7
HCT	(%)	48.2		34.0 - 53.0
MCV	(fL)	70.4		50.0 - 77.8
MCH	(pg)	22.7		16.0 - 23.1
MCHC	(g/dL)	32.2		28.2 - 34.1
RDW	(%)	19.1		12.0 - 27.0
RSD	(fL)			
Retics	(M/µL)			0.38 - 1.67
Retics	(%)			5.67 - 9.50
Thrombocytes:				
PLT	(K/µL)	285.	L	685. - 1436.
PCT	(%)			
MPV	(fL)	6.8		5.0 - 20.0
PDW	(%)			

Figure 5.3: Representative blood test result. The hematology profile of rat blood sample collected from tail vein was performed by Drew Scientific HemaVet 950FS Auto Blood Analyzer. The red boxed value is used to construct Table 1.

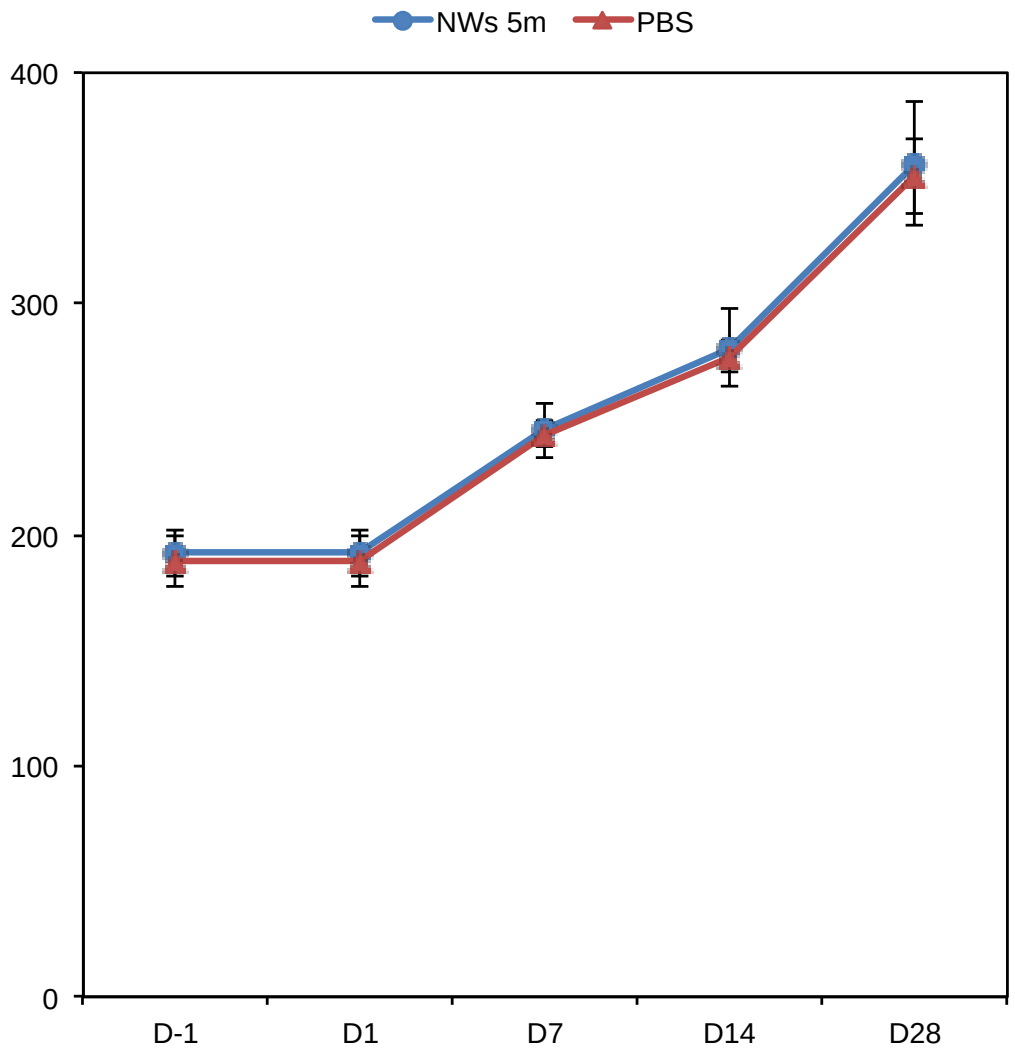

Figure 5.4: The rats followed a normal weight curve after e-SiNW injection. The rats with 5 million e-SiNWs or PBS (control) intramyocardial injection were weighed at time points of before injection (D-1) and after injection (D1, D7 and D28) to monitor the body growth. Error bars represent standard deviation. n=5 rats for e-SiNWs injection group and n=3 rat for PBS injection group.

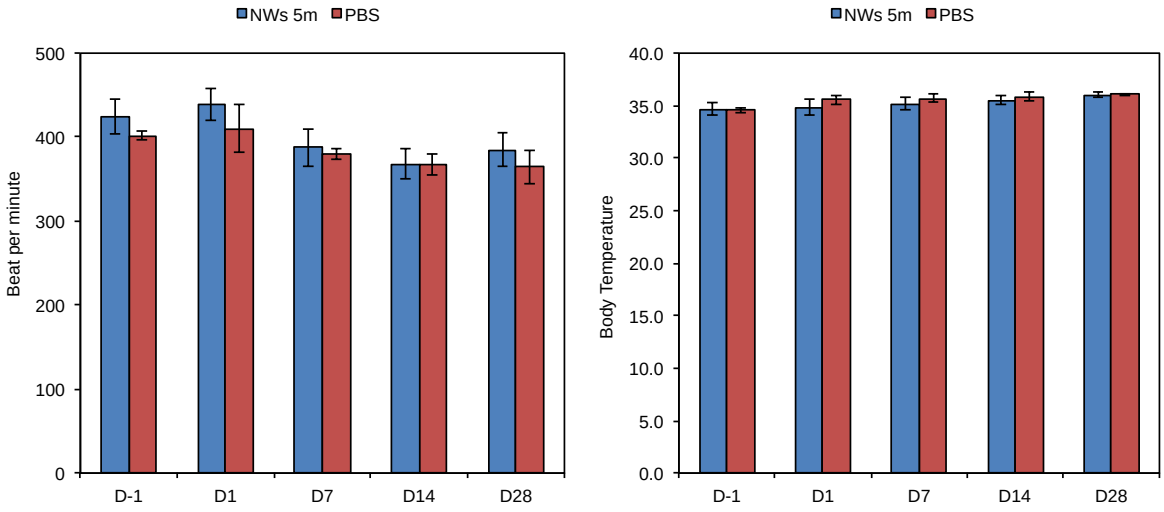

Figure 5.5: The rats followed a normal physiological condition after receiving NWs injection. Heart beat rate and rectal temperature were recorded for the rats with 5 million e-SiNWs or PBS (control) intramyocardial injection at time points of before injection (D-1) and after injection (D1, D7 and D28) to monitor the physiological condition. Error bars represent standard deviation. n=5 rats for e-SiNWs injection group and n=3 rat for PBS injection group.

Histological analysis was conducted to examine e-SiNW retention and degradation, as well as the effects of the injected e-SiNWs on myocardium inflammation and fibrosis. As shown in the Figure 5.7 A-B, a significant decrease in the amount of e-SiNWs was found in myocardium 7 days post-injection when compared to 1 day post-injection. After 28 days, few e-SiNWs were found in the injected myocardium, which was attributed to biodegradation and redistribution [195, 246]. In addition, H&E staining showed a minor inflammation 7 days post-injection in the myocardium and no sign of inflammation 28 days post-injection. Naphthol AS-D chloroacetate esterase staining (Figure 5.7 C) and CD68 staining (Figure 5.7 D) showed neutrophil and macrophage infiltration in the myocardium 1 day post-injection, and the infiltrated neutrophils/macrophages decreased by day 7 and disappeared on the day 28 post-

injection. Notably, CD68-positive macrophages at day 7 also showed colocalization with e-SiNWs, which supports the reported phagocytosis mechanism of internalization and biodegradation of the e-SiNWs (Figure 5.6) [196, 246]. These results clearly showed the injected e-SiNWs did not induce chronic inflammation or chronic foreign body response in the myocardium. In addition to inflammation, fibrosis after e-SiNW injection in the myocardium was examined. Vimentin staining (Figure 5.7 E) showed a minor fibroblast infiltration 7 days post-injection that disappeared by day 28 after e-SINW injection, which indicated the injected e-SiNWs did not induce a chronic fibrotic response. Collectively, our results showed the e-SiNW showed minimal toxicity to the adult myocardium after intramyocardial injection and lays down the foundation for the use of nanowired spheroids for heart repair.

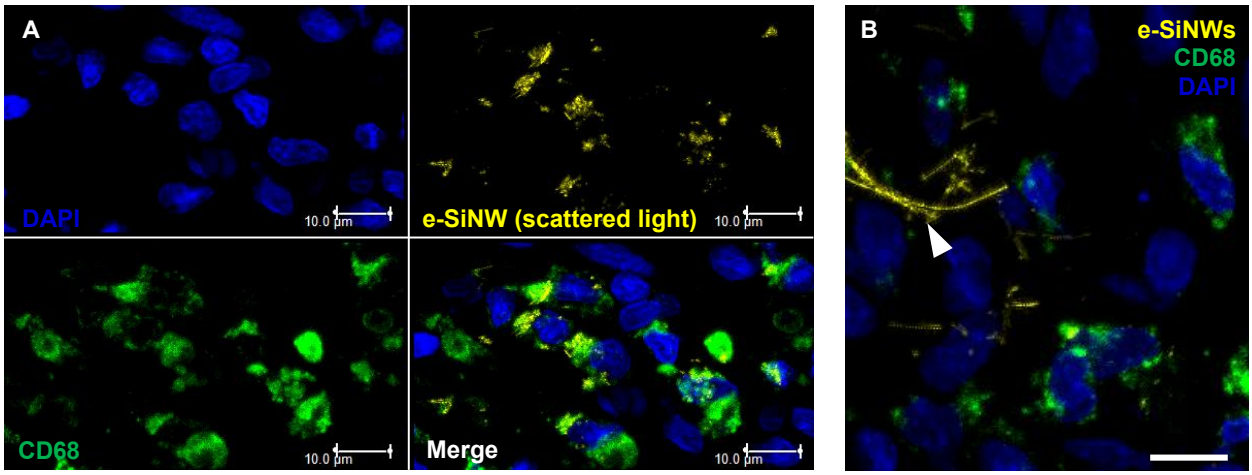

Figure 5.6: Injected nanowires colocalize with macrophages at D7 post-transplantation. (A) Colocalization of e-SiNWs with CD68-positive (green) macrophages supports reported phagocytosis mechanism of internalization and degradation. (B) Large nanowires (arrow) were often found outside the macrophages in line with size-limited internalization. Scale bars= 10 µm.

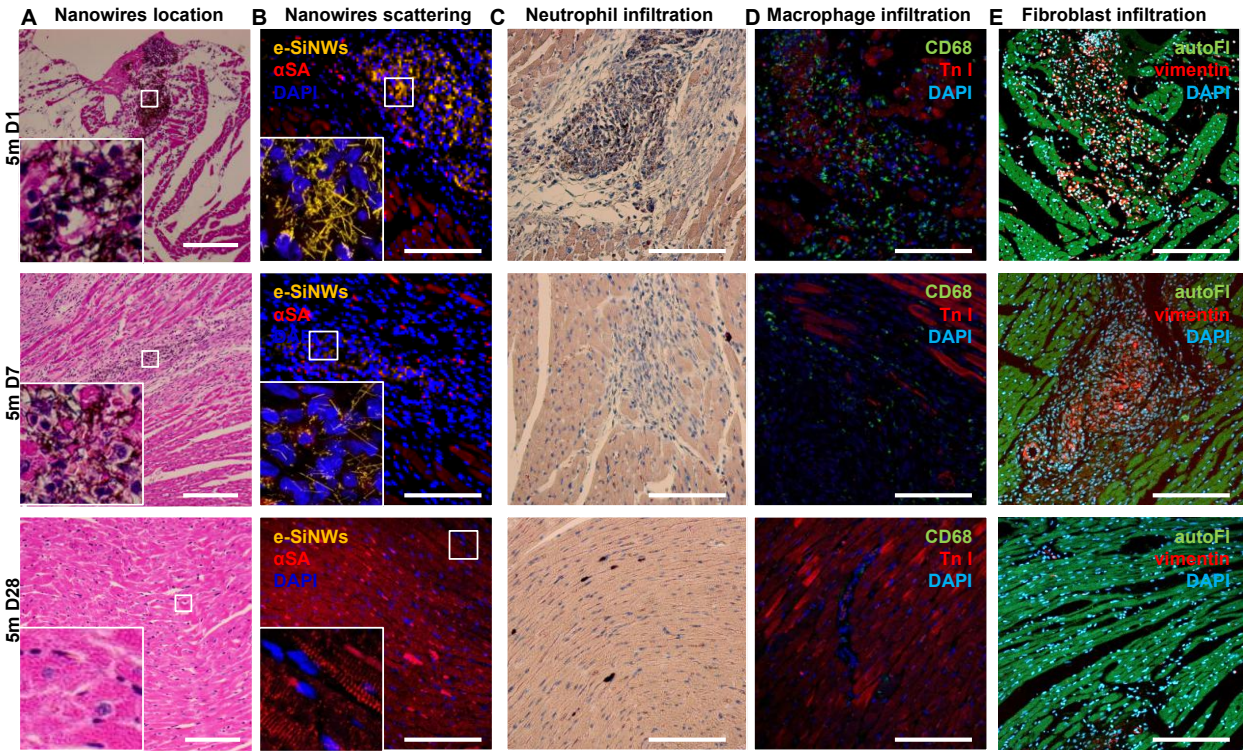

Figure 5.7: Histological analysis after e-SiNW injection into adult rat myocardium. (A) H&E staining shows location and density of e-SiNWs that decrease and disappear over 28 days after injection. (B) Confocal images of light scattering signal of e-SiNWs show similar results with H&E staining. (C) Neutrophils infiltration identified by naphthol AS-D chloroacetate staining (dark brown) shows short-term increase in inflammatory response that diminished by day 28. (D) Macrophages infiltration identified by CD68 staining shows short-term increase in inflammatory response that diminished by day 28. (E) Non-cardiomyocytes identified by vimentin staining in adult rat heart for 5 million e-SiNWs injection at day 1, day 7 and day 28 to indicate fibroblast infiltration. Vimentin-positive cells disappear by day 28 indicating no chronic fibrotic response. Scale bars: (A-E)= 200 μm

4.2 Fabrication and characterization of nanowired hiPSC cardiac spheroids for transplantation

To prepare spheroids suitable for injection, we fabricated nanowired hiPSC cardiac spheroids containing ~1,000 cells/spheroid using our previosuly established

method (Figure 5.8 A-B) [148]. After 7 days of spheroid formation, the diameter of the nanowired spheroids decreased to ~180 μm, an injectable size (i.e., less than inner diameter of 29 gauge needle) for rat myocardium (Figure 5.8 C). Further extended culture did not significantly reduce the size of the spheroids. Consistent with the changes in spheroid size, the amplitude of the spontaneous contraction of the nanowired spheroids gradually decreased over the time and stabilized after 7-9 days spheroid culture (Figure 8 D). The reduced size and contraction amplitude of the nanowired spheroids indicates the formation and stabilization/maturation of the human cardiac microtissues.

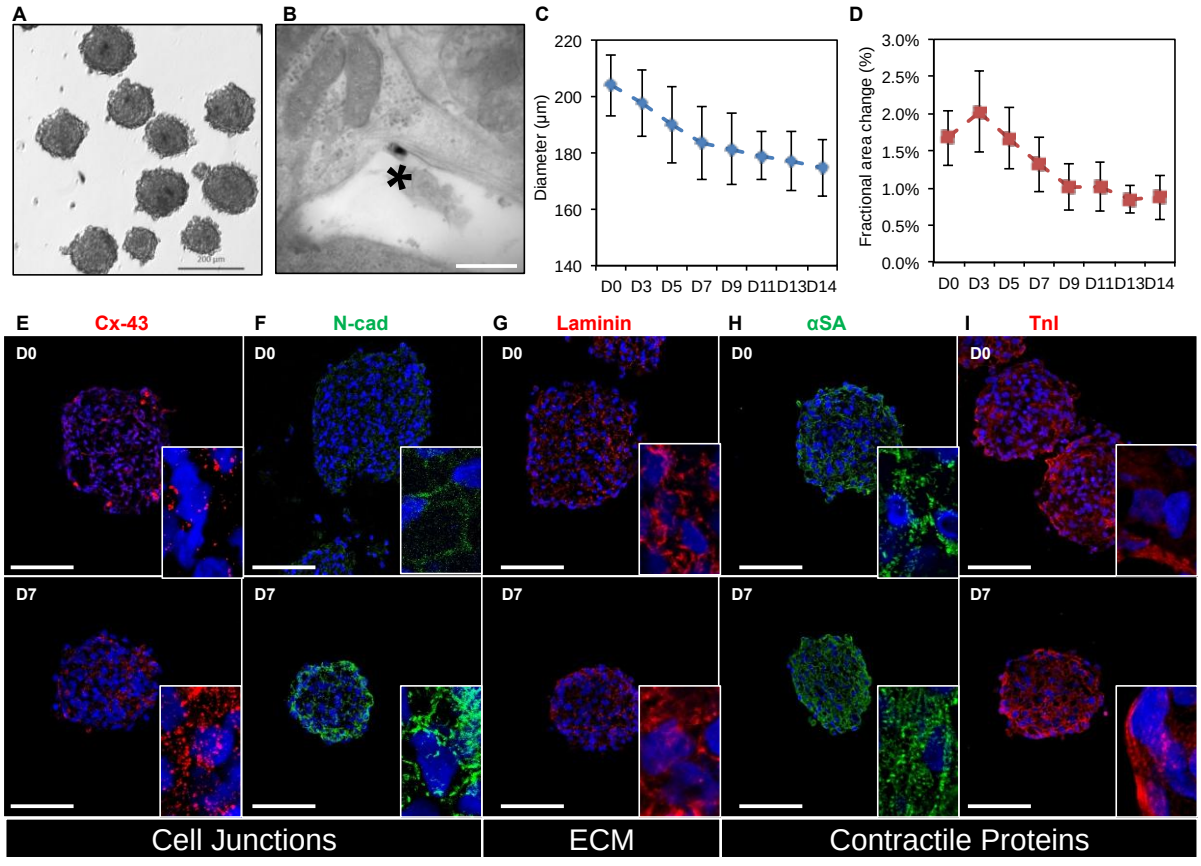

Figure 5.8: Fabrication and characterization of nanowired hiPSC cardiac spheroids for transplantation. (A) Bright field image images of nanowired hiPSC cardiac spheroids

after 7 days spheroid culture. (B) Transmission electron micrograph of nanowired spheroid section shows nanowire locates in extracellular space. Asterisk - nanowire location. (C) Diameter and (D) fractional area change of nanowired hiPSC cardiac spheroids from spheroid culture D0-D14. Error bars represent standard deviation (N=6). (E-I) Frozen sections of D0 and D7 spheroids characterize microtissue development according to cell junctions proteins (E: Cx-43; F: N-cadherin), ECM protein (G: laminin) and contractile proteins (H: alpha sacomeric actinin; I: troponin I). Scale bars: (A) =200 μm, (B) =500 nm, (E-I) =100 μm.

To validate the cardiac tissue formation and maturation, frozen sections of day 0 and day 7 spheroids were immunofluorescently stained to examine the formation of cellular junctions, extracellular matrix (ECM) protein production and contractile protein development. Consistent with our previous work, day 7 spheroids showed significant increase of cellular junction formation, including electrically conductive channel proteins, Connexin-43 (Cx-43) (Figure 5.8 E), and mechanical junction proteins, N-cadherin (N-cad), when compared to day 0 spheroids (Figure 5.8 F) [148]. In addition to cell-cell junctions, the cell-matrix interactions can facilitate cardiac tissue formation and development. Figure 5.8 F showed the abundant presence of basement membrane protein (laminin) in the nanowired spheroids (Figure 5.8 G). The formation and maturation of nanowired spheroids was also supported by significant development in the contractile protein such as alpha sarcomere actinin (Figure 5.8 H) and troponin I (Figure 5.8 I) in day 7 spheroids, when compared to day 0 spheroids. In addition, we observed that day 7 spheroids are mechanically stable for technical manipulations and intramyocardial injection protocols. Compared to dissociated hiPSC-CMs in Matrigel, the nanowired spheroids showed no significant difference in cell apoptosis (i.e., TUNEL) after a 29-gauge needle extrusion into a petri dish (Figure 5.9). Together, these results clearly

showed the nanowired spheroids provided a supportive microenvironment to form injectable 3D hiPSC cardiac microtissues for transplantation.

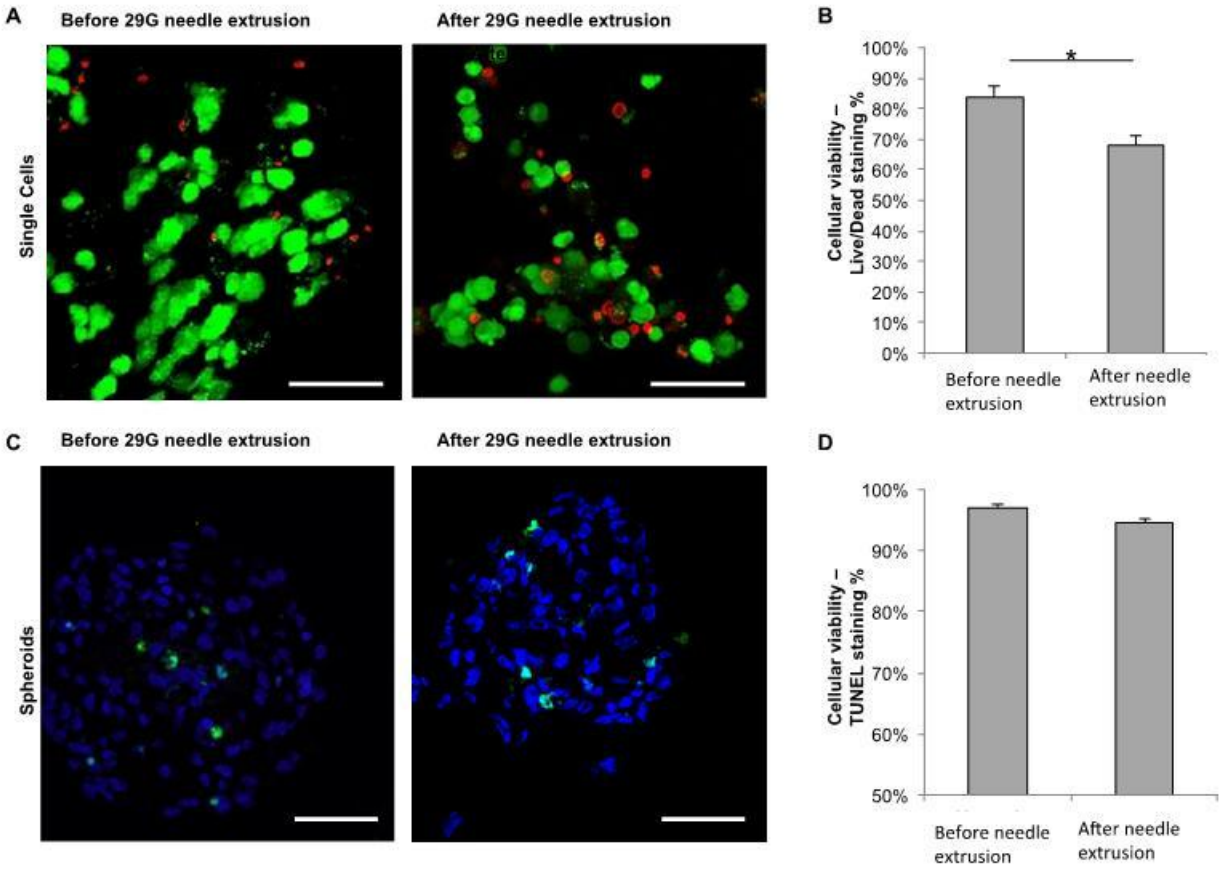

Figure 5.9: Viability of hiPSC-CMs in Matrigel and spheroids before and after needle extrusion. (A) Confocal images of Live/Dead staining of single hiPSC-CMs in Matrigel before and after extrusion through a 29 gauge syringe needle. Green- live cells; red- dead cells. (B) Quantification of the cell viability based on the Live/Dead staining. n=3. (C) Confocal images of TUNEL staining of spheroid sections before and after extrusion through a 29 gauge syringe needle. Green- apoptosis cells; blue- DAPI. (D) Quantification of the cell viability based on the TUNEL. n=3. Scale bars: (A, C)=50 μm. Asterisks (*) represent statistical significance with $p<0.05$; error bars represent standard deviation.

4.3 Nanowired hiPSC cardiac spheroid transplantation improve cell retention, engraftment and integration

To examine the capacity of the nanowired hiPSC cardiac spheroids to improve cell retention and engraftment, we injected nanowired hiPSC cardiac spheroids into healthy Athymic rat hearts. Healthy rats were selected due to their effectiveness to study hiPSC-CM engraftment and integration without the confounding factors presented in the injured animal models (e.g., variation among different injured animals) [182]. In this study, we injected a small number of nanowired hiPSC cardiac spheroids into each animal (~30 spheroids/rat; ~30k hiPSC-CMs/rat) to examine individual hiPSC cardiac spheroids' integration with the host myocardium. In addition, we conducted ECG and echocardiography measurement for the rat hearts before and after the injection of the nanowired spheroids to examine the effects of the injected nanowired spheroids. As shown in Figure 10 A-C, the injection of the nanowired spheroids did not interfere with the electrical conduction system as well as the normal function of the rat hearts.

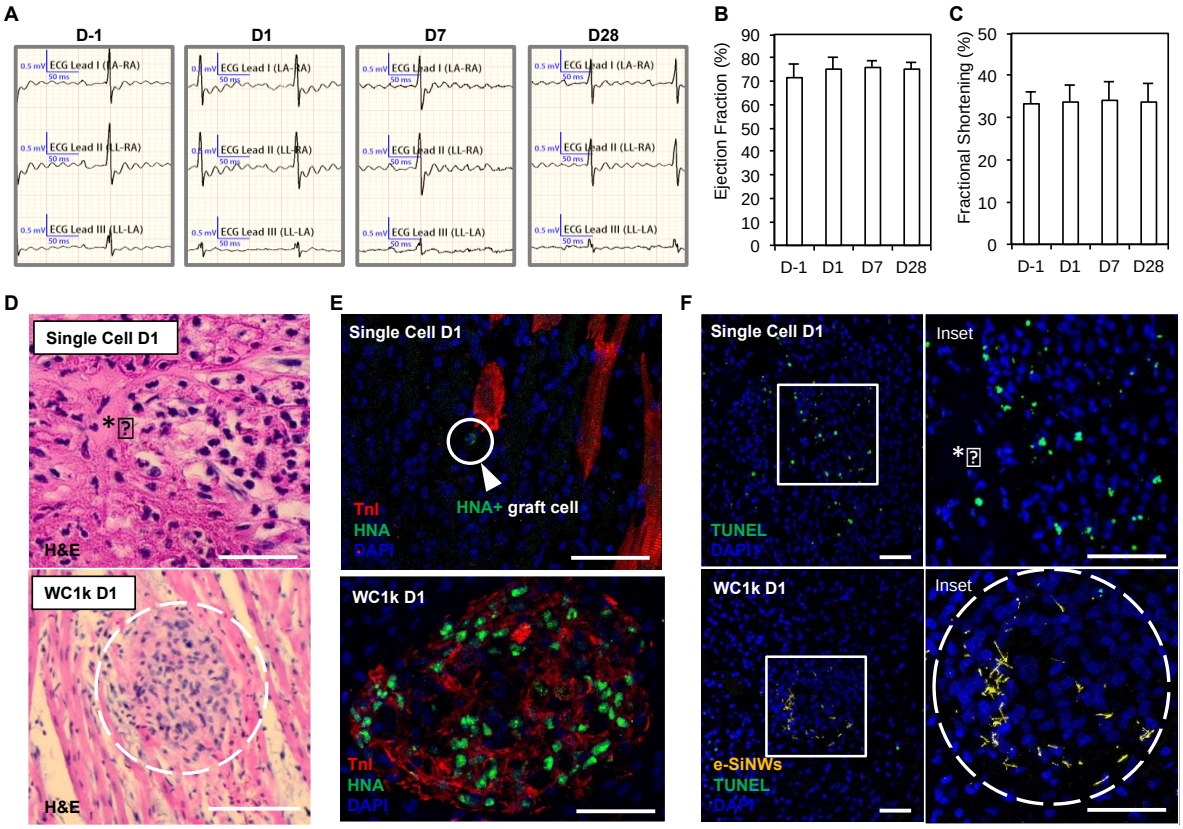

Figure 5.10: Nanowired spheroids transplantation improves cell retention and engraftment in adult rat myocardium. (A) Representative ECG profiles of rats with nanowired cardiac spheroids injection in the left ventricular myocardium at time points of before injection (D-1) and after injection (D1, D7 and D28) indicate healthy cardiac electrical signal propagation with no arrhythmias. (B) Ejection fraction and (C) fractional shortening as quantitative analysis for cardiac function for spheroids injection do not show deleterious effects of nanowired spheroid injection. Error bars represent standard deviation (N=4). (D) H&E staining of single cell injection sites (identified by Matrigel dense area – asterisk) and nanowired spheroids (WC1k) on D1 post transplantation. Dotted line encircles spheroid intramyocardial location. (E) Immunofluorescent staining of Matrigel dense regions of single cell and nanowired spheroids transplantation in myocardium on D1 indicate presence of troponin I (red) contractile protein in spheroid groups and minimal presence with HNA-positive cells (arrow) for single cell injection. Green-human nucleolar antigen (HNA); red-troponin I (TnI); blue-DAPI. (F) TUNEL staining (green) with high magnification inset of single cell injection sites (marked by Matrigel – asterisk) and nanowired spheroids on D1 post transplantation show a significantly reduced number of apoptotic cells in nanowired spheroid transplantation. Dotted line encircles spheroid intramyocardial location. Yellow-light scattered signal of

e-SiNWs, blue – DAPI nuclear stain. Scale bars: (D) top=50 μm, bottom= 100 μm; (E)= 50 μm; (F)= 50 μm.

The hearts were harvested on 1 day post-transplantation for histological analysis to examine spheroid retention and survival. Intramyocardial injections of dissociated hiPSC-CMs in Matrigel were used as a control [104]. As shown in Figure 5.10 D-E, the nanowired spheroids, identified by human nucleolar antigen (HNA) staining, did not dissociate upon injection and maintained their spherical shaped microtissue configuration after transplantation into beating hearts, which gave rise to excellent cell retention. In contrast, very few HNA-positive hiPSC-CMs were found in the myocardium, when single hiPSC-CMs were injected with Matrigel (Figure 5.10 D-E; Figure 5.11). In addition, all of these HNA-positive cells showed negative TnI staining. Further, an increase in TUNEL positive cells was found at the dissociated hiPSC-CM injection sites located by Matrigel dense regions, while few TUNEL positive cells were found within and around the transplanted spheroids (Figure 5.10 F). Scarcity of viable hiPSC-CMs after injection of dissociated hiPSC-CMs is consistent with the literature and was attributed to injection-induced and/or anoikis-mediated cell death pathways [173]. The improved cell retention and survival of the nanowired spheroid injection was attributed to the enhanced 3D cell-cell adhesion and stable microtissue configuration to better resist redistribution caused by the mechanical stress of the beating heart.

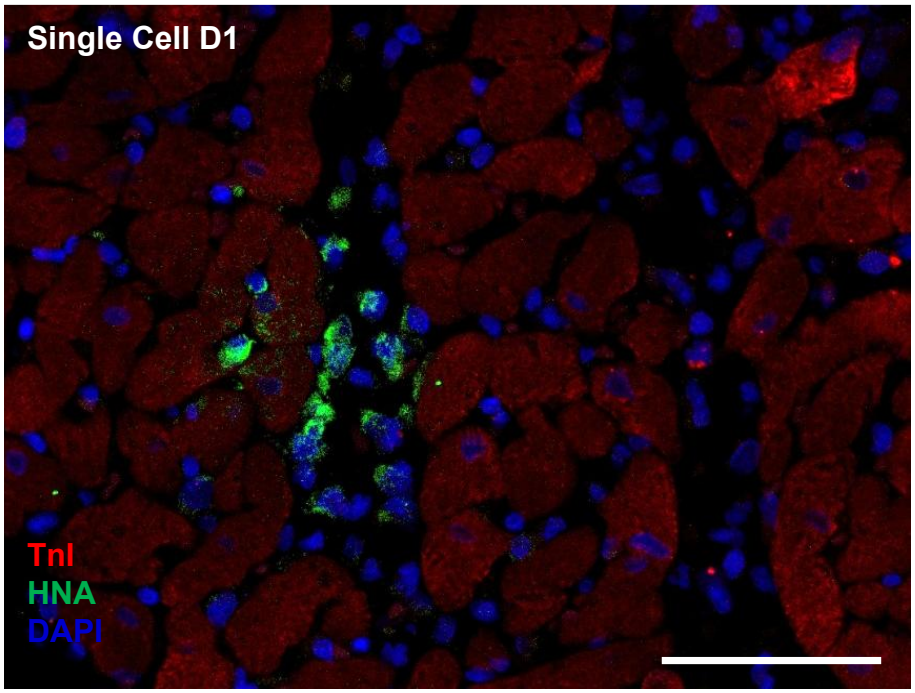

Figure 5.11: Limited cell retention using single hiPSC-CMs injection with Matrigel. Immunofluorescent staining of single cell injection on D1 post-transplantation in myocardium indicate presence of a small amount of human nucleolar antigen-positive cells that lack troponin I (red) contractile protein expression. Green-human nucleolar antigen (HNA); red-myocardium marker (troponin I); blue-DAPI. Scale bar = 50 μm

By 7 days post-transplantation, the injected nanowired spheroids showed excellent cellular engraftment (Figure 5.12). Compared with day 1 grafts, the day 7 grafts showed strong evidence of alignment with the host myocardium (Figure 5.12 A-B) and development of sarcomere structures (Figure 5.12A, C). The graft alignment with the host myocardium indicated that the grafts adapted to the local electrical/mechanical stimuli after transplantation. Alignment also serves as a structural foundation for the mechanical graft-host integration, supported by the improved expression and organization of contractile proteins in day 7 grafts. Together with no detection of arrhythmia (Figure

5.10 A), these results suggest the possibility of contractile integration of the transplanted spheroids with host myocardium.

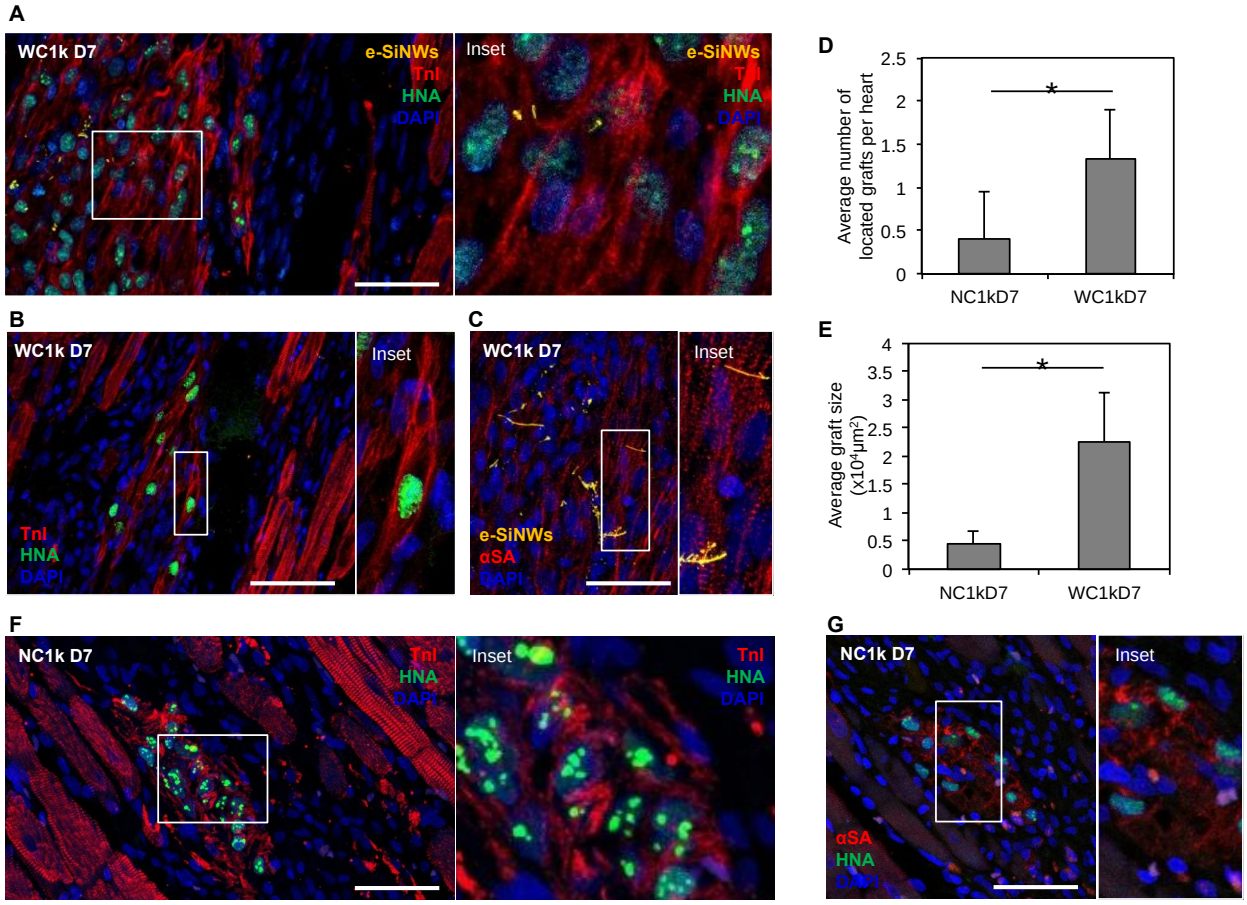

Figure 5.12: Nanowired spheroid transplantation improves the cell alignment and structural maturation. (A) Confocal images of the engraftment in rat myocardium on D7 for nanowired spheroids (WC1k) transplantation. Insets (right) reveal improved contractile development in nanowired spheroid grafts. Green-human nucleolar antigen (HNA); red-troponin I (TnI); yellow-e-SiNWs; blue-DAPI. (B) WC1k graft sections displayed aligned single cells from nanowired spheroids with host myocardium. Green-HNA; red-TnI; blue-DAPI. (C) WC1k spheroid grafts stained with alpha sarcomeric actinin (αSA) staining reveal sarcomere development by D7. (D) Average grafts per heart for unwired spheroids (NC1k) and nanowired spheroids (WC1k) transplantation calculated as number of slides per heart (observed using 30-40 total slides per heart) with visible grafts (N=5 rats, total of ~150 observed slides). (E) Average size of grafts in heart for NC1k and WC1k spheroids transplantation reveal increased graft size in WC1k treatment. (N=5 rats). Confocal imaging showed that NC1k grafts with poorly developed

contractile structure identified by TnI (F) and αSA (G) staining. Green-HNA; blue-DAPI. Scale bars: (A-C)= 50 μm; (F-G) = 50 μm. Asterisks (*) represent statistical significance with $p<0.05$; error bars represent standard deviation.

Notably, significantly less (Figure 5.12 D) and smaller (Figure 5.12 E) grafts have been found after the transplantation of unwired spheroids. Compared to the nanowired spheroids, the transplantation of the unwired spheroids led to the less developed contractile proteins (Figure 5.12F-G). In some cases, no detectable expression of contractile proteins was found for the unwired spheroid grafts (Figure 5.13). This difference strongly suggests the e-SiNWs in the spheroids can facilitate the electromechanical integration with the host myocardium. It is worth to note that we can reliably detect hiPSC-CM grafts with the nanowired spheroid injection of ~30k hiPSC-CMs/rat, whereas the literature uses ~5 million dissociated hESC-CMs/rat to detect hESC-CM engraftment in healthy myocardium [173]. This highlights the remarkable potential of using nanowired hiPSC cardiac spheroids as a cell delivery system for heart repair.

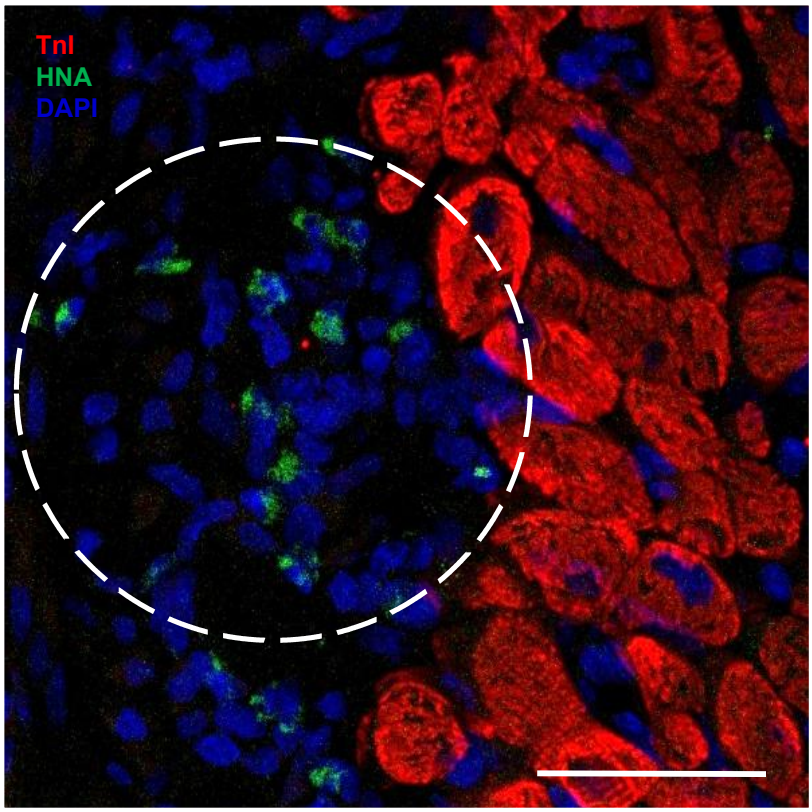

Figure 5.13: The unwired spheroids lose the cardiac phenotype identified by negative staining for troponin I by D7 post-transplantation. Confocal imaging showed that some NC1k grafts show no troponin I contractile protein staining. Green-human nucleolar antigen (HNA); red-troponin I; blue-DAPI. Scale bars: 50 μm.

By 28 days post-transplantation, nanowired hiPSC cardiac spheroids showed strong evidence of functional integration with host myocardium. As shown in Figure 5.14 A-C, nanowired spheroids have shifted from the original spherical shape on day 1 post-injection to a cardiac muscle bundle-like structure on day 28 post-injection. This indicates that the spherical configuration of nanowired hiPSC spheroid microtissues does not prevent alignment with the host myocardium after transplantation and suggests functional integration. This was further supported by histological analysis showing the

formation of electrical cellular junctions, Cx-43 (Figure 5.14 D), and mechanical cellular junctions, N-cad (Figure 5.14 E), between the transplanted spheroids and host myocardium. In addition, Isolectin B4 staining revealed capillary-like lumen structures that contained blood cells within the day 28 spheroids grafts (Figure 5.14 F). As the transplanted spheroids do not contain endothelial cells, this demonstrated the infiltration of the host vasculature into the transplanted spheroid grafts. Together, these results provided strong evidence that the electromechanical stimuli of host myocardium can effectively condition transplanted nanowired spheroids and facilitate electrical, mechanical, and vascular integration of the injected nanowired spheroids with the host myocardium by 28 days after transplantation.

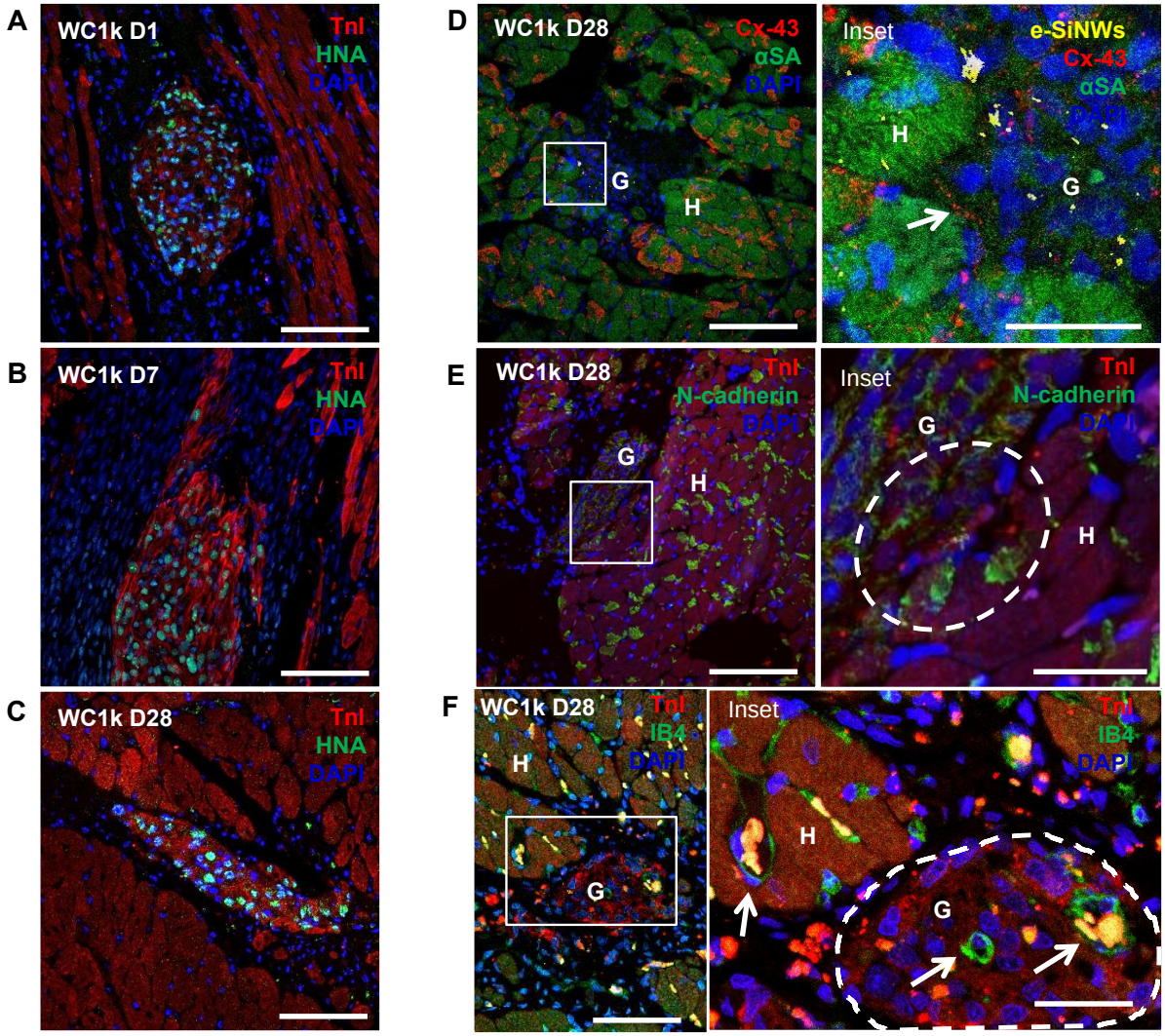

Figure 5.14: Nanowired spheroid transplantation improves functional integration with rat host myocardium. (A-C) Confocal images of nanowired spheroid grafts in rat myocardium at D1, D7 and D28 post-transplantation display adaptation and alignment of spherical microtissue over time. Green-human nucleolar antigen (HNA); red-troponin I (TnI); blue-DAPI. (D-F) Nanowired spheroid grafts integrate with host myocardium. The D28 post transplantation sample shows the presence of connexin-43 (Cx-43) staining (D) for graft-host gap junctions formation and N-cadherin staining (E) for mechanical integration between graft and host myocardium. Isolectin B4 (IB4) staining (F) shows capillary-like structures (arrow) with blood cells within the nanowired spheroid graft. Blood cells are identified by unspecific staining with TnI and IB4 (orange). Scale bars: (A-C)= 100 µm; (D-F) =100 µm, inset = 25µm.

As recent research has shown that chronic fibrosis can prevent electrical integration between the transplanted hiPSC-CMs epicardial patches and the host myocardium [182], we examined the fibrosis around the transplanted nanowired spheroids. As shown in the Figure 5.15, we observed minimal fibrosis on day 1, high fibrosis on day 7 and decreased fibrosis on day 28 post-injection. We reasoned that the reduced fibrosis around the day 28 grafts allowed for the formation of electrical and contractile integration of the grafts with host myocardium shown in the Figure 7. Notably, few e-SiNWs were found in the nanowired spheroid graft 28 days post-injection, which is consistent with the results from the e-SiNW intramyocardial injection experiments (Figure 5.7 A-B). The e-SiNWs in the day 28 grafts (Figure 5.14 D inset) are significantly smaller than the e-SiNWs in the day 1 graft (Figure 10 F inset), which has been attributed to the biodegradation of e-SiNWs [246].

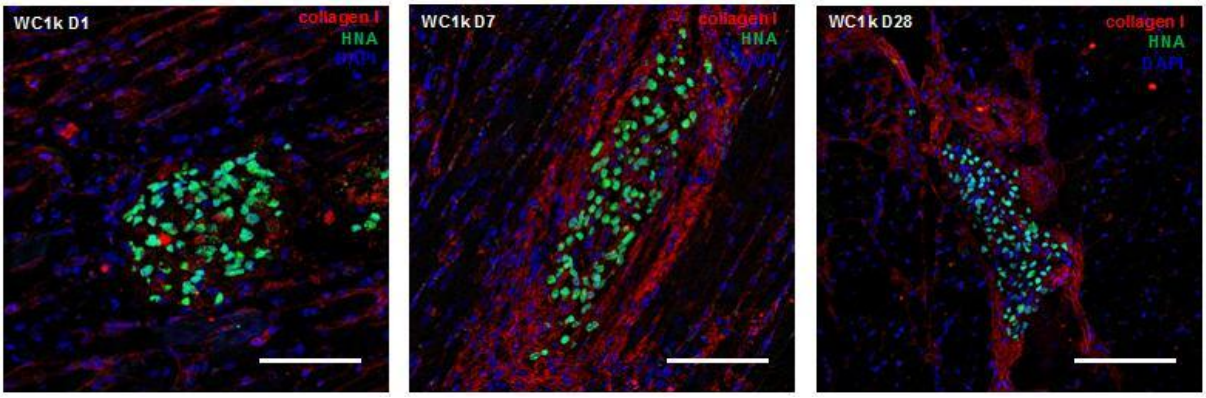

Figure 5.15: The fibrosis decreases on day 28 post nanowired spheroids transplantation. Collagen I staining (red) of human engraftment in rat myocardium with nanowired spheroids transplantation on D1, D7 and D28 post-transplantation indicated typical short term increase in fibrotic response that decreases by D28 for improved integration. Scale bars: 100 μm.

5. Discussion

In this study, we examined the cardiac biocompatibility of the e-SiNWs and cell retention, engraftment and integration after the injection of the nanowired hiPSC cardiac spheroids into adult rat hearts. The absence of major cell death or chronic inflammation/fibrosis from the e-SiNW intramyocardial injection indicated their high cardiac biocompatibility and is consistent with recent work by Zimmerman and coworkers demonstrating the biological interactions with SiNWs [196]. The observed cardiac functional biocompatibility of e-SiNWs seen by healthy ECG and echocardiogram characteristics was in line with previous studies using conductive nanomaterials in the heart [146]. The high cardiac compatibility of e-SiNWs supports the in vivo use of nanowired hiPSC cardiac spheroids for transplantation.

To this end, nanowired spheroids were then injected into rat hearts that led to the enhanced electrical/mechanical/vascular integration with the host tissue in contrast with single hiPSC-CM and unwired spheroid injections. We reasoned that the improvements seen in the nanowired spheroids treatment are partially due to the enhanced microtissue formation and maturation prior to transplantation [148]. Microtissue formation and maturation over 7 days in an in vitro spheroid culture allows for the development of cell-cell and cell-matrix interactions, which improved the cellular delivery, retention, and engraftment of spheroid injection. Although Matrigel provides a matrix/growth factor enriched microenvironment for dissociated hiPSC-CMs to reduce anoikis-related apoptosis and shear force-induced cell death from intramyocardial injection, our study has shown that the nanowired spheroids can better support cell viability and significantly

reduce the risk of these common cellular injection challenges [181]. Notably, even with the formation and maturation of spherical cardiac microtissues prior to transplantation, the nanowired spheroids did not inhibit adaptation and alignment with the host myocardium after transplantation. This directly addresses concerns over the suitability of the nanowired hiPSC spheroids based on the pre-alignment criteria.

In addition to alignment, nanowired spheroids showed significantly improved cellular integration and contractile development than single cell hiPSC-CM injections and unwired cardiac spheroid injections. The high electrical conductivity of e-SiNWs (150 - 500 µS/µm) in cardiac spheroids may lead to an enhanced ability to receive exogenous electromechanical pacing signals to initiate simultaneous contraction with the host myocardium. This was supported by the banded sarcomeric structures in the nanowired spheroid grafts. In comparison, the unwired spheroid grafts showed significantly less sarcomere development. Further, our recent report showed that e-SiNWs are essential for the use of electrical stimulation to promote contractile development of hiPSC cardiac spheroids [190]. In addition, previous studies have shown that the addition of electrically conductive gold nanowires to electrically insulating alginate hydrogels improves the range of the electrical propagation under exogenous electrical stimulation [147]. This may indicate that the presence of electrically conductive nanowires in the spheroids may enhance graft-host electrical coupling for improved contractile mechanics throughout integration. In addition, our results showed the e-SiNWs in the nanowired spheroids degrades over 28 days after transplantation. As non-biodegradable electrical nanomaterials (e.g., carbon tubes) can permanently stay in the myocardium after

transplantation and pose arrhythmogenic risk by interfering with the innate electrical conduction system [146], the biodegradability of e-SiNWs makes them an ideal nanoscaffolding material to promote hiPSC-CMs engraftment and integration with host myocardium.

The previous studies have clearly showed that there are diverse sets of challenges facing cardiac cell therapy. Most notably, cell therapy approaches using hiPSC-CMs have consistently resulted in insufficient cell retention to effectively remuscularize injured heart models. However, the reason for low cell retention is confounded by numerous factors, such as anoikis-mediated cell death, inflammation, ischemic microenvironment and variation among different injured animals. In this study, we aimed to improve the fundamental understanding of improving hiPSC-CM cellular retention and integration. To minimize the additional injury-induced variables and to effectively evaluate our hypothesis on the cell retention and integration of nanowired spheroids, we used a healthy rat heart model with a stringent cell injection condition (~30k cells/rat). The healthy rat model provides an ideal model to compare treatment-induced differences in cell retention and integration. Our data showed the use of injectable microtissues improve cell retention, consistent with the previous studies. Further, our data showed the nanowired spheroids improvements in graft-host integration after transplantation over unwired spheroids or single cell injections due to the presence of e-SiNWs in the nanowired spheroids. Notably, injectable nanowired spheroids provide a minimally invasive approach to deliver tissue constructs and induce mild fibrosis as opposed to surgically transplanted epicardial patches [175, 182]. Further, the effective engraftment

and integration of the nanowired hiPSC cardiac spheroids with ~30k hiPSC-CMs/rat hearts clearly demonstrated its potential to cost-effectively deliver the large number of hiPSC-CMs needed to treat injured human hearts [170]. While future studies will focus on injecting nanowired spheroids into injured rat hearts to examine their therapeutic/functional efficacy, it should be noted that these nanowired hiPSC spheroids may still pose an arrhythmogenic risk after transplantation due to their spontaneous contractions (~0.5Hz) [153]. While this cannot be directly addressed in the rat model due to the anti-arrhythmogenic nature of rat heart [182], we plan to use extended conditioning strategies (e.g., exogenous electrical stimulation) to decrease the spontaneous beating of the nanowired spheroids with the goal of preparing electrically quiescent hiPSC cardiac spheroids for transplantation [180, 190].

CHAPTER SIX

OVERALL CONCLUSIONS AND FUTURE DIRECTIONS

1. Summary of my research

MI causes a significant amount (around 25%) of irreversible cardiac cells death within the LV myocardium. So far, current clinical interventions have shown to slow down the progression of heart failure, none of them can reverse this deleterious process and regenerate new myocardium to replace the necrotic regions of the LV. Recent researches on MI treatment are focusing on cell therapies aiming to reverse heart remodeling and reduce scar formation with transplantation of various stem/ progenitor/ terminally differentiated cells. Among all the cell types of cell therapies for MI treatment, hiPSCs have emerged as a more promising cell resource for heart repair due to their proven capacity to produce patient-specific functional hiPSC-CMs. In addition, recent progress in cardiac differentiation of hiPSCs allows for the derivation of a large number of hiPSC-CMs (>10^9 cells/patient) needed for cardiac repair.

1.1 Accelerate structural and contractile maturation of hiPSC-CMs in nanowired spheroids system

The immature phenotypes of hiPSC-CMs pose a potential risk for arrhythmogenicity in vivo, which could hamper host conducting system and functional integration of transplanted cardiomyocytes with the host myocardium. In the past decade, physical stimuli (e.g. electrical and mechanical stimulation) has been applied to advance the immature cardiomyocytes towards more matured phenotypes with more organized sarcomere structures (width, length and alignment) and unregulated expression level of

gap junction protein (Connexin-43). In order to mimic the electrically conductive properties of native myocardium, conductive nanomaterials (gold nanowires, carbon tubes) have been used as scaffolding materials to fabricate engineered cardiac tissue with stronger contractile and electrical properties for promoting cardiomyocyte maturation in vitro and in vivo. However, above mentioned gold or carbon based conductive nanomaterials are non-biodegradable, which may hold potential risk of arrhythmogenicity and chronic immune response induce by these permanently resident foreign materials in the heart.

For the first time, we incorporated a trace amount of e-SiNWs into rat-neonatal and hiPSC cardiac spheroids to create electrically conducting microenvironments and induce synchronized and enhanced contraction, which was shown to promote structural and contractile maturation. e-SiNWs were selected because of their controllable electrical conductivity, tunable dimensions, and convenient surface tailorability. Further, the recent research showed SiNWs are biodegradable, and their degradation products are found mainly in the form of $Si(OH)_4$ and are metabolically tolerant in vivo. This makes them advantageous over other non-biodegradable, electrically conductive nanomaterials (e.g., gold nanowires, carbon nanotubes and nanofibers), especially for potential in vivo applications. We demonstated that e-SiNWs could facilitate the self-assembly of hiPSC-CMs to form nanowired hiPSC cardiac spheroids and improve the functions of the microtissues, which lead to significantly more advanced cellular structural and contractile maturation of hiPSC-CMs in nanowired spheroids system.

1.2 Optimize the size of nanowired spheroids and confirm the critical role of electrical conductivity of e-SiNWs in improving the function of cardiac spheroids

We demonstrated that addition of e-SiNWs into the human cardiac spheroids creates an electrically conductive microenvironment and improves tissue function and cellular maturation of hiPSC cardiac spheroids. In addition, recent research has shown that cellular spheroids/aggregates improve cell retention and survival after transplantation due to their 3D microtissue configuration. In my research, we try to examine two major factors that can affect the functions of the nanowired human cardiac spheroids: (1) the number of cells per spheroid (i.e., size of the spheroids), and (2) the role of the electrical conductivity of the e-SiNWs in improving tissue functions of the spheroids.

The optimal cell number in the spheroids is affected by two competing factors: 1) the improved 3D cell-cell adhesion, and 2) the reduced oxygen supply to the center of spheroids with the increase of cell number. Firstly, we experimentally identified the optimal cell number in the spheroids and developed a semi-quantitative theory to explain the finding. The functional analysis of contraction amplitude, IHC analysis of contractile and conductive proteins, and metabolic investigation demonstrated that spheroids with 3k cells per spheroids maximize the beneficial effects of the 3D spheroid microenvironment. In our previous report, we showed the addition of e-SiNWs in the human cardiac spheroids improved cellular maturation and tissue function. However, the role of electrical conductivity of the e-SiNWs has not been examined. Secondly, we prepared three types of the spheroids: spheroids without the addition of nanowires, spheroids with the addition of phosphorus doped silicon nanowires (electrically conductive), and

undoped silicon nanowires (none electrically conductive). We studied the functions of these three different types of spheroids and confirmed the critical role of electrical conductivity of e-SiNWs in improving tissue functions of the hiPSC cardiac spheroids. Additionally, the electrical conductivity of silicon nanowires was confirmed to contribute to accelerate structural and functional development of hiPSC-CMs in spheroids.

1.3 Injected nanowired spheroids improve cell retention, survival, maturation, long term engraftment and functional integration with rat hearts

While most of research utilized direct injection of the dissociated hiPSC-CMs into the injured myocardium, the success of this single cell delivery is limited by low cell retention and survival after cell transplantation. Additionally, lack of cell-to-cell adhesion amongst single cells leads to cell death caused by anoikis and/or ischemia. To improve the efficiency of cell delivery, significant efforts have been devoted to the development of tissue-engineered epicardial patches. The cardiac patch provides a better method to deliver cardiac cells to the injured myocardium to achieve better outcomes such as higher cell retention and survival, larger and more controlled infarction area coverage, reduced LV remodeling post MI. However, regarding this invasive surgical procedure as patches transplantation, recent research has shown there is limited electrical integration between the transplanted patches and host myocardium, largely attributed to the chronic fibrotic response that occurs after transplantation. In addition, the human engraftment formed from transplanted patch is totally isolated from host tissue by fibrosis and it does not contribute to functional improvements in MI model. This highlights an urgent need to develop a less invasive delivery approach to improve the retention, engraftment and

integration of the transplanted hiPSC-CMs with the host myocardium upon transplantation.

hiPSC cardiac spheroids have been proposed as an attractive cell delivery system for heart repair, given the recent literature showing spheroid/aggregate delivery improves cellular retention and post transplantation survival as less invasive approach (injectable). To this end, we recently utilized e-SiNWs to facilitate the self-assembly of hiPSC-CMs to form nanowired hiPSC cardiac spheroids and improve the functions of the microtissues, resulting in significantly more advanced cellular structural and contractile maturation of hiPSC-CMs. Here we reasoned that the presence of the e-SiNWs in the injectable spheroids improves their ability to receive exogenous electromechanical pacing from the host myocardium and enhances their integration with host tissues post-transplantation. This theory was inspired by our recent finding that the addition of e-SiNWs in hiPSC-CM spheroids are essential for exogenous electrical stimulation/pacing to promote hiPSC-CM development and maturation. Furthermore, recent reports showed the presence of electrical nanomaterials (e.g., gold nanowires) in cardiac tissue engineering constructs synergizes with exogenous electrical pacing to improve the function of the constructs. Compared to other electrical nanomaterials (e.g. gold nanowires, carbon nanotubes), e-SiNWs have distinct advantages, including their controllable electrical conductivity, tunable dimensions, and convenient surface tailorability. Additionally, both *in vitro* and *in vivo* biocompatibility studies have shown no significant cytotoxic effects for either undoped or n-type e-SiNWs. Notably, the absence of a pre-aligned structure within the nanowired hiPSC cardiac spheroids has raised concerns over their suitability for

transplantation.

We examined the cardiac biocompatibility of the e-SiNWs and cell retention, engraftment and integration after the injection of the nanowired hiPSC cardiac spheroids into adult rat hearts. The absence of major cell death or chronic inflammation/fibrosis from the e-SiNW intramyocardial injection indicated their high cardiac biocompatibility, which supports the in vivo use of nanowired hiPSC cardiac spheroids for transplantation. More importantly, our research showed the injected nanowired spheroids improve cell retention, survival, maturation, long term engraftment and functional integration with the host tissue compared with single cell and unwired spheroid transplantation.

2. Challenges and limitations

Past literatures indicates that mammalian heart consists of 30% cardiomyocytes and 70% non-cardiomyocytes (cardiac fibroblasts, endothelial cells, smooth muscle cells) [281]. Cardiac fibroblasts (CFs) play a critical role in maintaining normal heart function and LV remodeling post MI. In addition, CFs significantly contribute to the synthesis and deposition of ECM, cell–cell communication affecting the electrophysiological properties, secretion of growth factors and cytokines, and angiogenesis in the heart [282]. The extra vascular cells (endothelial cells, smooth muscle cells) could provide necessary components for new blood vessels formation in vivo. However, there is only cardiomyocytes in our nanowired cardiac spheroids system, which may be not the optimal cell resource for transplantation. We plan to add non-cardiomyocytes (cardiac fibroblasts, endothelial cells, smooth muscle cells) in our nanowired cardiac spheroids system to achieve better therapeutic outcomes upon transplantation in MI models.

It should be noted that nanowired hiPSC spheroids may still pose an arrhythmogenic risk after transplantation due to their spontaneous contractions (~0.5Hz). While this cannot be directly addressed in the rat model due to the anti-arrhythmogenic nature of rat heart, we plan to use extended conditioning strategies (e.g., exogenous electrical stimulation) to decrease the spontaneous beating of the nanowired spheroids with the goal of preparing electrically quiescent hiPSC cardiac spheroids for transplantation.

3. Future directions

3.1 Application of cardiac regenerative medicine

The future studies will focus on injecting nanowired spheroids into injured rat hearts to examine their therapeutic/functional efficacy. We will create a MI model on athymic adult rats, and delivery the injectable nanowires cardiac spheroids into the infarcted rat heart to investigate 1) whether these cardiac spheroids can survive and form engraftment in the ischemic environment in rat MI model; 2) whether these cardiac spheroids can reduce the fibrosis in MI site and form functional integration with host myocardium to replace the damaged heart tissue; 3) whether these cardiac spheroids can improve the heart function evaluated by echo measurement. If we could reach our experiment goals, this will be the great advance in the cardiac regenerative medicine by combined application of nanomaterials (electrically conductive silicon based nanowires), stem cells (hiPSCs derived cardiomyocytes) and engineering methods (non-invasive 3D scaffold-free spheroid delivery).

3.2 Potential application in brain tissue regeneration

Persistent cell dysfunction and poor neural regenerative capabilities at the lesion site after ischemic stroke lead to the formation of a cavity that is associated with prolonged neurological impairment. Transplantation of stem cells represents a promising strategy to reconstruct the lesion cavity and promote tissue regeneration after ischemic stroke. Despite the advances in deriving hiPSCs into neurons and specific functional subtypes, the progress in demonstrating cell engraftment, improving angiogenesis and promoting the integration of the differentiated neurons with the host tissue is limited.

We have established nanowired hiPSC-derived cardiac spheroids as a less-invassive injectable appoach to deliver cardiomyocytes with enhanced cell retention, engraftment, and functional integration with rat host myocardium. Since stem cell therapies for the treatment of MI and ischemic stroke have similar issues need to be addressed, such as low cell survival, lack control of cell differentiation, and low cell maturation and integration with host tissue, I propose to develop a nanowired prevascularized neural spheroid (NPNS) system based on hiPSC-derived neural stem cells and endothelial cells and to deliver this NPNS for brain tissue regeneration after ischemic stroke. This project will establish a framework to support the survival, maturation, and integration of transplanted cells to treat stroke-damaged brain tissue.

The overall objective of this project is to develop NPNS as a unique cell delivery system to transplant hiPSC-derived neural/progenitor stem cells (NSCs) at the lesion site following ischemic stroke for neural regeneration. We will examine whether the hiPSC-derived neurons can display specific patterns of axonal projections and dendritic outgrowth, and whether they integrate functionally with the host synaptic circuitry. We

will optimize the ratio of e-SiNWs, hiPSC NSCs and hiPSC ECs in vitro. We will examine the survival, organization, differentiation, maturation, and integration of transplanted NPNS, and demonstrate advantages of NPNS in promoting structural repair and functional recovery of stroke-injured brain.

We hypothesize that the NPNS system consisting three key elements to maximize regeneration outcomes after transplantation in the animal model of middle cerebral artery occlusion (MCAO). The first element in NPNS is e-SiNWs, which offer distinct advantages as nanoscaffolding materials for conductive tissue engineering (heart and brain), including their controllable electrical conductivity, tunable dimensions, and convenient surface tailorability. The e-SiNWs in the NPVS is capable of receiving the host electrical signal to stimulate the differentiated cells from the transplanted hiPSC NSCs at the lesion site of MCAO and enhance the electrically integration of the regenerated neurons with the host tissue. The second element in NPNS is 3D spheroid mainly consist of hiPSC NSCs, which have capability to differentiate to neurons, astrocytes and oligodendrocytes for in vivo regeneration. The spheroids act as a bridge between traditional 2D cell culture and in vivo tissue because they mimic in vivo microenvironment with enhanced cell-cell and cell-ECM interaction, which lead to spheroid's resistance to anoikis-mediate cell death pathways after transplantation in vivo. The last element in NPNS is hiPSC derived endothelial cells, which could form vascular structures in vitro and in vivo to improve nutrients and oxygen supply to maintain the survival of hiPSC NSCs in long term in vivo.

REFERENCE

[1] G.A. Mensah, D.W. Brown, An overview of cardiovascular disease burden in the United States, Health Aff (Millwood) 26(1) (2007) 38-48.

[2] D. Mozaffarian, E.J. Benjamin, A.S. Go, D.K. Arnett, M.J. Blaha, M. Cushman, S. de Ferranti, J.P. Despres, H.J. Fullerton, V.J. Howard, M.D. Huffman, S.E. Judd, B.M. Kissela, D.T. Lackland, J.H. Lichtman, L.D. Lisabeth, S. Liu, R.H. Mackey, D.B. Matchar, D.K. McGuire, E.R. Mohler, 3rd, C.S. Moy, P. Muntner, M.E. Mussolino, K. Nasir, R.W. Neumar, G. Nichol, L. Palaniappan, D.K. Pandey, M.J. Reeves, C.J. Rodriguez, P.D. Sorlie, J. Stein, A. Towfighi, T.N. Turan, S.S. Virani, J.Z. Willey, D. Woo, R.W. Yeh, M.B. Turner, C. American Heart Association Statistics, S. Stroke Statistics, Heart disease and stroke statistics--2015 update: a report from the American Heart Association, Circulation 131(4) (2015) e29-322.

[3] Z.N. Hatmi, S. Tahvildari, A. Gafarzadeh Motlag, A. Sabouri Kashani, Prevalence of coronary artery disease risk factors in Iran: a population based survey, BMC Cardiovasc Disord 7 (2007) 32.

[4] M.A. Laflamme, S. Zbinden, S.E. Epstein, C.E. Murry, Cell-based therapy for myocardial ischemia and infarction: pathophysiological mechanisms, Annu Rev Pathol 2 (2007) 307-39.

[5] H. Watkins, M. Farrall, Genetic susceptibility to coronary artery disease: from promise to progress, Nat Rev Genet 7(3) (2006) 163-73.

[6] E.G. Nabel, E. Braunwald, A tale of coronary artery disease and myocardial infarction, N Engl J Med 366(1) (2012) 54-63.

[7] F.M. Hoffman, Outcomes and complications after heart transplantation: a review, J Cardiovasc Nurs 20(5 Suppl) (2005) S31-42.

[8] A. Aliabadi, A.B. Cochrane, A.O. Zuckermann, Current strategies and future trends in immunosuppression after heart transplantation, Curr Opin Organ Transplant 17(5) (2012) 540-5.

[9] P. Stiefel, D. Malehsa, C. Bara, M. Strueber, A. Haverich, C. Kugler, Symptom experiences in patients after heart transplantation, J Health Psychol 18(5) (2013) 680-92.

[10] M.R. Afzal, A. Samanta, Z.I. Shah, V. Jeevanantham, A. Abdel-Latif, E.K. Zuba-Surma, B. Dawn, Adult Bone Marrow Cell Therapy for Ischemic Heart Disease: Evidence and Insights From Randomized Controlled Trials, Circ Res 117(6) (2015) 558-75.

[11] S. Pascual-Gil, E. Garbayo, P. Diaz-Herraez, F. Prosper, M.J. Blanco-Prieto, Heart regeneration after myocardial infarction using synthetic biomaterials, J Control Release 203 (2015) 23-38.

[12] S.K. Sanganalmath, R. Bolli, Cell therapy for heart failure: a comprehensive overview of experimental and clinical studies, current challenges, and future directions, Circ Res 113(6) (2013) 810-34.

[13] V.F. Segers, R.T. Lee, Stem-cell therapy for cardiac disease, Nature 451(7181) (2008) 937-42.

[14] K. Zhu, C. Guo, Y. Xia, H. Lai, W. Yang, Y. Wang, D. Song, C. Wang, Transplantation of novel vascular endothelial growth factor gene delivery system manipulated skeletal myoblasts promote myocardial repair, Int J Cardiol 168(3) (2013) 2622-31.

[15] H.C. Ott, N. Bonaros, R. Marksteiner, D. Wolf, E. Margreiter, T. Schachner, G. Laufer, S. Hering, Combined transplantation of skeletal myoblasts and bone marrow stem cells for myocardial repair in rats, Eur J Cardiothorac Surg 25(4) (2004) 627-34.

[16] D. Marelli, C. Desrosiers, M. el-Alfy, R.L. Kao, R.C. Chiu, Cell transplantation for myocardial repair: an experimental approach, Cell Transplant 1(6) (1992) 383-90.

[17] K. Tambara, Y. Sakakibara, G. Sakaguchi, F. Lu, G.U. Premaratne, X. Lin, K. Nishimura, M. Komeda, Transplanted skeletal myoblasts can fully replace the infarcted myocardium when they survive in the host in large numbers, Circulation 108 Suppl 1 (2003) II259-63.

[18] H. Reinecke, G.H. MacDonald, S.D. Hauschka, C.E. Murry, Electromechanical coupling between skeletal and cardiac muscle. Implications for infarct repair, J Cell Biol 149(3) (2000) 731-40.

[19] B. Leobon, I. Garcin, P. Menasche, J.T. Vilquin, E. Audinat, S. Charpak, Myoblasts transplanted into rat infarcted myocardium are functionally isolated from their host, Proc Natl Acad Sci U S A 100(13) (2003) 7808-11.

[20] K.G. Oldroyd, C. Berry, J. Bartunek, Myocardial repair and regeneration: bone marrow or cardiac stem cells?, Mol Ther 20(6) (2012) 1102-5.

[21] K.A. Jackson, S.M. Majka, H. Wang, J. Pocius, C.J. Hartley, M.W. Majesky, M.L. Entman, L.H. Michael, K.K. Hirschi, M.A. Goodell, Regeneration of ischemic cardiac muscle and vascular endothelium by adult stem cells, J Clin Invest 107(11) (2001) 1395-402.

[22] Scientists repair damage from heart attack using adult bone marrow stem cells in mice, J Am Coll Surg 192(6) (2001) 806.

[23] D. Galli, A. Innocenzi, L. Staszewsky, L. Zanetta, M. Sampaolesi, A. Bai, E. Martinoli, E. Carlo, G. Balconi, F. Fiordaliso, S. Chimenti, G. Cusella, E. Dejana, G. Cossu, R. Latini, Mesoangioblasts, vessel-associated multipotent stem cells, repair the infarcted heart by multiple cellular mechanisms: a comparison with bone marrow progenitors, fibroblasts, and endothelial cells, Arterioscler Thromb Vasc Biol 25(4) (2005) 692-7.

[24] N. Lee, T. Thorne, D.W. Losordo, Y.S. Yoon, Repair of ischemic heart disease with novel bone marrow-derived multipotent stem cells, Cell Cycle 4(7) (2005) 861-4.

[25] J.S. Da Silva, J.M. Hare, Cell-based therapies for myocardial repair: emerging role for bone marrow-derived mesenchymal stem cells (MSCs) in the treatment of the chronically injured heart, Methods Mol Biol 1037 (2013) 145-63.

[26] S. Apostolakis, G.Y. Lip, E. Shantsila, Monocytes in heart failure: relationship to a deteriorating immune overreaction or a desperate attempt for tissue repair?, Cardiovasc Res 85(4) (2010) 649-60.

[27] A. Deten, H.C. Volz, S. Clamors, S. Leiblein, W. Briest, G. Marx, H.G. Zimmer, Hematopoietic stem cells do not repair the infarcted mouse heart, Cardiovasc Res 65(1) (2005) 52-63.

[28] D. Orlic, J. Kajstura, S. Chimenti, I. Jakoniuk, S.M. Anderson, B. Li, J. Pickel, R. McKay, B. Nadal-Ginard, D.M. Bodine, A. Leri, P. Anversa, Bone marrow cells regenerate infarcted myocardium, Nature 410(6829) (2001) 701-5.

[29] B. Vrtovec, G. Poglajen, L. Lezaic, M. Sever, D. Domanovic, P. Cernelc, A. Socan, S. Schrepfer, G. Torre-Amione, F. Haddad, J.C. Wu, Effects of intracoronary CD34+ stem cell transplantation in nonischemic dilated cardiomyopathy patients: 5-year follow-up, Circ Res 112(1) (2013) 165-73.

[30] B. Vrtovec, G. Poglajen, M. Sever, L. Lezaic, D. Domanovic, P. Cernelc, F. Haddad, G. Torre-Amione, Effects of intracoronary stem cell transplantation in patients with dilated cardiomyopathy, J Card Fail 17(4) (2011) 272-81.

[31] J.M. Nygren, S. Jovinge, M. Breitbach, P. Sawen, W. Roll, J. Hescheler, J. Taneera, B.K. Fleischmann, S.E. Jacobsen, Bone marrow-derived hematopoietic cells generate cardiomyocytes at a low frequency through cell fusion, but not transdifferentiation, Nat Med 10(5) (2004) 494-501.

[32] C.E. Murry, M.H. Soonpaa, H. Reinecke, H. Nakajima, H.O. Nakajima, M. Rubart, K.B. Pasumarthi, J.I. Virag, S.H. Bartelmez, V. Poppa, G. Bradford, J.D. Dowell, D.A.

Williams, L.J. Field, Haematopoietic stem cells do not transdifferentiate into cardiac myocytes in myocardial infarcts, Nature 428(6983) (2004) 664-8.

[33] L.B. Balsam, A.J. Wagers, J.L. Christensen, T. Kofidis, I.L. Weissman, R.C. Robbins, Haematopoietic stem cells adopt mature haematopoietic fates in ischaemic myocardium, Nature 428(6983) (2004) 668-73.

[34] J. Rehman, J. Li, C.M. Orschell, K.L. March, Peripheral blood "endothelial progenitor cells" are derived from monocyte/macrophages and secrete angiogenic growth factors, Circulation 107(8) (2003) 1164-9.

[35] C. Kalka, H. Masuda, T. Takahashi, W.M. Kalka-Moll, M. Silver, M. Kearney, T. Li, J.M. Isner, T. Asahara, Transplantation of ex vivo expanded endothelial progenitor cells for therapeutic neovascularization, Proc Natl Acad Sci U S A 97(7) (2000) 3422-7.

[36] G.F. Zhao, Y.C. Fan, X.J. Jiang, [Effects of the proliferation state of the endothelial progenitor cells preconditioned with salvianolic acid B and bone marrow mesenchymal stem cells transplanted in acute myocardial infarction rats], Zhongguo Zhong Xi Yi Jie He Za Zhi 32(5) (2012) 671-5.

[37] H.Q. Li, Q. Zhao, D. Zhu, J. Liu, X.F. Ye, [Transplantation of bone marrow-derived endothelial progenitor cells preconditioned with ex vivo 17beta-estradiol enhances healing efficacy after acute myocardial infarction], Zhonghua Xin Xue Guan Bing Za Zhi 39(5) (2011) 420-3.

[38] Z. Xin, W. Meng, H. Ya-Ping, Z. Wei, Different biological properties of circulating and bone marrow endothelial progenitor cells in acute myocardial infarction rats, Thorac Cardiovasc Surg 56(8) (2008) 441-8.

[39] T. Thum, D. Fraccarollo, P. Galuppo, D. Tsikas, S. Frantz, G. Ertl, J. Bauersachs, Bone marrow molecular alterations after myocardial infarction: Impact on endothelial progenitor cells, Cardiovasc Res 70(1) (2006) 50-60.

[40] M.F. Pittenger, A.M. Mackay, S.C. Beck, R.K. Jaiswal, R. Douglas, J.D. Mosca, M.A. Moorman, D.W. Simonetti, S. Craig, D.R. Marshak, Multilineage potential of adult human mesenchymal stem cells, Science 284(5411) (1999) 143-7.

[41] C. Toma, M.F. Pittenger, K.S. Cahill, B.J. Byrne, P.D. Kessler, Human mesenchymal stem cells differentiate to a cardiomyocyte phenotype in the adult murine heart, Circulation 105(1) (2002) 93-8.

[42] H. Reinecke, E. Minami, W.Z. Zhu, M.A. Laflamme, Cardiogenic differentiation and transdifferentiation of progenitor cells, Circ Res 103(10) (2008) 1058-71.

[43] J.C. Garbern, R.T. Lee, Cardiac stem cell therapy and the promise of heart regeneration, Cell Stem Cell 12(6) (2013) 689-98.

[44] S.M. Wu, Y. Fujiwara, S.M. Cibulsky, D.E. Clapham, C.L. Lien, T.M. Schultheiss, S.H. Orkin, Developmental origin of a bipotential myocardial and smooth muscle cell precursor in the mammalian heart, Cell 127(6) (2006) 1137-50.

[45] A. Moretti, L. Caron, A. Nakano, J.T. Lam, A. Bernshausen, Y. Chen, Y. Qyang, L. Bu, M. Sasaki, S. Martin-Puig, Y. Sun, S.M. Evans, K.L. Laugwitz, K.R. Chien, Multipotent embryonic isl1+ progenitor cells lead to cardiac, smooth muscle, and endothelial cell diversification, Cell 127(6) (2006) 1151-65.

[46] A.P. Beltrami, L. Barlucchi, D. Torella, M. Baker, F. Limana, S. Chimenti, H. Kasahara, M. Rota, E. Musso, K. Urbanek, A. Leri, J. Kajstura, B. Nadal-Ginard, P. Anversa, Adult cardiac stem cells are multipotent and support myocardial regeneration, Cell 114(6) (2003) 763-76.

[47] L. Barile, I. Chimenti, R. Gaetani, E. Forte, F. Miraldi, G. Frati, E. Messina, A. Giacomello, Cardiac stem cells: isolation, expansion and experimental use for myocardial regeneration, Nat Clin Pract Cardiovasc Med 4 Suppl 1 (2007) S9-S14.

[48] W. Van't Hof, N. Mal, Y. Huang, M. Zhang, Z. Popovic, F. Forudi, R. Deans, M.S. Penn, Direct delivery of syngeneic and allogeneic large-scale expanded multipotent adult progenitor cells improves cardiac function after myocardial infarct, Cytotherapy 9(5) (2007) 477-87.

[49] R. Karra, S.M. Wu, Multipotent stem cells in cardiac regenerative therapy, Regen Med 3(2) (2008) 189-98.

[50] W.C. Chen, J.E. Baily, M. Corselli, M.E. Diaz, B. Sun, G. Xiang, G.A. Gray, J. Huard, B. Peault, Human myocardial pericytes: multipotent mesodermal precursors exhibiting cardiac specificity, Stem Cells 33(2) (2015) 557-73.

[51] S.E. Senyo, M.L. Steinhauser, C.L. Pizzimenti, V.K. Yang, L. Cai, M. Wang, T.D. Wu, J.L. Guerquin-Kern, C.P. Lechene, R.T. Lee, Mammalian heart renewal by pre-existing cardiomyocytes, Nature 493(7432) (2013) 433-6.

[52] Y. Nakada, D.C. Canseco, S. Thet, S. Abdisalaam, A. Asaithamby, C.X. Santos, A.M. Shah, H. Zhang, J.E. Faber, M.T. Kinter, L.I. Szweda, C. Xing, Z. Hu, R.J. Deberardinis, G. Schiattarella, J.A. Hill, O. Oz, Z. Lu, C.C. Zhang, W. Kimura, H.A. Sadek, Hypoxia induces heart regeneration in adult mice, Nature 541(7636) (2017) 222-227.

[53] J.O. Oberpriller, J.C. Oberpriller, Response of the adult newt ventricle to injury, J Exp Zool 187(2) (1974) 249-53.

[54] J.O. Oberpriller, J.C. Oberpriller, A.M. Arefyeva, V.I. Mitashov, B.M. Carlson, Nuclear characteristics of cardiac myocytes following the proliferative response to mincing of the myocardium in the adult newt, Notophthalmus viridescens, Cell Tissue Res 253(3) (1988) 619-24.

[55] M. Gemberling, R. Karra, A.L. Dickson, K.D. Poss, Nrg1 is an injury-induced cardiomyocyte mitogen for the endogenous heart regeneration program in zebrafish, Elife 4 (2015).

[56] C. Jopling, E. Sleep, M. Raya, M. Marti, A. Raya, J.C. Izpisua Belmonte, Zebrafish heart regeneration occurs by cardiomyocyte dedifferentiation and proliferation, Nature 464(7288) (2010) 606-9.

[57] R. Karra, A.K. Knecht, K. Kikuchi, K.D. Poss, Myocardial NF-kappaB activation is essential for zebrafish heart regeneration, Proc Natl Acad Sci U S A 112(43) (2015) 13255-60.

[58] E.R. Porrello, A.I. Mahmoud, E. Simpson, J.A. Hill, J.A. Richardson, E.N. Olson, H.A. Sadek, Transient regenerative potential of the neonatal mouse heart, Science 331(6020) (2011) 1078-80.

[59] O. Bergmann, R.D. Bhardwaj, S. Bernard, S. Zdunek, F. Barnabe-Heider, S. Walsh, J. Zupicich, K. Alkass, B.A. Buchholz, H. Druid, S. Jovinge, J. Frisen, Evidence for cardiomyocyte renewal in humans, Science 324(5923) (2009) 98-102.

[60] J. Kajstura, N. Gurusamy, B. Ogorek, P. Goichberg, C. Clavo-Rondon, T. Hosoda, D. D'Amario, S. Bardelli, A.P. Beltrami, D. Cesselli, R. Bussani, F. del Monte, F. Quaini, M. Rota, C.A. Beltrami, B.A. Buchholz, A. Leri, P. Anversa, Myocyte turnover in the aging human heart, Circ Res 107(11) (2010) 1374-86.

[61] T.A. Deisher, Cardiac-derived stem cells, IDrugs 3(6) (2000) 649-53.

[62] A. Linke, P. Muller, D. Nurzynska, C. Casarsa, D. Torella, A. Nascimbene, C. Castaldo, S. Cascapera, M. Bohm, F. Quaini, K. Urbanek, A. Leri, T.H. Hintze, J. Kajstura, P. Anversa, Stem cells in the dog heart are self-renewing, clonogenic, and multipotent and regenerate infarcted myocardium, improving cardiac function, Proc Natl Acad Sci U S A 102(25) (2005) 8966-71.

[63] C. Bearzi, M. Rota, T. Hosoda, J. Tillmanns, A. Nascimbene, A. De Angelis, S. Yasuzawa-Amano, I. Trofimova, R.W. Siggins, N. Lecapitaine, S. Cascapera, A.P. Beltrami, D.A. D'Alessandro, E. Zias, F. Quaini, K. Urbanek, R.E. Michler, R. Bolli, J. Kajstura, A. Leri, P. Anversa, Human cardiac stem cells, Proc Natl Acad Sci U S A 104(35) (2007) 14068-73.

[64] C. Stamm, B. Nasseri, R. Hetzer, Cardiac stem cells in patients with ischaemic cardiomyopathy, Lancet 379(9819) (2012) 891; author reply 891-2.

[65] B. Dawn, A.B. Stein, K. Urbanek, M. Rota, B. Whang, R. Rastaldo, D. Torella, X.L. Tang, A. Rezazadeh, J. Kajstura, A. Leri, G. Hunt, J. Varma, S.D. Prabhu, P. Anversa, R. Bolli, Cardiac stem cells delivered intravascularly traverse the vessel barrier, regenerate infarcted myocardium, and improve cardiac function, Proc Natl Acad Sci U S A 102(10) (2005) 3766-71.

[66] K.M. Fischer, C.T. Cottage, W. Wu, S. Din, N.A. Gude, D. Avitabile, P. Quijada, B.L. Collins, J. Fransioli, M.A. Sussman, Enhancement of myocardial regeneration through genetic engineering of cardiac progenitor cells expressing Pim-1 kinase, Circulation 120(21) (2009) 2077-87.

[67] D. Angert, R.M. Berretta, H. Kubo, H. Zhang, X. Chen, W. Wang, B. Ogorek, M. Barbe, S.R. Houser, Repair of the injured adult heart involves new myocytes potentially derived from resident cardiac stem cells, Circ Res 108(10) (2011) 1226-37.

[68] Q. Li, Y. Guo, Q. Ou, N. Chen, W.J. Wu, F. Yuan, E. O'Brien, T. Wang, L. Luo, G.N. Hunt, X. Zhu, R. Bolli, Intracoronary administration of cardiac stem cells in mice: a new, improved technique for cell therapy in murine models, Basic Res Cardiol 106(5) (2011) 849-64.

[69] R. Bolli, A.R. Chugh, D. D'Amario, J.H. Loughran, M.F. Stoddard, S. Ikram, G.M. Beache, S.G. Wagner, A. Leri, T. Hosoda, F. Sanada, J.B. Elmore, P. Goichberg, D. Cappetta, N.K. Solankhi, I. Fahsah, D.G. Rokosh, M.S. Slaughter, J. Kajstura, P. Anversa, Cardiac stem cells in patients with ischaemic cardiomyopathy (SCIPIO): initial results of a randomised phase 1 trial, Lancet 378(9806) (2011) 1847-57.

[70] R.R. Makkar, R.R. Smith, K. Cheng, K. Malliaras, L.E. Thomson, D. Berman, L.S. Czer, L. Marban, A. Mendizabal, P.V. Johnston, S.D. Russell, K.H. Schuleri, A.C. Lardo, G. Gerstenblith, E. Marban, Intracoronary cardiosphere-derived cells for heart regeneration after myocardial infarction (CADUCEUS): a prospective, randomised phase 1 trial, Lancet 379(9819) (2012) 895-904.

[71] J. Ye, A. Boyle, H. Shih, R.E. Sievers, Y. Zhang, M. Prasad, H. Su, Y. Zhou, W. Grossman, H.S. Bernstein, Y. Yeghiazarians, Sca-1+ cardiosphere-derived cells are enriched for Isl1-expressing cardiac precursors and improve cardiac function after myocardial injury, PLoS One 7(1) (2012) e30329.

[72] M. Valente, D.S. Nascimento, A. Cumano, O.P. Pinto-do, Sca-1+ cardiac progenitor cells and heart-making: a critical synopsis, Stem Cells Dev 23(19) (2014) 2263-73.

[73] M.A. Goodell, K. Brose, G. Paradis, A.S. Conner, R.C. Mulligan, Isolation and functional properties of murine hematopoietic stem cells that are replicating in vivo, J Exp Med 183(4) (1996) 1797-806.

[74] O. Pfister, F. Mouquet, M. Jain, R. Summer, M. Helmes, A. Fine, W.S. Colucci, R. Liao, CD31- but Not CD31+ cardiac side population cells exhibit functional cardiomyogenic differentiation, Circ Res 97(1) (2005) 52-61.

[75] T. Oyama, T. Nagai, H. Wada, A.T. Naito, K. Matsuura, K. Iwanaga, T. Takahashi, M. Goto, Y. Mikami, N. Yasuda, H. Akazawa, A. Uezumi, S. Takeda, I. Komuro, Cardiac side population cells have a potential to migrate and differentiate into cardiomyocytes in vitro and in vivo, J Cell Biol 176(3) (2007) 329-41.

[76] J. Yoon, S.C. Choi, C.Y. Park, W.J. Shim, D.S. Lim, Cardiac side population cells exhibit endothelial differentiation potential, Exp Mol Med 39(5) (2007) 653-62.

[77] A. Yellamilli, J.H. van Berlo, The Role of Cardiac Side Population Cells in Cardiac Regeneration, Front Cell Dev Biol 4 (2016) 102.

[78] C.L. Cai, X. Liang, Y. Shi, P.H. Chu, S.L. Pfaff, J. Chen, S. Evans, Isl1 identifies a cardiac progenitor population that proliferates prior to differentiation and contributes a majority of cells to the heart, Dev Cell 5(6) (2003) 877-89.

[79] E. Cagavi, O. Bartulos, C.Y. Suh, B. Sun, Z. Yue, Z. Jiang, L. Yue, Y. Qyang, Functional cardiomyocytes derived from Isl1 cardiac progenitors via Bmp4 stimulation, PLoS One 9(12) (2014) e110752.

[80] V. Di Felice, G. Zummo, Stem cell populations in the heart and the role of Isl1 positive cells, Eur J Histochem 57(2) (2013) e14.

[81] R. Genead, C. Danielsson, A.B. Andersson, M. Corbascio, A. Franco-Cereceda, C. Sylven, K.H. Grinnemo, Islet-1 cells are cardiac progenitors present during the entire lifespan: from the embryonic stage to adulthood, Stem Cells Dev 19(10) (2010) 1601-15.

[82] E. Messina, L. De Angelis, G. Frati, S. Morrone, S. Chimenti, F. Fiordaliso, M. Salio, M. Battaglia, M.V. Latronico, M. Coletta, E. Vivarelli, L. Frati, G. Cossu, A. Giacomello, Isolation and expansion of adult cardiac stem cells from human and murine heart, Circ Res 95(9) (2004) 911-21.

[83] M.T. Hensley, J. de Andrade, B. Keene, K. Meurs, J. Tang, Z. Wang, T.G. Caranasos, J. Piedrahita, T.S. Li, K. Cheng, Cardiac regenerative potential of cardiosphere-derived cells from adult dog hearts, J Cell Mol Med 19(8) (2015) 1805-13.

[84] K. Cheng, K. Malliaras, T.S. Li, B. Sun, C. Houde, G. Galang, J. Smith, N. Matsushita, E. Marban, Magnetic enhancement of cell retention, engraftment, and

functional benefit after intracoronary delivery of cardiac-derived stem cells in a rat model of ischemia/reperfusion, Cell Transplant 21(6) (2012) 1121-35.

[85] S.T. Lee, A.J. White, S. Matsushita, K. Malliaras, C. Steenbergen, Y. Zhang, T.S. Li, J. Terrovitis, K. Yee, S. Simsir, R. Makkar, E. Marban, Intramyocardial injection of autologous cardiospheres or cardiosphere-derived cells preserves function and minimizes adverse ventricular remodeling in pigs with heart failure post-myocardial infarction, J Am Coll Cardiol 57(4) (2011) 455-65.

[86] K. Malliaras, Y. Zhang, J. Seinfeld, G. Galang, E. Tseliou, K. Cheng, B. Sun, M. Aminzadeh, E. Marban, Cardiomyocyte proliferation and progenitor cell recruitment underlie therapeutic regeneration after myocardial infarction in the adult mouse heart, EMBO Mol Med 5(2) (2013) 191-209.

[87] J.A. Thomson, J. Itskovitz-Eldor, S.S. Shapiro, M.A. Waknitz, J.J. Swiergiel, V.S. Marshall, J.M. Jones, Embryonic stem cell lines derived from human blastocysts, Science 282(5391) (1998) 1145-7.

[88] C. Mummery, Cardiomyocytes from human embryonic stem cells: more than heart repair alone, Bioessays 29(6) (2007) 572-9.

[89] D. Kumar, T.J. Kamp, M.M. LeWinter, Embryonic stem cells: differentiation into cardiomyocytes and potential for heart repair and regeneration, Coron Artery Dis 16(2) (2005) 111-6.

[90] J. Nussbaum, E. Minami, M.A. Laflamme, J.A. Virag, C.B. Ware, A. Masino, V. Muskheli, L. Pabon, H. Reinecke, C.E. Murry, Transplantation of undifferentiated murine embryonic stem cells in the heart: teratoma formation and immune response, FASEB J 21(7) (2007) 1345-57.

[91] K. Takahashi, S. Yamanaka, Induction of pluripotent stem cells from mouse embryonic and adult fibroblast cultures by defined factors, Cell 126(4) (2006) 663-76.

[92] T.J. Nelson, A. Martinez-Fernandez, S. Yamada, C. Perez-Terzic, Y. Ikeda, A. Terzic, Repair of acute myocardial infarction by human stemness factors induced pluripotent stem cells, Circulation 120(5) (2009) 408-16.

[93] X. Li, F. Zhang, G. Song, W. Gu, M. Chen, B. Yang, D. Li, D. Wang, K. Cao, Intramyocardial Injection of Pig Pluripotent Stem Cells Improves Left Ventricular Function and Perfusion: A Study in a Porcine Model of Acute Myocardial Infarction, PLoS One 8(6) (2013) e66688.

[94] Y. Zhang, D. Wang, M. Chen, B. Yang, F. Zhang, K. Cao, Intramyocardial transplantation of undifferentiated rat induced pluripotent stem cells causes tumorigenesis in the heart, PLoS One 6(4) (2011) e19012.

[95] M. Halbach, G. Peinkofer, S. Baumgartner, M. Maass, M. Wiedey, K. Neef, B. Krausgrill, D. Ladage, A. Fatima, T. Saric, J. Hescheler, J. Muller-Ehmsen, Electrophysiological integration and action potential properties of transplanted cardiomyocytes derived from induced pluripotent stem cells, Cardiovasc Res 100(3) (2013) 432-40.

[96] K. Miki, H. Uenaka, A. Saito, S. Miyagawa, T. Sakaguchi, T. Higuchi, T. Shimizu, T. Okano, S. Yamanaka, Y. Sawa, Bioengineered myocardium derived from induced pluripotent stem cells improves cardiac function and attenuates cardiac remodeling following chronic myocardial infarction in rats, Stem Cells Transl Med 1(5) (2012) 430-7.

[97] L. Zwi-Dantsis, I. Huber, M. Habib, A. Winterstern, A. Gepstein, G. Arbel, L. Gepstein, Derivation and cardiomyocyte differentiation of induced pluripotent stem cells from heart failure patients, Eur Heart J 34(21) (2013) 1575-86.

[98] A.J. Kanelidis, C. Premer, J. Lopez, W. Balkan, J.M. Hare, Route of Delivery Modulates the Efficacy of Mesenchymal Stem Cell Therapy for Myocardial Infarction: A Meta-Analysis of Preclinical Studies and Clinical Trials, Circ Res 120(7) (2017) 1139-1150.

[99] A.L. Huu, A. Paul, S. Prakash, D. Shum-Tim, Route of delivery, cell retention, and efficiency of polymeric microcapsules in cellular cardiomyoplasty, Methods Mol Biol 1036 (2013) 121-35.

[100] H. Hamdi, A. Furuta, V. Bellamy, A. Bel, E. Puymirat, S. Peyrard, O. Agbulut, P. Menasche, Cell delivery: intramyocardial injections or epicardial deposition? A head-to-head comparison, Ann Thorac Surg 87(4) (2009) 1196-203.

[101] S.J. Brunskill, C.J. Hyde, C.J. Doree, S.M. Watt, E. Martin-Rendon, Route of delivery and baseline left ventricular ejection fraction, key factors of bone-marrow-derived cell therapy for ischaemic heart disease, Eur J Heart Fail 11(9) (2009) 887-96.

[102] K. Lunde, S. Solheim, S. Aakhus, H. Arnesen, M. Abdelnoor, T. Egeland, K. Endresen, A. Ilebekk, A. Mangschau, J.G. Fjeld, H.J. Smith, E. Taraldsrud, H.K. Grogaard, R. Bjornerheim, M. Brekke, C. Muller, E. Hopp, A. Ragnarsson, J.E. Brinchmann, K. Forfang, Intracoronary injection of mononuclear bone marrow cells in acute myocardial infarction, N Engl J Med 355(12) (2006) 1199-209.

[103] E.C. Perin, H.F. Dohmann, R. Borojevic, S.A. Silva, A.L. Sousa, C.T. Mesquita, M.I. Rossi, A.C. Carvalho, H.S. Dutra, H.J. Dohmann, G.V. Silva, L. Belem, R. Vivacqua, F.O. Rangel, R. Esporcatte, Y.J. Geng, W.K. Vaughn, J.A. Assad, E.T. Mesquita, J.T. Willerson, Transendocardial, autologous bone marrow cell transplantation for severe, chronic ischemic heart failure, Circulation 107(18) (2003) 2294-302.

[104] M.A. Laflamme, K.Y. Chen, A.V. Naumova, V. Muskheli, J.A. Fugate, S.K. Dupras, H. Reinecke, C. Xu, M. Hassanipour, S. Police, C. O'Sullivan, L. Collins, Y. Chen, E. Minami, E.A. Gill, S. Ueno, C. Yuan, J. Gold, C.E. Murry, Cardiomyocytes derived from human embryonic stem cells in pro-survival factors enhance function of infarcted rat hearts, Nat Biotechnol 25(9) (2007) 1015-24.

[105] H. Reinecke, C.E. Murry, Taking the death toll after cardiomyocyte grafting: a reminder of the importance of quantitative biology, J Mol Cell Cardiol 34(3) (2002) 251-3.

[106] A.H. Reddi, C.B. Huggins, Influence of geometry of transplanted tooth and bone on transformation of fibroblasts, Proc Soc Exp Biol Med 143(3) (1973) 634-7.

[107] R. Sui, X. Liao, X. Zhou, Q. Tan, The current status of engineering myocardial tissue, Stem Cell Rev 7(1) (2011) 172-80.

[108] E. Kawahara, A. Mukai, Y. Oda, I. Nakanishi, T. Iwa, Left ventriculotomy of the heart: tissue repair and localization of collagen types I, II, III, IV, V, VI and fibronectin, Virchows Arch A Pathol Anat Histopathol 417(3) (1990) 229-36.

[109] K.L. Christman, H.H. Fok, R.E. Sievers, Q. Fang, R.J. Lee, Fibrin glue alone and skeletal myoblasts in a fibrin scaffold preserve cardiac function after myocardial infarction, Tissue Eng 10(3-4) (2004) 403-9.

[110] N. Landa, L. Miller, M.S. Feinberg, R. Holbova, M. Shachar, I. Freeman, S. Cohen, J. Leor, Effect of injectable alginate implant on cardiac remodeling and function after recent and old infarcts in rat, Circulation 117(11) (2008) 1388-96.

[111] M.N. Giraud, E. Ayuni, S. Cook, M. Siepe, T.P. Carrel, H.T. Tevaearai, Hydrogel-based engineered skeletal muscle grafts normalize heart function early after myocardial infarction, Artif Organs 32(9) (2008) 692-700.

[112] W.N. Lu, S.H. Lu, H.B. Wang, D.X. Li, C.M. Duan, Z.Q. Liu, T. Hao, W.J. He, B. Xu, Q. Fu, Y.C. Song, X.H. Xie, C.Y. Wang, Functional improvement of infarcted heart by co-injection of embryonic stem cells with temperature-responsive chitosan hydrogel, Tissue Eng Part A 15(6) (2009) 1437-47.

[113] M.P. Lutolf, J.A. Hubbell, Synthetic biomaterials as instructive extracellular microenvironments for morphogenesis in tissue engineering, Nat Biotechnol 23(1) (2005) 47-55.

[114] S. Dobner, D. Bezuidenhout, P. Govender, P. Zilla, N. Davies, A synthetic non-degradable polyethylene glycol hydrogel retards adverse post-infarct left ventricular remodeling, J Card Fail 15(7) (2009) 629-36.

[115] L. Klouda, Thermoresponsive hydrogels in biomedical applications: A seven-year update, Eur J Pharm Biopharm 97(Pt B) (2015) 338-49.

[116] D.M. Nelson, Z. Ma, K.L. Fujimoto, R. Hashizume, W.R. Wagner, Intra-myocardial biomaterial injection therapy in the treatment of heart failure: Materials, outcomes and challenges, Acta Biomater 7(1) (2011) 1-15.

[117] J.M. Singelyn, K.L. Christman, Injectable materials for the treatment of myocardial infarction and heart failure: the promise of decellularized matrices, J Cardiovasc Transl Res 3(5) (2010) 478-86.

[118] S.B. Seif-Naraghi, M.A. Salvatore, P.J. Schup-Magoffin, D.P. Hu, K.L. Christman, Design and characterization of an injectable pericardial matrix gel: a potentially autologous scaffold for cardiac tissue engineering, Tissue Eng Part A 16(6) (2010) 2017-27.

[119] S. Pok, I.V. Stupin, C. Tsao, R.G. Pautler, Y. Gao, R.M. Nieto, Z.W. Tao, C.D. Fraser, Jr., A.V. Annapragada, J.G. Jacot, Full-Thickness Heart Repair with an Engineered Multilayered Myocardial Patch in Rat Model, Adv Healthc Mater 6(5) (2017).

[120] N. Li, R. Huang, X. Zhang, Y. Xin, J. Li, Y. Huang, W. Cui, J.F. Stoltz, Y. Zhou, Q. Kong, Stem cells cardiac patch from decellularized umbilical artery improved heart function after myocardium infarction, Biomed Mater Eng 28(s1) (2017) S87-S94.

[121] J. Lancaster, E. Juneman, T. Hagerty, R. Do, M. Hicks, K. Meltzer, P. Standley, M. Gaballa, R. Kellar, S. Goldman, H. Thai, Viable fibroblast matrix patch induces angiogenesis and increases myocardial blood flow in heart failure after myocardial infarction, Tissue Eng Part A 16(10) (2010) 3065-73.

[122] J.S. Wendel, L. Ye, R. Tao, J. Zhang, J. Zhang, T.J. Kamp, R.T. Tranquillo, Functional Effects of a Tissue-Engineered Cardiac Patch From Human Induced Pluripotent Stem Cell-Derived Cardiomyocytes in a Rat Infarct Model, Stem Cells Transl Med 4(11) (2015) 1324-32.

[123] J. Riegler, M. Tiburcy, A. Ebert, E. Tzatzalos, U. Raaz, O.J. Abilez, Q. Shen, N.G. Kooreman, E. Neofytou, V.C. Chen, M. Wang, T. Meyer, P.S. Tsao, A.J. Connolly, L.A. Couture, J.D. Gold, W.H. Zimmermann, J.C. Wu, Human Engineered Heart Muscles Engraft and Survive Long Term in a Rodent Myocardial Infarction Model, Circ Res 117(8) (2015) 720-30.

[124] L. Ye, Y.H. Chang, Q. Xiong, P. Zhang, L. Zhang, P. Somasundaram, M. Lepley, C. Swingen, L. Su, J.S. Wendel, J. Guo, A. Jang, D. Rosenbush, L. Greder, J.R. Dutton, J. Zhang, T.J. Kamp, D.S. Kaufman, Y. Ge, J. Zhang, Cardiac repair in a porcine model

of acute myocardial infarction with human induced pluripotent stem cell-derived cardiovascular cells, Cell Stem Cell 15(6) (2014) 750-61.

[125] A. Kushida, M. Yamato, C. Konno, A. Kikuchi, Y. Sakurai, T. Okano, Decrease in culture temperature releases monolayer endothelial cell sheets together with deposited fibronectin matrix from temperature-responsive culture surfaces, J Biomed Mater Res 45(4) (1999) 355-62.

[126] T. Shimizu, H. Sekine, J. Yang, Y. Isoi, M. Yamato, A. Kikuchi, E. Kobayashi, T. Okano, Polysurgery of cell sheet grafts overcomes diffusion limits to produce thick, vascularized myocardial tissues, FASEB J 20(6) (2006) 708-10.

[127] Y. Miyahara, N. Nagaya, M. Kataoka, B. Yanagawa, K. Tanaka, H. Hao, K. Ishino, H. Ishida, T. Shimizu, K. Kangawa, S. Sano, T. Okano, S. Kitamura, H. Mori, Monolayered mesenchymal stem cells repair scarred myocardium after myocardial infarction, Nat Med 12(4) (2006) 459-65.

[128] S. Miyagawa, Y. Sawa, S. Sakakida, S. Taketani, H. Kondoh, I.A. Memon, Y. Imanishi, T. Shimizu, T. Okano, H. Matsuda, Tissue cardiomyoplasty using bioengineered contractile cardiomyocyte sheets to repair damaged myocardium: their integration with recipient myocardium, Transplantation 80(11) (2005) 1586-95.

[129] S. Masuda, T. Shimizu, M. Yamato, T. Okano, Cell sheet engineering for heart tissue repair, Adv Drug Deliv Rev 60(2) (2008) 277-85.

[130] H. Sekine, T. Shimizu, K. Sakaguchi, I. Dobashi, M. Wada, M. Yamato, E. Kobayashi, M. Umezu, T. Okano, In vitro fabrication of functional three-dimensional tissues with perfusable blood vessels, Nat Commun 4 (2013) 1399.

[131] Y. Petrenko, E. Sykova, S. Kubinova, The therapeutic potential of three-dimensional multipotent mesenchymal stromal cell spheroids, Stem Cell Res Ther 8(1) (2017) 94.

[132] S.H. Bhang, S. Lee, J.Y. Shin, T.J. Lee, B.S. Kim, Transplantation of cord blood mesenchymal stem cells as spheroids enhances vascularization, Tissue Eng Part A 18(19-20) (2012) 2138-47.

[133] Q. Zhang, A.L. Nguyen, S. Shi, C. Hill, P. Wilder-Smith, T.B. Krasieva, A.D. Le, Three-dimensional spheroid culture of human gingiva-derived mesenchymal stem cells enhances mitigation of chemotherapy-induced oral mucositis, Stem Cells Dev 21(6) (2012) 937-47.

[134] E.J. Lee, S.J. Park, S.K. Kang, G.H. Kim, H.J. Kang, S.W. Lee, H.B. Jeon, H.S. Kim, Spherical bullet formation via E-cadherin promotes therapeutic potency of

mesenchymal stem cells derived from human umbilical cord blood for myocardial infarction, Mol Ther 20(7) (2012) 1424-33.

[135] F. Oltolina, A. Zamperone, D. Colangelo, L. Gregoletto, S. Reano, S. Pietronave, S. Merlin, M. Talmon, E. Novelli, M. Diena, C. Nicoletti, A. Musaro, N. Filigheddu, A. Follenzi, M. Prat, Human Cardiac Progenitor Spheroids Exhibit Enhanced Engraftment Potential, PLoS One 10(9) (2015) e0137999.

[136] C.W. Don, C.E. Murry, Improving survival and efficacy of pluripotent stem cell-derived cardiac grafts, J Cell Mol Med 17(11) (2013) 1355-62.

[137] L.W. van Laake, R. Passier, J. Monshouwer-Kloots, A.J. Verkleij, D.J. Lips, C. Freund, K. den Ouden, D. Ward-van Oostwaard, J. Korving, L.G. Tertoolen, C.J. van Echteld, P.A. Doevendans, C.L. Mummery, Human embryonic stem cell-derived cardiomyocytes survive and mature in the mouse heart and transiently improve function after myocardial infarction, Stem Cell Res 1(1) (2007) 9-24.

[138] J. Muller-Ehmsen, P. Whittaker, R.A. Kloner, J.S. Dow, T. Sakoda, T.I. Long, P.W. Laird, L. Kedes, Survival and development of neonatal rat cardiomyocytes transplanted into adult myocardium, J Mol Cell Cardiol 34(2) (2002) 107-16.

[139] C.J. Teng, J. Luo, R.C. Chiu, D. Shum-Tim, Massive mechanical loss of microspheres with direct intramyocardial injection in the beating heart: implications for cellular cardiomyoplasty, J Thorac Cardiovasc Surg 132(3) (2006) 628-32.

[140] D. Hou, E.A. Youssef, T.J. Brinton, P. Zhang, P. Rogers, E.T. Price, A.C. Yeung, B.H. Johnstone, P.G. Yock, K.L. March, Radiolabeled cell distribution after intramyocardial, intracoronary, and interstitial retrograde coronary venous delivery: implications for current clinical trials, Circulation 112(9 Suppl) (2005) I150-6.

[141] W. Hudson, M.C. Collins, D. deFreitas, Y.S. Sun, B. Muller-Borer, A.P. Kypson, Beating and arrested intramyocardial injections are associated with significant mechanical loss: implications for cardiac cell transplantation, J Surg Res 142(2) (2007) 263-7.

[142] D.M. Bers, Cardiac excitation-contraction coupling, Nature 415(6868) (2002) 198-205.

[143] A.W. Feinberg, Engineered tissue grafts: opportunities and challenges in regenerative medicine, Wiley Interdiscip Rev Syst Biol Med 4(2) (2012) 207-20.

[144] Y. Shiba, T. Gomibuchi, T. Seto, Y. Wada, H. Ichimura, Y. Tanaka, T. Ogasawara, K. Okada, N. Shiba, K. Sakamoto, D. Ido, T. Shiina, M. Ohkura, J. Nakai, N. Uno, Y. Kazuki, M. Oshimura, I. Minami, U. Ikeda, Allogeneic transplantation of iPS cell-derived cardiomyocytes regenerates primate hearts, Nature 538(7625) (2016) 388-391.

[145] X. Yang, L. Pabon, C.E. Murry, Engineering adolescence: maturation of human pluripotent stem cell-derived cardiomyocytes, Circ Res 114(3) (2014) 511-23.

[146] J. Zhou, J. Chen, H. Sun, X. Qiu, Y. Mou, Z. Liu, Y. Zhao, X. Li, Y. Han, C. Duan, R. Tang, C. Wang, W. Zhong, J. Liu, Y. Luo, M. Mengqiu Xing, C. Wang, Engineering the heart: evaluation of conductive nanomaterials for improving implant integration and cardiac function, Sci Rep 4 (2014) 3733.

[147] T. Dvir, B.P. Timko, M.D. Brigham, S.R. Naik, S.S. Karajanagi, O. Levy, H. Jin, K.K. Parker, R. Langer, D.S. Kohane, Nanowired three-dimensional cardiac patches, Nat Nanotechnol 6(11) (2011) 720-5.

[148] Y. Tan, D. Richards, R. Xu, S. Stewart-Clark, S.K. Mani, T.K. Borg, D.R. Menick, B. Tian, Y. Mei, Silicon nanowire-induced maturation of cardiomyocytes derived from human induced pluripotent stem cells, Nano Lett 15(5) (2015) 2765-72.

[149] Y. Tan, D. Richards, R.C. Coyle, J. Yao, R. Xu, W. Gou, H. Wang, D.R. Menick, B. Tian, Y. Mei, Cell number per spheroid and electrical conductivity of nanowires influence the function of silicon nanowired human cardiac spheroids, Acta Biomater (2017).

[150] P.W. Burridge, D. Anderson, H. Priddle, M.D. Barbadillo Munoz, S. Chamberlain, C. Allegrucci, L.E. Young, C. Denning, Improved human embryonic stem cell embryoid body homogeneity and cardiomyocyte differentiation from a novel V-96 plate aggregation system highlights interline variability, Stem Cells 25(4) (2007) 929-38.

[151] E. Poon, C.W. Kong, R.A. Li, Human pluripotent stem cell-based approaches for myocardial repair: from the electrophysiological perspective, Mol Pharm 8(5) (2011) 1495-504.

[152] G. Arbel, O. Caspi, I. Huber, A. Gepstein, M. Weiler-Sagie, L. Gepstein, Methods for human embryonic stem cells derived cardiomyocytes cultivation, genetic manipulation, and transplantation, Methods Mol Biol 660 (2010) 85-95.

[153] J.J. Chong, X. Yang, C.W. Don, E. Minami, Y.W. Liu, J.J. Weyers, W.M. Mahoney, B. Van Biber, S.M. Cook, N.J. Palpant, J.A. Gantz, J.A. Fugate, V. Muskheli, G.M. Gough, K.W. Vogel, C.A. Astley, C.E. Hotchkiss, A. Baldessari, L. Pabon, H. Reinecke, E.A. Gill, V. Nelson, H.P. Kiem, M.A. Laflamme, C.E. Murry, Human embryonic-stem-cell-derived cardiomyocytes regenerate non-human primate hearts, Nature 510(7504) (2014) 273-7.

[154] I. Kehat, A. Gepstein, A. Spira, J. Itskovitz-Eldor, L. Gepstein, High-resolution electrophysiological assessment of human embryonic stem cell-derived cardiomyocytes: a novel in vitro model for the study of conduction, Circ Res 91(8) (2002) 659-61.

[155] F. Cao, S. Lin, X. Xie, P. Ray, M. Patel, X. Zhang, M. Drukker, S.J. Dylla, A.J. Connolly, X. Chen, I.L. Weissman, S.S. Gambhir, J.C. Wu, In vivo visualization of embryonic stem cell survival, proliferation, and migration after cardiac delivery, Circulation 113(7) (2006) 1005-14.

[156] X. Hu, J. Wang, J. Chen, R. Luo, A. He, X. Xie, J. Li, Optimal temporal delivery of bone marrow mesenchymal stem cells in rats with myocardial infarction, Eur J Cardiothorac Surg 31(3) (2007) 438-43.

[157] J. Muller-Ehmsen, B. Krausgrill, V. Burst, K. Schenk, U.C. Neisen, J.W. Fries, B.K. Fleischmann, J. Hescheler, R.H. Schwinger, Effective engraftment but poor mid-term persistence of mononuclear and mesenchymal bone marrow cells in acute and chronic rat myocardial infarction, J Mol Cell Cardiol 41(5) (2006) 876-84.

[158] P.V. Johnston, T. Sasano, K. Mills, R. Evers, S.T. Lee, R.R. Smith, A.C. Lardo, S. Lai, C. Steenbergen, G. Gerstenblith, R. Lange, E. Marban, Engraftment, differentiation, and functional benefits of autologous cardiosphere-derived cells in porcine ischemic cardiomyopathy, Circulation 120(12) (2009) 1075-83, 7 p following 1083.

[159] H. Hamamoto, J.H. Gorman, 3rd, L.P. Ryan, R. Hinmon, T.P. Martens, M.D. Schuster, T. Plappert, M. Kiupel, M.G. St John-Sutton, S. Itescu, R.C. Gorman, Allogeneic mesenchymal precursor cell therapy to limit remodeling after myocardial infarction: the effect of cell dosage, Ann Thorac Surg 87(3) (2009) 794-801.

[160] M.C. Keith, R. Bolli, "String theory" of c-kit(pos) cardiac cells: a new paradigm regarding the nature of these cells that may reconcile apparently discrepant results, Circ Res 116(7) (2015) 1216-30.

[161] S.A. Fisher, C. Doree, A. Mathur, E. Martin-Rendon, Meta-analysis of cell therapy trials for patients with heart failure, Circ Res 116(8) (2015) 1361-77.

[162] M. Gyongyosi, W. Wojakowski, P. Lemarchand, K. Lunde, M. Tendera, J. Bartunek, E. Marban, B. Assmus, T.D. Henry, J.H. Traverse, L.A. Moye, D. Surder, R. Corti, H. Huikuri, J. Miettinen, J. Wohrle, S. Obradovic, J. Roncalli, K. Malliaras, E. Pokushalov, A. Romanov, J. Kastrup, M.W. Bergmann, D.E. Atsma, A. Diederichsen, I. Edes, I. Benedek, T. Benedek, H. Pejkov, N. Nyolczas, N. Pavo, J. Bergler-Klein, I.J. Pavo, C. Sylven, S. Berti, E.P. Navarese, G. Maurer, A. Investigators, Meta-Analysis of Cell-based CaRdiac stUdiEs (ACCRUE) in patients with acute myocardial infarction based on individual patient data, Circ Res 116(8) (2015) 1346-60.

[163] Y. Guo, M. Wysoczynski, Y. Nong, A. Tomlin, X. Zhu, A.M. Gumpert, M. Nasr, S. Muthusamy, H. Li, M. Book, A. Khan, K.U. Hong, Q. Li, R. Bolli, Repeated doses of cardiac mesenchymal cells are therapeutically superior to a single dose in mice with old myocardial infarction, Basic Res Cardiol 112(2) (2017) 18.

[164] Y. Tokita, X.L. Tang, Q. Li, M. Wysoczynski, K.U. Hong, S. Nakamura, W.J. Wu, W. Xie, D. Li, G. Hunt, Q. Ou, H. Stowers, R. Bolli, Repeated Administrations of Cardiac Progenitor Cells Are Markedly More Effective Than a Single Administration: A New Paradigm in Cell Therapy, Circ Res 119(5) (2016) 635-51.

[165] M.N. Hirt, A. Hansen, T. Eschenhagen, Cardiac tissue engineering: state of the art, Circ Res 114(2) (2014) 354-67.

[166] B. Liau, D. Zhang, N. Bursac, Functional cardiac tissue engineering, Regen Med 7(2) (2012) 187-206.

[167] G. Vunjak-Novakovic, N. Tandon, A. Godier, R. Maidhof, A. Marsano, T.P. Martens, M. Radisic, Challenges in cardiac tissue engineering, Tissue Eng Part B Rev 16(2) (2010) 169-87.

[168] A.B. Prowse, N.E. Timmins, T.M. Yau, R.K. Li, R.D. Weisel, G. Keller, P.W. Zandstra, Transforming the promise of pluripotent stem cell-derived cardiomyocytes to a therapy: challenges and solutions for clinical trials, Can J Cardiol 30(11) (2014) 1335-49.

[169] L. Barad, R. Schick, N. Zeevi-Levin, J. Itskovitz-Eldor, O. Binah, Human embryonic stem cells vs human induced pluripotent stem cells for cardiac repair, Can J Cardiol 30(11) (2014) 1279-87.

[170] J.J. Chong, X. Yang, C.W. Don, E. Minami, Y.W. Liu, J.J. Weyers, W.M. Mahoney, B. Van Biber, N.J. Palpant, J.A. Gantz, J.A. Fugate, V. Muskheli, G.M. Gough, K.W. Vogel, C.A. Astley, C.E. Hotchkiss, A. Baldessari, L. Pabon, H. Reinecke, E.A. Gill, V. Nelson, H.P. Kiem, M.A. Laflamme, C.E. Murry, Human embryonic-stem-cell-derived cardiomyocytes regenerate non-human primate hearts, Nature (2014).

[171] X. Lian, C. Hsiao, G. Wilson, K. Zhu, L.B. Hazeltine, S.M. Azarin, K.K. Raval, J. Zhang, T.J. Kamp, S.P. Palecek, Robust cardiomyocyte differentiation from human pluripotent stem cells via temporal modulation of canonical Wnt signaling, Proceedings of the National Academy of Sciences of the United States of America (2012).

[172] P.W. Burridge, E. Matsa, P. Shukla, Z.C. Lin, J.M. Churko, A.D. Ebert, F. Lan, S. Diecke, B. Huber, N.M. Mordwinkin, J.R. Plews, O.J. Abilez, B. Cui, J.D. Gold, J.C. Wu, Chemically defined generation of human cardiomyocytes, Nat Methods 11(8) (2014) 855-60.

[173] M.A. Laflamme, J. Gold, C. Xu, M. Hassanipour, E. Rosler, S. Police, V. Muskheli, C.E. Murry, Formation of Human Myocardium in the Rat Heart from Human Embryonic Stem Cells, The American journal of pathology 167(3) (2005) 663-671.

[174] Y. Shiba, S. Fernandes, W.Z. Zhu, D. Filice, V. Muskheli, J. Kim, N.J. Palpant, J. Gantz, K.W. Moyes, H. Reinecke, B. Van Biber, T. Dardas, J.L. Mignone, A. Izawa, R.

Hanna, M. Viswanathan, J.D. Gold, M.I. Kotlikoff, N. Sarvazyan, M.W. Kay, C.E. Murry, M.A. Laflamme, Human ES-cell-derived cardiomyocytes electrically couple and suppress arrhythmias in injured hearts, Nature 489(7415) (2012) 322-5.

[175] K.R. Stevens, K.L. Kreutziger, S.K. Dupras, F.S. Korte, M. Regnier, V. Muskheli, M.B. Nourse, K. Bendixen, H. Reinecke, C.E. Murry, Physiological function and transplantation of scaffold-free and vascularized human cardiac muscle tissue, Proc Natl Acad Sci U S A 106(39) (2009) 16568-73.

[176] L.R. Madden, D.J. Mortisen, E.M. Sussman, S.K. Dupras, J.A. Fugate, J.L. Cuy, K.D. Hauch, M.A. Laflamme, C.E. Murry, B.D. Ratner, Proangiogenic scaffolds as functional templates for cardiac tissue engineering, Proc Natl Acad Sci U S A 107(34) (2010) 15211-6.

[177] S.H. Moon, S.W. Kang, S.J. Park, D. Bae, S.J. Kim, H.A. Lee, K.S. Kim, K.S. Hong, J.S. Kim, J.T. Do, K.H. Byun, H.M. Chung, The use of aggregates of purified cardiomyocytes derived from human ESCs for functional engraftment after myocardial infarction, Biomaterials 34(16) (2013) 4013-26.

[178] O. Caspi, I. Huber, I. Kehat, M. Habib, G. Arbel, A. Gepstein, L. Yankelson, D. Aronson, R. Beyar, L. Gepstein, Transplantation of human embryonic stem cell-derived cardiomyocytes improves myocardial performance in infarcted rat hearts, J Am Coll Cardiol 50(19) (2007) 1884-93.

[179] T.E. Robey, M.K. Saiget, H. Reinecke, C.E. Murry, Systems approaches to preventing transplanted cell death in cardiac repair, Journal of molecular and cellular cardiology 45(4) (2008) 567-81.

[180] B.M. Ogle, N. Bursac, I. Domian, N.F. Huang, P. Menasche, C.E. Murry, B. Pruitt, M. Radisic, J.C. Wu, S.M. Wu, J. Zhang, W.H. Zimmermann, G. Vunjak-Novakovic, Distilling complexity to advance cardiac tissue engineering, Sci Transl Med 8(342) (2016) 342ps13.

[181] F. Weinberger, K. Breckwoldt, S. Pecha, A. Kelly, B. Geertz, J. Starbatty, T. Yorgan, K.H. Cheng, K. Lessmann, T. Stolen, M. Scherrer-Crosbie, G. Smith, H. Reichenspurner, A. Hansen, T. Eschenhagen, Cardiac repair in guinea pigs with human engineered heart tissue from induced pluripotent stem cells, Science translational medicine 8(363) (2016) 363ra148.

[182] K.A. Gerbin, X. Yang, C.E. Murry, K.L. Coulombe, Enhanced Electrical Integration of Engineered Human Myocardium via Intramyocardial versus Epicardial Delivery in Infarcted Rat Hearts, PLoS One 10(7) (2015) e0131446.

[183] W.Y. Lee, H.J. Wei, W.W. Lin, Y.C. Yeh, S.M. Hwang, J.J. Wang, M.S. Tsai, Y. Chang, H.W. Sung, Enhancement of cell retention and functional benefits in myocardial

infarction using human amniotic-fluid stem-cell bodies enriched with endogenous ECM, Biomaterials 32(24) (2011) 5558-67.

[184] B.R. Desroches, P. Zhang, B.R. Choi, M.E. King, A.E. Maldonado, W. Li, A. Rago, G. Liu, N. Nath, K.M. Hartmann, B. Yang, G. Koren, J.R. Morgan, U. Mende, Functional scaffold-free 3-D cardiac microtissues: a novel model for the investigation of heart cells, Am J Physiol Heart Circ Physiol 302(10) (2012) H2031-42.

[185] J.M. Kelm, V. Djonov, S.P. Hoerstrup, C.I. Guenter, L.M. Ittner, F. Greve, A. Hierlemann, C.D. Sanchez-Bustamante, J.C. Perriard, E. Ehler, M. Fussenegger, Tissue-transplant fusion and vascularization of myocardial microtissues and macrotissues implanted into chicken embryos and rats, Tissue Eng 12(9) (2006) 2541-53.

[186] J.M. Kelm, V. Djonov, L.M. Ittner, D. Fluri, W. Born, S.P. Hoerstrup, M. Fussenegger, Design of custom-shaped vascularized tissues using microtissue spheroids as minimal building units, Tissue engineering 12(8) (2006) 2151-60.

[187] J.M. Kelm, E. Ehler, L.K. Nielsen, S. Schlatter, J.C. Perriard, M. Fussenegger, Design of artificial myocardial microtissues, Tissue Eng 10(1-2) (2004) 201-14.

[188] M.Y. Emmert, P. Wolint, N. Wickboldt, G. Gemayel, B. Weber, C.E. Brokopp, A. Boni, V. Falk, A. Bosman, M.E. Jaconi, S.P. Hoerstrup, Human stem cell-based three-dimensional microtissues for advanced cardiac cell therapies, Biomaterials 34(27) (2013) 6339-54.

[189] M.Y. Emmert, P. Wolint, S. Winklhofer, P. Stolzmann, N. Cesarovic, T. Fleischmann, T.D. Nguyen, T. Frauenfelder, R. Boni, J. Scherman, D. Bettex, J. Grunenfelder, R. Schwartlander, V. Vogel, M. Gyongyosi, H. Alkadhi, V. Falk, S.P. Hoerstrup, Transcatheter based electromechanical mapping guided intramyocardial transplantation and in vivo tracking of human stem cell based three dimensional microtissues in the porcine heart, Biomaterials 34(10) (2013) 2428-41.

[190] D.J. Richards, Y. Tan, R. Coyle, Y. Li, R. Xu, N. Yeung, A. Parker, D.R. Menick, B. Tian, Y. Mei, Nanowires and Electrical Stimulation Synergistically Improve Functions of hiPSC Cardiac Spheroids, Nano letters 16(7) (2016) 4670-8.

[191] S.R. Shin, S.M. Jung, M. Zalabany, K. Kim, P. Zorlutuna, S.B. Kim, M. Nikkhah, M. Khabiry, M. Azize, J. Kong, K.T. Wan, T. Palacios, M.R. Dokmeci, H. Bae, X.S. Tang, A. Khademhosseini, Carbon-nanotube-embedded hydrogel sheets for engineering cardiac constructs and bioactuators, ACS nano 7(3) (2013) 2369-80.

[192] V. Schmidt, J.V. Wittemann, S. Senz, U. Gosele, Silicon Nanowires: A Review on Aspects of their Growth and their Electrical Properties, Adv Mater 21 (2009) 2681-2702.

[193] V. Schmidt, J.V. Wittemann, U. Gosele, Growth, thermodynamics, and electrical properties of silicon nanowires, Chemical reviews 110(1) (2010) 361-88.

[194] B. Garipcan, S. Odabas, G. Demirel, J. Burger, S.S. Nonnenmann, M.T. Coster, E.M. Gallo, B. Nabet, J.E. Spanier, E. Piskin, In Vitro Biocompatibility of n-Type and Undoped Silicon Nanowires, Adv. Eng. Mater. 13 (2009) B3-B9.

[195] M.A. Tolli, M.P. Ferreira, S.M. Kinnunen, J. Rysa, E.M. Makila, Z. Szabo, R.E. Serpi, P.J. Ohukainen, M.J. Valimaki, A.M. Correia, J.J. Salonen, J.T. Hirvonen, H.J. Ruskoaho, H.A. Santos, In vivo biocompatibility of porous silicon biomaterials for drug delivery to the heart, Biomaterials 35(29) (2014) 8394-405.

[196] J.F. Zimmerman, R. Parameswaran, G. Murray, Y. Wang, M. Burke, B. Tian, Cellular uptake and dynamics of unlabeled freestanding silicon nanowires, Sci Adv 2(12) (2016) e1601039.

[197] N. Vermeulen, G. Haddow, T. Seymour, A. Faulkner-Jones, W. Shu, 3D bioprint me: a socioethical view of bioprinting human organs and tissues, J Med Ethics (2017).

[198] Y.S. Zhang, A. Arneri, S. Bersini, S.R. Shin, K. Zhu, Z. Goli-Malekabadi, J. Aleman, C. Colosi, F. Busignani, V. Dell'Erba, C. Bishop, T. Shupe, D. Demarchi, M. Moretti, M. Rasponi, M.R. Dokmeci, A. Atala, A. Khademhosseini, Bioprinting 3D microfibrous scaffolds for engineering endothelialized myocardium and heart-on-a-chip, Biomaterials 110 (2016) 45-59.

[199] D.B. Kolesky, K.A. Homan, M.A. Skylar-Scott, J.A. Lewis, Three-dimensional bioprinting of thick vascularized tissues, Proc Natl Acad Sci U S A 113(12) (2016) 3179-84.

[200] F.Y. Hsieh, H.H. Lin, S.H. Hsu, 3D bioprinting of neural stem cell-laden thermoresponsive biodegradable polyurethane hydrogel and potential in central nervous system repair, Biomaterials 71 (2015) 48-57.

[201] F. Pati, J. Jang, D.H. Ha, S. Won Kim, J.W. Rhie, J.H. Shim, D.H. Kim, D.W. Cho, Printing three-dimensional tissue analogues with decellularized extracellular matrix bioink, Nat Commun 5 (2014) 3935.

[202] B. Derby, Printing and prototyping of tissues and scaffolds, Science 338(6109) (2012) 921-6.

[203] M.S. Baguneid, A.M. Seifalian, H.J. Salacinski, D. Murray, G. Hamilton, M.G. Walker, Tissue engineering of blood vessels, Br J Surg 93(3) (2006) 282-90.

[204] S.M. Ravenscroft, A. Pointon, A.W. Williams, M.J. Cross, J.E. Sidaway, Cardiac Non-myocyte Cells Show Enhanced Pharmacological Function Suggestive of Contractile

Maturity in Stem Cell Derived Cardiomyocyte Microtissues, Toxicol Sci 152(1) (2016) 99-112.

[205] P. Beauchamp, W. Moritz, J.M. Kelm, N.D. Ullrich, I. Agarkova, B.D. Anson, T.M. Suter, C. Zuppinger, Development and Characterization of a Scaffold-Free 3D Spheroid Model of Induced Pluripotent Stem Cell-Derived Human Cardiomyocytes, Tissue Eng Part C Methods 21(8) (2015) 852-61.

[206] J.M. Kelm, M. Fussenegger, Microscale tissue engineering using gravity-enforced cell assembly, Trends Biotechnol 22(4) (2004) 195-202.

[207] N. Thavandiran, N. Dubois, A. Mikryukov, S. Masse, B. Beca, C.A. Simmons, V.S. Deshpande, J.P. McGarry, C.S. Chen, K. Nanthakumar, G.M. Keller, M. Radisic, P.W. Zandstra, Design and formulation of functional pluripotent stem cell-derived cardiac microtissues, Proc Natl Acad Sci U S A 110(49) (2013) E4698-707.

[208] S.J. Hollister, Porous scaffold design for tissue engineering, Nat Mater 4(7) (2005) 518-24.

[209] R. Langer, J.P. Vacanti, Tissue engineering, Science 260(5110) (1993) 920-6.

[210] V. Mironov, R.P. Visconti, V. Kasyanov, G. Forgacs, C.J. Drake, R.R. Markwald, Organ printing: tissue spheroids as building blocks, Biomaterials 30(12) (2009) 2164-74.

[211] V. Mironov, V. Kasyanov, R.R. Markwald, Organ printing: from bioprinter to organ biofabrication line, Curr Opin Biotechnol 22(5) (2011) 667-73.

[212] C. Norotte, F.S. Marga, L.E. Niklason, G. Forgacs, Scaffold-free vascular tissue engineering using bioprinting, Biomaterials 30(30) (2009) 5910-7.

[213] A.N. Mehesz, J. Brown, Z. Hajdu, W. Beaver, J.V. da Silva, R.P. Visconti, R.R. Markwald, V. Mironov, Scalable robotic biofabrication of tissue spheroids, Biofabrication 3(2) (2011) 025002.

[214] D.M. Dean, A.P. Napolitano, J. Youssef, J.R. Morgan, Rods, tori, and honeycombs: the directed self-assembly of microtissues with prescribed microscale geometries, FASEB J 21(14) (2007) 4005-12.

[215] W. Lee, V. Lee, S. Polio, P. Keegan, J.H. Lee, K. Fischer, J.K. Park, S.S. Yoo, On-demand three-dimensional freeform fabrication of multi-layered hydrogel scaffold with fluidic channels, Biotechnol Bioeng 105(6) (2010) 1178-86.

[216] T. Billiet, E. Gevaert, T. De Schryver, M. Cornelissen, P. Dubruel, The 3D printing of gelatin methacrylamide cell-laden tissue-engineered constructs with high cell viability, Biomaterials 35(1) (2014) 49-62.

[217] K. Pataky, T. Braschler, A. Negro, P. Renaud, M.P. Lutolf, J. Brugger, Microdrop printing of hydrogel bioinks into 3D tissue-like geometries, Adv Mater 24(3) (2012) 391-6.

[218] C. Xu, W. Chai, Y. Huang, R.R. Markwald, Scaffold-free inkjet printing of three-dimensional zigzag cellular tubes, Biotechnol Bioeng 109(12) (2012) 3152-60.

[219] J.A. Rowley, G. Madlambayan, D.J. Mooney, Alginate hydrogels as synthetic extracellular matrix materials, Biomaterials 20(1) (1999) 45-53.

[220] N.C. Hunt, R.M. Shelton, D.J. Henderson, L.M. Grover, Calcium-alginate hydrogel-encapsulated fibroblasts provide sustained release of vascular endothelial growth factor, Tissue Eng Part A 19(7-8) (2013) 905-14.

[221] N.C. Hunt, R.M. Shelton, L.M. Grover, Reversible mitotic and metabolic inhibition following the encapsulation of fibroblasts in alginate hydrogels, Biomaterials 30(32) (2009) 6435-43.

[222] G. Orive, A.M. Carcaboso, R.M. Hernandez, A.R. Gascon, J.L. Pedraz, Biocompatibility evaluation of different alginates and alginate-based microcapsules, Biomacromolecules 6(2) (2005) 927-31.

[223] A.B. Lansdown, M.J. Payne, An evaluation of the local reaction and biodegradation of calcium sodium alginate (Kaltostat) following subcutaneous implantation in the rat, J R Coll Surg Edinb 39(5) (1994) 284-8.

[224] K. Smetana, Jr., Cell biology of hydrogels, Biomaterials 14(14) (1993) 1046-50.

[225] A.D. Augst, H.J. Kong, D.J. Mooney, Alginate hydrogels as biomaterials, Macromol Biosci 6(8) (2006) 623-33.

[226] C.K. Kuo, P.X. Ma, Ionically crosslinked alginate hydrogels as scaffolds for tissue engineering: part 1. Structure, gelation rate and mechanical properties, Biomaterials 22(6) (2001) 511-21.

[227] A.C.U.G.L.S.D.J.M.J. McGrath, Calcium-sensitivity of smooth muscle contraction in the isolated perfused rat tail artery, African Journal of Biomedical Research 5(1-2) (2002).

[228] C.E. Yellowley, J.C. Hancox, H.J. Donahue, Effects of cell swelling on intracellular calcium and membrane currents in bovine articular chondrocytes, J Cell Biochem 86(2) (2002) 290-301.

[229] I. Raizman, J.N. De Croos, R. Pilliar, R.A. Kandel, Calcium regulates cyclic compression-induced early changes in chondrocytes during in vitro cartilage tissue formation, Cell Calcium 48(4) (2010) 232-42.

[230] K.H. Kang, L.A. Hockaday, J.T. Butcher, Quantitative optimization of solid freeform deposition of aqueous hydrogels, Biofabrication 5(3) (2013) 035001.

[231] E.E. Robinson, K.M. Zazzali, S.A. Corbett, R.A. Foty, Alpha5beta1 integrin mediates strong tissue cohesion, J Cell Sci 116(Pt 2) (2003) 377-86.

[232] V.L. Roger, A.S. Go, D.M. Lloyd-Jones, R.J. Adams, J.D. Berry, T.M. Brown, M.R. Carnethon, S. Dai, G. de Simone, E.S. Ford, C.S. Fox, H.J. Fullerton, C. Gillespie, K.J. Greenlund, S.M. Hailpern, J.A. Heit, P.M. Ho, V.J. Howard, B.M. Kissela, S.J. Kittner, D.T. Lackland, J.H. Lichtman, L.D. Lisabeth, D.M. Makuc, G.M. Marcus, A. Marelli, D.B. Matchar, M.M. McDermott, J.B. Meigs, C.S. Moy, D. Mozaffarian, M.E. Mussolino, G. Nichol, N.P. Paynter, W.D. Rosamond, P.D. Sorlie, R.S. Stafford, T.N. Turan, M.B. Turner, N.D. Wong, J. Wylie-Rosett, C. American Heart Association Statistics, S. Stroke Statistics, Heart disease and stroke statistics--2011 update: a report from the American Heart Association, Circulation 123(4) (2011) e18-e209.

[233] J.L. Mignone, K.L. Kreutziger, S.L. Paige, C.E. Murry, Cardiogenesis from human embryonic stem cells, Circ J 74(12) (2010) 2517-26.

[234] S.S. Nunes, J.W. Miklas, J. Liu, R. Aschar-Sobbi, Y. Xiao, B. Zhang, J. Jiang, S. Masse, M. Gagliardi, A. Hsieh, N. Thavandiran, M.A. Laflamme, K. Nanthakumar, G.J. Gross, P.H. Backx, G. Keller, M. Radisic, Biowire: a platform for maturation of human pluripotent stem cell-derived cardiomyocytes, Nat Methods 10(8) (2013) 781-7.

[235] S.D. Lundy, W.Z. Zhu, M. Regnier, M.A. Laflamme, Structural and functional maturation of cardiomyocytes derived from human pluripotent stem cells, Stem Cells Dev 22(14) (2013) 1991-2002.

[236] D.K. Lieu, J.D. Fu, N. Chiamvimonvat, K.C. Tung, G.P. McNerney, T. Huser, G. Keller, C.W. Kong, R.A. Li, Mechanism-based facilitated maturation of human pluripotent stem cell-derived cardiomyocytes, Circ Arrhythm Electrophysiol 6(1) (2013) 191-201.

[237] G. Kensah, A. Roa Lara, J. Dahlmann, R. Zweigerdt, K. Schwanke, J. Hegermann, D. Skvorc, A. Gawol, A. Azizian, S. Wagner, L.S. Maier, A. Krause, G. Drager, M. Ochs, A. Haverich, I. Gruh, U. Martin, Murine and human pluripotent stem cell-derived cardiac bodies form contractile myocardial tissue in vitro, Eur Heart J 34(15) (2013) 1134-46.

[238] D. Zhang, I.Y. Shadrin, J. Lam, H.Q. Xian, H.R. Snodgrass, N. Bursac, Tissue-engineered cardiac patch for advanced functional maturation of human ESC-derived cardiomyocytes, Biomaterials 34(23) (2013) 5813-20.

[239] A. Mihic, J. Li, Y. Miyagi, M. Gagliardi, S.H. Li, J. Zu, R.D. Weisel, G. Keller, R.K. Li, The effect of cyclic stretch on maturation and 3D tissue formation of human embryonic stem cell-derived cardiomyocytes, Biomaterials 35(9) (2014) 2798-808.

[240] V.W. Schmidt, J. V.; Senz, S.; Gosele, U., Silicon Nanowires: A Review on Aspects of their Growth and their Electrical Properties, Adv Mater 21(25-26) (2009) 2681-2702.

[241] B. Tian, C.M. Lieber, Synthetic nanoelectronic probes for biological cells and tissues, Annu Rev Anal Chem (Palo Alto Calif) 6 (2013) 31-51.

[242] Bora Garipcan, Sedat Odabas, Gokhan Demirel, Joan Burger, Stephen S. Nonnenmann, Michael T. Coster, Eric M. Gallo, Bahram Nabet, Jonathan E. Spanier, E. Piskin, In Vitro Biocompatibility of n-Type and Undoped Silicon Nanowires, Adv Mater 13(1-2) (2011) B3-B9.

[243] K. Jiang, D. Fan, Y. Belabassi, G. Akkaraju, J.L. Montchamp, J.L. Coffer, Medicinal surface modification of silicon nanowires: impact on calcification and stromal cell proliferation, ACS Appl Mater Interfaces 1(2) (2009) 266-9.

[244] D. K. Nagesha, M. A. Whitehead, J.L. Coffer, Biorelevant Calcification and Non-Cytotoxic Behavior in Silicon Nanowires, Adv Mater 17(7) (2005) 921-924.

[245] S. H. C. Anderson, H. Elliott, D. J. Wallis, L. T. Canham, J.J. Powell, Dissolution of different forms of partially porous silicon wafers under simulated physiological conditions, physica status solidi A 197(2) (2003) 331-335.

[246] W. Zhou, X. Dai, T.M. Fu, C. Xie, J. Liu, C.M. Lieber, Long term stability of nanowire nanoelectronics in physiological environments, Nano Lett 14(3) (2014) 1614-9.

[247] G. Zheng, W. Lu, S. Jin, C.M. Lieber, Synthesis and Fabrication of High-Performance n-Type Silicon Nanowire Transistors, adv Mater 16(21) (2004) 1890-1893.

[248] A.P. Mazzoleni, B.F. Sisken, R.L. Kahler, Conductivity values of tissue culture medium from 20 degrees C to 40 degrees C, Bioelectromagnetics 7(1) (1986) 95-9.

[249] M. Radisic, H. Park, H. Shing, T. Consi, F.J. Schoen, R. Langer, L.E. Freed, G. Vunjak-Novakovic, Functional assembly of engineered myocardium by electrical stimulation of cardiac myocytes cultured on scaffolds, Proc Natl Acad Sci U S A 101(52) (2004) 18129-34.

[250] P. Beauchamp, C. Choby, T. Desplantez, K. de Peyer, K. Green, K.A. Yamada, R. Weingart, J.E. Saffitz, A.G. Kleber, Electrical propagation in synthetic ventricular myocyte strands from germline connexin43 knockout mice, Circ Res 95(2) (2004) 170-8.

[251] P. Beauchamp, T. Desplantez, M.L. McCain, W. Li, A. Asimaki, G. Rigoli, K.K. Parker, J.E. Saffitz, A.G. Kleber, Electrical coupling and propagation in engineered ventricular myocardium with heterogeneous expression of connexin43, Circ Res 110(11) (2012) 1445-53.

[252] J.O. You, M. Rafat, G.J. Ye, D.T. Auguste, Nanoengineering the heart: conductive scaffolds enhance connexin 43 expression, Nano Lett 11(9) (2011) 3643-8.

[253] V. Martinelli, G. Cellot, F.M. Toma, C.S. Long, J.H. Caldwell, L. Zentilin, M. Giacca, A. Turco, M. Prato, L. Ballerini, L. Mestroni, Carbon Nanotubes Instruct Physiological Growth and Functionally Mature Syncytia: Nongenetic Engineering of Cardiac Myocytes, ACS nano (2013).

[254] P. Rana, B. Anson, S. Engle, Y. Will, Characterization of human-induced pluripotent stem cell-derived cardiomyocytes: bioenergetics and utilization in safety screening, Toxicol Sci 130(1) (2012) 117-31.

[255] T.M. Casey, P.G. Arthur, Hibernation in noncontracting mammalian cardiomyocytes, Circulation 102(25) (2000) 3124-9.

[256] M. Radisic, J. Malda, E. Epping, W. Geng, R. Langer, G. Vunjak-Novakovic, Oxygen gradients correlate with cell density and cell viability in engineered cardiac tissue, Biotechnol Bioeng 93(2) (2006) 332-43.

[257] N.H. van den Heuvel, T.A. van Veen, B. Lim, M.K. Jonsson, Lessons from the heart: mirroring electrophysiological characteristics during cardiac development to in vitro differentiation of stem cell derived cardiomyocytes, J Mol Cell Cardiol 67 (2014) 12-25.

[258] A.G. Rodriguez, S.J. Han, M. Regnier, N.J. Sniadecki, Substrate stiffness increases twitch power of neonatal cardiomyocytes in correlation with changes in myofibril structure and intracellular calcium, Biophys J 101(10) (2011) 2455-64.

[259] G. Bub, P. Camelliti, C. Bollensdorff, D.J. Stuckey, G. Picton, R.A. Burton, K. Clarke, P. Kohl, Measurement and analysis of sarcomere length in rat cardiomyocytes in situ and in vitro, Am J Physiol Heart Circ Physiol 298(5) (2010) H1616-25.

[260] M. Heron, D.L. Hoyert, S.L. Murphy, J. Xu, K.D. Kochanek, B. Tejada-Vera, Deaths: final data for 2006, Natl Vital Stat Rep 57(14) (2009) 1-134.

[261] X. Lian, C. Hsiao, G. Wilson, K. Zhu, L.B. Hazeltine, S.M. Azarin, K.K. Raval, J. Zhang, T.J. Kamp, S.P. Palecek, Robust cardiomyocyte differentiation from human pluripotent stem cells via temporal modulation of canonical Wnt signaling, Proc Natl Acad Sci U S A 109(27) (2012) E1848-57.

[262] M.A. Laflamme, J. Gold, C. Xu, M. Hassanipour, E. Rosler, S. Police, V. Muskheli, C.E. Murry, Formation of human myocardium in the rat heart from human embryonic stem cells, Am J Pathol 167(3) (2005) 663-71.

[263] M.E. Anderson, J. Goldhaber, S.R. Houser, M. Puceat, M.A. Sussman, Embryonic stem cell-derived cardiac myocytes are not ready for human trials, Circ Res 115(3) (2014) 335-8.

[264] G. Eng, B.W. Lee, L. Protas, M. Gagliardi, K. Brown, R.S. Kass, G. Keller, R.B. Robinson, G. Vunjak-Novakovic, Autonomous beating rate adaptation in human stem cell-derived cardiomyocytes, Nat Commun 7 (2016) 10312.

[265] S.H. Bhang, S.W. Cho, W.G. La, T.J. Lee, H.S. Yang, A.Y. Sun, S.H. Baek, J.W. Rhie, B.S. Kim, Angiogenesis in ischemic tissue produced by spheroid grafting of human adipose-derived stromal cells, Biomaterials 32(11) (2011) 2734-47.

[266] R. Glicklis, J.C. Merchuk, S. Cohen, Modeling mass transfer in hepatocyte spheroids via cell viability, spheroid size, and hepatocellular functions, Biotechnol Bioeng 86(6) (2004) 672-80.

[267] D.A. Brown, W.R. MacLellan, H. Laks, J.C. Dunn, B.M. Wu, R.E. Beygui, Analysis of oxygen transport in a diffusion-limited model of engineered heart tissue, Biotechnol Bioeng 97(4) (2007) 962-75.

[268] W.L. Rumsey, C. Schlosser, E.M. Nuutinen, M. Robiolio, D.F. Wilson, Cellular energetics and the oxygen dependence of respiration in cardiac myocytes isolated from adult rat, J Biol Chem 265(26) (1990) 15392-402.

[269] K.K. Papas, C.K. Colton, R.A. Nelson, P.R. Rozak, E.S. Avgoustiniatos, W.E. Scott, 3rd, G.M. Wildey, A. Pisania, G.C. Weir, B.J. Hering, Human islet oxygen consumption rate and DNA measurements predict diabetes reversal in nude mice, Am J Transplant 7(3) (2007) 707-13.

[270] D.C. Nguyen, T.A. Hookway, Q. Wu, R. Jha, M.K. Preininger, X. Chen, C.A. Easley, P. Spearman, S.R. Deshpande, K. Maher, M.B. Wagner, T.C. McDevitt, C. Xu, Microscale generation of cardiospheres promotes robust enrichment of cardiomyocytes derived from human pluripotent stem cells, Stem Cell Reports 3(2) (2014) 260-8.

[271] T.J. Bartosh, J.H. Ylostalo, A. Mohammadipoor, N. Bazhanov, K. Coble, K. Claypool, R.H. Lee, H. Choi, D.J. Prockop, Aggregation of human mesenchymal stromal

cells (MSCs) into 3D spheroids enhances their antiinflammatory properties, Proc Natl Acad Sci U S A 107(31) (2010) 13724-9.

[272] X. Li, X. Liu, Y. Tan, V. Tran, N. Zhang, X. Wen, Improve the viability of transplanted neural cells with appropriate sized neurospheres coated with mesenchymal stem cells, Med Hypotheses 79(2) (2012) 274-7.

[273] Bora Garipcan, Sedat Odabas, Gokhan Demirel, Joan Burger, Stephen S. Nonnenmann, Michael T. Coster, Eric M. Gallo, Bahram Nabet, Jonathan E. Spanier, E. Piskin, In Vitro Biocompatibility of n-Type and Undoped Silicon Nanowires, advanced engineering materials 13(1-2) (2011) B3-B9.

[274] Y. He, C. Fan, S. Lee, Silicon nanostructures for bioapplications, Nano Today 5(4) (2010) 282-295.

[275] A. Vreeker, L. van Stuijvenberg, T.J. Hund, P.J. Mohler, P.G. Nikkels, T.A. van Veen, Assembly of the cardiac intercalated disk during pre- and postnatal development of the human heart, PLoS One 9(4) (2014) e94722.

[276] K. Sekine, Y. Kagawa, E. Maeyama, H. Ota, Y. Haraguchi, K. Matsuura, T. Shimizu, Oxygen consumption of human heart cells in monolayer culture, Biochem Biophys Res Commun 452(3) (2014) 834-9.

[277] R.H. Hoyt, M.L. Cohen, J.E. Saffitz, Distribution and three-dimensional structure of intercellular junctions in canine myocardium, Circ Res 64(3) (1989) 563-74.

[278] H.J. Cho, H.J. Lee, Y.J. Chung, J.Y. Kim, H.J. Cho, H.M. Yang, Y.W. Kwon, H.Y. Lee, B.H. Oh, Y.B. Park, H.S. Kim, Generation of human secondary cardiospheres as a potent cell processing strategy for cell-based cardiac repair, Biomaterials (2012).

[279] W.Y. Lee, H.J. Wei, J.J. Wang, K.J. Lin, W.W. Lin, D.Y. Chen, C.C. Huang, T.Y. Lee, H.Y. Ma, S.M. Hwang, Y. Chang, H.W. Sung, Vascularization and restoration of heart function in rat myocardial infarction using transplantation of human cbMSC/HUVEC core-shell bodies, Biomaterials 33(7) (2012) 2127-36.

[280] Y. Tan, D. Richards, R.C. Coyle, J. Yao, R. Xu, W. Gou, H. Wang, D.R. Menick, B. Tian, Y. Mei, Cell number per spheroid and electrical conductivity of nanowires influence the function of silicon nanowired human cardiac spheroids, Acta Biomater 15(51) (2017) 495-504.

[281] L.M. Popescu, A. Curici, E. Wang, H. Zhang, S. Hu, M. Gherghiceanu, Telocytes and putative stem cells in ageing human heart, J Cell Mol Med 19(1) (2015) 31-45.

[282] C.A. Souders, S.L. Bowers, T.A. Baudino, Cardiac fibroblast: the renaissance cell, Circ Res 105(12) (2009) 1164-76.